



António João Camões Alves

**Study, modelling, and dynamic analysis of  
construction solutions for doors and  
windows of buildings**

**Universidade do Minho**  
Escola de Engenharia







**Universidade do Minho**  
Escola de Engenharia

António João Camões Alves

**Study, modelling, and dynamic analysis of  
construction solutions for doors and  
windows of buildings**

Dissertação de Mestrado

Mestrado em Engenharia Mecânica

Trabalho efetuado sob a orientação de

**Professor Doutor Nuno Ricardo Maia Peixinho**

**Professor Doutor Vítor Hugo Pimenta Carneiro**

**Professor Doutor João Pedro Mendonça Assunção Silva**

maio de 2022

## **DIREITOS DE AUTOR E CONDIÇÕES DE UTILIZAÇÃO DO TRABALHO POR TERCEIROS**

Este é um trabalho académico que pode ser utilizado por terceiros desde que respeitadas as regras e boas práticas internacionalmente aceites, no que concerne aos direitos de autor e direitos conexos.

Assim, o presente trabalho pode ser utilizado nos termos previstos na licença abaixo indicada.

Caso o utilizador necessite de permissão para poder fazer um uso do trabalho em condições não previstas no licenciamento indicado, deverá contactar o autor, através do RepositóriUM da Universidade do Minho.

### ***Licença concedida aos utilizadores deste trabalho***



**Atribuição-NãoComercial-SemDerivações**

**CC BY-NC-ND**

<https://creativecommons.org/licenses/by-nc-nd/4.0/>

# AGRADECIMENTOS

Ao Sr. Joaquim Nogueira, por ter lançado o desafio e ter proporcionado todas as condições para que o trabalho pudesse prosseguir na JFAN Steel.

Ao Engenheiro Orlando Rodrigues, por todo o conhecimento, confiança, prestabilidade, apoio e amizade, que motivaram e acompanharam toda a dissertação.

Aos Professores Nuno Peixinho e Vítor Carneiro, pelas numerosas reuniões, encaminhamentos, lições e entusiasmo que motivou e facilitou a dissertação desde o início, assim como pela confiança, que permitiu que a dissertação chegasse aonde pretendia.

Ao Professor João Mendonça, por todo o envolvimento e fluidez que incutiu na relação entre a Universidade do Minho e a JFAN Steel.

Ao Sr. Fernando Araújo, Engenheiro Sérgio Carvalho e Engenheiro Filipe Marques, do DEM, pelos conselhos e auxílios nos diversos experimentos realizados ao longo da dissertação.

Ao Professor António Brito e ao técnico, pela ajuda nos ensaios de tração da Poliamida.

Aos trabalhadores da JFAN Steel, que de uma forma ou de outra estiveram envolvidos no projeto, partilhando e expondo o conhecimento gerado da sua arte.

À Sofia Alves pela companhia ao longo deste ano que tornou este projeto mais agradável.

Às amigas que deixo na Universidade pelas memórias e companheirismo que me ofereceram, e às amigas que levo pelas memórias e companheirismo que me vão dar.

Às amigas que trago do secundário, algumas do infantário, que provaram ser duradouras e pelas quais tenho muita estima.

À Inês, a minha namorada de sete anos, por quem eu tenho um enorme apreço. A minha confidente, a minha Amiga, a minha paixão.

À minha família, inclusive aos que já partiram, por contribuírem para o meu crescimento e para a pessoa que me tornei.

À Mariana, a minha irmã, que chata e empertigada, quer sempre o meu bem. Com quem eu sempre pude e sei que sempre posso contar, um pilar na minha vida.

Aos meus pais, a quem eu devo tudo. Por investirem na minha educação, pelas lições de trabalho, por me chamarem à razão no tempo certo, por todos os atos de bondade que demonstraram e que presenciei, e por tudo que faria esta lista continuar, pois todas essas coisas definem hoje o meu carácter. São a minha bússola moral. Fica a dedicatória e espero que estejam orgulhosos.

## **STATEMENT OF INTEGRITY**

I hereby declare having conducted this academic work with integrity. I confirm that I have not used plagiarism or any form of undue use of information or falsification of results along the process leading to its elaboration.

I further declare that I have fully acknowledged the Code of Ethical Conduct of the University of Minho.

## RESUMO

Recentes exigências do mercado levaram a que portas e janelas compostas por vidros e caixilhos com corte térmico sejam produzidas pela JFAN Steel com dimensões não abrangidas pelas classes de certificação dadas pelo fornecedor do caixilho (Secco). As classes de certificação, acompanhadas pela marcação CE, são dadas com base num conjunto de testes que uma porta ou uma janela deve suportar. Para aumentar as hipóteses destes sistemas passarem nos testes estruturais, foi selecionado um caso de estudo de um sistema porta com duas folhas para testar a influencia de diferentes reforços. Os testes à resistência do sistema às cargas verticais, à torção estática, e à carga de vento foram escolhidos como os mais críticos. Foi também criado um critério para avaliar o desempenho do sistema exposto a um terremoto, devido à preocupação relativamente ao comportamento vibratório dos sistemas em certas regiões geográficas do mercado. Primeiramente, os caixilhos, que têm uma secção composta por dois componentes metálicos (latão, aço corten, aço galvanizado, ou aço inoxidável) separados por um núcleo polimérico (poliamida no meio e poliuretano nos lados), tiveram algumas propriedades do latão, aço inoxidável, e poliamida verificadas através de ensaios de tração e densidade, enquanto as propriedades dos outros materiais foram verificadas em paralelo pela empresa. Um caixilho foi testado à flexão em três pontos após ter sido utilizado para uma análise modal experimental, e os dados destas experiências foram utilizados para avaliar os modelos do caixilho. Um modelo analítico, um de elementos de viga, um de elementos sólidos, e um que utiliza elementos de viga e de casca foram utilizados para capturar o comportamento estático e dinâmico do caixilho. Este último mostrou os resultados mais promissores, e foi selecionado para integrar o modelo do caso de estudo. Em seguida, os três testes mencionados foram simulados com o modelo do sistema caso de estudo, onde foram testadas diferentes configurações de reforços colocados dentro do caixilho com módulos de elasticidade distintos, bem como algumas melhorias da vidraça. As melhorias da vidraça, apesar de aumentarem muito o peso do sistema, provaram ser a melhor opção para aumentar o seu desempenho. Simulações simplificadas através de análises harmónicas deram confiança na resistência do sistema a um terremoto de intensidade instrumental V, no entanto, foram utilizadas algumas simplificações no próprio modelo. Finalmente, uma análise térmica numérica baseada na normalização europeia mostrou alterações insignificantes na transmitância térmica do sistema com a introdução dos reforços internos de aço.

**Palavras-chave:** análise modal, flexão em três pontos, viga com vários materiais, testes da normalização europeia, transmitância térmica



# ABSTRACT

Recent market demands require JFAN Steel to produce doors and windows comprised of glazing and frames with a thermal break and with dimensions that are not covered by the certification classes given by the frame's supplier (Secco). The certification classes, accompanied by the CE marking, are given based on a set of tests that a door or a window must endure. To increase the structural test passing rate, a case study of a double leafed door system was selected and used in this work to test out the influence of different reinforcements. The tests of the system's resistance to vertical loads, static torsion, and wind load were isolated as the most critical ones. Additionally, a criterion to evaluate the performance of the system exposed to an earthquake was created as a concern regarding the vibratory behaviour of the systems in certain geographic regions of the company's market. Firstly, the multi-material beams, that have a section comprised of two metallic components (brass, corten steel, galvanized steel, or stainless steel) separated by a polymeric core (polyamide in the middle and polyurethane at the sides) had some properties of brass, stainless steel, and polyamide verified through tensile and density tests, while the properties of the other materials were parallelly verified by the company. A multi-material beam underwent a three-point bending experiment after being used for experimental modal analysis, and the data from these experiments was later used to evaluate the models of the beam. An analytical model, a beam elements model, a solid elements model, and a model that uses beam and shell elements were used to capture the static and dynamic behaviour of the multi-material beam. The latter showed the more promising results and was selected to integrate the model of the case study system. Then, the three mentioned tests were simulated with the model of the case study system, where different configurations of reinforcements placed inside the frames with distinct elastic modulus as well as some glazing improvements were tested. Despite increasing the weight of the system, the glazing improvements proved to be the best option for increasing the overall performance. Simplified simulations through harmonic analyses gave confidence in the strength of the system to withstand an earthquake of instrumental intensity V, however, some simplifications were used in the model itself. Lastly, a numerical thermal analysis based on the European standardization showed insignificant changes in the thermal transmittance of the system with the introduction of the internal steel reinforcements.

**Keywords:** European standardization tests, modal analysis, multi-material beam, thermal transmittance, three-point bending

# TABLE OF CONTENTS

<b>Agradecimientos</b> .....	iii
<b>Resumo</b> .....	vi
<b>Abstract</b> .....	vii
<b>Table of Contents</b> .....	viii
<b>List of Figures</b> .....	xii
<b>List of Tables</b> .....	xxiv
<b>List of Symbols</b> .....	xxv
<b>List of Abbreviations</b> .....	xxx
<b>Chapter 1 Introduction</b> .....	1
1.1 Objectives .....	2
1.2 Chapters' Layout.....	3
<b>Chapter 2 System Definition and Review of CE Standardization</b> .....	4
2.1 Door System .....	4
2.1.1 Frame Structure .....	7
2.1.2 Glazing.....	11
2.1.3 Hardware .....	15
2.2 Problem Definition/CE Marking Tests .....	17
2.2.1 Mechanical Durability and Operating Forces.....	19
2.2.2 Resistance to Vertical Loads.....	20
2.2.3 Resistance to Static Torsion .....	21
2.2.4 Resistance to Body Impact.....	22
2.2.5 Resistance to Wind Load.....	23
2.2.6 Air Permeability and Watertightness .....	25
2.2.7 Thermal Transmittance.....	26
2.2.8 Dynamic Vibration Test.....	31
<b>Chapter 3 Experimental Tests</b> .....	34
3.1 Tensile Test.....	34

3.1.1	Test Specimens .....	34
3.1.2	Equipment.....	35
3.1.3	Procedures.....	36
3.1.4	Data Treatment .....	37
3.1.5	Material Properties and Bilinear Model .....	38
3.2	Determination of Density .....	43
3.2.1	Method Overview .....	43
3.2.2	Specimens .....	45
3.2.3	Equipment.....	45
3.2.4	Procedure .....	46
3.2.5	Data Treatment .....	47
3.2.6	Properties.....	47
3.3	Three-Point Bending.....	48
3.3.1	Test Specimen.....	48
3.3.2	Equipment and Setup .....	49
3.3.3	Procedure .....	50
3.3.4	Data Treatment .....	51
3.4	Experimental Modal Analysis .....	51
3.4.1	Hammer Impulse Method Brief Overview .....	51
3.4.2	Equipment and Setup .....	53
3.4.3	Procedure .....	54
3.4.4	Data Treatment .....	54
3.4.5	Half-Power Bandwidth Method .....	55
<b>Chapter 4 Analytical Methods .....</b>		<b>56</b>
4.1	Governing Equation of the Elastic Curve of a Multi-Material Beam.....	57
4.2	Principal Axis of a Multi-Material Beam with an Unsymmetrical Cross-Section .....	61
4.3	Natural Frequencies and Vibration Modes of a Multi-Material Beam.....	66
4.3.1	Transverse vibration.....	66
4.3.2	Longitudinal vibration.....	71

4.4	Three-Point Bending of a Multi-Material Beam .....	75
<b>Chapter 5 Numerical Methods .....</b>		<b>77</b>
5.1	Simulation notes .....	77
5.2	Multi-Material Beam Models .....	80
5.2.1	Beam Elements Model.....	80
5.2.2	Solid elements model .....	86
5.2.3	Beam + Shell model .....	94
5.3	Door System .....	98
5.3.1	Frame Structure .....	101
5.3.2	Glazing.....	103
5.3.3	Locking Points .....	112
5.3.4	Resistance to Wind Loads .....	118
5.3.5	Resistance to Static Torsion .....	120
5.3.6	Resistance to Vertical Loads.....	121
5.3.7	Dynamic Vibrations Test .....	123
5.3.8	Thermal Transmittance.....	124
<b>Chapter 6 Results and Discussion .....</b>		<b>128</b>
6.1	Multi-Material Beam .....	128
6.1.1	Three-Point Bending .....	128
6.1.2	Structural Optimization .....	133
6.1.3	Multi-Material Beam Torsion .....	133
6.1.4	Multi-Material Beam's Vibration.....	134
6.2	Door System .....	140
6.2.1	Resistance to Wind Loads .....	140
6.2.2	Resistance to Static Torsion .....	145
6.2.3	Resistance to Vertical Loads.....	149
6.2.4	Dynamic Vibrations Test .....	153
6.2.5	Change in Thermal Transmittance .....	156

<b>Chapter 7 General Conclusions and Future Work</b> .....	158
7.1 General Conclusions.....	158
7.2 Future Work .....	161
<b>References</b> .....	162
<b>Annex A Profiles and DLD Component’s Dimensions</b> .....	170
A.1 Multi-Material Beam’s Profiles .....	170
A.2 DLD System .....	172
A.3 Hardware .....	174
<b>Annex B ISO 10077-2:2017 Software Validation and Infilling Gas Thermal Conductivity</b> .....	176
B.1 ISO 10077-2:2017 Validation .....	176
B.2 Infilling Gas Equivalent Thermal Conductivity .....	177
<b>Annex C Validation of the Numerical Models</b> .....	180
C.1 Beam Elements Model: Verification of Mesh Independence .....	180
C.2 Beam + Shell Model: Verification of Mesh Independence.....	180
C.3 Solid Elements Model: Verification of Mesh Independence.....	181
C.4 Model of the DLD System: Verification of Mesh Independence and Influence of Other Modelling Choices .....	182
<b>Annex D Internal Reinforcement’s Material Selection</b> .....	185
<b>Annex E Numerical Analysis of the Brass Tensile Test and Tensile Test Specimens’ Technical Drawings</b> .....	190
E.1 Numerical Analysis of the Brass Tensile Test .....	190
E.2 Tensile Test Specimens’ Technical Drawings .....	191
<b>Annex F Simulation strategies for dynamic and static behaviour of composite beams</b> .....	194

# LIST OF FIGURES

**Figure 2.1.** Double leafed door from a project in Sicilia, Italy [4]. ..... 5

**Figure 2.2.** Closed DLD with general dimensions and its different components. .... 6

**Figure 2.3.** Detailed section view of the connections between the glazing and the frames on the Side (A) and on the centre (B)..... 7

**Figure 2.4.** MMB with the P.2992 profile (A) and rollers that shape a sheet to achieve the final metal components of the beam (B). Figure B reproduced from [11]. ..... 8

**Figure 2.5.** Brackets used in the connection between frames with the P.2962 and P.2963 profiles (A), exterior (B) and interior (C) views the corner of a system. Figure A reproduced from [10], and figures B and C reproduced from [11]. ..... 11

**Figure 2.6.** Glazing with the detail that allows for the introduction of the locking mechanism. .... 13

**Figure 2.7.** Hypothetical variation of the internal cavity’s volume by an amount  $\Delta V$ , due to a reduction in pressure outside glass panel 1, had glass panes 2 and 3 remained in place. This does not happen due to the load that the change in pressure incites on glass panels 2 and 3, which instead deform as well. .... 14

**Figure 2.8.** Complete hinge set (A) and hinge placement between the fixed and movable frames (B). Image A adapted from [10]. ..... 15

**Figure 2.9.** Drawing of the lock (A), lock assembled on the frame of the primary leaf (B), and steel plate assembled on the secondary leaf, where the lock plugs itself. Figure A adapted from [10]. ..... 16

**Figure 2.10.** Placement of the locking mechanism between the movable frames (A), assembled plug pin (B), assembled socket (C), and drawing of the locking mechanism above the main lock in an engaged position (D). Figure D reproduced [10]. ..... 16

**Figure 2.11.** Drawing of the locking mechanism (A), steel pin that moves when the locking mechanism is activated (B), and side view of the locking mechanism engaged, where the pin is already through the steel plate (C). Figures A and C reproduced from [10]. ..... 17

**Figure 2.12.** Difference between systems with profiles of the OS2 75 and the OS2 65 series, reproduced from [11]. ..... 18

**Figure 2.13.** Apparatus of the test from EN 947:1999, where the displayed values have units in degrees and millimetres. A load is applied on the end of the top of the leaf, and a gauge records deformations on the end of the bottom of the leaf. Reproduced from [25]. ..... 20

<b>Figure 2.14.</b> Apparatus of the test from EN 948:1999, where the displayed values have units in degrees and millimetres. The top corner of the leaf is fixed, and a load is applied in the bottom corner, where a gauge, on the other side of the leaf records the measurements. Reproduced from [26].	21
<b>Figure 2.15.</b> Apparatus of the test from EN 13049:2004, where an impactor works as a pendulum and is dropped from a certain height hitting the door system when its kinetic energy is at the maximum. Adapted from [28].	22
<b>Figure 2.16.</b> Points where the deflection is measured by the gauges (Based on tests already performed using EN 12211:2016 on DLD).	24
<b>Figure 2.17.</b> Test sequence with the timing of the different operations, timings of the gauge measurements, test pressures and how they are achieved, and when other related tests must be performed. Adapted from [30].	25
<b>Figure 2.18.</b> Projected area viewed from the interior ( $A_{r,i}$ ) and the exterior ( $A_{r,e}$ ), and area of the glazing ( $A_g$ ), ignoring the rubber gaskets. Adapted from [36].	27
Figure 2.19 – Surfaces thermal resistances, dimensional parameters and boundary conditions presented in ISO 10077-2:2017, for a frame connection example with a double glazing. Adapted from [37].	28
<b>Figure 2.20.</b> Distinct types of cavities considered by ISO 10077-2:2017: Unventilated cavities(A), slightly ventilated cavities (B and C), and well-ventilated cavities (D and E). Adapted from [37].	29
<b>Figure 2.21.</b> Reduction of the interior surface thermal resistance when $d_s < 30$ mm, hence $b_s = d_s$ (A), when the $b_s > 30$ mm, and the junction involves a sloped surface (B), and when $d_s > 30$ , and $b_s = 30$ mm (C). Adapted from [37].	30
<b>Figure 2.22.</b> Spectral densities of earthquakes and winds. Adapted from [43].	32
<b>Figure 2.23.</b> The PGA of an earthquake and correspondent instrumental intensity, among other parameters. Reproduced from [50].	33
<b>Figure 3.1.</b> Brass (A) and PA (B) test specimens numbered and with the length of the central region marked.	35
<b>Figure 3.2.</b> Instron 8874 (A) and Zwick/Roell z005 (B) testing machines.	35
<b>Figure 3.3.</b> PA test specimen (A) and brass test specimen (B) with a mechanical strain gauge mounted and ready for the tensile test.	36
<b>Figure 3.4.</b> Initial length of the central region, $L_c$ , and initial length, $L_0$ , of the brass and PA test specimens.	37
<b>Figure 3.5.</b> Brass experimental stress strain curve for the elastic region of the three test specimens, which are differentiated by colour. The elastic modulus was found from the slope of the line equations,	

and the yield strength from the intersection with the curves of lines of the same slope that cross the strain axis at 0,002. .... 39

**Figure 3.6.** Conceptual plot of the bilinear hardening model (green) of brass with the engineering (orange) and true (blue) curves stress-strain curves. .... 40

**Figure 3.7.** True stress - true strain curve of the PA test specimen 4, with the elastic region in yellow used for the calculation of the elastic modulus, the plastic region in green, where the curve approximates to a linear behaviour, and from where the tangent modulus was found, and the yield point, in red. Before the elastic region, an artefact, no representative of the material's behaviour can be observed. .... 41

**Figure 3.8.** True stress – true stain curves from the PA test specimen's tensile test. .... 42

**Figure 3.9.** Free body diagrams of the specimen when out (A) and immersed (B) in water. The grey rectangle symbolizes the scale, which is set to zero, before the introduction of the specimen, and that displays the mass and apparent mass, when the specimen is out (A) or immersed in water (B). .... 44

**Figure 3.10.** Test specimens of brass, stainless steel and PA (from top to bottom) used in the experiment and numbered for each material. .... 45

**Figure 3.11.** Equipment used in the density experiment: a DU-32 Argo Lab digital ultrasonic cleaner (1), a hair dryer (2), rubber ear wash ball (3), a set of tweezers (4), and an aluminium foil container with ethanol (5). Additionally, a Mettler AE240 precision analytical digital balance scale with a small structure to support the test specimens and a beaker with distilled water were used but are missing from this image. .... 46

**Figure 3.12.** Mettler AE240 precision analytical digital balance scale with a small structure to support the stainless steel test specimen (A), and the same setup but with a beaker filled with distilled water, where the specimen is submerged (B). .... 47

**Figure 3.13.** Brass MMB with a P.2992 profile, during the three-point bending experimental test. ... 48

**Figure 3.14.** Schematic setup of the three-point bending experiment, with the diameter of the loading pin and of the supports, the distance between supports, as well as a picture of the whole setup, and close-ups to the centre and to the support pin. .... 49

**Figure 3.15.** Digital gauge with a magnetic base on a steel table for the measurement of the residual deformation on the MMB, after the three-point bending experiment. Black lines can be seen every 50 mm that mark the measuring points, and the gauge is set to zero on the first measured extremity. .... 50

**Figure 3.16.** Difference between an idealized impulse function, and the practical application of this concept. Reality images reproduced from [65]. .... 52



<b>Figure 3.17.</b> Setup of the experimental modal analysis, where the analogue signals from the hammer and accelerometer were converted into digital signals in the LMS Scadas mobile, that was controlled by a laptop running the LMS Test.Xpress, that stores and processes the signals.....	54
<b>Figure 3.18.</b> Schematic of half-power bandwidth method on a resonant frequency. Based on the representation of the method from [68].....	55
<b>Figure 4.1.</b> The internal moments from the five components of a MMB compose the internal bending moment that results from applying the external loads. ....	57
<b>Figure 4.2.</b> Representation of the cross-section of the equivalent beam, from the cross-section of an MMB, where the material of the different components influences the weight of its elemental areas in the equivalent beam's cross-section. In this case, equivalent beam is illustrated by expanding each elemental area by the correspondent factor $n_i$ in a direction parallel to the axis of rotation. The variables $d$ and $b$ represent the distance between the centroid of a component's cross-section and the neutral plane of the equivalent beam or the axis of the CAD software, respectively. ....	59
<b>Figure 4.3.</b> $b_i$ , $A_i$ and $I_i'$ , taken from SpaceClaim for the metal component highlighted in orange, of the P.2942 profile. ....	60
<b>Figure 4.4.</b> Point Q and three coordinate systems (CS), where CS 3 shares an origin with CS 2, but its axes are rotated, and CS2 is translated in relation to CS 1.....	61
<b>Figure 4.5.</b> Forces and moments acting on an elemental portion with infinitesimal length of the MMB subjected to bending. ....	67
<b>Figure 4.6.</b> Five first bending mode shapes of a free-free beam. ....	71
<b>Figure 4.7.</b> Axial forces and displacements acting on an element infinitesimal length, due to deformation in the axial direction.....	71
<b>Figure 4.8.</b> Beam of length $L$ subjected to a load $P_c$ at the centre.....	75
<b>Figure 5.1.</b> Beam elements model modelling, starting with the dwg file (A), extruding solid beams (B), extracting beam bodies from the solids (C), making the cross-section of this bodies visible (D), and giving offsets to the different cross-sections with the beam bodies in place (E), so that they were considered in the right position by the software in the simulation. ....	82
<b>Figure 5.2.</b> Mesh from the three-point bending simulation of the beam elements model, with the cross-section of the elements graphically displayed. ....	83
<b>Figure 5.3.</b> B.C. on the three-point bending (A) and torsion (B) simulations of the beam elements model. ....	85

<b>Figure 5.4.</b> SOLID186 element, with the different shapes it can take, by merging some nodes (A) (reproduced from [81]), and P.2972 profile (B). .....	86
<b>Figure 5.5.</b> Mesh from the three-point bending simulation of the solid elements model, and the slashes done in the geometry, from two perspectives (A and B), and geometry (C) and mesh (D) of the extremity of the solid elements model from the structural optimization simulation. In A, the letter P is pointing towards the small space on the cross-section, where contact was defined near the loading pin. ....	88
<b>Figure 5.6.</b> Mesh from the torsion simulation of the solid elements model, with a detail view of the cross-section. ....	89
<b>Figure 5.7.</b> Connections from the three-point bending simulation, where the red faces represent the contacts, and the faces in blue represent the target, although some are hiding from this perspective. ....	90
<b>Figure 5.8.</b> Boundary conditions of the three-point bending (A), torsion (B), and structural optimization (C) using solid elements models. ....	92
<b>Figure 5.9.</b> Points on the bottom (A) and top (B) of the MMB's centre used to find the displacements, for the force-displacement curves, and paths created on the bottom and on top, to find the residual deformation, along the length of the beam (C). ....	93
<b>Figure 5.10.</b> Modified input drawing to introduce the central line, which would be used to create the surface (A), beam bodies and surface created (B) and joined together (C). ....	95
<b>Figure 5.11.</b> Mesh from the three-point bending simulation of the beam + shell model, with the cross-section of the elements graphically displayed. ....	96
<b>Figure 5.12.</b> B.C. on the three-point bending (A) and torsion (B) simulations of the beam + shell model. ....	97
<b>Figure 5.13.</b> DLD model, discretized and with a few details, which show the original, and graphical representation of the beams and surfaces' cross-sections. From this graphical representation, it was possible to verify that the orientation of the beam elements was correct. ....	99
<b>Figure 5.14.</b> Unreinforced central junction (A), screws modelled with joints that only allow rotation around the Z axis (B), frictionless connection between the fixed frame (red) and the surface (blue) that mimics a wall (C), central junction with a complete reinforcement (D), and with an optimized reinforcement (E). The internal reinforcements could not occupy one of the cavities since it is occupied by rods and other components of the locking mechanism. ....	102
<b>Figure 5.15.</b> Configurations of internal reinforcement's locations tested: on all locations (A), partially located (B), and only at the centre (C). ....	103

**Figure 5.16.** Three defined regions for the glazing (A) with the geometry cut to facilitate mesh generation and connections, sizings defined on the edges of the spacer region viewed from outside (B) and from inside the glazing (C) represented by yellow cylinders, and corner of glazing after the mesh generation (D), with a courser mesh in the centre, and a finer mesh in the spacer region. .... 104

**Figure 5.17.** Graphically displayed cross-sections of the surfaces and offsets of the glazing (A and B, near the lock), and of the polymeric part of the frame on the connection from the secondary leaf to the fixed frame, at the centre of the system (C). In this image, the layered surfaces don't have their layers with distinct colours, and only the thickness and the offset are noticeable..... 106

**Figure 5.18.** Connection between the beam bodies of the frame (red) and the edges of the spacer region of the glazing (blue) (A), beams created on the interior and exterior from the beam formulation viewed perpendicularly to the façade (B) and from a different angle (C), pinball from all connections between the frame and the glazing (D), and these connections, displayed in the post-processing in green (E), along with the hardware connections that are in red, except for the lock that is also in green. .... 107

**Figure 5.19.** HSFLD242 element, with the pressure node Q (A), tire with HSFLD242 created with positive (B) and negative (C) volumes, and faces' normal of the cavity's walls of the primary leaf closer to the exterior pointing to the inside of the cavity. In D, a face highlighted in the detail can be seen, pointing away from the pressure point M, that was responsible for compensating the positive volume that goes through the outside of the cavity, as well as the duplicated positive volume that was created from the pressure node, up to the lock area, leaving the cavity with the correct volume. .... 109

**Figure 5.20.** APDL commands for the creation of HSFLD242 elements on the cavity of the primary leaf closer to the exterior. Adapted and rewritten from [81], [86]–[88]. .... 110

**Figure 5.21.** APDL commands for the creation of an image with the HSFLD242 elements created in the simulation. Adapted from [89]...... 111

**Figure 5.22.** Image with the HSFLD242 elements created in the simulation, with the elements of the different cavities with distinct colours. One detail shows the elements created outside the cavity that were two types of elements overlapped i.e., elements with positive and negative volumes. .... 111

**Figure 5.23.** Main lock geometry (A), fixed joint created with the beam formulation to represent the lock (B), and joints created to represent the plug and socket mechanism of the lock between the primary and secondary leaf's frames (C). On the surfaces 1 and 3, a layered section of PU (5,6 mm) – PA (0,8 mm) – PU (2,6 mm) – Steel (3 mm), with the steel layer on the further side of the correspondent glazing. On C, the joints have freedom in the translational X (red vector) and Z (blue vector) directions, as well as on the rotations about the Y axis (green vector). .... 113

**Figure 5.24.** Hinge joint with the detail of the dummy beam (A), mesh near the hinge (B), lateral view of the hinge without (C) and with (D) cross-sections graphically displayed, and joint connections as well as beam formulations created around the hinges (E). The hinge joints only allow rotation on the Z axis (blue vector), and on B, excluding the dummy beams, the grey beam elements represent the location of the internal reinforcements of the hinge. .... 114

**Figure 5.25.** Joint representing the AC2695S locking device (A), which had fixed the translations between the two remote points in the Y direction (green vector) and the rotations about the Z axis (blue vector). This joint was defined through constraint equations (B). .... 116

**Figure 5.26.** Joint connecting the secondary leaf to the fixed frame in the centre of the system (A), geometry simplification of the pin mechanism (B), and mesh around the joint (C). In surface 1 (sizing of 1 mm), a layered section of PU (5,6 mm) – PA (0,8 mm) – PU (5,6 mm) – Steel (3 mm) was specified with the steel layer closer to the leaves. Surface 2 had a layered section of PU (5,6 mm) – PA (0,8 mm) – PU (3,6 mm) – Aluminium (2 mm), and surface 3 had a layered section of PU (5,6 mm) – PA (0,8 mm) – PU (2,6 mm) – Steel (5 mm), with the metal layers on both surfaces, placed on the side further from the glazing. Additionally, on surfaces 1 and 3, an offset was given. .... 118

**Figure 5.27.** Loads and constraints of the wind pressure test simulations, without the joints that fix the screw holes to the ground. The pressure was applied on transition and centre surfaces on the exterior side of the glazing, and the fixed support was applied on the wall surface and is not present in the figure. .... 119

**Figure 5.28.** Loads and constraints of the static torsion test simulations, without the joints that fix the screw holes to the ground. The loads and remote displacements were applied on the elemental faces, as can be seen in the detail, and the fixed support was applied on the wall surface and is not present in the figure. .... 121

**Figure 5.29.** Loads and constraints of the vertical loads test simulations, without the joints that fix the screw holes to the ground. The loads and remote displacements were applied on the elemental faces, as can be seen in the detail, and the fixed support was applied on the wall surface and is not present in the figure. .... 122

**Figure 5.30.** Harmonic acceleration of 0,092g in the Z direction, X and Y directions, from three different simulations. .... 123

**Figure 5.31.** Geometry, mesh, and materials colour coded with the correspondent  $\lambda$ , of the two models (side and centre sections) in the thermal transmittance simulation. The details show the material colour of the spacer (aluminium) and the introduction of the insulation panel [37]. .... 125

<b>Figure 5.32.</b> B.C. in the in the thermal transmittance simulation, where the red edges were made adiabatic, and the other edges (that don't represent cuts on the glazing) had a convection B.C. applied. The green edges with a film coefficient of 25 W/(m <sup>2</sup> K) (at 273,15 K), and the blue and colourless edges with a film coefficient of 7,6923 W/(m <sup>2</sup> K) and 5 W/(m <sup>2</sup> K), respectively, at a temperature of 293,15 K. When simulating with the insulation panel, the B.C. were identical.....	126
<b>Figure 5.33.</b> Probe specified for the external B.C. in green (A) and "path" that was used to find the average value of the directional heat flux, perpendicular to the façade. ....	127
<b>Figure 6.1.</b> P.2992 1600 mm brass MMB before (A) and after (B) the abrupt change in stiffness that concluded the experiment. In B a perceptible drawback in the lower brass component is perceptible when compared to A, which exposes the sliding between this component and the rest of the MMB, that is also perceptible in C. The deformation on the MMB could be captured with some detail by the solid elements model, as can be seen, e.g., by the gap that occurs in the top face (D).....	129
<b>Figure 6.2.</b> Initial part of the force-displacement curve of all the brass MMB numerical and analytical models defined as well as of the physical MMB (A), and complete curve of the solid elements model and of the physical MMB, on the top and lower face at the centre (B). In figure B, the detail P highlights the point where the final and sudden drop in stiffness took place. ....	130
<b>Figure 6.3.</b> Deformation at the end of the MMB by a factor of 40 for the numerical models, where the beam elements model is the only one who keeps the cross-section of the MMB in-plane. ....	132
<b>Figure 6.4.</b> Residual deformation along the length of the P.2992 brass MMB on the bottom (A) and top (B) faces, from the experimental test and solid elements model.....	132
<b>Figure 6.5.</b> Results before and after the structural optimization simulation of a 1600 mm brass MMB with the P.2972 profile, where the optimized geometry is in a light blue. ....	133
<b>Figure 6.6.</b> Torsional stiffness and behaviour from the simulation of a MMB with 1600 mm of length and the P.2992 profile, using the beam elements, beam + shell, and solid elements models. ....	134
<b>Figure 6.7.</b> FRF from the experimental modal analysis of a 1600 mm brass MMB with the P.2992 profile, with the frequencies of the peaks displayed next to them. ....	135
<b>Figure 6.8.</b> Study of the natural frequency of the torsional mode shape of a 1600 mm P.2992 brass MMB, considering the same elastic modulus for the two polymers, and parameterizing this value. The values of the first three natural frequencies with bending mode shapes are also depicted in this image. ....	137
<b>Figure 6.9.</b> Stress on the beam elements from the resistance to the wind loads test simulation of the unreinforced brass DLD system. ....	140

**Figure 6.10.** Maximum displacement on the frame structure and relative increase in stiffness against the elastic modulus of the reinforcement for the brass (A and B), corten steel (C and D), and galvanized steel (E and F) DLD systems, from the wind loads test simulations. Charts continue in Figure 6.11, where the legend is presented..... 142

**Figure 6.11.** Maximum displacement on the frame structure (G) and relative increase in stiffness (H) against the elastic modulus of the reinforcement for the stainless steel DLD system, from the wind loads test simulations. .... 143

**Figure 6.12.** Maximum displacement on the frame structure (A) and relative increase in stiffness against (B) the outer glass panels thickness for the brass, corten steel, galvanized steel, and stainless steel DLD systems, from the wind loads test simulations..... 144

**Figure 6.13.** Stress on the beam elements from the resistance to static torsion test simulation of the unreinforced brass DLD system. .... 145

**Figure 6.14.** Maximum displacement on the frame structure and relative increase in stiffness against the elastic modulus of the reinforcement for the brass, corten steel (CS), galvanized steel (GS), and stainless steel (SS) DLD systems in the primary (A and B) and secondary (C and D) leaves, from the static torsion test simulations. .... 147

**Figure 6.15.** Maximum displacement on the frame structure and relative increase in stiffness against the outer glass panels thickness for the brass, corten steel, galvanized steel, and stainless steel DLD systems in the primary (A and B) and secondary (C and D) leaves, from the resistance to static torsion test simulations. .... 148

**Figure 6.16.** Stress on the beam elements from the resistance to vertical loads test simulation of the unreinforced brass DLD system. .... 150

**Figure 6.17.** Maximum displacement on the frame structure and relative increase in stiffness against the elastic modulus of the reinforcement for the brass, corten steel (CS), galvanized steel (GS), and stainless steel (SS) DLD systems in the primary (A and B) and secondary (C and D) leaves, from the vertical loads test simulations. .... 151

**Figure 6.18.** Maximum displacement on the frame structure and relative increase in stiffness against the outer glass panels thickness for the brass, corten steel, galvanized steel, and stainless steel DLD systems in the primary (A and B) and secondary (C and D) leaves, from the resistance to vertical loads test simulations. .... 152

<b>Figure 6.19.</b> First three mode shapes of the DLD brass system. For clearness, the images of the 2 <sup>nd</sup> and 3 <sup>rd</sup> modes only show the middle glass panel, as the two outer glass panels, were just blue surfaces, meaning they were not excited.....	154
<b>Figure 6.20.</b> FRFs of the amplitude of the frame structure in the direction of the harmonic acceleration (X, Y, and Z), and FRFs with more resolution around the highest peak. ....	155
<b>Figure 6.21.</b> Colour coded temperature after the thermal simulation on the reinforced and unreinforced side cross-sections of the DLD brass system. ....	157
<b>Figure A.1.</b> Additional MMBs used in the modal analyses with the beam elements model and in the analytical model to find the first natural frequencies with bending and longitudinal mode shapes. The dimensions are in millimetres, the grey area represents the base metal, the orange area represents the PU, and the white area limited by an orange line represents the PA. ....	170
<b>Figure A.2.</b> MMBs and bead profiles used for the DLD system. The MMBs were also used in the modal analyses with the beam elements model and in the analytical model to find the first natural frequencies with bending and longitudinal mode shapes. The dimensions are in millimetres, the grey area represents the base metal, the orange area represents the PU, and the white area limited by an orange line represents the PA. ....	171
<b>Figure A.3.</b> MMBs profiles used in the structural optimization (P.2972) and experimental tests, three-point bending, torsion and modal analyses simulations with the beam + shell model, and solid elements model (P.2992). Both profiles were used in the modal analyses with the beam elements model and in the analytical model to find the first natural frequencies with bending and longitudinal mode shapes. The P.2992 model was also used in the three-point bending analytical model and three-point bending, torsion simulations with the beam elements model. The dimensions are in millimetres, the grey area represents the base metal, the orange area represents the PU, and the white area limited by an orange line represents the PA. ....	171
<b>Figure A.4.</b> Dimensions in millimetres between the different components of the system, needed for the definition of the DLD numerical model. The locking devices are illustrated in red, the hinges in blue, the screws in green, and the frame and glazing drawn with black lines. ....	172
<b>Figure A.5.</b> Detailed section view of the connections between the glazing and the frames on the Side (A) and on the centre (B), with some dimensions in millimetres between the components, needed for the definition of the DLD numerical model. ....	173
<b>Figure A.6.</b> Main lock dimensions in millimetres on the primary (A) and secondary (B) leaves that were used in the definition of the DLD numerical model. ....	174

<b>Figure A.7.</b> Hinge dimensions in millimetres that were used in the definition of the DLD numerical model.....	174
<b>Figure A.8.</b> AC2695S when the primary leaf stops onto the secondary leaf (A), the device after it is activated and locks above (B) and below (C) the main lock, and the position of the device on the frames. The dimensions in millimetres were used in the definition of the DLD numerical model.....	175
<b>Figure A.9.</b> Simplified geometry of the AC2621 RX locking device (A), the plate on the fixed frame (B), and the position of the device on the frame. The dimensions in millimetres were used in the definition of the DLD numerical model. ....	175
<b>Figure B.1.</b> Sections from ISO 10077-2:2017 that were simulated, to validate the software [37]. The colour profile of the sections represents the Temperature distribution under the steady state conditions of the simulation. The images of the sections had their insulation panels and glazing slashed, so that they could be presented in a more compact manner, and even though sections D.8 and D.9, are form a roller shutter box and PVC shutter profile, respectively, they were still tested. ....	176
<b>Figure B.2.</b> Different thermal resistance components in series, in the middle of the glazing, without the influence of the aluminium spacer or the frame.....	178
<b>Figure C.1.</b> Verification of mesh independence on the three-point bending (A), torsion (B), and undamped modal (C) simulations with the beam elements model of a P.2992 MMB with 1600 mm of length.....	180
<b>Figure C.2.</b> Verification of mesh independence on the three-point bending (A), torsion (B), and undamped modal (C) simulations with the beam + shell model of a P.2992 frame with 1600 mm of length.....	181
<b>Figure C.3.</b> Verification of mesh independence on the three-point bending (A), torsion (B), and undamped modal (C) simulations with the solid elements model of a P.2992 MMB with 1600 mm of length.....	182
<b>Figure C.4.</b> Verification of mesh independence on the maximum displacement on the frame structure (A) and on the maximum combined stress on the beam elements of the frame structure (B), in the wind loads test simulation of the DLD system. The lack of convergence from the maximum principal stress on the glass panels for small models can be seen in C.....	183
<b>Figure D.1.</b> Ashby chart from Matmach, resultant of the application filter: “Aerospace Structures”, “Composite Reinforcements”, “Building Structures”, “Construction Materials”, “Other Shafts & Couplings” and “General Automotive Parts”. In the chart, the minimum elastic modulus defined was	



draws by a red line, the material index for a bending application of a beam is circled in green, and four groups are highlighted by black circles (A, B, C, and D). Adapted from [97]. ..... 186

**Figure D.2.** Price per unite weight for materials. The shaded band spans the range where the most widely used commodity materials of manufacture and construction. Reproduced from [96]. ..... 188

**Figure E.1.** Boundary conditions (A), mesh (B), and results of the elastic component of the strain in the X direction (B) of the simulation of the brass test specimen's the tensile test. .... 190

# LIST OF TABLES

<b>Table 2.1.</b> Mechanical and physical properties of the metals given by the supplier [11].	9
<b>Table 2.2.</b> Mechanical and physical properties of the polymers given by the supplier.	9
<b>Table 2.3.</b> Mechanical and physical properties of PU, Galvanized Steel, and Corten Steel given by JFAN Steel.	10
<b>Table 2.4.</b> Mechanical and physical properties of tempered glass and AL3003 [14]–[16].	13
<b>Table 2.5.</b> Tests and their correspondent standards used by Secco for the certification of doors and windows.	18
<b>Table 3.1.</b> Properties found from the brass and PA tensile tests, with relative error to the supplier’s brass and the PBT properties, respectively.	42
<b>Table 3.2.</b> Material’s density from the experiment, with the relative error calculated from the values given by the supplier for the same materials, except the PA, where the error is in relation to the PBT.	48
<b>Table 4.1.</b> First five solutions to Equation 4-63.	70
<b>Table 5.1.</b> Ansys Workbench modules used and their objective.	78
<b>Table 6.1.</b> Comparison of the natural and resonant frequencies of a 1600 mm brass MMB with the P.2992 profile, between the results from the analytical and different numerical models, and from the experimental modal analysis.	136
<b>Table 6.2.</b> 1 <sup>st</sup> , 2 <sup>nd</sup> and 3 <sup>rd</sup> bending, 1 <sup>st</sup> torsional, and 1 <sup>st</sup> longitudinal mode shapes, resultant from the modal analyses of a P.2992 brass MMB with 1600 mm of length using the beam elements, beam + shell, and solid elements models.	138
<b>Table 6.3.</b> Comparison of the natural frequencies with bending (1 <sup>st</sup> and 2 <sup>nd</sup> ) and longitudinal (1 <sup>st</sup> ) mode shapes between the analytical and the beam elements models, of 1600 mm brass MMBs with all the OS2 75 profiles.	139
<b>Table 6.4.</b> Thermal transmittance of the frame ( $U_f$ ), door ( $U_d$ ), and linear thermal transmittance ( $\Psi_g$ ) of reinforced and unreinforced DLD systems with all base metals.	156
<b>Table B.1.</b> Thermal conductance and thermal transmittance validation results for cases D.1 to D.9 of ISO 10077-2:2017 [37].	177
<b>Table B.2.</b> Thermal conductance and linear thermal transmittance validation for the case D.10 of ISO 10077-2:2017.	177
<b>Table C.1.</b> Influence of additional changes in the model of the DLD system.	184

# LIST OF SYMBOLS

(By order of appearance)

## Chapter 2

$\rho$	• Density [ $\text{kg m}^{-3}$ ]
$\lambda$	• Thermal conductivity [ $\text{W m}^{-1} \text{K}^{-1}$ ]
$E$	• Elastic modulus in MPa [Pa]
$\nu$	• Poisson's ratio [ - ]
$\Delta P$	• Pressure variation [Pa]
$\Delta V\%$	• Relative change in volume
$P_{\text{atm}}$	• Atmospheric pressure [Pa]
$F_{\text{rp}}$	• Relative frontal deflection
$U_{\text{W/D}}$	• Thermal transmittance of the window/door [ $\text{W m}^{-2} \text{K}^{-1}$ ]
$U_{\text{f}}$	• Thermal transmittance of the frame [ $\text{W m}^{-2} \text{K}^{-1}$ ]
$U_{\text{g}}$	• Thermal transmittance of the glazing [ $\text{W m}^{-2} \text{K}^{-1}$ ]
$A_{\text{f}}$	• Projected area of the frame [ $\text{m}^2$ ]
$A_{\text{f,i}}$	• Projected area of the frame from an interior perspective [ $\text{m}^2$ ]
$A_{\text{f,e}}$	• Projected area of the frame from an exterior perspective [ $\text{m}^2$ ]
$A_{\text{g}}$	• Projected area of the glazing [ $\text{m}^2$ ]
$\Psi_{\text{g}}$	• Linear thermal transmittance [ $\text{W m}^{-1} \text{K}^{-1}$ ]
$l_{\text{g}}$	• Total perimeter of the glazing [m]
$\lambda_{\text{eq}}$	• Equivalent thermal transmittance [ $\text{W m}^{-1} \text{K}^{-1}$ ]
$rR_{\text{si}}$	• Reduced interior surface thermal resistance [ $\text{m}^2 \text{K W}^{-1}$ ]
$R_{\text{si}}$	• Interior surface thermal resistance [ $\text{m}^2 \text{K W}^{-1}$ ]
$R_{\text{se}}$	• Exterior surface thermal resistance [ $\text{m}^2 \text{K W}^{-1}$ ]
$\Delta T$	• Temperature difference [K]
$b_{\text{f}}$	• Width of the frame [m]
$b_{\text{g}}$	• Width of the glazing in the simulation [m]
$b_{\text{c}}$	• Width of the cavity's entrance [m]

$L_f^{2D}$		▪ Two-dimensional thermal conductance [ $W\ m^{-1}\ K^{-1}$ ]
$L_\Psi^{2D}$		

### Chapter 3

$\sigma$		▪ Engineering stress [Pa]
$\varepsilon$		
$\bar{\sigma}$		▪ True stress [Pa]
$\bar{\varepsilon}$		
$A$		▪ area [ $m^2$ ]
$\Delta L$		
$L_0$		▪ Specimen length variation [m]
$L_0$		
$\vec{F}_b$		▪ Initial specimen length [m]
$\vec{F}_b$		
$\vec{W}$		▪ Buoyancy force [N]
$\vec{W}$		
$\vec{R}$		▪ Weight [N]
$\vec{R}$		
$\vec{W}_{ap}$		▪ Reaction force [N]
$\vec{W}_{ap}$		
$\rho_{water}$		▪ Apparent weight [N]
$\rho_{water}$		
$V$		▪ Density of water [ $kg\ m^{-3}$ ]
$V$		
$g$		▪ Volume [ $m^3$ ]
$g$		
$m$		▪ Earth's acceleration of gravity [ $m\ s^{-2}$ ]
$m$		
$m_{ap}$		▪ Mass [kg]
$m_{ap}$		
$\xi$		▪ Apparent mass [kg]
$\xi$		
$\omega_r$		▪ Damping ratio [ - ]
$\omega_r$		
$\omega_r$		▪ Resonance frequency [ $rad\ s^{-1}$ ]
$\omega_r$		

### Chapter 4

$M$		▪ Moment [N m]
$M_i$		
$E_i$		▪ Moment from component i [N m]
$E_i$		
$I_i$		▪ Elastic modulus of component i [Pa]
$I_i$		
$E_b$		▪ Second moment of area relative to the MMB's neutral plane of component i [ $m^4$ ]
$E_b$		
$I_{eq}$		▪ Elastic modulus of the base material of the equivalent beam [Pa]
$I_{eq}$		
$I_{eq}$		▪ Second moment of area of the equivalent beam [ $m^4$ ]
$I_{eq}$		

$n_i$	<ul style="list-style-type: none"> <li>▪ Ratio between the elastic modulus of component i and of the base material of the equivalent beam [ - ]</li> </ul>
$\bar{Y} \vee \bar{Z}$	<ul style="list-style-type: none"> <li>▪ Distance of the centroid of the section of the equivalent beam to the axis of a coordinate system [m]</li> </ul>
$b_i$	<ul style="list-style-type: none"> <li>▪ Distance of the centroid of the section of the component I to the software's axis</li> </ul>
$I_i'$	<ul style="list-style-type: none"> <li>▪ Second moment of area of component i [m<sup>4</sup>]</li> </ul>
$A_i$	<ul style="list-style-type: none"> <li>▪ Transversal area of component i [m<sup>2</sup>]</li> </ul>
$d_i$	<ul style="list-style-type: none"> <li>▪ Distance between the neutral plane of component i and the neutral plane of the equivalent beam [m]</li> </ul>
$I_{zz}^B$	<ul style="list-style-type: none"> <li>▪ Second moment of area about the z principal axis of coordinate system B [m<sup>4</sup>]</li> </ul>
$I_{yy}^B$	<ul style="list-style-type: none"> <li>▪ Second moment of area about the y principal axis of coordinate system B [m<sup>4</sup>]</li> </ul>
$I_{zy}^B$	<ul style="list-style-type: none"> <li>▪ Product moment of area on coordinate system B [m<sup>4</sup>]</li> </ul>
$I_{zz}^A$	<ul style="list-style-type: none"> <li>▪ Second moment of area about the z axis of coordinate system A [m<sup>4</sup>]</li> </ul>
$I_{yy}^A$	<ul style="list-style-type: none"> <li>▪ Second moment of area about the y axis of coordinate system A [m<sup>4</sup>]</li> </ul>
$I_{zy}^A$	<ul style="list-style-type: none"> <li>▪ Product moment of area on coordinate system A [m<sup>4</sup>]</li> </ul>
$I_{zz,i}^B$	<ul style="list-style-type: none"> <li>▪ Second moment of area of component i about the z principal axis of coordinate system B, relative to the MMB's centroid [m<sup>4</sup>]</li> </ul>
$I_{yy,i}^B$	<ul style="list-style-type: none"> <li>▪ Second moment of area of component i about the y principal axis of coordinate system B, relative to the MMB's centroid [m<sup>4</sup>]</li> </ul>
$I_{zy,i}^B$	<ul style="list-style-type: none"> <li>▪ Product moment of area of component i on coordinate system B, relative to the MMB's centroid [m<sup>4</sup>]</li> </ul>
$I_{zz,i}^A$	<ul style="list-style-type: none"> <li>▪ Second moment of area of component i about the z axis of coordinate system A, relative to the MMB's centroid [m<sup>4</sup>]</li> </ul>
$I_{yy,i}^A$	<ul style="list-style-type: none"> <li>▪ Second moment of area of component i about the y axis of coordinate system A, relative to the MMB's centroid [m<sup>4</sup>]</li> </ul>
$I_{zy,i}^A$	<ul style="list-style-type: none"> <li>▪ - Product moment of area of component i on coordinate system A, relative to the MMB's centroid [m<sup>4</sup>]</li> </ul>
$I_{zy,i}^A$	<ul style="list-style-type: none"> <li>▪ - Product moment of area of component i on coordinate system A [m<sup>4</sup>]</li> </ul>
$I_{zz,beam}^B$	<ul style="list-style-type: none"> <li>▪ - Second moment of area of the equivalent beam about the z principal axis of coordinate system B [m<sup>4</sup>]</li> </ul>

$I_{yy,beam}^B$	<ul style="list-style-type: none"> <li>▪ - Second moment of area of the equivalent beam about the y principal axis of coordinate system B [m<sup>4</sup>]</li> </ul>
$I_{zy,beam}^B$	<ul style="list-style-type: none"> <li>▪ Product moment of area of the equivalent beam on coordinate system B [m<sup>4</sup>]</li> </ul>
$I_{zz,beam}^A$	<ul style="list-style-type: none"> <li>▪ Second moment of area of the equivalent beam about the z axis of coordinate system A [m<sup>4</sup>]</li> </ul>
$I_{yy,beam}^A$	<ul style="list-style-type: none"> <li>▪ Second moment of area of the equivalent beam about the y axis of coordinate system A [m<sup>4</sup>]</li> </ul>
$I_{zy,beam}^A$	<ul style="list-style-type: none"> <li>▪ Product moment of area of the equivalent beam on coordinate system A [m<sup>4</sup>]</li> </ul>
$Q$	<ul style="list-style-type: none"> <li>▪ Transversal load [N]</li> </ul>
$\rho_i$	<ul style="list-style-type: none"> <li>▪ Density of the material of component i [kg m<sup>-3</sup>]</li> </ul>
$\omega_n$	<ul style="list-style-type: none"> <li>▪ N<sup>th</sup> natural frequency [rad s<sup>-1</sup>]</li> </ul>
$L$	<ul style="list-style-type: none"> <li>▪ MMB's length [m]</li> </ul>
$P$	<ul style="list-style-type: none"> <li>▪ Axial force on the MMB [N]</li> </ul>
$P_i$	<ul style="list-style-type: none"> <li>▪ Axial force on component i [N]</li> </ul>
$P_C$	<ul style="list-style-type: none"> <li>▪ Central load on the three-point bending [N]</li> </ul>
$M_{0 \rightarrow L/2}$	<ul style="list-style-type: none"> <li>▪ Moment from x=0 to x=L/2 [N m]</li> </ul>
$M_{L/2 \rightarrow L}$	<ul style="list-style-type: none"> <li>▪ Moment from x=L/2 to x=L [N m]</li> </ul>
$y_{0 \rightarrow L/2}$	<ul style="list-style-type: none"> <li>▪ Vertical displacement from x=0 to x=L/2 [m]</li> </ul>
$y_{L/2 \rightarrow L}$	<ul style="list-style-type: none"> <li>▪ Vertical displacement from x=L/2 to x=L [m]</li> </ul>
$y_{max}$	<ul style="list-style-type: none"> <li>▪ Maximum vertical displacement [m]</li> </ul>

## Chapter 5

$\{F\}$	<ul style="list-style-type: none"> <li>▪ Force vector [N]</li> </ul>
$\{u\}$	<ul style="list-style-type: none"> <li>▪ Displacement vector [m]</li> </ul>
$\{\dot{u}\}$	<ul style="list-style-type: none"> <li>▪ Velocity vector [m s<sup>-1</sup>]</li> </ul>
$\{\ddot{u}\}$	<ul style="list-style-type: none"> <li>▪ Acceleration vector [m s<sup>-2</sup>]</li> </ul>
$[K]$	<ul style="list-style-type: none"> <li>▪ Stiffness matrix [N m<sup>-1</sup>]</li> </ul>
$[M]$	<ul style="list-style-type: none"> <li>▪ Mass matrix [kg]</li> </ul>
$[D]$	<ul style="list-style-type: none"> <li>▪ Damping matrix [N s m<sup>-1</sup>]</li> </ul>
$\omega_i$	<ul style="list-style-type: none"> <li>▪ Natural frequencies (eigenvalues) [rad s<sup>-1</sup>]</li> </ul>
$\{\Phi\}_i$	<ul style="list-style-type: none"> <li>▪ Mode shapes (eigenvectors) [ - ]</li> </ul>

$\alpha$	• Mass constant of the Rayleigh damping [ $s^{-1}$ ]
$\beta$	• Stiffness constant of the Rayleigh damping [s]
$\xi_i$	• Damping ratio at a natural frequency $i$ [-]
$\Omega$	• Imposed circular frequency [ $rad\ s^{-1}$ ]
$u_x$	• Translational displacement in the x direction [m]
$u_y$	• Translational displacement in the y direction [m]
$u_z$	• Translational displacement in the z direction [m]
$rot_x$	• Rotation in the x direction [rad]
$rot_y$	• Rotation in the y direction [rad]
$rot_z$	• Rotation in the z direction [rad]
$k$	• Stiffness [ $N\ m^{-1}$ ]
$\delta$	• Displacement [m]

## Annex B

$R_g$	• Thermal resistance on the centre of the glazing [ $m^2\ K\ W^{-1}$ ]
$\Delta x_i$	• Thickness of element $i$ [m]
$\lambda_i$	• Thermal conductivity of element $i$ [ $W\ m^{-1}\ K^{-1}$ ]
$\lambda_{infill}$	• Equivalent thermal conductivity of the infilling gas cavity [ $W\ m^{-1}\ K^{-1}$ ]

# LIST OF ABBREVIATIONS

(By order of appearance)

MMB	▪ Multi-Material Beam
EEA	▪ European Economic Area
DLD	▪ Double Leafed Door
PU	▪ Polyurethane
PA	▪ Polyamide
PBT	▪ Polybutylene terephthalate
PVB	▪ Polyvinyl Butyral
B.C.	▪ Boundary Conditions
PSD	▪ Power Spectral Density
PGA	▪ Peak Ground Acceleration
PHGA	▪ Peak Horizontal Ground Acceleration
FRF	▪ Frequency Response Function
DFT	▪ Discrete Fourier Transform
FFT	▪ Fast Fourier Transform
SNR	▪ Signal to Noise Ratio
PDE	▪ Partial Differential Equation
ODE	▪ Ordinary Differential Equation
CAE	▪ Computer Aided Engineering
CAD	▪ Computer Aided Design
FEM	▪ Finite Element Method
MSUP	▪ Mode Superposition
DOF	▪ Degrees Of Freedom
MPC	▪ Multipoint Constraint
APDL	▪ Ansys Parametric Design Language



# Chapter 1

## INTRODUCTION

In a world where sustainability is already a discussion topic, the efficiency of our homes and infrastructures gains a major relevance [1]. The heat loss through doors and windows is estimated to be around 20% to 30% of the heat consumption of a building, which lead to the development of technologies that minimize the heat transfer through these elements, such as the use of an insulating glass unit with double or triple glazing or the use of Multi-Material Beams (MMBs) with a polymeric core on the frame, that acts as a thermal barrier [1], [2].

Windows and doors with glazing and thermal break MMBs are the main product of JFAN Steel, which is the metalwork/architectural company that endorsed the dissertation [3]. The company uses frames from an Italian supplier (Secco) which produces beams with a polymeric core that offer good insulation capabilities, bond to separated metal elements, providing the frames with higher strength and stiffness to bending [4].

A door or a window is a structural system comprised of a frame fixed to the wall, and at least one movable leaf, which is the standardized terminology for a frame and attached glazing that move together [5]. In addition, the fixed frame and the movable leaves are assembled with hardware, which comprises the hinges, locking mechanisms, or other mechanisms that dictate the movement or position of the leaves.

To reach the market in the European Economic Area (EEA), these systems must endure some tests made in laboratory that are covered by the European standardization, and which empower them with a classification as well as the CE marking, meaning that the product has been assessed to meet high safety, health, and environmental protection requirements [6]. Although some countries outside the EEA, demand different certifications from diverse associations, like Canada and the United States of America (that follows the AAMA/WDMA/CSA 101/I.S.2/A440, North American Fenestration Standard (NAFS)), the European classification already gives some assurance of the capabilities of a system [7].

Providing JFAN Steel uses the frames and glazing's dimensions, as well as the hardware given by the supplier, and follows its instructions in the production of a window or a door, the final product is covered by the classification given by the supplier.

The market of JFAN Steel is demanding, and clients reach out to the company to produce large windows and doors, with dimensions that are not covered by Secco. Hence, for the product to be classified and have the CE marking, it must be sent to a laboratory, and endure the tests from the standardization, resulting in a costly process, that must be avoided to be repeated, which would be the case if the system fails in any test [6]. So far, the company's improvements to the system before it is sent to testing, rely on trial and error. This dissertation aims to change that, bringing structural engineering methods and tools to help improve the system's performance.

Moreover, JFAN Steel's projects are mostly outside of national territory, and the company keeps trying different markets in the pursuit of expansion. Some of these markets cover geographic regions known for earthquake risk (e.g., Jordan) and big storms like hurricanes (e.g., Florida), which are natural phenomena that cause a vibratory response in the systems [8], [9]. Consequently, it is also in the company's interest for the systems to be able to avoid or endure resonant regimes.

## **1.1 Objectives**

The first objective is to build a better understanding of the static and dynamic behaviour of the MMBs, and to capture said behaviour in analytical and numerical models of these beams. Hence a correct characterization of the materials and experimental tests of a physical MMB must be performed, to serve as the ground for comparison with these models.

Using as foundation the most prominent MMB's numerical model, the next objective becomes the creation of a model of a door system that can capture the behaviour of the physical system, as well as be used in a simulated reproduction of the relevant tests used to achieve the CE marking.

Using the created door system's numerical modal, the subsequent goal is to describe its change in performance in the various tests with the introduction of different reinforcements with distinct configurations, in order to determine the best course of action to improve the physical system, before it is sent to the laboratory for testing.

Lastly, because there is a chance that the heat insulation performance of the system could be influenced by including internal reinforcements on the frames, the thermal properties of the system must be evaluated for this kind of reinforcement.

## 1.2 Chapters' Layout

After the introduction, meant to enlighten the reader about the problem that the dissertation addresses, as well as its objective, Chapter 2 is presented. This chapter starts with the introduction of a case study, i.e., the system that serves as the basis for the evaluation of the reinforcements that would come later. The second part of this chapter introduces the standards used by the supplier and their respective tests that combined provide a class dependent CE marking to a system and addresses the vibration problematic that the system must endure.

Chapter 3 approaches all experimental methods used in the dissertation, starting with the material characterization of brass and polyamide, achieved through tensile and density tests, the three-point bending of a physical MMB, and an experimental modal analysis previously performed on the same beam. In this chapter, the experimental setup, its procedure, and the data processing are described in detail.

In Chapter 4 there were extracted analytical equations that attempt to describe the behaviour of an MMB statically and dynamically.

Subsequently, in Chapter 5 different numerical models of the MMB are studied on their static and dynamic behaviour, and the most prominent is chosen to integrate the model of a door system, modelled with detail. In this chapter, the relevant tests from Chapter 2 are replicated on different simulations with said system model, and the different reinforcements and configurations are introduced. In addition, a numerical thermal analysis of the system is presented, to evaluate the introduction of the internal reinforcements in the frames of the system.

Chapter 6 presents and discusses the results from the experimental tests of the physical MMB, as well as the results gathered from the analytical and numerical models.

The dissertation ends with Chapter 7, which exposes the main conclusions and proposes future work along the lines of the dissertation's thematic.

# Chapter 2

## SYSTEM DEFINITION AND REVIEW OF CE STANDARDIZATION

This chapter is an introduction to the type of system fabricated by JFAN Steel, and to what tests it is meant to withstand to achieve the CE marking. Hence, a door system and its components are exposed, before describing the standardized physical tests and numerical methods (to evaluate the thermal transmittance). The chapter concludes with the introduction of the dynamic problem.

### 2.1 Door System

To evaluate the efficiency of the reinforcements, a door system was idealized, serving as the basis for the following numerical analyses. A door system comprises the frame structure, the glazing, and the hardware that brings together the different elements. It must also have at least one leaf that can be opened and closed, allowing for passage, connected to a fixed frame by hinges, and have other locking points.

The system chosen to be studied is a double leafed door (DLD) of external opening, that occupies a space on the façade that surpasses the certified frontal dimensions allowed by the supplier (2900×2000 mm) by 25%, to reach 3625×2500 mm [10]. A similar door can be found in Figure 2.1, which was assembled in a project in Sicilia, Italy [4].



**Figure 2.1.** Double leafed door from a project in Sicilia, Italy [4].

The case study door has two leaves, one called primary that opens first, where the handle is attached, and which can be locked onto the secondary leaf. The latter can be opened only after the primary leaf is opened and can be locked on the top and bottom of the fixed MMBs frame. Each leaf is composed of a frame of MMBs, a triple glazing unit, as well as other additional hardware, which includes the hinges, that allow for the rotation of the leaves, and the locking devices that provide different locking points between the frames of the system [10]. The leaves are connected through the hinges to the fixed frame, which in turn is coupled to the wall by 3.9 DIN-7982 stainless steel screws. Together, the three mentioned frames are referred to as the frame structure. This type of system was picked by the company to be studied and is inspired by two other projects. The position of the different components can be visualized in Figure 2.2.

The system considers frames with profiles of the OS2 75 series (Annex A), which is the focus of the dissertation. This series has several profiles, but two are selected for the DLD, the profile P. 2963 for the fixed frame and for the edge of the secondary leaf that interacts with the primary leaf, and the profile P.2962 for the rest of the edges of the system. The glazing is fixed on the frame through beads (metal beams that integrate a frame alongside the MMBs), with a particular section, that along with the rubber

elements locks the glazing in place [10]. The bead can be removed with the right equipment, which makes it mandatory to always place it on the interior side since having a system where it is installed on the outside would make it susceptible to burglary.

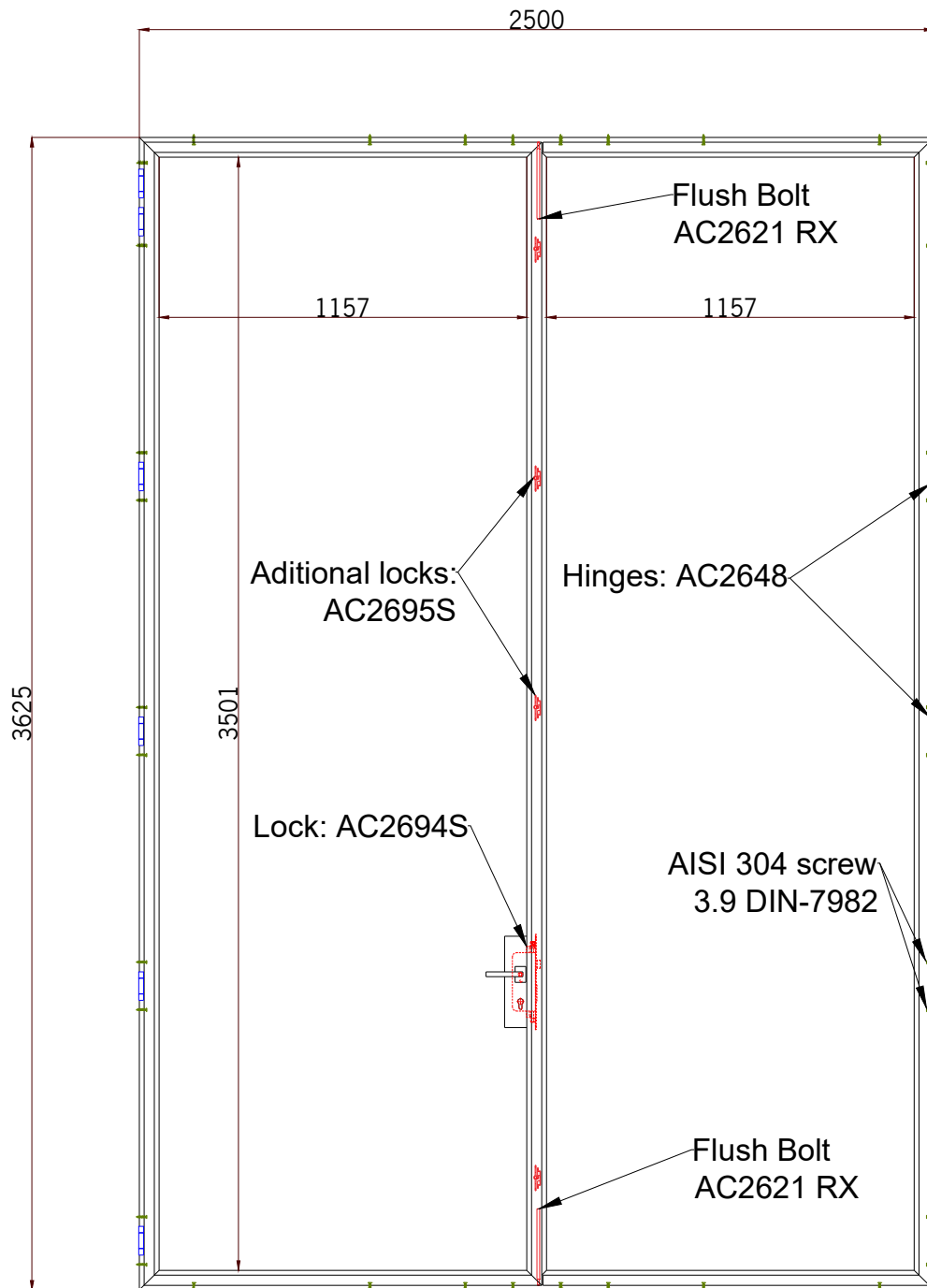


**Figure 2.2.** Closed DLD with general dimensions and its different components.

A detailed view of the section of the junction between the frame and glazing can be found in Figure 2.3, where the used hardware is also represented.

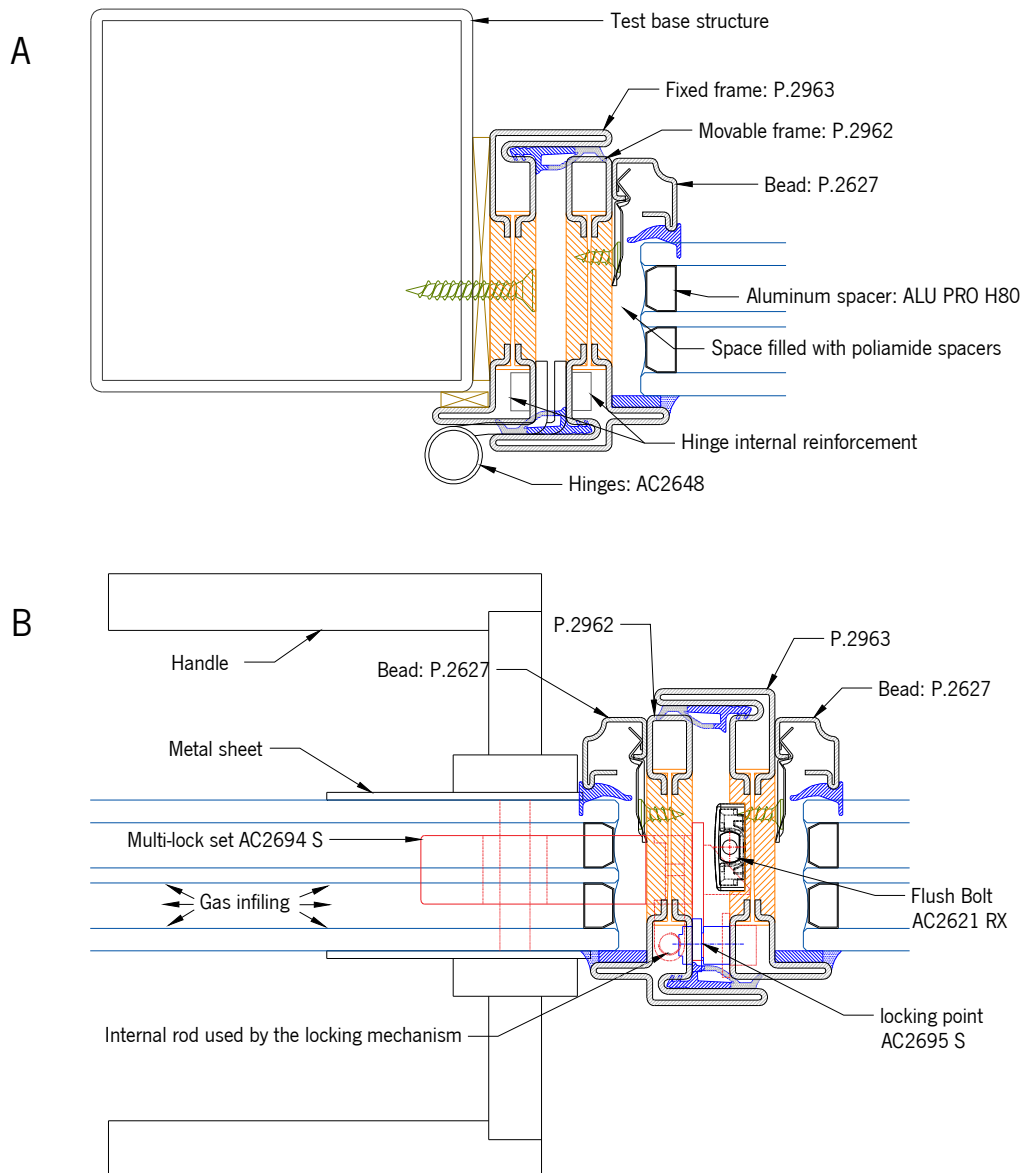


**Figure 2.3.** Detailed section view of the connections between the gazing and the frames on the Side (A) and on the centre (B).

### 2.1.1 Frame Structure

One of the main advantages of the Secco frames is the junction of multiple materials that allow for several advantageous properties to be joined in the same frame. Metal is used as the material of the frame's components that face the exterior and interior environment, i.e., the components that can be viewed after the system is assembled and locked [11]. An MMB with brass as metal is illustrated in Figure 2.4 - A, with a clear view of the profile. The metal elements are fabricated from a long sheet strip that goes through several rollers being cold formed to achieve the desired profile (Figure 2.4 - B). At the core of the MMB, two polymers are used: polyamide (PA), which connects the two metal elements, and

polyurethane (PU), which is the last element added to the profile, gluing the whole MMB together after cooling from a vulcanization process and becoming rigid.

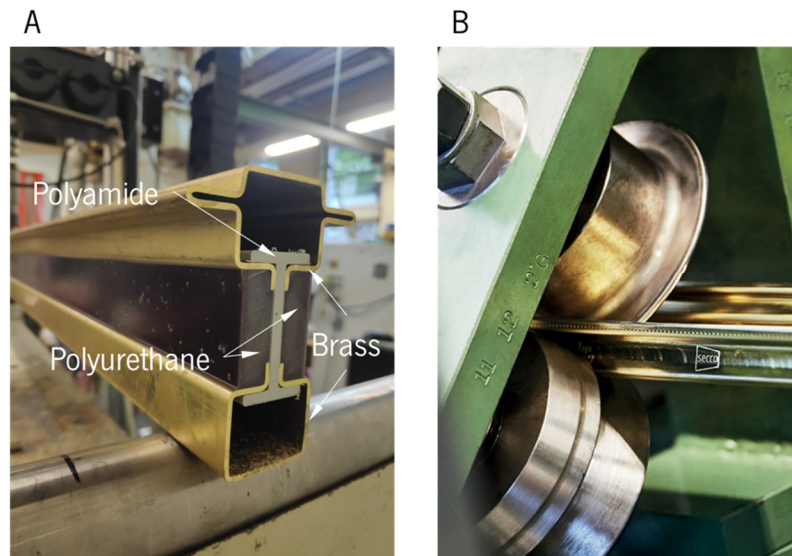


**Figure 2.4.** MMB with the P.2992 profile (A) and rollers that shape a sheet to achieve the final metal components of the beam (B). Figure B reproduced from [11].

Having a polymer-based core provides an excellent thermal barrier to the frame while distancing the stronger metal elements from the neutral axis increases its strength and stiffness to bending, caused by loads perpendicular to the façade. These two characteristics make this type of frame ideal for structurally defiant and thermally efficient windows and doors. The metal components can be of brass, stainless steel, corten steel, or galvanized steel, and after reaching JFAN Steel’s installations, they can endure different surface treatments to obtain aesthetically desired qualities, such as colour or surface roughness. Table 2.1 presents some mechanical and physical properties of all the metals used by the supplier [11].



**Table 2.1.** Mechanical and physical properties of the metals given by the supplier [11].

Material	Brass	Galvanized Steel	Corten Steel	Stainless Steel	
Known nomenclature	CuZn33 CW506 (EN) – OT 67	Fe P02 GZ 200 (UNI)	S355J0WP (EN)	304 (AISI)	316L (AISI)
Density, $\rho$ (kg/m <sup>3</sup> )	8500	7870	7870	7910	8000
Thermal conductivity at 20 °C, $\lambda$ (W/mK)	116,4	60	60	17	17
Elastic modulus, E (GPa)	110	210	210	196	196
Yield strength (MPa)	200 - 360	220-300	355	230	240
Ultimate tensile strength (MPa)	350 - 430	500	510 - 680	540 - 750	530 - 680
Elongation at break (min%)	23	22	14	45	40

On the other hand, the polymer's mechanical and physical properties are not provided in the supplier's catalogue, but access was given to a report from the supplier, which contains such properties for PU. A second report was provided, of a polybutylene terephthalate (PBT) reinforced with 30% glass fibre (GF), called Ultradur B4300 G6, with the indication of it being used in the place of the PA component. The properties of these materials can be found in Table 2.2.

**Table 2.2.** Mechanical and physical properties of the polymers given by the supplier.

Material	PU	Ultradur B4300 G6
Density, $\rho$ (kg/ m <sup>3</sup> )	800-1100	1530
Thermal conductivity at 10 °C, $\lambda$ (W/mK)	0,17	0,27 [12]
Elastic modulus, E (GPa)	2,2	10
Yield strength (MPa)	46	-
Ultimate tensile strength (MPa) -40 °C	-	204
Ultimate tensile strength (MPa) 23 °C	-	135

Some mechanical properties of the brass and PA materials are presented in Chapter 3, through tensile tests. In the same chapter, the densities of brass, stainless steel, and PA are also verified through an Archimedes' principle-based method. The company also provided verified data on the mechanical properties and density of galvanized steel, corten steel, and PU, shown in Table 2.3.

**Table 2.3.** Mechanical and physical properties of PU, Galvanized Steel, and Corten Steel given by JFAN Steel.

Material	PU	Galvanized Steel	Corten Steel
Density, $\rho$ (kg/ m <sup>3</sup> )	1134	7863	7797
Elastic modulus, E (MPa)	0,57	168,64	178,11
Yield strength (MPa)	24,7	274,2	389,7
Ultimate tensile strength (MPa)	31,1	370,7	498,4
Tangent modulus (MPa) – Bilinear hardening material model	20,4	-	-
Deformation after break (%)	7,7%	29,6%	26,3%

Most of the properties of Table 2.3 are very different from the ones in Table 2.1, and Table 2.2, and were used in the analyses performed in the following chapters. The thermal conductivities considered were those provided by the supplier, apart from the PA's thermal conductivity, which was deemed to be 0,27 W/(mK), the same as Ultradur B4300 G6 [12].

On the corners of a frame, the connection between the plastic components of two MMBs is made with an ethyl 2-cyanoacrylate based glue (from the supplier Soudal), and the metal components are generally welded together. However, the client can demand the exterior metal components to not be welded, so that the weld is not noticeable, in which case the glue is also used to connect these components. To help with the alignment, brackets are used, which stay loose on the cavities of the frame (Figure 2.5 - A). Figure 2.5 - B and C show the view of an assembled corner from the outside and inside perspective, respectively [10].

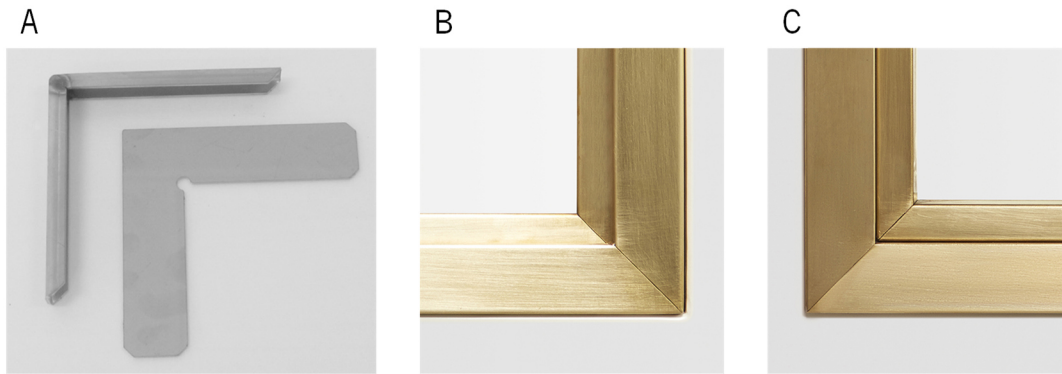


**Figure 2.5.** Brackets used in the connection between frames with the P.2962 and P.2963 profiles (A), exterior (B) and interior (C) views the corner of a system. Figure A reproduced from [10], and figures B and C reproduced from [11].

Throughout the project, different MMBs profiles were used, the most relevant being the P.2992, exhibited in Figure 2.4 - A, which was physically tested in the three-point bending test and in the experimental modal analysis that were performed in laboratory. The symmetric shape of this profile made it ideal to verify if the proposed analytical and numerical models correctly describe the behaviour of the frame, before attempting a model of the entire system. Furthermore, because an MMB was physically tested, a validation of the material's properties, found in the tensile tests, could be done by comparing the experimental results with the results of the idealized analytical and numeric models. Since the internal void is the most convenient way to reinforce the frame, a topology optimization for reinforcement inside of the frame's cavities was performed. However, the P.2992 profile has a much larger internal space than most profiles of the OS2-75 series, so the P.2972 symmetrical profile, with an internal space similar to that of most of the profiles of the series, was used instead. Other profiles, including asymmetric ones, were used mainly to compare the analytical and numerical free vibration models. All profiles used can be found in Annex A.

### 2.1.2 Glazing

When facing the exterior, the window and doors systems usually use double or triple glazing, which has two or three separated glass panels, respectively. Typically, each glass panel can be composed of a single thermally toughened glass, commonly known as tempered glass, or two glass plies joined by an interlayer usually of PVB (polyvinyl butyral) or resins like acrylic that act as a bonding agent, forming a sandwiched structure [13]. When a panel is composed of a single ply, it is common for it to be of tempered glass.

The tempered glass differs from the common annealed glass used in the laminated glass panels by the thermal treatment that it receives after the final shape is cut [13]. This glass, unlike the name suggests, is heated up to 620 °C and then is quenched (cooled rapidly), causing the surface to be cooled first [13]. As the core of the glass ply starts to cool, compression stresses emerge at the surface, and traction stresses start to appear at the core [13]. This is advantageous, as annealed glass has a much higher compression strength (1000 MPa) than tensile strength (40 MPa), and can afford to trade one for another, reaching a tensile strength from 120 to 200 MPa, which can be very advantageous in bending applications, for instance [13], [14]. On the other hand, since the surface is in compression, cracks on the surface don't propagate, making it possible to sustain higher stresses[13]. Because the quenching process also leaves the glass ply in a constant state of internal stress, when this type of glass breaks, it shatters into small pieces [13].

It is important to note that glass does not yield, it simply fractures, and properties such as tensile strength are stochastic, i.e., are statistical in nature [13]. When referring to the most common structural materials (e.g., steel), because they have the capacity to endure plastic deformation, if they are locally overstressed or have a lack of fit that generates a concentration of stresses, it is generally not a big problem [13]. However, in the case of glass, the structure can simply shatter, hence the use of rubbers to minimize contact between the frame and the glazing [13]. In the case of laminated glass, due to the interlayer, when the glass cracks the shattered parts are kept in place by the interlayer [13]. Considering that the tempered glass is being requested in target countries such as the United Kingdom, triple glazing with a tempered glass of 6 mm in the outer plies and of 4 mm in the middle ply was considered in the case study, with each cavity filled with air, and with a void "thickness" of 12 mm, giving the glazing a total thickness of 40 mm. An image of glazing used in the primary leaf, with a detail that allows for the locking mechanism to be inserted is exhibited in Figure 2.6.



**Figure 2.6.** Glazing with the detail that allows for the introduction of the locking mechanism.

In order to keep the different glass panels together, as well as seal the cavities, spacers are used, usually made from aluminium with a desiccant in the middle with the purpose of keeping the air in the cavity dry. An ALU Pro H80 aluminium spacer (AL3003) was used and is represented in Figure 2.3. Table 2.4 presents properties of the used materials for the glass and spacer.

**Table 2.4.** Mechanical and physical properties of tempered glass and AL3003 [14]–[16].

Material	Tempered Glass	AL3003
Density, $\rho$ (kg/m <sup>2</sup> )	2500	2730
Thermal conductivity $\lambda$ (W/mK)	1	162 (at 25 °C)
Elastic modulus, E (GPa)	70	70-80
Yield strength (MPa)	-	125
Ultimate tensile strength (MPa)	120-200	-
Poisson's ratio ( $\nu$ )	0,22	0,33

The cavity that separates the glass panels is hermetically sealed and often filled with an inert gas that offers further thermal insulation [13]. A high thermal conductivity of the cavity's infilling gas comes with an increase in the glazing cost, which depends on whether the cavity is filled with air, Argon or Krypton (the most usual infilling gases), with thermal conductivities of  $2,496 \times 10^{-2}$ ,  $1,684 \times 10^{-2}$ , and  $0,9 \times 10^{-2}$  W/(m K), respectively [17].

The cavities are hermetically sealed and the gas inside is at atmospheric pressure, which is particularly important because it forces the different panels to move with each other when positive or negative relative pressures are applied. A better way to visualize this is to picture a change in the volume inside one cavity, due to a relative pressure being applied in one of the panels. Assuming an isothermal compression, from the ideal gas law, equation 2-1 can easily be found to calculate the variation of pressure ( $\Delta P$ ) from a relative volume change ( $\Delta V\%$ ) inside a cavity that was at atmospheric pressure ( $P_{atm} = 101325 \text{ Pa}$ ) [18].

$$\Delta P = -\frac{\Delta V\%}{1 + \Delta V\%} P_{atm} \quad 2-1$$

To put things in perspective, an increase of 1% of the volume inside the cavity due to a pressure reduction on the outside of one side of the cavity, would cause a variation of the internal pressure by 1000 Pa, which in the case of glazing with panels with an area of around  $4 \text{ m}^2$  means about 4000 N of force that would be loaded on the opposite panel of the cavity, had it not followed the deformation of the solicited panel. Fortunately, the atmospheric pressure in the adjacent cavity forces the second glass pane to deform, and consequently, the atmospheric pressure on the other side of the glazing forces the third panel to deflect. Hence, despite the deformation not being precisely the same on all panels, they do tend to follow one another when pressure varies on one side of the glazing due to the cavities being hermetically sealed, and it is something that needs to be accounted for in an analysis of the system. An attempt to illustrate an exaggerated variation of pressure in the first cavity is made in Figure 2.7.

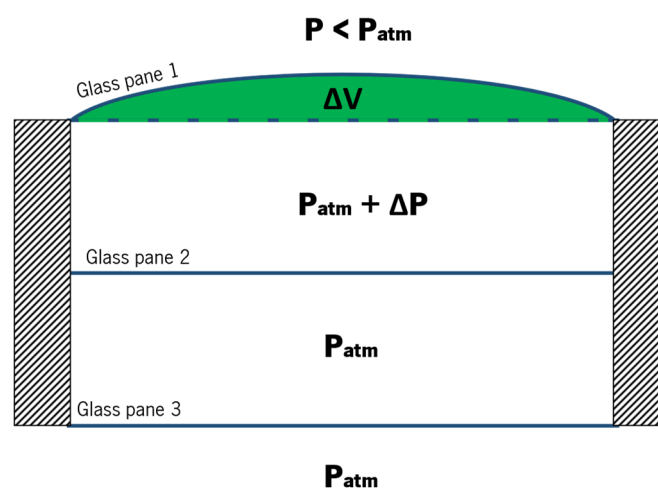


**Figure 2.7.** Hypothetical variation of the internal cavity's volume by an amount  $\Delta V$ , due to a reduction in pressure outside glass panel 1, had glass panes 2 and 3 remained in place. This does not happen due to the load that the change in pressure incites on glass panels 2 and 3, which instead deform as well.

### 2.1.3 Hardware

The testing of the hardware is not the focus of the dissertation, but it is important to understand the way it is integrated into the system, to comprehend how it restricts or dictates its deformation. The hinges are fundamental in the system as they attach the leaves to the fixed frame, providing them with the capacity to be rotated, and consequently opened or closed [10]. They are made from the same material as the frame structure and can even have the same type of surface treatment [11]. During the assembly stage, the hinges are attached through the metal elements of the fixed frame and of the leaf's frame, to a steel reinforcement, that goes inside the frame [10]. For the studied system, there were used three-winged hinges of the type AC2648, which can be observed in Figure 2.8.

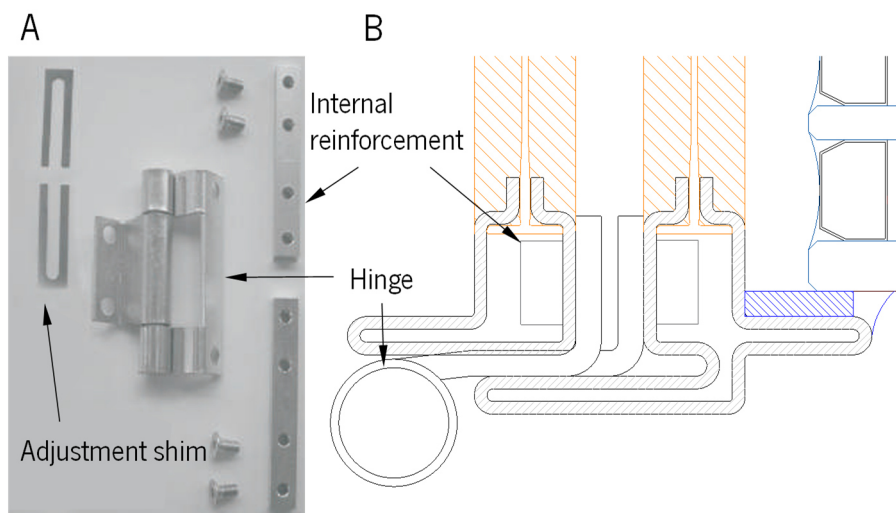


**Figure 2.8.** Complete hinge set (A) and hinge placement between the fixed and movable frames (B). Image A adapted from [10].

The main lock is placed in the polymeric part of the frame and goes into the glazing, as the latter has a shape that accounts for it (Figure 2.6) [10]. The lock, located in the primary leaf's frame, is coupled to a stainless-steel plate of 3 mm thickness that locks onto the polymeric part of the secondary leaf's frame, on a plate with the same thickness [10]. Figure 2.9 - A shows a sketch of the lock, which can be observed in Figure 2.9 - B on the primary leaf (the main locking mechanism) and in Figure 2.9 - C on the secondary leaf (the steel plate where the lock plugs itself).

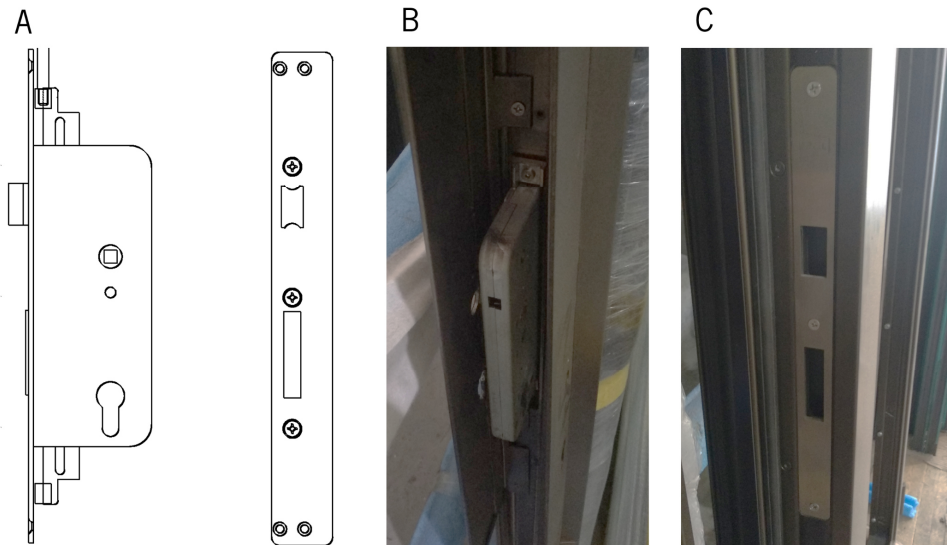


**Figure 2.9.** Drawing of the lock (A), lock assembled on the frame of the primary leaf (B), and steel plate assembled on the secondary leaf, where the lock plugs itself. Figure A adapted from [10].

The chosen lock is part of a locking mechanism, designated AC2694S, that also activates other locking devices with the rotation of the keys, which are placed along the junction of the primary and secondary leaves, forcing the two leaves to stay together [10]. These additional locking devices, made of steel, are located on the metal components of the frame, as illustrated in Figure 2.10 - A, and are activated through a rod that passes on the inside of the profile, moving upwards or downwards, that is triggered by the main lock mechanism [10]. The device is designated AC2695S and is essentially a plug pin (Figure 2.10 - B) and socket (Figure 2.10 - C) lock, where the plug pin located in the primary leaf, goes into the socket located in the secondary leaf [10]. Then, to be locked, the pin goes up, if the device is above the main lock, or down if below. Figure 2.10 - D shows the device, located above the main lock, in a locked position [10].

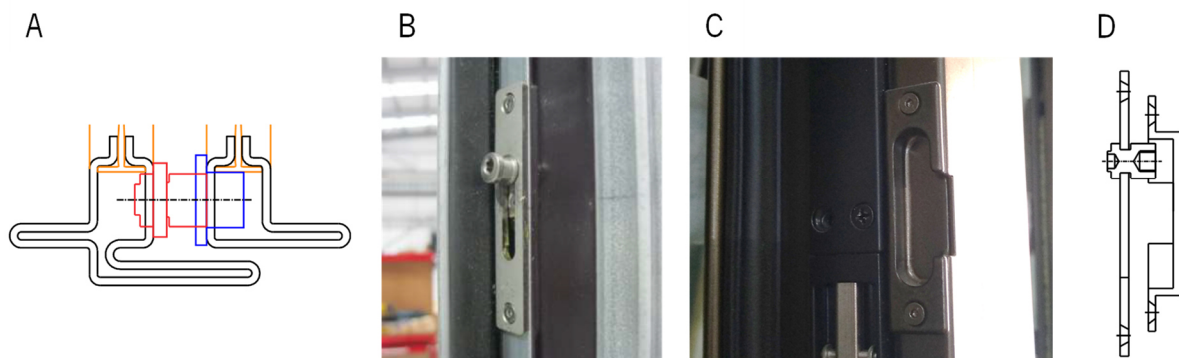


**Figure 2.10.** Placement of the locking mechanism between the movable frames (A), assembled plug pin (B), assembled socket (C), and drawing of the locking mechanism above the main lock in an engaged position (D). Figure D reproduced [10].



The last hardware considered is placed on the polymeric part of the extremes of the MMB of the second leaf's frame, located at the centre of the system, that was previously entailed (Figure 2.11 – A) [10]. It is designated AC2621 RX and has the function of locking the second leaf to the top and bottom of the fixed frame [10]. A steel pin (Figure 2.11 - B) emerges from the device, which is mainly aluminium and locks onto a steel plate that is screwed onto the polymeric part of the fixed frame (Figure 2.11 - C) [10].

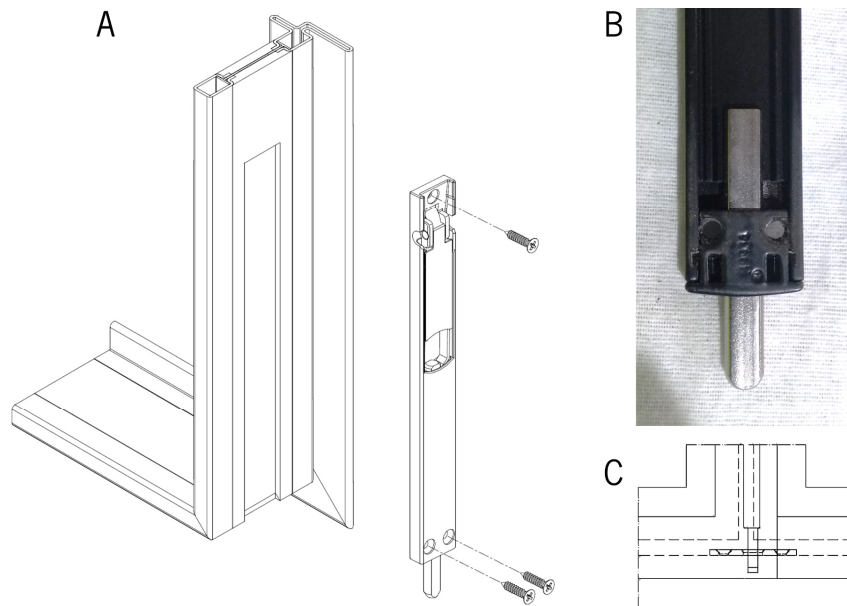


**Figure 2.11.** Drawing of the locking mechanism (A), steel pin that moves when the locking mechanism is activated (B), and side view of the locking mechanism engaged, where the pin is already through the steel plate (C). Figures A and C reproduced from [10].

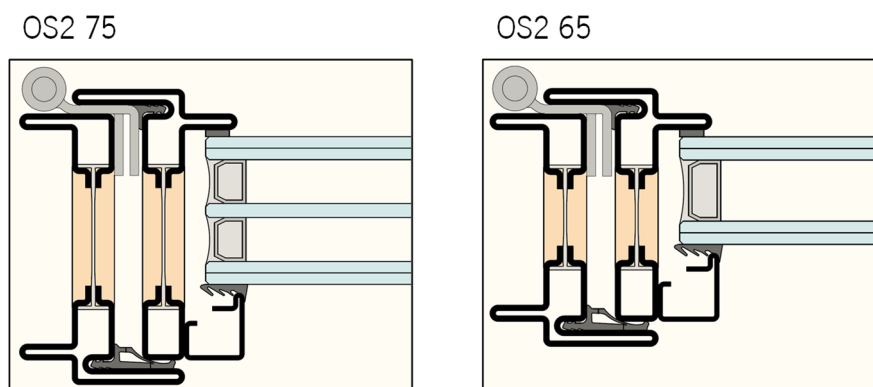
## 2.2 Problem Definition/CE Marking Tests

In the path to achieving the CE marking for a certain door or window system, it must pass a set of tests that evaluate the system's capability. Each of these tests is described and given a certain class by specific standards evoked by EN 14351-1:2006+A2 2019, which is the reference standard for all the performance characteristics of these systems [19]. The list of standardization tests used by Secco for the certification of doors and windows, more precisely of DLD, is presented in Table 2.5.

**Table 2.5.** Tests and their correspondent standards used by Secco for the certification of doors and windows.

Test	Standards
Mechanical durability	EN 13115:2020, EN 12400:2002
Operating forces	EN 13115:2020, EN 12046-1:2020
Resistance to vertical loads	EN 1192:2000, EN 947:1999
Resistance to static torsion	EN 1192:2000, EN 948:1999
Resistance to body impact	EN 13049:2003, EN 12600:2002
Resistance to wind load	EN 12210:2016, EN 12211:2016
Air permeability	EN 12207:2016, EN 1026:2016
Watertightness	EN 12208:2000, EN 1027:2016
Acoustic performance	ISO 717-1:2020, ISO 140-3:2021
Thermal transmittance	ISO 10077-1:2017, ISO 10077-2:2017

The information of the company reports presented in this introduction to the standards is limited by the confidentiality imposed by the supplier, to whom the reports belong. The objective is to study the tests that assess the system's structural and thermal capacity, which consequently means that the acoustic performance standards are not discussed. The classes of the DLD were achieved using a system of 2900x2000 mm, assembled with a double glazing with laminated glass panels, and frames comprised of MMB with profiles of the OS2 65 series, which is a series with identical profiles to those of the OS2 75 series (Figure 2.12), but with a shorter polymeric part between the metal components, and consequently, with a smaller second moment of area [20].

**Figure 2.12.** Difference between systems with profiles of the OS2 75 and the OS2 65 series, reproduced from [11].

The classification of this system can then be extended to systems that are slightly different, but with differences that are expected to improve the performance of the systems, e.g., introducing a triple glazing, or improving the performance of the frames to bending, by increasing the distance between the metal components of the MMBs (which is the case of the OS2 75 series). This is possible due to clause 3.4, “similar design”, of EN 14351-1:2006+A2 2019, which was employed by the supplier [19]. This also means that if the system of study had dimensions on the façade of 2900x2000 mm, because it uses superior frames and glazing, it would be expected to already have a performance increase.

### **2.2.1 Mechanical Durability and Operating Forces**

Mechanical durability test is executed using EN 13115:2020 and evaluated using EN 12400:2002, consisting of cycle-based tests that open and close the doors, with a pre-determined velocity to each movement that depends on the door’s weight [21], [22]. These tests place some effort on the frame, but mainly on the gaskets, and hardware. After the cycle completion, if the door is working properly, which is measured by defined criteria such as hardware loosening, retesting the operating forces, etc, the respective classification is given [21]. The classification is based on the cycles endured, and for a DLD the class obtained is the 3<sup>rd</sup> (20 000 cycles), which is the maximum for pedestrian windows [22]. Although more classes are available for pedestrian doors, there is no indication of such an attempt in the supplier classification report, so there is a possibility it could achieve a higher classification.

The operating forces are tested in accordance with EN 12046-1:2020 and classified in the terms of EN 13115:2020. The tests performed determine the force and torque necessary for the leaf and handle manoeuvrability, respectively. There are only two classes to be considered in EN 13115:2020, where the higher the class the lowest the operating loads [21]. For a DLD the supplier provides the first and lowest class (minimum of 100 N and 10 Nm for operating the leaf and handle respectively), although reviewing the test report, the operating forces come very close to class 2 (minimum of 30 N and 5Nm for operating the leaf and handle respectively) [21]. The tests are repeated fifteen times, but in sets of three and one minute apart, to allow for the weather stripping to relax, as it could have some influence on the performance [23]. As firstly mentioned, this test is also used to evaluate if a certain class was achieved in the mechanical durability test, after which the classification of the operating forces shall remain the same. These two tests depend mainly on the hardware’s fatigue strength, friction in the hinges, etc, and apart from this brief mention, do not take part in the dissertation’s work.

## 2.2.2 Resistance to Vertical Loads

The classification provided to assess the capacity of doors to resist deformation caused by vertical loads is given by EN 1192:2000. This standard exhibits four classes, corresponding to the load that the leaf withstood, which ranges from 400 N (1<sup>st</sup> class) to 1000 N (4<sup>th</sup> class), spaced by 200 N between each class [24]. The test is performed in accordance with EN 947:1999, from where Figure 2.13 containing the test apparatus was taken, and where the tested load is requested to be applied or removed with increments lower than 100 N of at least 1 second each, to avoid dynamic effects [25].

A particular door system obtains a certain class if in all its leaves the residual deformations after the removal of the corresponding load are no greater than 2 mm [24]. Two residual deformations must be recorded, the residual deformation measured in the gauge, and the residual deformation expressed by the difference in the measurements of the diagonal “D” before and after the test (Figure 2.13) [25]. In EN 947:1999, all the procedures, such as the timings of the test operations, are also described. For instance, the load is applied for about 300 seconds, and the residual force is measured 180 seconds after the load removal. For a DLD a class 2 (600 N) was achieved, with residual deformations of 0 mm on both leaves, and maximum deformation of 1 mm and 0 mm, on the primary and secondary leaves, respectively.

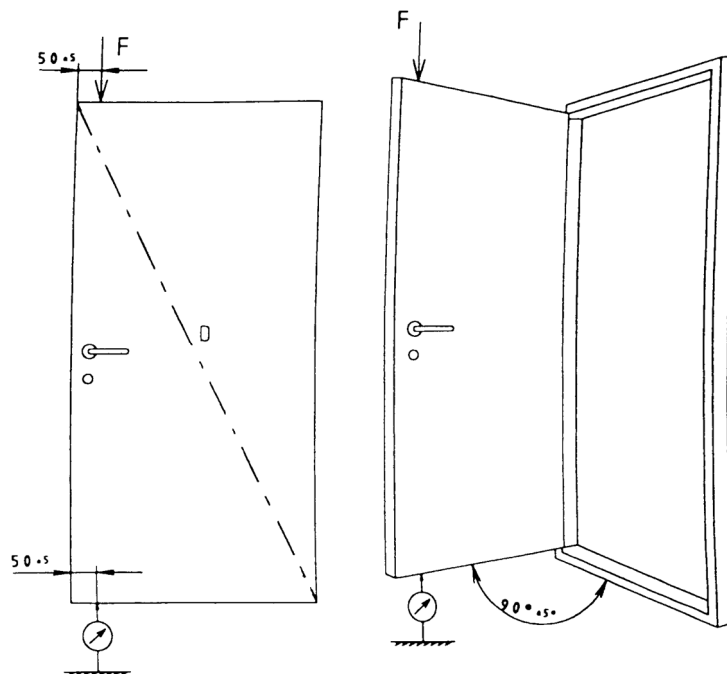


**Figure 2.13.** Apparatus of the test from EN 947:1999, where the displayed values have units in degrees and millimetres. A load is applied on the end of the top of the leaf, and a gauge records deformations on the end of the bottom of the leaf. Reproduced from [25].

### 2.2.3 Resistance to Static Torsion

The classification to static torsion is also provided by EN 1192:2000, which states four classes defined by the load the leaf can withstand, ranging from 200 N (1<sup>st</sup> class) to 350 N (4<sup>th</sup> class), with 50 N intervals [24]. And like in the previous test, the load must be applied or removed with increments lower than 100 N with at least 1 second each, to avoid dynamic effects [24].

For a door to qualify for a particular performance class, the resultant residual deformation measured in accordance with EN 948:1999 must not exceed 2 mm [24], [26]. A scheme of the test described in EN 948:1999 is represented in Figure 2.14, where the top “F” represents the fixed corner, and the lower “F” represents the point where the force is applied to evaluate the static torsion of the leaf [26]. On the other side of the lower “F” point in the leaf, a gauge is placed, that is used to evaluate the residual deformation, based on measurements made before and after applying the load [26]. Similar to EN 947:1999, in EN 948:1999 the procedure’s sequential steps and timings of operations are well defined, for example, applying the load (300 seconds) and measuring the residual deformation after the load is removed (180 seconds) [26]. For a DLD the classification achieved was class 2 (250 N), with residual deformations of 46,1 mm and 1,5 mm, and maximum deformation of 99,6 mm and 56,6 mm, on the primary and secondary leaves, respectively.

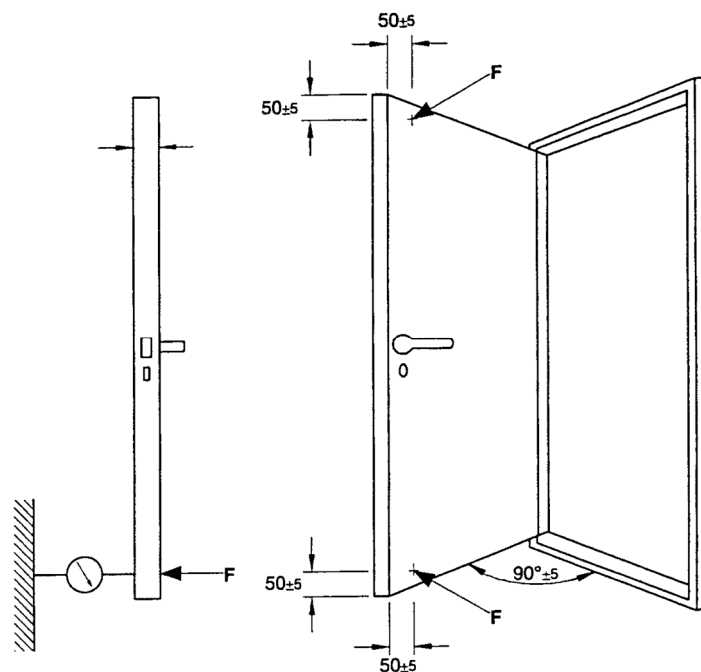


**Figure 2.14.** Apparatus of the test from EN 948:1999, where the displayed values have units in degrees and millimetres. The top corner of the leaf is fixed, and a load is applied in the bottom corner, where a gauge, on the other side of the leaf records the measurements. Reproduced from [26].

## 2.2.4 Resistance to Body Impact

The strength capacity of the door to impact must be tested and evaluated according to EN 13049:2003, where a pendulum, with an impactor attached to the end, is dropped from a specified height, contacting the door when the impactor is at its lowest position (maximum kinetic energy) [27]. A complete description of the pendulum is provided by EN 12600:2002, including wires, pulleys, hooks, height adjusting devices and the impactor that is essentially a weight surrounded by two pneumatic tires, with a total mass of 50 kg [28]. An apparatus of the test is illustrated in Figure 2.15.

Classification is determined by the drop height at which the impactor is released, which can range from 200 mm (Class 1) to 950 mm (Class 5) [27]. The impact direction is specified by the applicant or manufacturer, and the resultant damage is evaluated in the three most vulnerable points of the structure that relate to the centre of the infill (that in this case is the glazing), a corner of the infill and the centre of the longest edge of the largest area of the infill [27]. A class is obtained if there is no major damage to the structure after impact, which is determined, for instance, by disconnected hardware, disconnected infilling retaining components, or by composite parts becoming dislodged or shattered in a dangerous manner [27]. The mass of any dislodged part shall be kept below 50 g for a class to be achieved. In the case of DLD, the maximum classification was achieved (class 5), without any damage being recorded in any point of the structure [27].

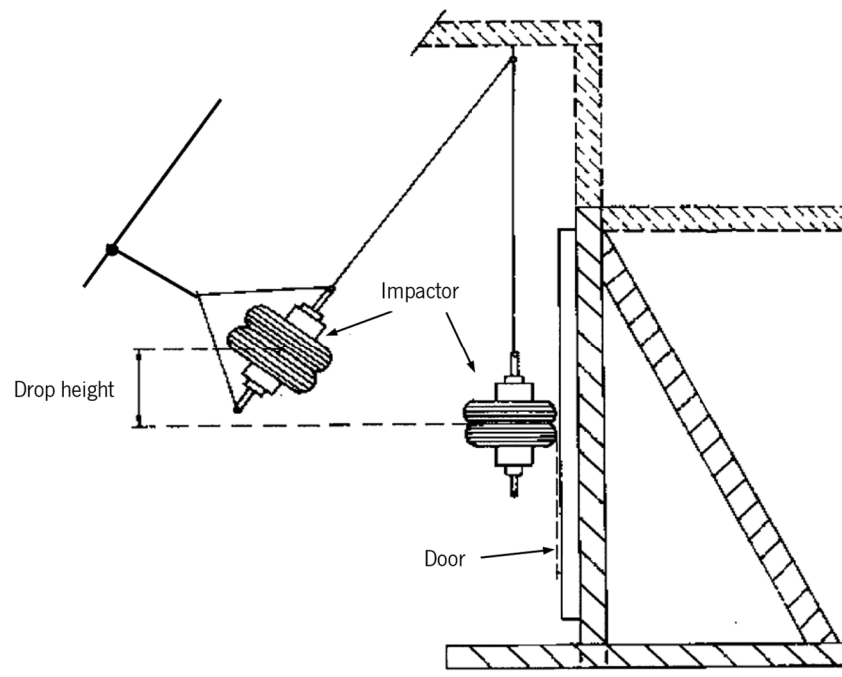


**Figure 2.15.** Apparatus of the test from EN 13049:2004, where an impactor works as a pendulum and is dropped from a certain height hitting the door system when its kinetic energy is at the maximum. Adapted from [28].

Because the best possible classification was achieved, it is probable for a system with increased dimensions to pass the test, even if it is with a lower class. Additionally, the glazing is also tested separately in an experiment with similar characteristics to those of this system's test, using the same impactor, and achieving its own classification [28]. So, the strength of the glazing to impact can be directly evaluated through the classification given by the glazing supplier. Therefore, this test was not reproduced in simulation.

### **2.2.5 Resistance to Wind Load**

When it comes to the classification of the strength and stiffness of a door system to wind loads, the standard EN 12210:2016 must be used. To achieve a certain classification, three tests must be successfully completed [29]. The first test (Deflection test) uses a pressure load, that takes the designation of P1, and varies from 400 Pa (class 1) to 2000 Pa (class 5), with intervals of 400 Pa [29]. A superior class can be achieved by using a pressure above 2000 Pa and is labelled Exxxx, where the x's are replaced by the pressure used in the test [29]. A pressure P2 corresponding to half the pressure P1 and a pressure P3 with a value of  $1,5 \times P1$  are used in the Repeated test (second test) and Safety test (third test), respectively [29]. EN12210:2016 provides an additional classification of three classes, A, B and C, based on the relative frontal deflection from the first test being less than 1/150, 1/200 and 1/300, respectively [29]. The relative frontal deflection,  $F_{rp}$ , of a DLD can be determined using equation 2-2, which uses the deflection measured by gauges located in the points highlighted in Figure 2.16,  $M_A$ ,  $M_B$ , and  $M_C$ , respectively [30].

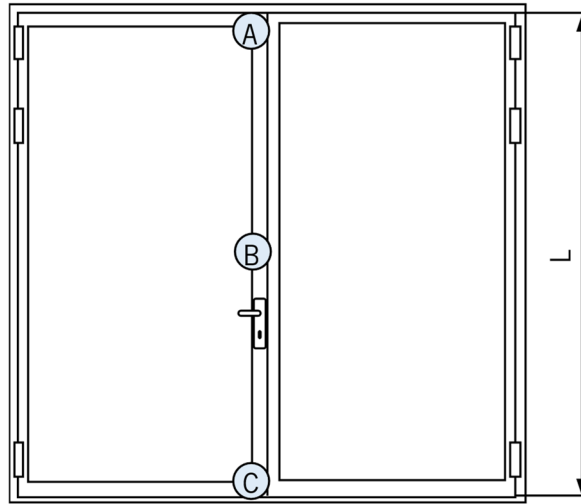


**Figure 2.16.** Points where the deflection is measured by the gauges (Based on tests already performed using EN 12211:2016 on DLD).

$$F_{rp} = \frac{M_B - (M_A + M_C)/2}{L} \quad 2-2$$

All three tests must be performed in accordance with EN 12211:2016, and in a chamber with an open side, where the test specimen can be fitted [30]. The first test is usually performed posteriorly to the air permeability test, and after a class is chosen to be tested, three pulses 10 % greater than the matching pressure, P1, are applied and the gauges set to zero [30]. The relative positive pressure P1 is then applied on the door system, and the gauges measure the resultant deflections, which are used to calculate the relative frontal deflection [30]. Afterwards, the same test is executed for a relative negative pressure -P1 [30]. The second test is cyclic, with the pressure that is applied on the door varying between -P2 to P2, in 50 cycles [30]. To evaluate exceptional loading conditions, the last test is performed, where a relative negative pressure, -P3, is applied on the door, and then the same is repeated but with a relative positive pressure, P3 [30]. In Figure 2.17 the timings of the tests, as well other particularities such as gauge measurements, are displayed.



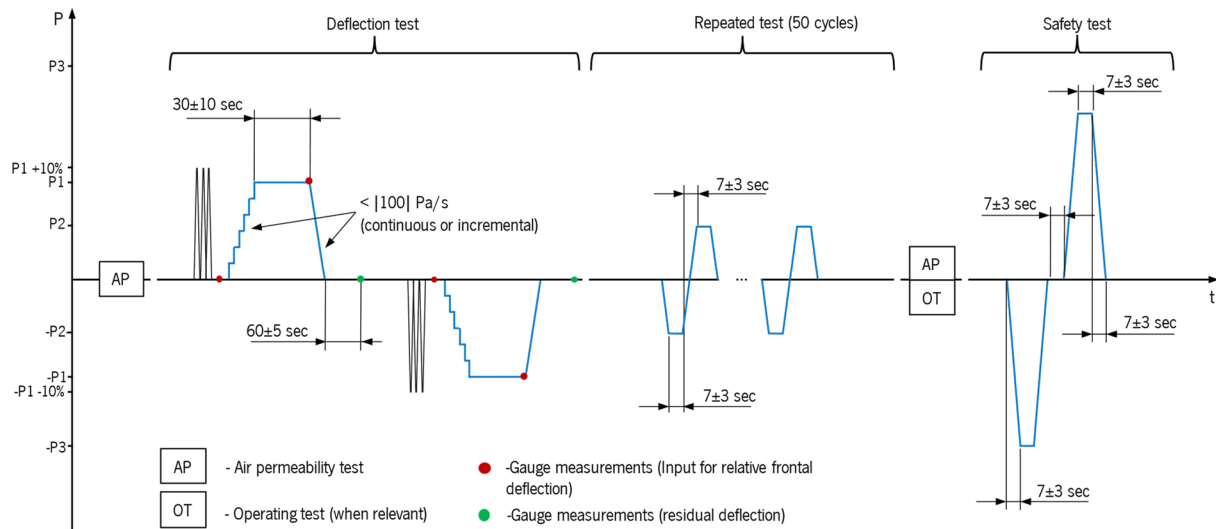


**Figure 2.17.** Test sequence with the timing of the different operations, timings of the gauge measurements, test pressures and how they are achieved, and when other related tests must be performed. Adapted from [30].

For the Deflection test to be successful, failures must be visible, and the relative frontal deflection must meet at least one of the classes A, B, or C, already mentioned [29]. After the second test, the door shall be manoeuvred to verify that it remains functional, and no damages should be noticeable [29]. An air permeability test must be retaken, and the specimen shall not exceed the upper limits of the flow rate claimed by the air permeability class by more than 20% [29].

The Safety test requirements, only demand the door to remain closed and that no parts become detached [29]. Hence, some bending and twisting of hardware, or splitting and cracking of frame members is allowed [29]. For a DLD a class B3 ( $P_1 = 1200 \text{ Pa}$ ,  $P_2 = 600 \text{ Pa}$ ,  $P_3 = 1800 \text{ Pa}$ , and  $F_{rp} < 1/200$ ) was obtained. The maximum displacement on the Deflection test was registered with a relative negative pressure, at the point  $M_B$  of Figure 2.16, resulting in a value of -13 mm.

## 2.2.6 Air Permeability and Watertightness

The classification of the air permeability is regulated by EN 12207:2016, based on the flow rate related to the overall area ( $\text{m}^3/(\text{hm}^2)$ ), and related to the length of the opening joint ( $\text{m}^3/(\text{hm})$ ) [31]. The air permeability test is performed in a test chamber, and in accordance with EN 1026:2016, which provides the correct procedures [32]. Inside the chamber, the pressure varies from 0 to  $\pm 600 \text{ Pa}$  by steps, and at the end of each step the air flow is recorded, allowing for the determination of the flow rate per unit area and per unit length [31], [32]. These values are then compared to a graph that defines the classes [31]. A DLD achieved the maximum classification of 4.

Watertightness classification is defined in EN 12208:2000, and the test is performed as instructed in EN 1027:2016 [33], [34]. The test uses several nozzles that spray water with a specified pressure, based on two methods, labelled A and B, for products that are fully exposed or partially shielded, respectively, and that differ only on the inclination of the nozzles [34]. Starting the test, the pressure is incremented by 50 Pa from 0 Pa up to 300 Pa, and then by 150 Pa, with each step being maintained by 5 minutes, except for the first step at 0 Pa, which takes 15 min [33]. The class, accompanied by the letter of the method, is determined by the correspondent pressure at which leakage occurred, varying from 0 Pa (class 1B) to 300 Pa (class 7B) for method B, and from 0 Pa (class 1A) to 600 Pa (class 9A) for method A. With method A, a higher class can be obtained, E<sub>xxx</sub>, where the xxx represents the maximum test pressure in Pa [33]. A DLD achieved a 7A class.

Both classifications depend on the stiffness of the door to lateral pressure loads (in the case of water tightness only relative positive pressures), similarly to the resistance to wind load classification, although the loads in the latter are higher. Hence, an increase in performance in the wind pressure tests has a good chance of being accompanied by an increase in performance in these two tests, but since the air permeability and the watertightness tests depend largely on the sealants, it is not certain that would happen. The study of the sealants is not addressed in the dissertation, and because the structural component from these tests is similar to that from the resistance to wind load test, only the latter was evaluated through numerical simulations.

### **2.2.7 Thermal Transmittance**

The reason that led to the use of polymers between the metal sheets of the MMBs was to reduce the heat transfer between the outside and the inside of the window/door. This is one of the most desired characteristics of the frame, and therefore it is imperative that its thermal properties don't become significantly affected by the introduction of reinforcement elements.

The European standardization provides a method for the determination of the thermal transmission of windows and doors. The thermal transmittance, commonly known as the U-value, can be interpreted as the ability of an element (or elements) of a structure to transmit heat under steady-state conditions [35]. The lower the value of the thermal transmittance the better the element's thermal insulation performance.

ISO 10077-1:2017, provides the method for the calculation of the thermal transmittance of doors and windows, that for the case of a single window or door with the absence of opaque panels, is given by [36]:

$$U_{W/D} = \frac{\sum A_g U_g + \sum A_f U_f + l_g \psi_g}{\sum A_g + \sum A_f} \quad 2-3$$

Where U represent the thermal transmittance, A the projected area,  $l_g$  the total perimeter of the glazing, and  $\Psi_g$  linear thermal transmittance due to the combined thermal effects of glazing, spacer, and frame. The subscript g or f is a reference to the glazing or frame, respectively. The projected areas are exemplified in Figure 2.18, and the value of  $A_f$  considered in equation 2-3, is the higher value between the projected area viewed from an interior ( $A_{f,i}$ ) and exterior ( $A_{f,e}$ ) perspective.

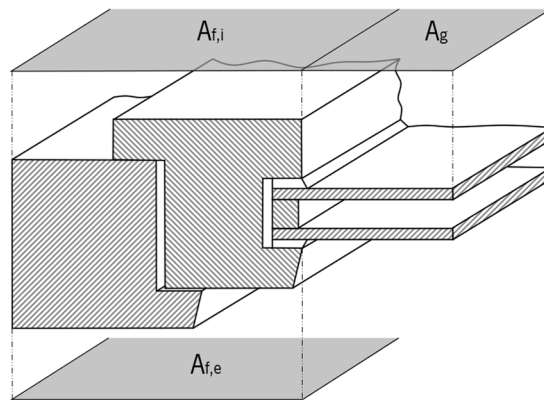


**Figure 2.18.** Projected area viewed from the interior ( $A_{f,i}$ ) and the exterior ( $A_{f,e}$ ), and area of the glazing ( $A_g$ ), ignoring the rubber gaskets. Adapted from [36].

The thermal transmittance of the glazing is usually given by the supplier, and the thermal transmittance of the frame, as well as the linear thermal transmittance, can be determined numerically in accordance with ISO 10077-2:2017, which provides guidelines for a numerical method based on a 2D representation of the frame and glazing sections [37]. This method is presented below, contemplating an interior ambient temperature of 20 °C and an exterior ambient temperature of 0 °C [37].

Primarily, any overlaps of the frame on the wall, as well as any protruding gasket over the glazing must be excluded, and the length of the glazing that surpasses the frame shall be larger than 190 mm, as shown in (Figure 2.19) [37]. For the determination of  $U_f$ , a panel with thermal conductivity of 0,035

$W/(mK)$  needs to be used (represented by the yellow rectangular region, in Figure 2.19), and for the calculation of  $\Psi_g$ , the glazing must be used [37].

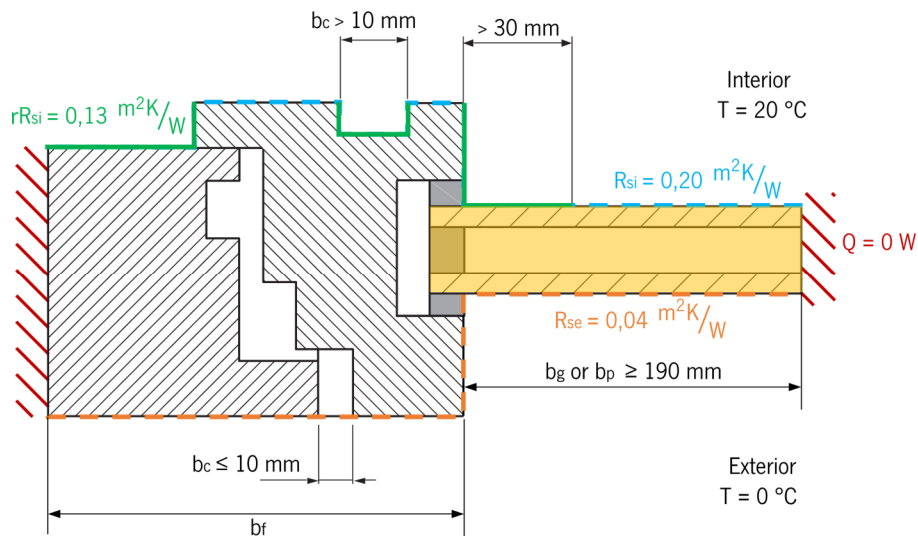


Figure 2.19 – Surfaces thermal resistances, dimensional parameters and boundary conditions presented in ISO 10077-2:2017, for a frame connection example with a double glazing. Adapted from [37].

Thermal conductivities are assigned to the solid materials, and to spaces filled with air or a specific gas, i.e., cavities and glazing gas infilling, an equivalent thermal conductivity that accounts for heat transfers in the form of convection and radiation must be assigned, except for well-ventilated cavities [37]. In the case of the glazing gas infilling, a value of  $0,034 W/(mK)$  is suggested for the validation example D.10 [37]. However, this value was calculated for a glazing with specific dimensions, that had a thermal transmittance of  $1,3 W/(m^2K)$  on its central area, i.e., the area without the influence of the spacer or the connection with the frame [37]. The calculation of this value for the studied system's glazing on its central area can be consulted in Annex B.

The cavities present in the frame are considered unventilated when fully closed or when with an opening smaller than 2 mm [37]. This type of cavity, as stated, is treated like a solid with an equivalent thermal conductivity,  $\lambda_{eq}$ , in  $W/(mK)$ , determined based on its dimensions by equation 2-4 [37].

$$\lambda_{eq} = \begin{cases} \sqrt{A_c \frac{d_c}{b_c}} \cdot \left[ \frac{0,025}{\sqrt{A_c \frac{d_c}{b_c}}} + 2,11 \left( 1 + \sqrt{1 + \left(\frac{d_c}{b_c}\right)^2} - \frac{d_c}{b_c} \right) \right] & ; b_c < 5mm \\ \sqrt{A_c \frac{d_c}{b_c}} \cdot \left[ \max \left\{ \frac{0,025}{\sqrt{A_c \frac{d_c}{b_c}}}; 1,57 \right\} + 2,11 \left( 1 + \sqrt{1 + \left(\frac{d_c}{b_c}\right)^2} - \frac{d_c}{b_c} \right) \right] & ; b_c \geq 5mm \end{cases} \quad 2-4$$

In equation 2-4,  $A_c$  is the cavity's area, and the variables  $d_c$  and  $b_c$  are the depth and width of the smallest circumscribing rectangle, measured parallelly and perpendicularly to the direction of the heat flow, respectively (Figure 2.20 - A) [37].

Ventilated cavities are divided into 2 groups: the slightly ventilated cavities, which have openings between 2 mm and 10 mm (Figure 2.20 - B and C), and well-ventilated cavities, which include all the cavities that weren't already mentioned, particularly the case where the opening is larger than 10 mm (Figure 2.20 - D, E) [37]. For slightly ventilated cavities, double the equivalent thermal conductivity of an unventilated cavity with the same dimensions is considered [37]. On the other hand, for the well-ventilated cavities, a surface thermal resistance is applied [37]. If the area covered by a cavity's walls is 10 times larger than the area of the opening, a surface thermal resistance with reduced radiation is considered [37].

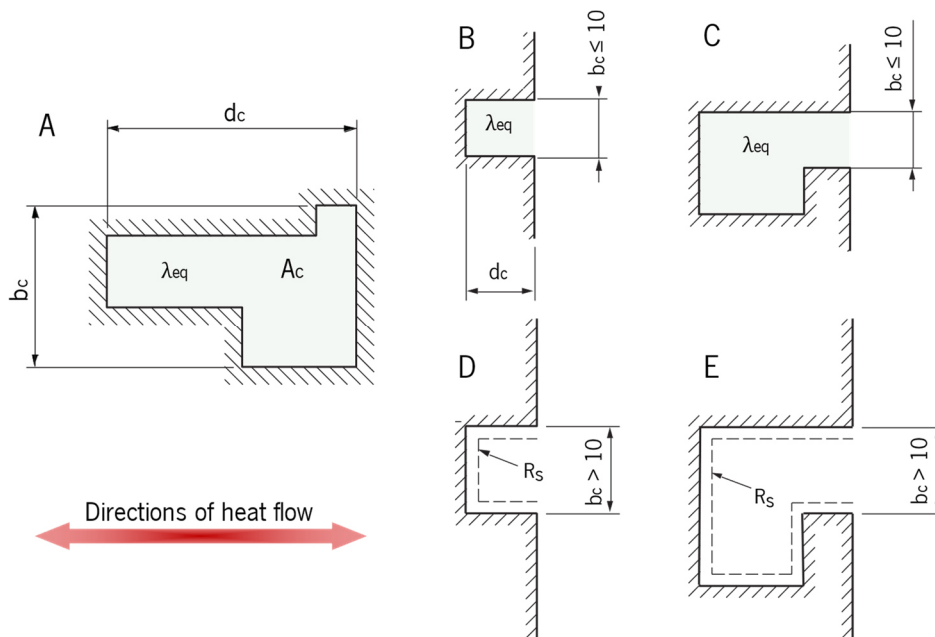


**Figure 2.20.** Distinct types of cavities considered by ISO 10077-2:2017: Unventilated cavities(A), slightly ventilated cavities (B and C), and well-ventilated cavities (D and E). Adapted from [37].

The boundaries outlined by the wall and the opposite end of the panel or glazing are adiabatic [37]. To the rest of the boundaries, a surface thermal resistance must be assigned [37]. The surface thermal resistance is defined as the reciprocal of the sum of the convection and radiation heat transfer coefficients, allowing the heat transfer to be described by a unique thermal resistance value [35]. In the exterior boundary, the standard defines a surface thermal resistance of 0,04 m<sup>2</sup>K/W ( $R_{se}$ ), and on the interior boundary, a surface thermal resistance of 0,13 m<sup>2</sup>K/W ( $R_{si}$ ) must be assigned, except for some surfaces that are considered to have reduced radiation/convection, where it must have a surface thermal resistance ( $rR_{si}$ ) of 0,20 m<sup>2</sup>K/W [37].

A surface is considered to have reduced radiation/convection in edges or junctions between two surfaces, as exemplified in Figure 2.21, where the grey area represents the distances over which the surfaces have increased thermal resistance [37]. The distance  $b_s$  is equal to  $d_s$  up to a limit of 30 mm, and the same applies if a surface is sloped [37].

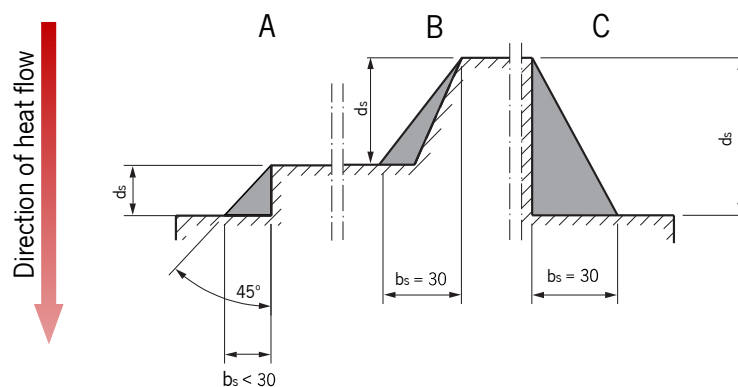


**Figure 2.21.** Reduction of the interior surface thermal resistance when  $d_s < 30$  mm, hence  $b_s = d_s$  (A), when the  $b_s > 30$  mm, and the junction involves a sloped surface (B), and when  $d_s > 30$ , and  $b_s = 30$  mm (C). Adapted from [37].

As stated, the thermal transmittance of the frame is calculated considering an insulation panel instead of the glazing, and it can be determined by equation 2-5, where  $L_f^{2D}$  is the thermal conductance of the section, in W/(mK), determined by equation 2-6,  $U_p$  is the thermal transmittance of the central area of the panel, in W/(m<sup>2</sup>K), and  $b_p$  and  $b_f$  are dimensional parameters present in Figure 2.19 [37].

$$U_f = \frac{L_f^{2D} - U_p b_p}{b_f} \quad 2-5$$

$$L_f^{2D} = \frac{Q}{\Delta T} \quad 2-6$$

In equation 2-6,  $Q$  represents the heat per unit length, and  $\Delta T$  the difference in temperature, i.e., 20 K [37]. Lastly, the value of the linear thermal transmittance,  $\Psi_g$ , is found, after simulating with the glazing, through equation 2-7, where  $L_{\psi}^{2D}$  is the thermal conductance of the section,  $U_g$  is the thermal transmittance of the central area of the glazing, and  $b_g$  is a dimensional parameter that is also defined in Figure 2.19 [37].

$$\psi_g = L_{\psi}^{2D} - U_f b_f - U_g b_g \quad 2-7$$

To assure that a software is suitable for the calculations, EN10077-2:2017 provides ten examples that should be carried out [37]. A software is valid if the resultant values of the thermal conductance ( $L^{2D}$ ) don't differ from the values given by the standard by more than 3%, and if the values of the thermal transmittance of the frame,  $U_f$ , and of the linear thermal transmittance,  $\Psi_g$ , reveal an accuracy of about 5% [37].

### 2.2.8 Dynamic Vibration Test

There are no standards from the European Commission that account for a dynamic vibration analysis. However, the company is expanding its market to geographic regions known for earthquake risk (e.g., Jordan) and big storms like hurricanes (e.g., Florida), hence, the vibration analyses are performed in the interest of escaping the frequencies of the loads caused by these natural phenomena, to prevent resonant effects on the system [8], [9].

Both wind and earthquakes loads are random processes, and therefore non-deterministic, meaning that the future of the displacements, velocities, and accelerations generated by these loads cannot be predicted [38]. This kind of phenomena produces loads distributed in all frequencies for a certain range, without significant peaks occurring in the frequency domain graphs [39]. However, if a phenomenon has been measured on many occasions for a sufficiently long period of time, its statistical properties can be deduced [39]. These phenomena are then described as a stationary stochastic process, and it is a good approximation to assume that they follow, e.g., a Gaussian distribution [38], [39]. The frequencies at which the loads are applied can be plotted in a statistical sense using a power spectral density (PSD), which could represent for example  $g^2/\text{Hz}$ , where  $g$  represents acceleration [38]–[40].

The important feature to retain about the PSD is that it can express the relative importance of frequency to a certain variable, such as acceleration, which is normalized to the frequency. The name power doesn't relate to a physical property, but to the squaring of the measured variable, which is done to obtain a positive quantity whose mean is nonzero (since a mean value of zero is common in random processes) [40]. A common PSD describing the wind and earthquake phenomena is presented in Figure 2.22 [41]–[43].

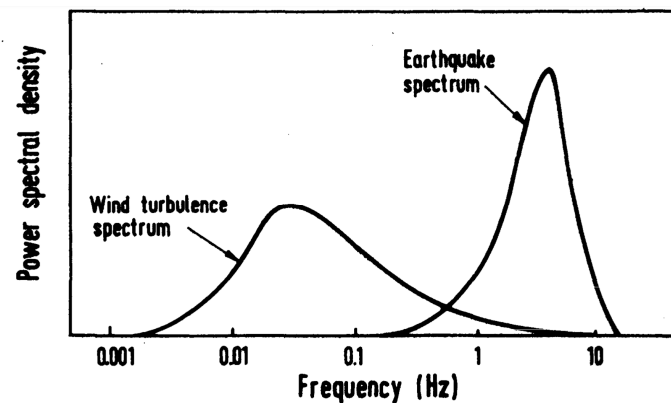


**Figure 2.22.** Spectral densities of earthquakes and winds. Adapted from [43].

Although the wind spectra from Figure 2.22 can be commonly found in the literature, with the energy of the wind loads being essentially below the 1 Hz mark, it was found that the spectrum of the earthquakes loads is very characteristic of the specific natural phenomena and depends on several factors, such as the terrain, distance to the epicentre, etc [42], [44]–[48]. The design to resist earthquake loads is particularly important in structures larger than doors and windows, like buildings. This analysis is based on the response spectrum technique, in which a dynamic analysis is replaced by an equivalent static analysis with the assumption that structures that resonate at similar frequencies and possess similar damping, suffer the same peak displacements, and uses variables like pseudo-velocity and pseudo-acceleration, that are not discussed in this work [45], [49]. Of special relevance to the seismic analysis and design, are the ground motion parameters such as the peak ground acceleration (PGA), that as the name suggests is the maximum acceleration that occurred during an earthquake, and that is used as an intensity measure [45], [50]. The PGA is an absolute measurement and can be divided in the vertical and horizontal components, where the latter is usually (but not always) larger [45].

The seismic design of building is covered by standardization. However these standards don't apply in a standalone analysis of doors or windows (that doesn't consider the building), and because these systems don't have a strong contribution to the building's structural integrity, they must be treated



as a non-structural component. The strength of this kind of component to earthquake loads can be evaluated by considering an amplification of the peak horizontal ground acceleration (PHGA) as a function of the storey of the building at which the components are located [51]–[53]. However, since the object of study is a door, it is likely to be located, precisely, at ground level. Hence, no amplification should be applied.

There isn't a flawless method of evaluating the dynamic response of a DLD to an earthquake, so a design criterion was created, and the system is deemed fit to withstand a certain earthquake if it can endure the PGA acceleration (in both vertical and horizontal directions), as if it was a sinusoidal load, with a frequency varying between 0 and 50 Hz, which is a frequency range broader than that on which the peak acceleration occurs, based on the data found in the literature [44]–[46]. This criterion allows for a conservative result since the structure doesn't vibrate at peak amplitude during the earthquake. The PGA corresponding to the different earthquake classes can be found in Figure 2.23.

PERCEIVED SHAKING	Not felt	Weak	Light	Moderate	Strong	Very strong	Severe	Violent	Extreme
POTENTIAL DAMAGE	none	none	none	Very light	Light	Moderate	Moderate/Heavy	Heavy	Very Heavy
PEAK ACC.(%g)	<.17	.17-1.4	1.4-3.9	3.9-9.2	9.2-18	18-34	34-65	65-124	>124
PEAK VEL.(cm/s)	<0.1	0.1-1.1	1.1-3.4	3.4-8.1	8.1-16	16-31	31-60	60-116	>116
INSTRUMENTAL INTENSITY	I	II-III	IV	V	VI	VII	VIII	IX	X+

**Figure 2.23.** The PGA of an earthquake and correspondent instrumental intensity, among other parameters. Reproduced from [50].

It is also important to keep in mind that to estimate the performance of the system, its displacements and stresses must be evaluated. Consequently, since these values depend on the damping of the system, a correct damping characterization is essential to predict the dynamic behaviour of the structure.

# Chapter 3

## EXPERIMENTAL TESTS

In this chapter, tensile test results and density test results are presented, providing the models that are exhibited in the following chapters with the most trustworthy material properties. Additionally, a three-point bending, and an experimental modal analysis, were performed on a physical MMB, so that the different MMB models could be evaluated. These experiments are also presented in this chapter.

### 3.1 Tensile Test

As the metallic components of the MMB are made through a cold rolling process that from an initial metal sheet gives them their final shape/section, some local plastic hardening occurs, and the mechanical properties given by the supplier may not be completely accurate, since there is a chance the test specimens used to determine these mechanical properties were collected from an undeformed area (i.e., not locally hardened). The injection process or the composition of the polymeric part of the MMBs could also have suffered a slight change. Therefore, to verify the mechanical properties given by the supplier, and achieve more realistic analytical and numerical models of the MMBs, tensile tests were performed. The properties of materials such as corten/galvanized steel and PU were tested by the company, thus, this study focused on the characterization of brass and PA. The properties of stainless steel used in the numerical models were given by the supplier.

#### 3.1.1 Test Specimens

The brass and PA test specimens (Figure 3.1) were obtained from an MMB of the EBE 85 profile series, with the appropriate dimensions and tolerances as defined by ISO 6892-1:2009 for the brass test specimen and by ISO 527-2:2012(E) for the PA test specimen (Annex E). A laser cutting machine was used to extract the brass test specimens from the MMB, while to acquire the PA test specimens, a skilled factory worker used a grinding wheel followed by sanding paper to obtain the desired dimensions.

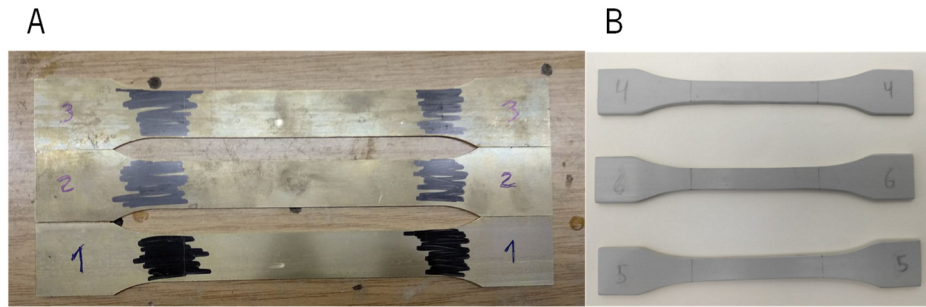


**Figure 3.1.** Brass (A) and PA (B) test specimens numbered and with the length of the central region marked.

### 3.1.2 Equipment

For the brass tensile test, an Instron 8874 testing system (Figure 3.2 - A) was used, which had a capacity of up to 25 kN of linear force, provided by a servo-hydraulic motor. Along with it, the Bluehill software was used for data collection and test preparation, and a mechanical strain gauge with an initial length of 25 mm, the 2620-602 Instron Dynamic Extensometer, was used to measure the strain in the linear elastic regime. Different equipment was available for the PA tensile test, and a Zwick/Roell z005 (Figure 3.2 - B), with a capacity of up to 5 kN and the software testXpert V10.1 Standard, was used. All the dimensional measurements outside the tensile test itself were made with a vernier calliper.

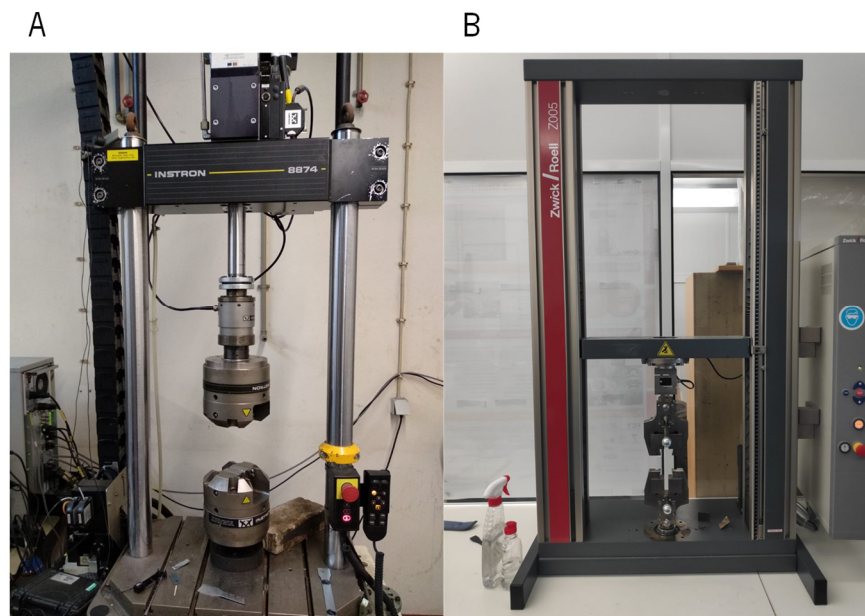


**Figure 3.2.** Instron 8874 (A) and Zwick/Roell z005 (B) testing machines.

### 3.1.3 Procedures

In the brass test specimens, a central region ( $L_c$ ) of 100 mm was marked and would later be used to determine the elongation, after fracture. For the cross-sectional area, an average was made, after measuring and then multiplying the width and thickness on several points of the central region, to consider small deviations.

The test specimen was placed on the tensile machine (Figure 3.3 - A) and the mechanical strain gauge in the middle of the specimen. Then, the test parameters were introduced in the Bluehill software, the more important being the test velocity, which consisted of two ramps. The first ramp was intended for the linear region of the stress strain curve and had a velocity of 0,005 mm/s, that because the length of the mechanical strain gauge was 25 mm, resulted in a strain velocity of  $0,0002 \text{ s}^{-1}$ . These values fall within the recommended values according to the standard ISO 6892-1, for the determination of the upper yield strength ( $0,00025 \text{ s}^{-1}$ ) [54].

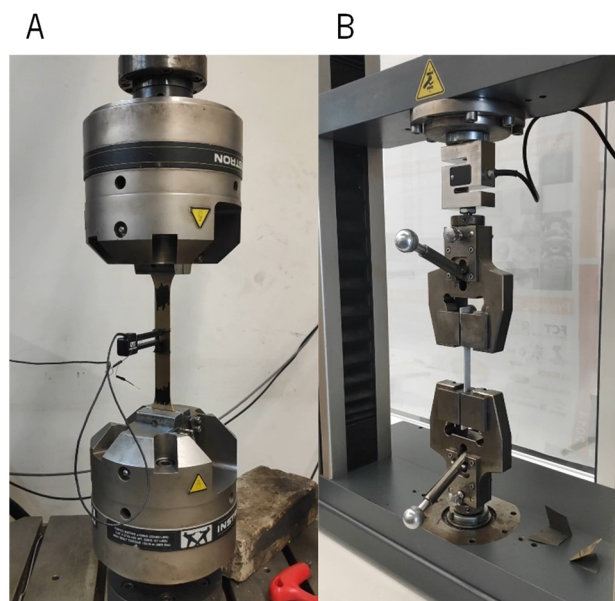


**Figure 3.3.** PA test specimen (A) and brass test specimen (B) with a mechanical strain gauge mounted and ready for the tensile test.

The test was accompanied by a monitor that showed live results, showing a stress-strain curve calculated with input parameters, such as the area and length between grips. The monitor provided a qualitative view of the curve, and after the yield was surpassed, the mechanical strain gauge was removed. Around the same time, the second ramp of velocity took place, at a faster speed of 0,2 mm/seg and was kept until fracture occurred. The strain at which the second ramp of velocity took over was defined

accordingly to the experience of the technician responsible for the test machine. After fracture, the test specimen was removed from the equipment and put together, to measure the distance of the marking that initially defined the central region, making it possible to calculate the elongation.

In the PA test specimen (Figure 3.3 - B), the procedure was very much alike, although with few differences. In the absence of a mechanical strain gauge, the displacement was measured at the grips and the test specimen was held closer to the centre, away from the intended grip sections, resulting in a constant cross-section of the specimen between grips. This distance was measured in every test, and it would be the  $L_0$  used to calculate the strain. The initial central region was not considered in the PA test specimens, since a different approach was used to calculate the elongation, with a parallel line to the elastic region in the engineering stress-strain curve. Additionally, only one velocity was used during the test 0,0167 mm/seg (1 mm/min), which is the recommended value by the Standards ISO 527-1 and ISO 527-2 [55], [56]. Figure 3.4 shows the initial length and initial length of the central region on the test specimens, and the technical drawings of the test specimens, which were sent for laser cutting and to the JFAN factory, can be found in Annex E.

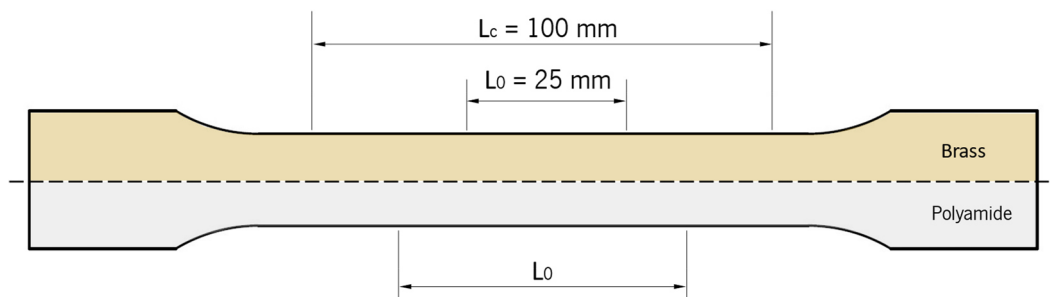


**Figure 3.4.** Initial length of the central region,  $L_c$ , and initial length,  $L_0$ , of the brass and PA test specimens.

### 3.1.4 Data Treatment

Using Microsoft Excel, the data from the test was imported (RAW file and TRA file, from the brass and PA tests, respectively), and several columns of values belonging to certain variables emerged. To obtain the engineering stress-strain curve, the values in the force ( $F$ ) column were divided by the average area of the central region ( $A$ ), to determine the stress (equation 3-1), and the values in the deformation ( $\Delta L$ ) column were divided by the initial length ( $L_0$ ), to determine the strain (equation 3-2) [57]. For the brass specimens,  $L_0$  was 25 mm, and for the PA specimens,  $L_0$  was the distance measured between the grips.

$$\sigma = \frac{F}{A} \quad 3-1$$

$$\varepsilon = \frac{\Delta L}{L_0} \quad 3-2$$

### 3.1.5 Material Properties and Bilinear Model

Since a bending test was performed in laboratory, where the materials were expected to undergo plastic deformation, bi-linear models were developed for brass and PA. These models, as well as a set of material properties, were found using different methods.

#### 3.1.5.1 Brass

Due to the fact that the mechanical strain gauge had to be removed before the fracture, a complete stress-strain curve would not be possible in the brass tensile test. Although the displacement at the grips was also measured and could be used to construct the complete curve, it would not be representative of the behaviour of the material, since the cross-sectional area of the specimen in between grips was not constant. This means that the stress and strain were not uniform at all points between grips in the axial direction, and were smaller in the curved region, resulting in the central area reaching plasticity before the curved area that was closer to the grips.

A well-defined elastic region can be observed in the stress-strain curve and using the values in this region, a straight line was extracted with the slope being the elastic modulus of the material. The tensile strength was obtained by moving the straight line in the strain axis by 0,2%, as is recommended for metals [54]. A representation of these values can be found in Figure 3.5.

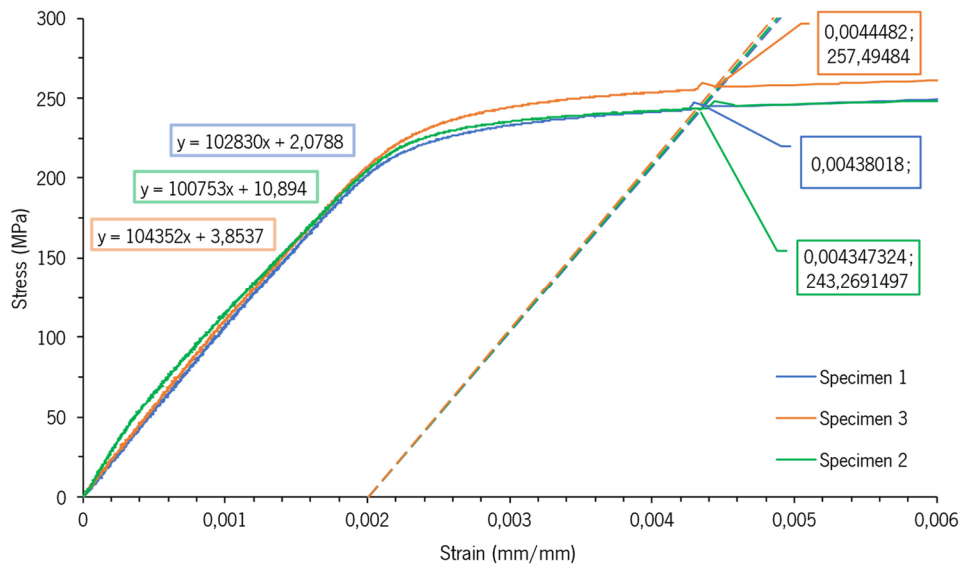


**Figure 3.5.** Brass experimental stress strain curve for the elastic region of the three test specimens, which are differentiated by colour. The elastic modulus was found from the slope of the line equations, and the yield strength from the intersection with the curves of lines of the same slope that cross the strain axis at 0,002.

Additionally, the values of the ultimate stress and elongation were found. The first, by applying equation 3-1 to the maximum force value, and the latter, by putting together the separated pieces of the specimen, measuring the distance in the central region, and finding the relative increase to the initial length of the central region [54].

To consider the plasticity that occurs on the different elements of the MMB, a bilinear hardening model of the material was defined. In the case of brass, the most convenient method to approximate the material behaviour to a bilinear model was to establish 3 points that include: the origin of the graph, the yield stress, which defines the end of the elastic line, and the ultimate stress, which represent the beginning of the necking that occurred in the tensile test. Along with the yield point, the ultimate stress point defined the tangent modulus that characterizes the plastic region. This approach mimics the methods used by [58]–[60], even though the ultimate stress point used in this work belongs to the true stress-strain curve.

This was accomplished through a simple numerical analysis of the brass test specimen in the Static Structural module of Ansys Workbench, where the tangent modulus was parameterized, and its correct value was found to be 0,926 MPa. The analysis took as input the elastic modulus, yield strength, and Poisson's ratio (0,3) and having the maximum load and the correspondent displacement from the experimental data at the grips, the numerical analysis was used to search for a tangent modulus that passed through this point, which is where the ultimate stress occurred in the real experiment. Hence, by

measuring the reaction force when a displacement was applied at the grip region of the numerical model, the tangent modulus was found, and the bilinear model (green) from Figure 3.6 was defined. This simulation is addressed in Annex E.

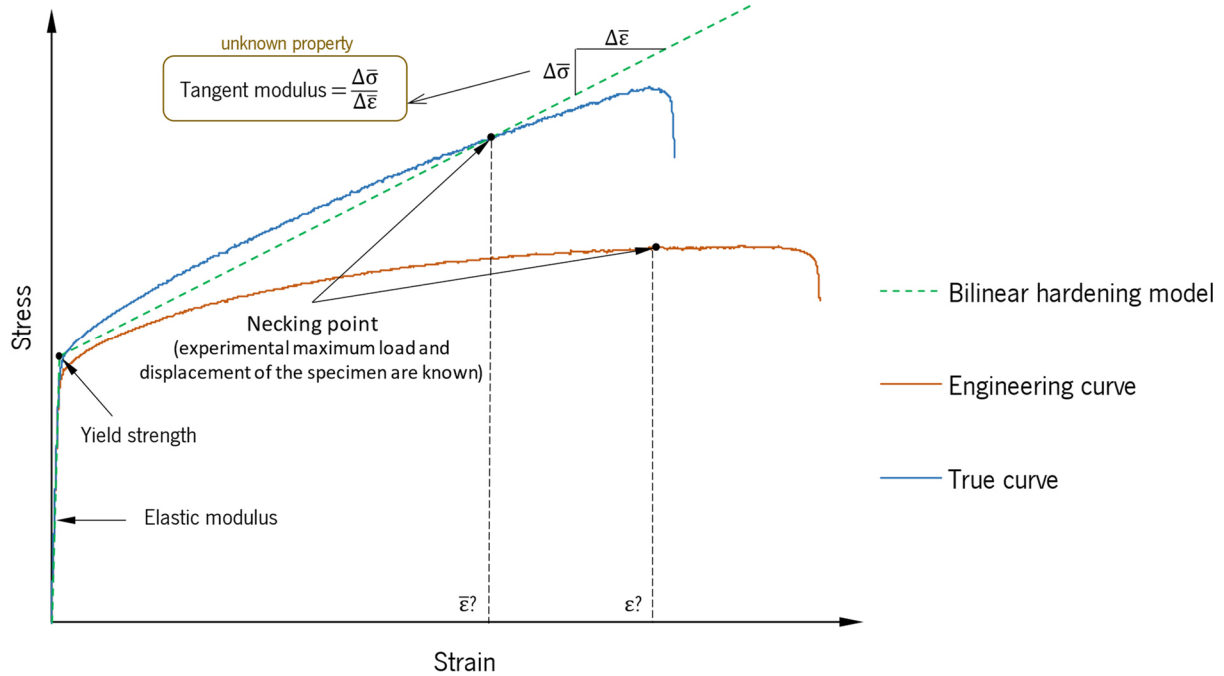


**Figure 3.6.** Conceptual plot of the bilinear hardening model (green) of brass with the engineering (orange) and true (blue) curves stress-strain curves.

### 3.1.5.2 Polyamide

Since the cross-sectional area was constant in the PA specimens and the displacement was measured at the grips, a complete stress-strain curve representation was feasible. Because to define the plasticity of the material the true stress-strain curve is needed, from the values of the engineering curve, using equations 3-3 and 3-4 to find the true stress and true strain, respectively, the true stress-strain curve was defined [57].

$$\bar{\sigma} = \sigma(1 + \varepsilon) \quad 3-3$$

$$\bar{\varepsilon} = \ln(1 + \varepsilon) \quad 3-4$$

The tensile tests of this polymer resulted in stress-strain curves with a few particularities. The first one was that the elastic region was preceded by an initial region (Figure 3.7) that does not represent the real behaviour of the material, being instead an artefact caused by take-up of slack, and alignment or



seating of the specimen [61]. Thus, this region was ignored, and the elastic line compensated with an offset [61].

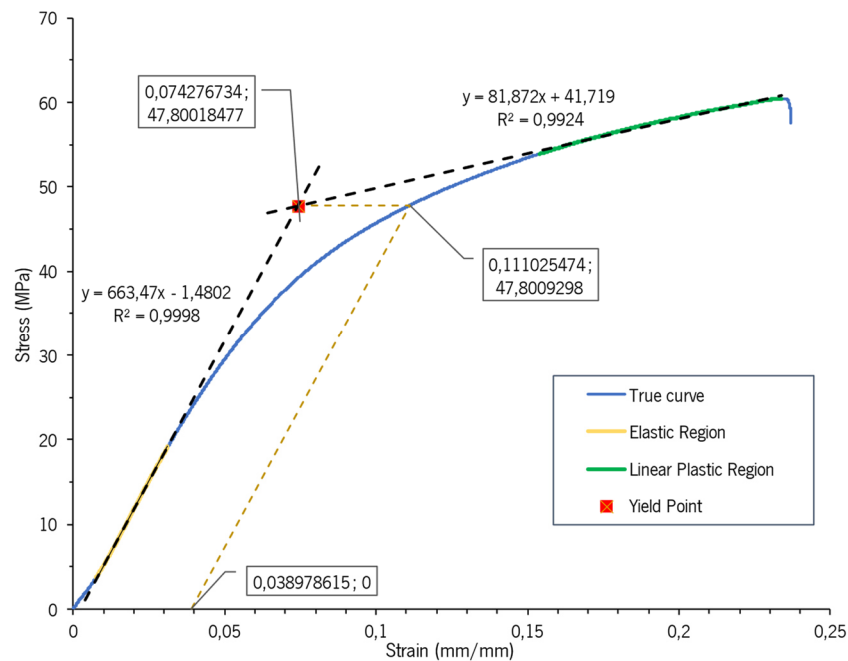


**Figure 3.7.** True stress - true strain curve of the PA test specimen 4, with the elastic region in yellow used for the calculation of the elastic modulus, the plastic region in green, where the curve approximates to a linear behaviour, and from where the tangent modulus was found, and the yield point, in red. Before the elastic region, an artefact, no representative of the material's behaviour can be observed.

The second particularity was that although there was a well-identified elastic line, there was no well-defined transition region from the elastic to the plastic region. A common solution to find the yield point was adopted, which involved finding the intersection of the line from the elastic region and the almost linear region past the yield point [62], [63]. Additionally, the slope from these lines (elastic and tangent modulus) defined the bilinear model [62], [63].

Besides these two particularities, that affect the way the yield point was found, the position of the elastic line and formulation of the bilinear model, the elongation was also determined differently in the PA specimens, and this value was found by drawing a parallel to the elastic line that intersects the end of the engineering curve and measuring the intersection with the strain axis. Lastly, the ultimate tensile strength was calculated in an analogous way to that of the brass test specimens. All the mentioned values were found for each test specimen and then averaged. The PA true stress-strain curves are displayed in Figure 3.8.

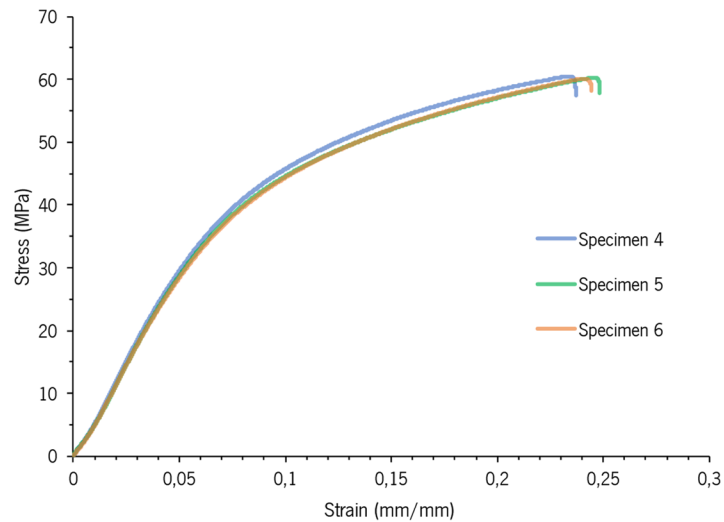


**Figure 3.8.** True stress – true strain curves from the PA test specimen's tensile test.

### 3.1.5.3 Properties

All the properties found from the brass and PA tensile tests can be found in Table 3.1.

**Table 3.1.** Properties found from the brass and PA tensile tests, with relative error to the supplier's brass and the PBT properties, respectively.

Material	Brass	$\Delta$	PA	$\Delta$
Elastic modulus, E (GPa)	102,65	-6,7%	0,65	-93,5%
Tangent modulus (MPa)	926	-	87	-
Yield strength (MPa)	248,6	$\approx 0\%$	46,3	-
Ultimate tensile strength (MPa)	371,3	$\approx 0\%$	47,5	-64,8%
Elongation after fracture (%)	43,9	-	20,0	-

The values of the yield strength and the ultimate tensile strength of brass are within the intervals given by the supplier, however, the elastic modulus has a decrease of about 6,7% to the value from the supplier. The values of the PA are quite different from those of the polybutylene terephthalate (PBT) presented in Chapter 2, where the elastic modulus and the ultimate tensile strength of the PA are about 6,5% and 35% of the values of PBT, respectively. Although two distinct materials are being compared, the change to a material with significantly worst performance, by the supplier doesn't seem likely. It is also possible, for the properties of the polymer to have degraded during the manufacturing process of the

component, e.g., air intrusions, or during the assemblage of the MMB, possibly during the vulcanization process of the PU.

## 3.2 Determination of Density

In a given dynamic analysis, a correct mass definition is especially important since it is necessary to account for the inertial effects. Hence, the need for a correct definition of a material's density values.

### 3.2.1 Method Overview

The test consisted of a series of weightings of the test specimen, that along with the Archimedes principle allowed for the determination of the material's density.

Archimedes' principle states that the upward buoyant force that is exerted on a body immersed in a fluid, whether fully or partially, is equal to the weight of the fluid that the body displaces [18]. This means that when a specimen of volume  $V$  is immersed in water with density  $\rho_{\text{water}}$ , the buoyancy force ( $\vec{F}_b$ ) exerted in it is given by equation 3-5, where  $g$  is the acceleration of gravity.

$$\vec{F}_b = \rho_{\text{water}} V g \quad 3-5$$

On the other hand, when underwater, from static equilibrium, the buoyancy force along with the reaction force ( $\vec{R}$ ) counters the weight of the specimen ( $\vec{W}$ ).

$$\vec{W} = \vec{R} + \vec{F}_b \quad 3-6$$

Free body diagrams of the specimen out and immersed in water are portrayed in Figure 3.9 – A and B, respectively.

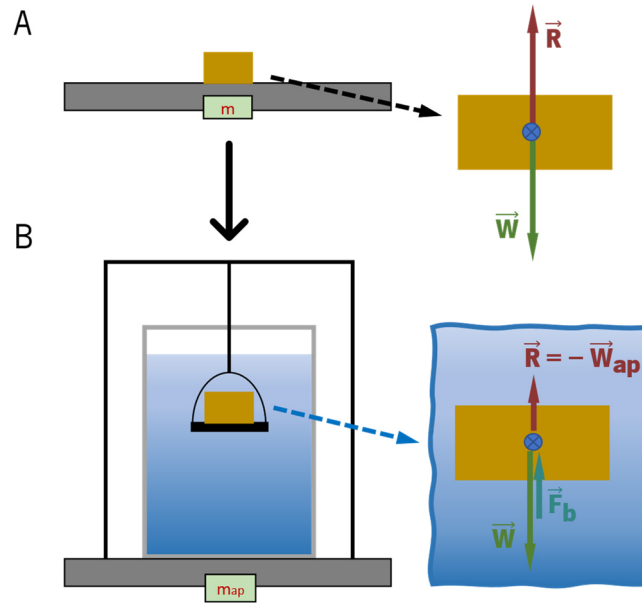


**Figure 3.9.** Free body diagrams of the specimen when out (A) and immersed (B) in water. The grey rectangle symbolizes the scale, which is set to zero, before the introduction of the specimen, and that displays the mass and apparent mass, when the specimen is out (A) or immersed in water (B).

The reaction force is equal in magnitude and opposite in direction to the value of the apparent weight ( $\vec{W}_{ap}$ ), that is the difference between the true weight and the buoyancy force. Equation 3-6 then becomes equation 3-7.

$$\vec{F}_b = \vec{W} + \vec{W}_{ap} \quad 3-7$$

Matching equation 3-5 and equation 3-7, and replacing the weight and apparent weight, by the mass ( $m$ ) and apparent mass ( $m_{ap}$ ), respectively, both multiplied by the acceleration of gravity, equation 3-8 is left.

$$\rho_{water}Vg = mg + m_{ap}g \quad 3-8$$

Discarding the acceleration of gravity, it follows:

$$\rho_{water}V = m + m_{ap} \quad 3-9$$

At last, replacing the volume in equation 3-9 by the ratio between the mass of the specimen and its density ( $\rho$ ), and rearranging, equation 3-10 is left. Therefore, it is possible to relate the density of water

to the density of the specimen's material, by weighting the specimen outside and inside water, which would allow us to find its mass and apparent mass, respectively.

$$\rho = \frac{1}{1 - \frac{m_{ap}}{m}} \rho_{water} \quad 3-10$$

### 3.2.2 Specimens

The specimens (Figure 3.10) were obtained from MMBs or scrap MMB parts, with the aid of a guillotine and a grinding wheel for the brass and stainless-steel specimens, and an electric bandsaw for the PU ones.

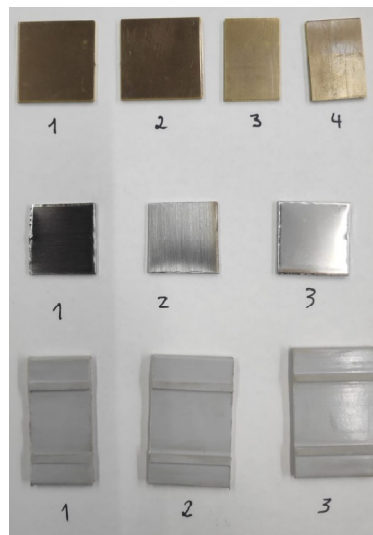


**Figure 3.10.** Test specimens of brass, stainless steel and PA (from top to bottom) used in the experiment and numbered for each material.

### 3.2.3 Equipment

The equipment used was a DU-32 Argo Lab digital ultrasonic cleaner, a Mettler AE240 precision analytical digital balance scale with a small structure to support the test specimens, a beaker with distilled water, an aluminium foil container with ethanol, a set of tweezers, a rubber ear wash ball, and a hairdryer. All equipment can be easily identified in Figure 3.11, except for the precision scale and the beaker, which can be found in Figure 3.12.



**Figure 3.11.** Equipment used in the density experiment: a DU-32 Argo Lab digital ultrasonic cleaner (1), a hair dryer (2), rubber ear wash ball (3), a set of tweezers (4), and an aluminium foil container with ethanol (5). Additionally, a Mettler AE240 precision analytical digital balance scale with a small structure to support the test specimens and a beaker with distilled water were used but are missing from this image.

### 3.2.4 Procedure

For each material, the test specimens were placed on the aluminium foil recipient with ethanol, which was then moved to the DU-32 to be cleaned in an ultrasonic bath. After, the container was removed from the ultrasonic cleaner, and the test specimens were removed using tweezers from the container. Similarly, from this point forward, each operation involving the test specimens was done with the tweezers, to keep the specimens clean. To remove excessive ethanol, a rubber ear wash ball was used, and subsequently a hairdryer to dry each specimen.

On the Mettler AE240, a precision of  $1 \times 10^{-4} \pm 5$  grams was defined. One at a time, the mass of the (already cleaned) test specimen was measured on the scale without the beaker, before being measured with the specimen immersed in the distilled water of the beaker, to find the apparent mass. Several measurements were made, and the scale was always set to zero before placing the specimen on the support structure, with and without the beaker containing distilled water.

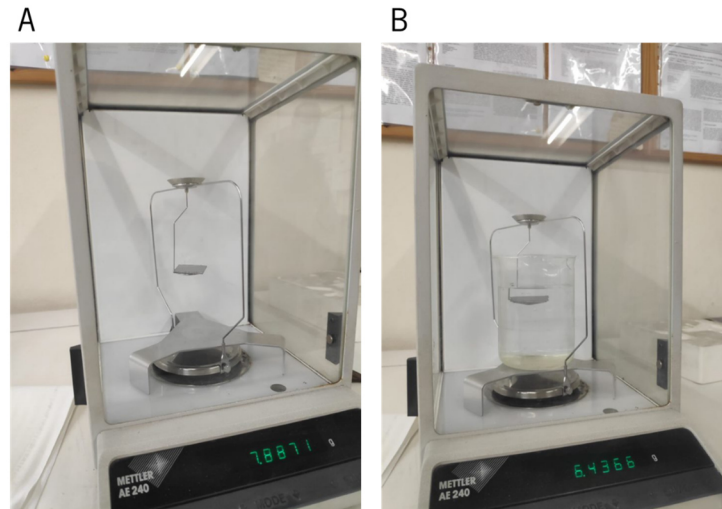


**Figure 3.12.** Mettler AE240 precision analytical digital balance scale with a small structure to support the stainless steel test specimen (A), and the same setup but with a beaker filled with distilled water, where the specimen is submerged (B).

### 3.2.5 Data Treatment

For each test specimen, the registered mass and apparent mass were averaged and using equation 3-10, the density was calculated, with a water density of  $998,2 \text{ kg/m}^3$ , which according to ASTM D4052-16, it is the density of pure water at  $20^\circ\text{C}$  [64]. The density of the material was found by averaging the densities found for each test specimen. All calculations were made using Microsoft Excel.

### 3.2.6 Properties

Table 3.2 shows the densities extracted from the measurements, and a relative error, which was calculated from the values given by the supplier for the same materials, except for the PA, which had the error determined in relation to the PBT. The densities of the metals have a strong agreement with the values from the supplier, which doesn't happen between the densities of the PA and the PBT.

**Table 3.2.** Material's density from the experiment, with the relative error calculated from the values given by the supplier for the same materials, except the PA, where the error is in relation to the PBT.

Material	Density (kg/m <sup>3</sup> )	$\Delta$
Brass	8492	-0,1%
Stainless steel	8002	$\approx 0\%$
PA	1336	-12,7%

### 3.3 Three-Point Bending

The three-point bending test was performed on an MMB, after the experimental modal analysis, with the objective of having data that would allow for an evaluation of the results from the different models of the MMB, developed in the following chapters, and determine the level of trust in their application in a full DLD system.

#### 3.3.1 Test Specimen

For the three-point bending test, a brass MMB with the symmetric P.2992 profile, with a length of 1600 mm was used (Figure 3.13).

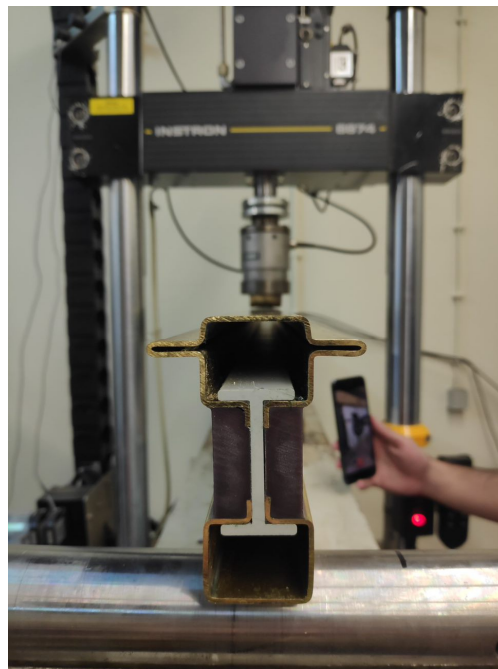


**Figure 3.13.** Brass MMB with a P.2992 profile, during the three-point bending experimental test.



### 3.3.2 Equipment and Setup

Similar to the brass tensile test, the three-point bending test was performed in the Instron 8874, but with a pin mounted at the end of the hydraulic cylinder and a steel base structure with two pins, fixed to the base of the Instron 8874. The supporting pins were 1540 mm apart, and the base structure was mounted so that the loading pin, which was attached to the hydraulic cylinder, was at the same distance from each supporting pin. The MMB was then placed on the supporting pins, in such a manner that a transversal plane passing through the centre of the MMB would pass through the centre of the loading pin. This pin was then lowered so that it would be tangent to the top face of the MMB.

Subsequently, a digital gauge with a magnetic base was placed on the base structure, measuring the displacement of the MMB on the bottom face on its mid-length. Pointing to the digital gauge, a camera was recording the gauge's values, and in the computer, the Bluehill software was running, collecting data from the test. A sketch of the setup can be found in Figure 3.14.

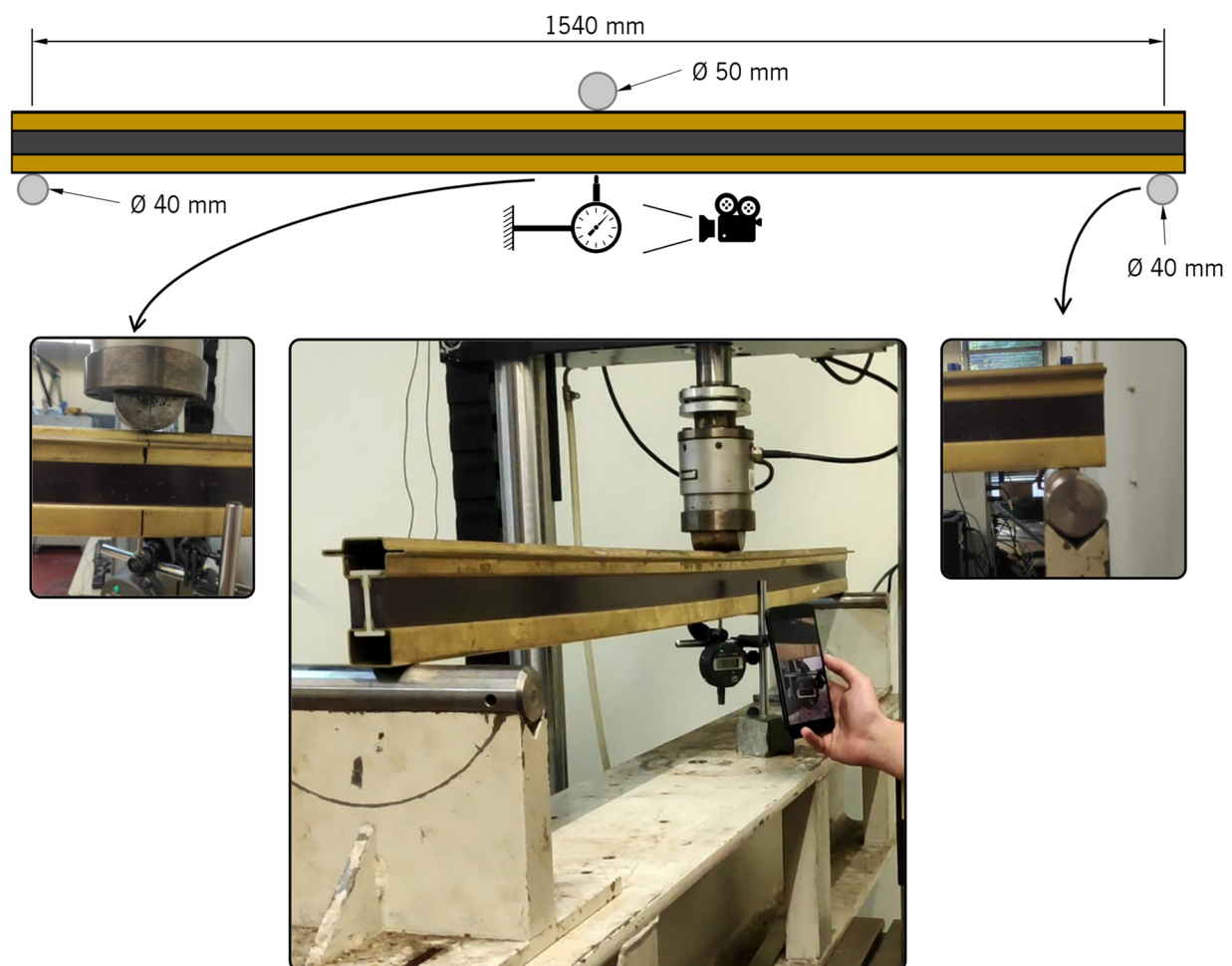


**Figure 3.14.** Schematic setup of the three-point bending experiment, with the diameter of the loading pin and of the supports, the distance between supports, as well as a picture of the whole setup, and close-ups to the centre and to the support pin.

### 3.3.3 Procedure

The command was given for the test to begin, and at the same time, the recording of the camera pointing to the digital gauge was initiated. This way, the time of the recording could be perfectly matched to the time of the test registered by the Bluehill software, or at least as close as possible. Thus, two displacement measurements took place on the mid-length of the MMB during the test, one on the top face of the MMB, registered by the Bluehill software, and another at the bottom face of the MMB, being registered by the camera. Close to the 10 mm displacement mark, the digital gauge was removed, as it had already registered sufficient information for the calculation of the stiffness of the MMB, from the bottom face. Another reason for the gauge removal was the sounds that were coming from the MMB, indicating that the MMB could collapse, which in turn could damage the measuring equipment.

During the test, a velocity of 0,025 mm/s was employed on the downward movement of the hydraulic cylinder until the test stoppage, which took place after the load on the auxiliary graphic that accompanied the test on a side screen dropped to zero. After the test, the MMB was dismounted from the testing rig and using the digital gauge, the residual deformation was measured at points spaced by 50 mm along the MMB's length (on the bottom and top face), on a metallic table (Figure 3.15). The measurements performed, were relative to the values at MMB's extremes.



**Figure 3.15.** Digital gauge with a magnetic base on a steel table for the measurement of the residual deformation on the MMB, after the three-point bending experiment. Black lines can be seen every 50 mm that mark the measuring points, and the gauge is set to zero on the first measured extremity.

### 3.3.4 Data Treatment

The data collected by the Bluehill software was exported as a Raw file and opened in Microsoft Excel. Then, the load and displacement (maximum) on the top face of the MMB were plotted together. From the video recording, the displacement was registered in a Microsoft Excel sheet along with the corresponding time, every five seconds. The load from the machine's data was matched to the displacements from the video recording with the same timestamp. This was the reason why it was important to start the recording at the exact beginning of the test, since time would be the common variable that would allow for the correlation between the data of the machine collected by the Bluehill software and the data of the recording video. The load and displacement (maximum) at the bottom face of the MMB were then plotted together, with a total of 95 points. Lastly, the registered residual displacements on the top and bottom face of the beam were plotted against its length, to a total of 55 points on each graph.

## 3.4 Experimental Modal Analysis

The experimental modal analysis was performed with the same P.2992 brass MMB used in the three-point bending test, which followed this dynamic analysis. The objective of this experiment was to obtain an experimental foundation that could be compared with the different models of the MMB presented in the following chapters, providing confidence in their use in more complex applications, such as the model of a DLD system.

### 3.4.1 Hammer Impulse Method Brief Overview

To find the frequencies at which the MMB resonates, a vibrations test using an impact hammer was performed. The method was chosen due to its simplicity when compared to other methods used to measure the frequency responses on mechanical systems like using a shaker excitation [40]. The impact force from the hammer is meant to mimic an impulse, which is a mathematical concept of a time function that is null, except on a single peak of infinite magnitude that occurs on an infinitesimal time duration (Dirac impulse) [40]. This function has a Fourier transform that has a constant value across all frequencies, usually 1. Consequently, if an impulse is used as the input of a frequency response function (FRF), all frequencies will be excited with the same magnitude. Practically, it is not possible to produce

an impulse, but it is possible to produce a force excitation in a sufficiently short time window, that produces a broad (although not infinite) spectrum [40]. Figure 3.16 attempts to illustrate this concept.

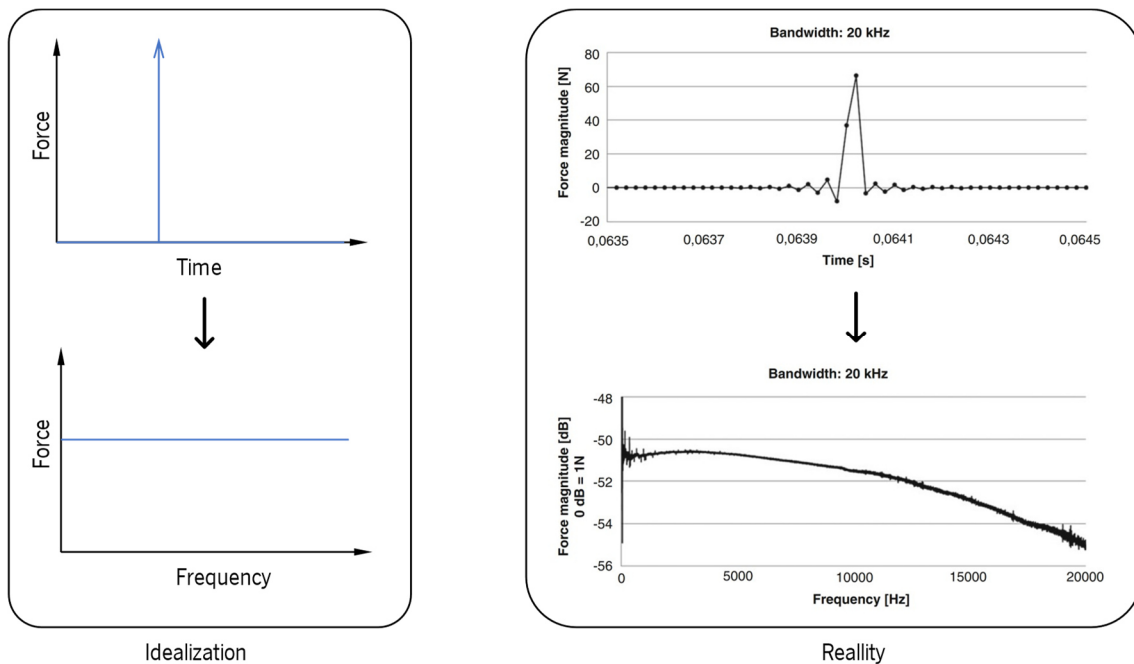


**Figure 3.16.** Difference between an idealized impulse function, and the practical application of this concept. Reality images reproduced from [65].

The method considers a force impulse caused by the hammer, which excites the MMB on a broad range of frequencies [40], [66]. The impulse force is measured on a transducer in the hammer, and the motion of the specimen can be captured for example with a laser to measure velocities or with an accelerometer, which was used in this experiment [40], [66]. It is important for the impact to avoid any point along the length of the beam that corresponds to a modal node since it would not excite the resonant frequency correspondent to said mode shape [66]. The hammer and accelerometer are connected to specific hardware (data acquisition system) that transforms their analogue signals into digital signals, resulting in a registered set of discrete values, instead of a continuous function [40], [66]. The hardware is controlled by a software, usually implemented on a laptop, that stores and processes the excitation and response data, so that FRFs can be calculated and displayed [40], [66]. As discrete quantities are being used, the objective is to find the discrete Fourier transform (DFT) from the inputs and outputs, so that the FRF can be found [40], [66]. The way the software does this is by implementing fast Fourier transform (FFT) algorithms [40], [66]. From the ratio of the frequency response from the accelerometer to the impulse force frequency response, the FRF is found [40], [66].

Multiple FRFs calculated with the accelerometer at different points along the length of the MMB can be used to find its mode shapes [40], [66]. As proven by Maxwell's reciprocity relation, the frequency response between two points is the same if a structure is excited on a first point and the response measured on a second, or if the excitation and measurement points are reversed [40]. This means that to find the mode shapes along the MMB the same point can be excited and the accelerometer moved along the MMB, or keep the accelerometer fixed and vary the point of impact on the MMB along its length [40]. A third solution would be to use several accelerometers placed at different positions along the MMB's length and chose an impact point [40].

Despite its simplicity, this method has a few drawbacks, like the relatively small signal to noise ratio (SNR), when compared to methods that use a continuous excitation signal, such as a shaker [40]. Because it measures the free decay of the structure, the contaminating noise leads to smaller SNR the longer the time record is extended, affecting the quality of the signal, since it deteriorates [40].

### **3.4.2 Equipment and Setup**

Eleven equidistant markings were made in the MMB, and the MMB was suspended with polymeric rigid wire in two locations, coinciding with the nodes of the first two bending modes of a free beam, located at  $0,224 \times \text{length}$  from the extremes. Since the MMB had a length of 1600 mm, each wire was located at 358,4 mm from the extremes.

The impact hammer used was a PCB Piezoelectronics model 086c01, which consists of a handle, a head, and a force transducer with an aluminium tip (which was the only tip available). A triaxial piezoelectric accelerometer was used, with the designation PCB Piezoelectronics model 356A1 SN 179622, and was attached to the MMB using a wax. The impact hammer and the accelerometer were connected to the input channels of the data acquisition system LMS Scadas Mobile, to a total of four input channels, one that received the force signal from the hammer, and three from the accelerometer each one transmitting the analogue signal corresponding to the acceleration in one of the three directions: X, Y or Z. To convert the analogue signals from the hammer and accelerometer into digital signals, it was used a data acquisition system, the LMS Scadas Mobile, which was controlled by the software LMS Test.Xpress, which was implemented on a laptop computer, where the signals were stored and processed [40], [66]. An illustration of the setup can be found in Figure 3.17.

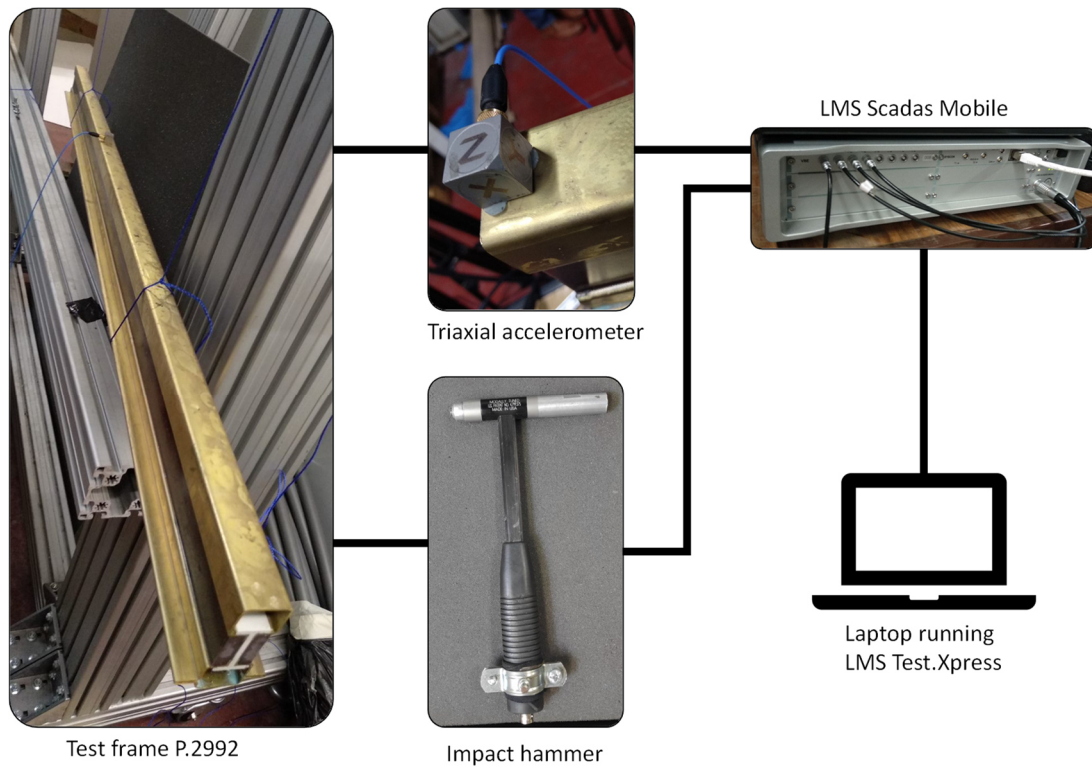


**Figure 3.17.** Setup of the experimental modal analysis, where the analogue signals from the hammer and accelerometer were converted into digital signals in the LMS Scadas mobile, that was controlled by a laptop running the LMS Test.Xpress, that stores and processes the signals.

### 3.4.3 Procedure

With the setup arranged, and the equipment and software running, eleven hammer impulses, and the respective MMB response were recorded. All hammer impulses were made with an impact in the same spot, each with the accelerometer attached to the MMB at a marked location that varied along its length. The signals were automatically processed and stored, and the result was a set of FRFs, three for each impact point, corresponding to one in each direction. During the test, the FRF with the peaks corresponding to the resonant frequencies could be viewed, which was used as an evaluation of the impact, based on the quality of the graphs displayed.

### 3.4.4 Data Treatment

After the test, the general FRF solution of the MMB in the Z direction was provided in Microsoft Excel and is presented in Chapter 6. Unfortunately, the modal shape results from the experiment were not coherent. From the provided data the half-power bandwidth method was performed, to find the damping ratio, from the 1<sup>st</sup> resonant frequency.

### 3.4.5 Half-Power Bandwidth Method

Because of its simplicity, the half-power bandwidth method is extensively used in mechanical structures, considering a linear viscous damping [67]. By assuming small damping ratios, in conjunction with an acceleration frequency response transfer function, an estimation of the damping ratio ( $\xi$ ) can be accomplished using equation 3-11 [67].

$$\xi = \frac{\omega_2 - \omega_1}{2\omega_r} \quad 3-11$$

In equation 3-11, variable  $\omega_r$  corresponds to the frequency at resonance, and  $\omega_1$  and  $\omega_2$  are the frequencies before and after resonance, respectively, at the amplitude illustrated in Figure 3.18 [67].

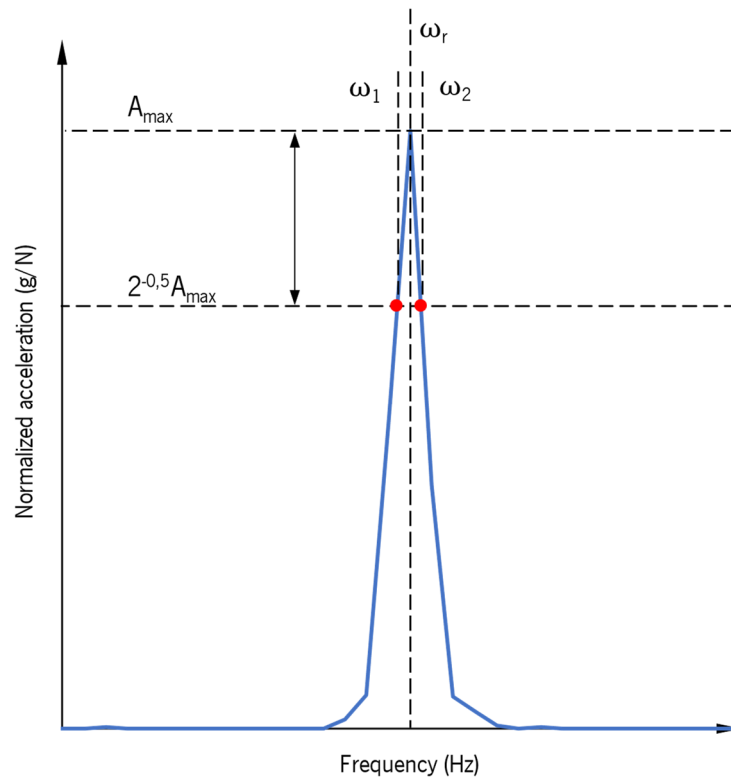


**Figure 3.18.** Schematic of half-power bandwidth method on a resonant frequency. Based on the representation of the method from [68].

This method was used in the first resonance frequency of the beam, to find its damping ratio.

# Chapter 4

## ANALYTICAL METHODS

The study of beams that possess particularities that increase the complexity of their behaviour, such as a variable cross-section along their length or multiple components, is still evolving. For example, R. D. Copetti et al. [69] approached a block matrix formulation of an uncoupled double Timoshenko beam, separated by a Winker elastic interlayer, that can find its modal response, and R. Eberle and M. Oberguggenberger [70], developed a computationally efficient method, based on experimental data from a bending test and calculus of variations, for the determination of the bending stiffness of an Euler-Bernoulli beam with un-uniform cross-section along the beam's length. The first could be useful, for instance, in depicting the modal response of sandwich composites, or laminated beams, and the latter defining the bending stiffness of irregular beams, for instance, bones [69], [70].

In this chapter, the theory from 4.1 and 4.4 was based on F. P. Beer et al. [71], and the theory from 4.2 and 4.3 was adapted for an MMB from T. H. G. Megson [72] and Clarence W. da Silva [73], respectively. Additionally, 4.3 was written with the aid of Jorge Figueiredo and Carolina Ribeiro [74].

The MMB can be treated as a beam that is composed of several elements that are themselves beams, and to mathematically define a multi-material beam with the Euler-Bernoulli beam theory, some assumptions were made: the different components of the MMB are bonded together at the various interfaces, and the section of the whole MMB remains unchanged after bending [71]. The last assumption allows for the multi-material beam to be defined as one, since the centre of curvature of each of the different components, all following the same theory, is the same for any point along the length of the MMB [71].

Adopting the MMB as a beam with all components cohesively bonded, there is one general neutral plane with zero deformation along the length of the MMB, where its curvature is represented [71]. As shown ahead, the presence of materials with different properties, namely different elastic moduli, changes the behaviour of the MMB due to bending, in comparison to what would happen if the MMB was of only one material. This reflects in the way the section properties of the MMB are calculated, e.g., the location of the centroid.



The formulation presented in this chapter was applied on Microsoft Excel sheets, using the material properties from Table 2.3, Table 3.1, and Table 3.2. A brass MMB of 1540 mm with the P.2992 profile was used for the comparison of the three-point bending analytical model with the experimental data and the different numerical models. Additionally, brass MMBs of several profiles had their natural frequencies, with bending and longitudinal mode shapes, compared to the ones acquired with the numerical beam elements model, or in the case of the P.2992, with all the numerical models and the experimental data. Thus, the dynamic formulation was applied to the P.2901, P.2915, P.2942, P.2942, P.2943, P.2961, P.2962, P.2963, P.2965, P.2971, P.2972, P.2991, P.2995, and P.2992 profiles (Annex A), all with a length of 1600 mm.

## 4.1 Governing Equation of the Elastic Curve of a Multi-Material Beam

Starting with the analysis of the moment balance, the bending moment resultant of the external loads is matched by the inertia offered by the different components to that same bending moment, and so, the total moment resistance to the bending of the MMB can be represented by the summation of the moments supported by each of the different components (Figure 4.1).

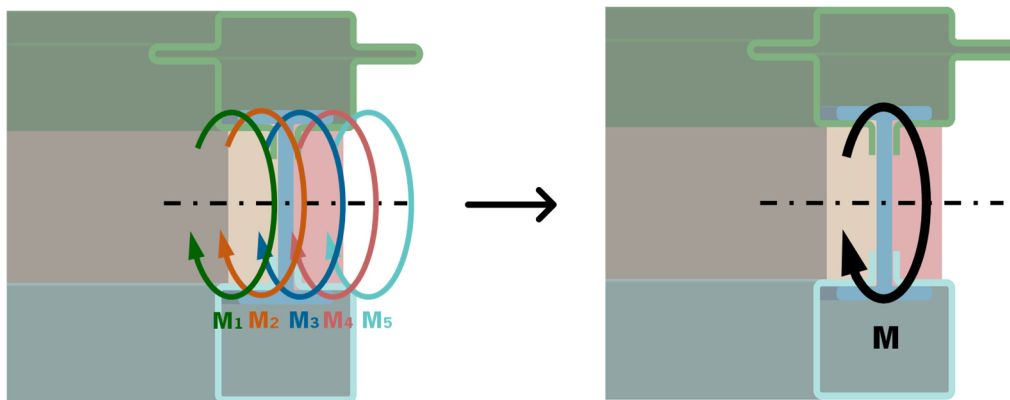


**Figure 4.1.** The internal moments from the five components of a MMB compose the internal bending moment that results from applying the external loads.

This summation is expressed by equation 4-1.

$$M = \sum M_i \quad 4-1$$

And because an assumption was made that the cross-section of the MMB remains unchanged and that all components have the same centre of curvature, defining  $y$  to be the distance to the neutral plane of the MMB, and  $x$ , as the independent variable, along the length of the MMB, from beam theory, it follows [71]:

$$M_i = -E_i I_i \frac{d^2 y}{dx^2} \quad 4-2$$

Where  $E_i$  represents the elastic modulus of the element  $i$ 's material, and  $I_i$  its second moment of area.

The assumption that the cross-sections of the components of the MMB remain in-plane with one another was made, and therefore every component's cross-section rotates around the same axis, meaning that the centre of curvature for each component at any point along the length of the MMB when bending occurs must be the same. This means that the second moment of area of each component's cross-section must be determined about one neutral plane, which is the neutral plane of the whole MMB. Consequently, because the same neutral plane is considered, the curvature of each component when bent as part of the MMB is also the same, and equation 4-1 becomes:

$$M = \sum -E_i I_i \frac{d^2 y}{dx^2} \quad 4-3$$

At this point, from equation 4-3, it is noticeable that the flexural rigidity ( $EI$ ) of the resultant beam is the summation of the flexural rigidity of the different components of the MMB, with each second moment of area being calculated about the general neutral plane of the MMB. However, it is convenient to rearrange the equation 4-3 as:

$$M = -E_b I_{eq} \frac{d^2 y}{dx^2} \quad 4-4$$

$$I_{eq} = \sum \frac{E_i}{E_b} I_i \quad 4-5$$

From equation 4-4, an equivalent beam, made of only one base material (arbitrarily chosen) with an elastic modulus  $E_b$ , emerges, with an equivalent second moment of area ( $I_{eq}$ ), calculated from equation

4-5. Further analysing the contribution of a single component  $i$  in the equivalent second moment of area, the following is obtained [71]:

$$\frac{E_i}{E_b} I_i = n_i I_i = n_i \int y^2 dA = \int y^2 n_i dA \quad 4-6$$

This result allows for a better visualization of the equivalent beam since a distinction of the importance of the small elemental areas is made, based on their material of origin. This importance is captured by the factor  $n_i$  which is the ratio between the elastic modulus of the material of origin and the base material chosen for the equivalent beam. One way to visualize this equivalent beam is to imagine an expansion of each elemental area by the correspondent factor  $n_i$  in the parallel direction of the axis of rotation (Figure 4.2), another interpretation is to simply identify the different factors in the different component's cross-sections.

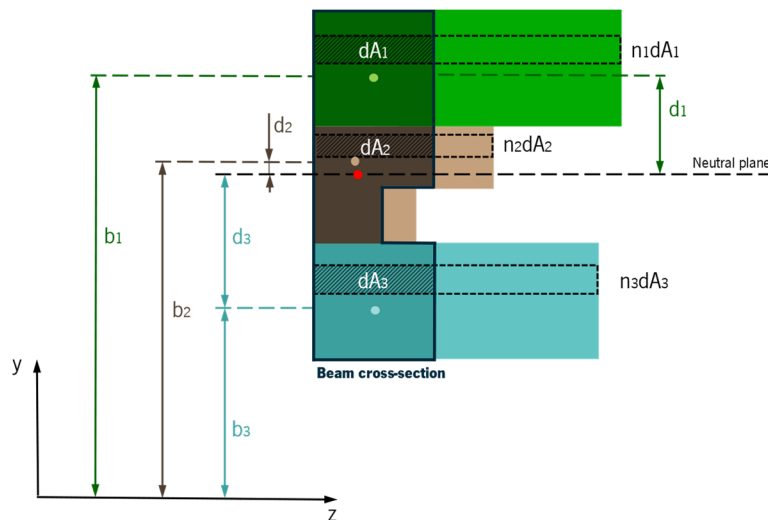


**Figure 4.2.** Representation of the cross-section of the equivalent beam, from the cross-section of an MMB, where the material of the different components influences the weight of its elemental areas in the equivalent beam's cross-section. In this case, equivalent beam is illustrated by expanding each elemental area by the correspondent factor  $n_i$  in a direction parallel to the axis of rotation. The variables  $d$  and  $b$  represent the distance between the centroid of a component's cross-section and the neutral plane of the equivalent beam or the axis of the CAD software, respectively.

Because different components with distinct materials have a different weight in the equivalent beam's cross-section, properties like the distance of the centroid of the section of the beam to the software axis ( $\bar{Y}$ ) are changed too [71].

$$\bar{Y} = \frac{\sum \int y n_i dA}{\sum \int n_i dA} = \frac{\sum n_i \int y dA}{\sum n_i \int dA} = \frac{\sum n_i b_i A_i}{\sum n_i A_i} \quad 4-7$$

Where  $A_i$  and  $b_i$  are the area of the component's cross-section and the distance of the centroid of this section to the axis of the CAD software (Figure 4.2), respectively.

Given the complexity of the cross-sections, to determine the second moment of area of the different components about the centroid of the MMB ( $I_i$ ), it is convenient to calculate the second moment of area about the centroid of each component's cross-section ( $I'_i$ ), which can be done with the aid of the numerical methods used by a CAD software, and then make use of Steiner's theorem of the parallel axis to calculate the second moment of area about the centroid of the equivalent beam. The distance between these centroids is denoted by  $d_i$ , and the theorem is applicable as follows [71]:

$$I_i = I'_i + d_i^2 A_i \quad 4-8$$

In fact, it is the values  $b_i$ ,  $A_i$  and  $I'_i$ , obtained by the CAD software, along with the elastic modulus of the component's materials that allow for the calculation of all the other parameters that lead to the flexural rigidity ( $E_b I_{eq}$ ) of the equivalent beam. The CAD software used was SpaceClaim (Figure 4.3).

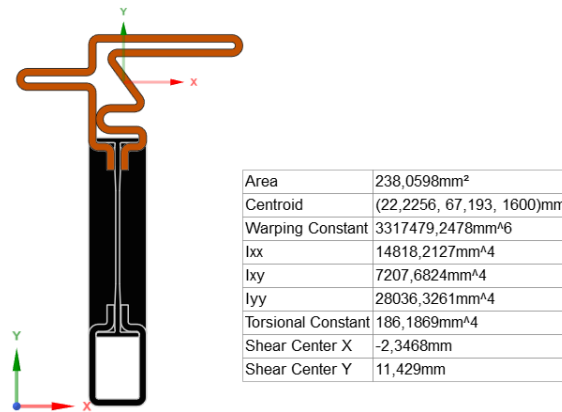


**Figure 4.3.**  $b_i$ ,  $A_i$  and  $I'_i$ , taken from SpaceClaim for the metal component highlighted in orange, of the P.2942 profile.

The flexural rigidity can be calculated directly from the input parameters by:

$$E_b I_{eq} = \sum \left[ E_i \left( I'_i + A_i \left( b_i - \frac{\sum E_i b_i A_i}{\sum E_i A_i} \right)^2 \right) \right] \quad 4-9$$

## 4.2 Principal Axis of a Multi-Material Beam with an Unsymmetrical Cross-Section

The cross-sectional properties of each component of the beam, namely second moments of area and product moments of area, are firstly calculated by the CAD software SpaceClaim. Then, these properties are mathematically treated, and then presented, to be in respect to a coordinate system (CS) whose axes are parallel to those of the CS used by SpaceClaim, and whose origin is at the centroid of the MMB/equivalent beam's cross-section.

In the case of a symmetric cross-section, the axes of SpaceClaim's CS can easily be made to be parallel to the principal axis, but when dealing with an unsymmetric cross-section it becomes a much harder job. Therefore, a relation between the mentioned cross-sectional properties of the equivalent beam about the principal axes and about two arbitrary convenient axes must be found.

The axes of the CS used by SpaceClaim are perpendicular, and so are the principal axes of the cross-section.

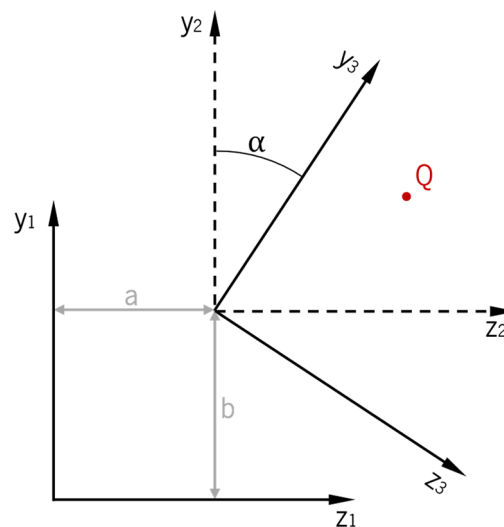


**Figure 4.4.** Point Q and three coordinate systems (CS), where CS 3 shares an origin with CS 2, but its axes are rotated, and CS2 is translated in relation to CS 1.

Because the calculation of the centroid of the composite beam is a more complex exercise than the calculation for a one material beam, three coordinate systems are defined, with CS 3 suffering a rotation and a translation about CS 1, to make sure the calculation of the centroid isn't affected by the coordinate system on which it is calculated. Using Figure 4.4 as support, a point in CS 2 can be written, by its coordinates in CS 1, by equations 4-10 and 4-11.

$$y_2 = y_1 + b \quad 4-10$$

$$z_2 = z_1 + a \quad 4-11$$

Similarly, a point in CS 3 can be written by its coordinates in CS 2 by equations 4-12 and 4-13.

$$y_3 = y_2 \cos(\alpha) + z_2 \sin(\alpha) \quad 4-12$$

$$z_3 = z_2 \cos(\alpha) - y_2 \sin(\alpha) \quad 4-13$$

Substituting equations 4-10 and 4-11 in equations 4-12 and 4-13, a point in CS 3 can be determined by its position in CS1.

$$y_3 = (y_1 + b) \cos(\alpha) + (z_1 + a) \sin(\alpha) \quad 4-14$$

$$z_3 = (z_1 + a) \cos(\alpha) - (y_1 + b) \sin(\alpha) \quad 4-15$$

The centroid of the beam in the axes Y and Z is determined by equations 4-16 and 4-17, respectively.

$$\bar{Y}_3 = \frac{\sum \int y_3 n_i dA}{\sum \int n_i dA} \quad 4-16$$

$$\bar{Z}_3 = \frac{\sum \int z_3 n_i dA}{\sum \int n_i dA} \quad 4-17$$

Introducing equations 4-14 and 4-15 in equations 4-16 and 4-17, respectively, yields:

$$\bar{Y}_3 = \frac{\sum \int [(y_1 + b) \cos(\alpha) + (z_1 + a) \sin(\alpha)] n_i dA}{\sum \int n_i dA} \quad 4-18$$

$$\bar{Z}_3 = \frac{\sum \int [(z_1 + a) \cos(\alpha) - (y_1 + b) \sin(\alpha)] n_i dA}{\sum \int n_i dA} \quad 4-19$$

Solving equations 4-18 and 4-19, the result is equations 4-20 and 4-21, respectively, which represent the position of the centroid in the arbitrary CS 3, as a function of its coordinates in CS 1. This function represents exactly the transformation of a point from CS 1 to CS 3, as can be verified in 4-14 and 4-15, meaning that the centroid doesn't move its position in the MMB, just like it wouldn't in a one material beam.

$$\bar{Y}_3 = (\bar{Y}_1 + b) \cos(\alpha) + (\bar{Z}_1 + a) \sin(\alpha) \quad 4-20$$

$$\bar{Z}_3 = (\bar{Z}_1 + a) \cos(\alpha) - (\bar{Y}_1 + b) \sin(\alpha) \quad 4-21$$

The cross-sectional properties taken from SpaceClaim are in respect to a CS A that has the centroid of the beam as its origin, and since the principal axes pass through the centroid, CS B composed of the principal axes also has the origin on the centroid of the beam's cross-section. Hence, because the beam's centroid doesn't move with the change in coordinate system, CS A and CS B have the same origin, and making use of equations 4-12 and 4-13, a point from CS A can be written in CS B by equations 4-22 and 4-23.

$$y_B = y_A \cos(\alpha) + z_A \sin(\alpha) \quad 4-22$$

$$z_B = z_A \cos(\alpha) - y_A \sin(\alpha) \quad 4-23$$

The second moments of area about the z principal axis ( $I_{zz}^B$ ), y principal axis ( $I_{yy}^B$ ), and the product moment of area accordingly to CS B ( $I_{zy}^B$ ), are determined by equations 4-24, 4-25, and 4-26, respectively.

$$I_{zz}^B = \int y_B^2 dA \quad 4-24$$

$$I_{yy}^B = \int z_B^2 dA \quad 4-25$$

$$I_{zy}^B = \int z_B y_B dA \quad 4-26$$

Replacing equations 4-22 and 4-23, in equations 4-24, 4-25 and 4-26, the following equations emerge:

$$I_{zz}^B = \int (y_A \cos(\alpha) + z_A \sin(\alpha))^2 dA \quad 4-27$$

$$I_{yy}^B = \int (z_A \cos(\alpha) - y_A \sin(\alpha))^2 dA \quad 4-28$$

$$I_{zy}^B = \int (z_A \cos(\alpha) - y_A \sin(\alpha))(y_A \cos(\alpha) + z_A \sin(\alpha)) dA \quad 4-29$$

Solving these equations, and performing some algebraic manipulation it follows:

$$I_{zz}^B = I_{zz}^A \cos^2(\alpha) + I_{yy}^A \sin^2(\alpha) + I_{zy}^A \sin(2\alpha) \quad 4-30$$

$$I_{yy}^B = I_{yy}^A \cos^2(\alpha) + I_{zz}^A \sin^2(\alpha) - I_{zy}^A \sin(2\alpha) \quad 4-31$$

$$I_{zy}^B = \left( \frac{I_{zz}^A - I_{yy}^A}{2} \right) \sin(2\alpha) + I_{zy}^A \cos(2\alpha) \quad 4-32$$

To obtain the second moments of area about the z principal axis ( $I_{zz,beam}^B$ ), y principal axis ( $I_{yy,beam}^B$ ), and the product moment of area accordingly to CS B ( $I_{zy,beam}^B$ ), of the whole beam, the theory exposed in 4.1 is used along with the concept of using an equivalent one material beam to represent a multi-material beam. Hence, the equations 4-33, 4-34, and 4-35, arise.

$$I_{zz,beam}^B = \sum n_i I_{zz,i}^B \quad 4-33$$

$$I_{yy,beam}^B = \sum n_i I_{yy,i}^B \quad 4-34$$

$$I_{zy,beam}^B = \sum n_i I_{zy,i}^B \quad 4-35$$

Applying equations 4-30, 4-31, and 4-32, it follows:

$$I_{zz,beam}^B = \cos^2(\alpha) \sum n_i I_{zz,i}^A + \sin^2(\alpha) \sum n_i I_{yy,i}^A + \sin(2\alpha) \sum n_i I_{zy,i}^A \quad 4-36$$



$$I_{yy,beam}^B = \cos^2(\alpha) \sum n_i I_{yy,i}^A + \sin^2(\alpha) \sum n_i I_{zz,i}^A - \sin(2\alpha) \sum n_i I_{zy,i}^A \quad 4-37$$

$$I_{zy,beam}^B = \sin(2\alpha) \left( \frac{\sum n_i I_{zz,i}^A - \sum n_i I_{yy,i}^A}{2} \right) + \cos(2\alpha) \sum n_i I_{zy,i}^A \quad 4-38$$

To calculate the product moment of area of component  $i$  ( $I_{zy,i}^A$ ) of a section about a point located at a distance  $dz$  and  $dy$ , in the  $z$  and  $y$  directions, respectively, from the point where this property was originally calculated ( $I_{zy,i}^A$ ) one can use equation 4-39 [72]. This equation comes in handy, since SpaceClaim gives the product moment of area of a component's section about its centroid, allowing for the calculation of this property about the centroid of the equivalent beam.

$$I_{zy,i}^A = I_{zy,i}^A + d_z d_y A_i \quad 4-39$$

For the second moments of area of component  $i$  in CS A ( $I_{zz,i}^A$  and  $I_{yy,i}^A$ ), the theorem from equation 4-8 applies. The summations present in equations 4-36, 4-37 and 4-38 represent, precisely, the equivalent second moments of area,  $I_{zz,beam}^A$  and  $I_{yy,beam}^A$ , and product moment of area,  $I_{zy,beam}^A$ , about CS A. Hence, it is possible to update these equations, as follows:

$$I_{zz,beam}^B = \cos^2(\alpha) I_{zz,beam}^A + \sin^2(\alpha) I_{yy,beam}^A + \sin(2\alpha) I_{zy,beam}^A \quad 4-40$$

$$I_{yy,beam}^B = \cos^2(\alpha) I_{yy,beam}^A + \sin^2(\alpha) I_{zz,beam}^A - \sin(2\alpha) I_{zy,beam}^A \quad 4-41$$

$$I_{zy,beam}^B = \sin(2\alpha) \left( \frac{I_{zz,beam}^A - I_{yy,beam}^A}{2} \right) + \cos(2\alpha) I_{zy,beam}^A \quad 4-42$$

Since CS B is defined by the principal axes, by definition, it follows that  $I_{zy,beam}^B = 0$ , and equation 4-43 emerges, and from it, equations 4-44 and 4-45 are extracted.

$$\tan(2\alpha) = \frac{2I_{zy,beam}^A}{I_{yy,beam}^A - I_{zz,beam}^A} \quad 4-43$$

$$\cos(2\alpha) = \frac{(I_{yy,beam}^A - I_{zz,beam}^A)/2}{\sqrt{[(I_{yy,beam}^A - I_{zz,beam}^A)/2]^2 + (I_{zy,beam}^A)^2}} \quad 4-44$$

$$\sin(2\alpha) = \frac{I_{zy,beam}^A}{\sqrt{[(I_{yy,beam}^A - I_{zz,beam}^A)/2]^2 + (I_{zy,beam}^A)^2}} \quad 4-45$$

Writing the  $\sin(\alpha)$  and  $\cos(\alpha)$  terms in equations 4-40 and 4-41, as a function of  $\cos(2\alpha)$ , and then replacing the  $\cos(2\alpha)$  and  $\sin(2\alpha)$  terms in these equations by equations 4-44 and 4-45, and rearranging, equations 4-46 and 4-47 are obtained, which allow for the determination of the equivalent second moments of area of the equivalent beam about the two principal axis, from the equivalent second moments of area and product moment of area of the equivalent beam in respect to an arbitrary coordinate system located at the centroid.

$$I_{zz,beam}^B = \frac{I_{zz,beam}^A + I_{yy,beam}^A}{2} - \frac{1}{2} \sqrt{(I_{zz,beam}^A - I_{yy,beam}^A)^2 + 4(I_{zy,beam}^A)^2} \quad 4-46$$

$$I_{yy,beam}^B = \frac{I_{zz,beam}^A + I_{yy,beam}^A}{2} + \frac{1}{2} \sqrt{(I_{zz,beam}^A - I_{yy,beam}^A)^2 + 4(I_{zy,beam}^A)^2} \quad 4-47$$

Taking  $I_{zz,beam}^B$  or  $I_{yy,beam}^B$  as  $I_{eq}$ , and keeping the same base material for the equivalent beam throughout the calculations, the following chapters are applicable for beams with unsymmetric profiles.

## 4.3 Natural Frequencies and Vibration Modes of a Multi-Material Beam

### 4.3.1 Transverse vibration

Figure 4.5 shows an element of a MMB with infinitesimal length, and the internal transversal forces and moments generated after it is deformed due to the transversal free motion (no exterior forces acting on the MMB).

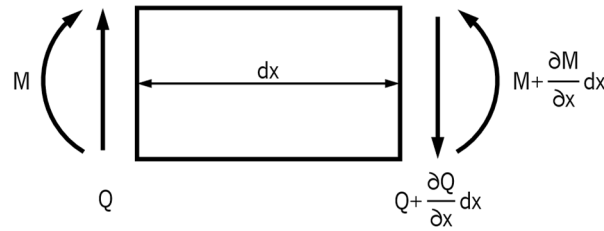


**Figure 4.5.** Forces and moments acting on an elemental portion with infinitesimal length of the MMB subjected to bending.

Considering an elemental portion of the MMB (Figure 4.5) and applying Newton's second law, without external forces (in other to identify the natural frequencies of the beam), the movement equation in the vertical direction can be defined as follows:

$$\frac{\partial Q}{\partial x} dx = m \frac{\partial^2 y}{\partial t^2} \quad 4-48$$

Where  $Q$  is the transverse load,  $m$  is the mass of the elemental portion, and  $t$  is the time variable. From the Euler-Bernoulli beam theory, it is known that:

$$Q = \frac{\partial M}{\partial x} \quad 4-49$$

Bringing in the moment equation deduced in the previous section, and since the flexural rigidity is constant, the transverse load becomes:

$$Q = -E_b I_{eq} \frac{\partial^3 y(x, t)}{\partial x^3} \quad 4-50$$

Substituting equation 4-50 in equation 4-48, and rewriting the mass as though  $A_i$  and  $\rho_i$  (the density of component  $i$ ) the following expression takes place:

$$-E_b I_{eq} \frac{\partial^4 y(x, t)}{\partial x^4} dx = \sum \rho_i A_i dx \frac{\partial^2 y(x, t)}{\partial t^2} \quad 4-51$$

Equation 4-50 is a linear homogenous partial differential equation (PDE), that can be solvable by separation of variables (given that the boundary conditions, B.C., are also linear and homogeneous, which they are, as stated further ahead) with the assumption that the  $y$  function can be written as:

$$y(x, t) = G(x)F(t) \quad 4-52$$

Replacing equation 4-52 in equation 4-51 and rearranging it, equation 4-53 is obtained.

$$\frac{-E_b I_{eq}}{G(x) \sum \rho_i A_i} \frac{\partial^4 G(x)}{\partial x^4} = \frac{1}{F(t)} \frac{\partial^2 F(t)}{\partial t^2} \quad 4-53$$

In general, a function of  $x$  cannot be equal to a function of  $t$  unless each function is equal to the same constant. Thus, the constant  $-\omega^2$  is conveniently defined, as the negative sign forces the characteristic equation, of the linear homogeneous ordinary differential equation (ODE) of constant variables defined in equation 4-54 (the time dependent equation), to have complex roots, consequently introducing the sine and cosine terms that define the oscillatory motion. The square of  $\omega$  ensures that the variable becomes isolated in multiplying the time variable, inside the sine and cosine, defining the frequency of the oscillatory motion. From equalizing the right-hand and left-hand sides of equation 4-53 to  $-\omega^2$ , and rearranging, the following ODEs emerge:

$$\frac{d^2 F(t)}{dt^2} + \omega^2 F(t) = 0 \quad 4-54$$

$$\frac{d^4 G(x)}{dx^4} - \beta^4 G(x) = 0 \quad 4-55$$

$$\beta = \frac{\sum \rho_i A_i}{E_b I_{eq}} \omega^2 \quad 4-56$$

The solutions for these equations are known. After solving and some algebraic manipulation, equations 4-57 and 4-58 embody the solutions to  $F(t)$  and  $G(x)$ , respectively.

$$F(t) = C_1 \sin(\omega t) + C_2 \cos(\omega t) \quad 4-57$$

$$Y(x) = C_3 \sin(\beta x) + C_4 \cos(\beta x) + C_5 \sinh(\beta x) + C_6 \cosh(\beta x) \quad 4-58$$

The general solution is given by equation 4-59, which is the result of substituting Equations 4-57 and 4-58 in equation 4-52. This way, the general solution is the combination of a spatial part, given by equation 4-57, and a time domain part, given by equation 4-58.

$$y(x, t) = [C_3 \sin(\beta x) + C_4 \cos(\beta x) + C_5 \sinh(\beta x) + C_6 \cosh(\beta x)] \cdot [C_1 \sin(\omega t) + C_2 \cos(\omega t)] \quad 4-59$$

For a beam with free ends on both edges, the following boundary conditions (B.C.) are true:

$$\begin{cases} M(0) = 0 \\ Q(0) = 0 \\ M(L) = 0 \\ Q(L) = 0 \end{cases} \Leftrightarrow \begin{cases} \frac{d^2 y(0, t)}{dx^2} = 0 \\ \frac{\partial^3 y(0, t)}{\partial x^3} = 0 \\ \frac{d^2 y(L, t)}{dx^2} = 0 \\ \frac{\partial^3 y(L, t)}{\partial x^3} = 0 \end{cases} \quad 4-60$$

After performing the necessary derivations on equation 4-59 and applying the B.C. in equation 4-60, the system of equations 4-61 results. Focusing on the spatial part, the time dependent equation 4-57, which is part of equation 4-59 was taken as non-zero, during the derivation.

$$\begin{cases} -C_4 + C_6 = 0 \\ -C_3 + C_5 = 0 \\ C_3 \sin(\beta L) - C_4 \cos(\beta L) + C_5 \sinh(\beta L) + C_6 \cosh(\beta L) = 0 \\ C_3 \sin(\beta L) + C_4 \cos(\beta L) + C_5 \cosh(\beta L) + C_6 \sinh(\beta L) = 0 \end{cases} \quad 4-61$$

The 3<sup>rd</sup> and 4<sup>th</sup> rows in system of equations 4-61 can be written in the matrix form as follows:

$$\begin{bmatrix} \sinh(\beta L) - \sin(\beta L) & \cosh(\beta L) - \cos(\beta L) \\ \cosh(\beta L) - \cos(\beta L) & \sinh(\beta L) + \sin(\beta L) \end{bmatrix} \begin{bmatrix} C_3 \\ C_4 \end{bmatrix} = \begin{bmatrix} 0 \\ 0 \end{bmatrix} \quad 4-62$$

For a non-trivial solution, i.e., a solution where the variables on the variable matrix ( $C_3$  and  $C_4$ ) are nonzero, the determinant of the matrix needs to be null. Thus, the following equation results:

$$\cosh(\beta L) \cos(\beta L) = 1 \quad 4-63$$

Equation 4-63 is transcendental and has an infinite number of solutions. It can be numerically solved, for example, using the *vpaolve* function in MatLab. The first five solutions, excluding 0, for  $\beta_n L$ , where  $n$  is the mode of vibration's order, can be found in Table 4.1.

**Table 4.1.** First five solutions to Equation 4-63.

Mode of vibration's order (n)	$\beta_n L$
1	4,7300
2	7,8532
3	10,9956
4	14,1372
5	17,2788

It is now possible to find the first five natural frequencies ( $\omega_n$ ), using equation 4-64 and Table 4.1.

$$\omega_n = \beta_n^2 \sqrt{\frac{E_b I_{eq}}{\sum \rho_i A_i}}; \quad \beta_n = 4,7300L; 7,8532L; \dots \quad 4-64$$

Finally, the mode shapes can be retrieved, writing all the constants in the system equations 4-61 in function of only one of the constants, and performing the substitution in the spatial equation 4-58, after some algebraic manipulation, equation 4-65 can be extracted.

$$Y_n(x) = C_n \left[ \sin(\beta_n x) + \sinh(\beta_n x) - \frac{\sinh(\beta_n L) - \sin(\beta_n L)}{\cosh(\beta_n L) - \cos(\beta_n L)} \cdot (\cos(\beta_n x) + \cosh(\beta_n x)) \right] \quad 4-65$$

Plotting this equation in Microsoft Excel for the first five modes, five curves emerge, as Figure 4.6 portrays.

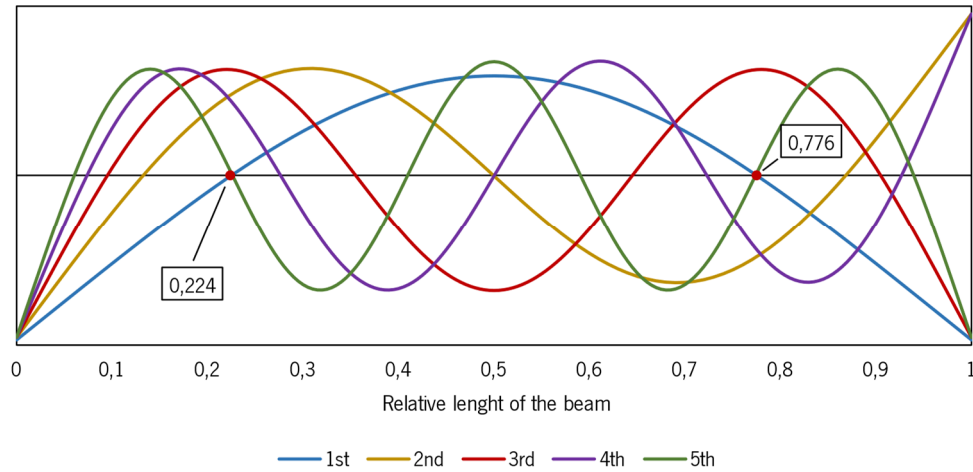


**Figure 4.6.** Five first bending mode shapes of a free-free beam.

### 4.3.2 Longitudinal vibration

Figure 4.7 shows an element of the MMB with infinitesimal length that endures longitudinal motion and reaches its deformed shape, and the forces acting on it in the axial direction.

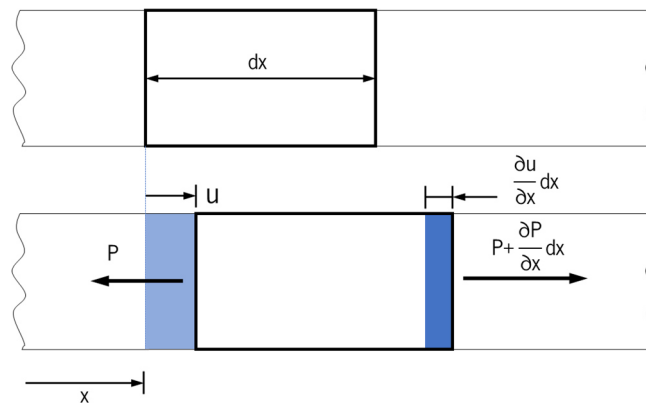


**Figure 4.7.** Axial forces and displacements acting on an element infinitesimal length, due to deformation in the axial direction.

The change in length of an infinitesimal element (Figure 4.7) of length  $dx$  that suffers a displacement  $u$  is given by:

$$\Delta dx = \frac{\partial u(x, t)}{\partial x} dx \quad 4-66$$

The strain can be written by:

$$\epsilon = \frac{\Delta dx}{dx} = \frac{\partial u}{\partial x} \quad 4-67$$

The displacement variable ( $u$ ), as well as the internal MMB force variable ( $P$ ), are functions of both the position in the MMB ( $x$ ) and time ( $t$ ). For a matter of convenience, the arguments ( $x,t$ ) only appear in the equations when relevant. Combining the axial stress equation with Hooke's law results:

$$\sigma = \frac{P}{A} \Leftrightarrow E\epsilon = \frac{P}{A} \quad 4-68$$

Substituting the strain in equation 4-68 with equation 4-67, and rearranging, it follows:

$$P = EA \frac{\partial u}{\partial x} \quad 4-69$$

Once again, using the assumption that the MMB's components' cross-sections remain in-plane to one another, they all move together in the longitudinal/axial direction, and the total internal force ( $P$ ) becomes the summation of the all the components' internal forces, hence:

$$P = \sum P_i = \sum E_i A_i \frac{\partial u}{\partial x} \quad 4-70$$

Differentiating with respect to  $x$  it results that:

$$\frac{\partial P}{\partial x} = \sum E_i A_i \frac{\partial^2 u}{\partial x^2} \quad 4-71$$

Making use of Newton's second law in the axial direction, equation 4-72 appears:

$$\frac{\partial P}{\partial x} dx = \sum \rho_i A_i \frac{\partial^2 u}{\partial t^2} dx \quad 4-72$$

From the combination of equation 4-71 with equation 4-72, equation 4-73 arises.

$$\frac{\partial u^2}{\partial x^2} \sum E_i A_i = \frac{\partial^2 u}{\partial t^2} \sum \rho_i A_i \quad 4-73$$

Equation 4-73 can be written more conveniently, resulting in equation 4-74.



$$\frac{\partial^2 u}{\partial x^2} = \frac{1}{c^2} \frac{\partial^2 u}{\partial t^2}, \quad \text{with} \quad c = \sqrt{\frac{\sum E_i A_i}{\sum \rho_i A_i}} \quad 4-74$$

Much like the transverse vibration case, this linear homogeneous PDE can be solved by separation of variables, and thus, it is assumed that the solution to equation 4-74 is of the type:

$$u(x, t) = U(x) \cdot G(t) \quad 4-75$$

Substituting equation 4-75 in equation 4-74 and partially differentiating with respect to x and t, equation 4-76 arises.

$$\frac{1}{U} \frac{d^2 U}{dx^2} = \frac{1}{c^2 G} \frac{d^2 G}{dt^2} \quad 4-76$$

Similarly, to what happened previously, a function of x cannot be equal to a function of t unless each function is equal to the same constant, and for identical reasons to those presented above, the constant, conveniently chosen, was  $-(\omega/c)^2$ . Matching the right-hand and left-hand sides of equation 4-76, to  $-(\omega/c)^2$ , and rearranging the following ODEs occur:

$$\frac{d^2 U}{dx^2} + (\omega/c)^2 U = 0 \quad 4-77$$

$$\frac{d^2 G}{dt^2} + \omega^2 G = 0 \quad 4-78$$

Equations 4-77 and 4-78 have known solutions, and after solving and some algebraic manipulation, the solutions to F(t) and G(t) can be found in equations 4-79 and 4-80, respectively.

$$U(x) = C_1 \sin\left(\frac{\omega}{c}x\right) + C_2 \cos\left(\frac{\omega}{c}x\right) \quad 4-79$$

$$G(t) = C_3 \sin(\omega t) + C_4 \cos(\omega t) \quad 4-80$$

Subsequently, the general solution to the displacement is given by equation 4-81.

$$u(x, t) = \left[ C_1 \sin\left(\frac{\omega}{c}x\right) + C_2 \cos\left(\frac{\omega}{c}x\right) \right] \cdot [C_3 \sin(\omega t) + C_4 \cos(\omega t)] \quad 4-81$$

For a beam free at both ends, the B.C. can be written as:

$$P(0, t) = P(L, t) = 0 \quad 4-82$$

Which looking at equation 4-69, is equivalent to saying:

$$\frac{\partial u(0, t)}{\partial x} = \frac{\partial u(L, t)}{\partial x} = 0 \quad 4-83$$

Focusing on the spatial part of equation 4-81, and assuming the time part as nonzero (to find non trivial solutions), after differentiating and applying the B.C., first, equation 4-84 is found, and then, after acquiring the constant  $C_1$ , equation 4-85 is obtained.

$$\frac{\partial u(0, t)}{\partial x} \Rightarrow C_1 = 0 \quad 4-84$$

$$\frac{\partial u(L, t)}{\partial x} \Rightarrow C_2 G(t) \frac{\omega}{c} \sin\left(\frac{\omega}{c}L\right) = 0 \quad 4-85$$

From equation 4-85, because the other terms are nonzero, the following equation results:

$$\sin\left(\frac{\omega}{c}L\right) = 0 \quad 4-86$$

Equation 4-87 represents the solution to equation 4-86, allowing the calculation of the  $n^{\text{th}}$  natural frequency of the MMB ( $\omega_n$ ), in the longitudinal direction.

$$\omega_n = \frac{n\pi c}{L}, \quad n \in N \quad 4-87$$

The mode shapes can be found introducing the natural frequencies found through equation 4-87, as well as the constant  $C_1$  to the spatial equation 4-79, which yields equation 4-88.

$$U(x) = C_n \cos\left(\frac{\omega_n}{c}x\right) \quad 4-88$$

## 4.4 Three-Point Bending of a Multi-Material Beam

Figure 4.8 depicts a beam, which could have multiple materials, subjected to a load  $P_c$  at the centre. The length of the beam that surpasses the supports is not considered in this analysis since no transverse loads or moments are acting on it, rendering its presence irrelevant.

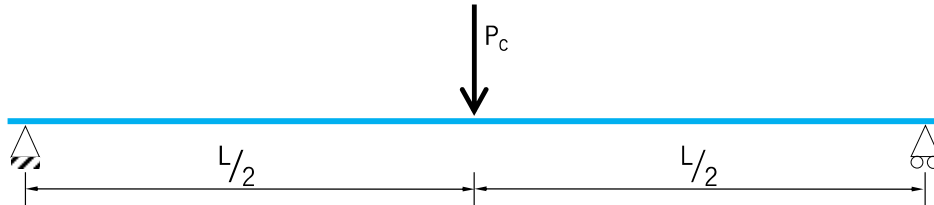


**Figure 4.8.** Beam of length L subjected to a load  $P_c$  at the centre.

Equations 4-89 and 4-90 define the bending moment diagrams from  $x=0$  to  $x=L/2$  and from this point to  $x=L$ , respectively, as the subscript suggests.

$$M_{0 \rightarrow L/2}(x) = \frac{P_c}{2}x \quad 4-89$$

$$M_{L/2 \rightarrow L}(x) = -\frac{P_c}{2}x + \frac{P_c}{2} \quad 4-90$$

Relating these equations to equation 4-4, it yields:

$$-E_b I_{eq} \frac{d^2 y_{0 \rightarrow L/2}}{dx^2} = \frac{P_c}{2}x \quad 4-91$$

$$-E_b I_{eq} \frac{d^2 y_{L/2 \rightarrow L}}{dx^2} = -\frac{P_c}{2}x + \frac{P_c}{2} \quad 4-92$$

For the case of an MMB subjected to a three-point bending test, the B.C. are given by the system of equation 4-93.

$$\left\{ \begin{array}{l} M_{0 \rightarrow L/2}(0) = 0 \\ M_{L/2 \rightarrow L}(L) = 0 \\ \theta_{0 \rightarrow L/2}\left(\frac{L}{2}\right) = \theta_{L/2 \rightarrow L}\left(\frac{L}{2}\right) \\ y_{0 \rightarrow L/2}\left(\frac{L}{2}\right) = y_{L/2 \rightarrow L}\left(\frac{L}{2}\right) \end{array} \right\} \Leftrightarrow \left\{ \begin{array}{l} y_{0 \rightarrow L/2}(0) = 0 \\ y_{L/2 \rightarrow L}(L) = 0 \\ \frac{dy_{0 \rightarrow L/2}\left(\frac{L}{2}\right)}{dx} = \frac{dy_{L/2 \rightarrow L}\left(\frac{L}{2}\right)}{dx} \\ y_{0 \rightarrow L/2}\left(\frac{L}{2}\right) = y_{L/2 \rightarrow L}\left(\frac{L}{2}\right) \end{array} \right. \quad 4-93$$

Integrating equations 4-91 e 4-92, one and two times, the following system of equations emerges, and with it four new constants. The 2<sup>nd</sup> and 4<sup>th</sup> rows of the system of equations 4-94 can define the displacement in the y direction of the MMB along all its length when a force P is applied at the centre.

$$\left\{ \begin{array}{l} -E_b I_{eq} \frac{dy_{0 \rightarrow L/2}(x)}{dx} = \frac{P_c}{4} x^2 + C_1 \\ -E_b I_{eq} y_{0 \rightarrow L/2}(x) = \frac{P_c}{12} x^3 + C_1 x + C_2 \\ -E_b I_{eq} \frac{dy_{L/2 \rightarrow L}(x)}{dx} = -\frac{P_c}{4} x^2 + \frac{P_c L}{2} x + C_3 \\ -E_b I_{eq} y_{L/2 \rightarrow L}(x) = -\frac{P_c}{12} x^3 + \frac{P_c L}{4} x^2 + C_3 x + C_4 \end{array} \right. \quad 4-94$$

Applying the B.C. to the linear system of equations it becomes feasible to solve it for the four constants. Subsequently, it is possible to find the displacement along the MMB, through the 2<sup>nd</sup> and 4<sup>th</sup> rows of system of equations 4-94. The displacement of the MMB in the y direction along its length is presented in system of equations 4-95.

$$y = \left\{ \begin{array}{l} -\frac{P_c}{48E_b I_{eq}} (4x^3 - 3L^2 x), \quad x \in \left[0; \frac{L}{2}\right] \\ -\frac{P_c}{48E_b I_{eq}} (-4x^3 + 12Lx^2 - 9L^2 x + L^3), \quad x \in \left[\frac{L}{2}; L\right] \end{array} \right. \quad 4-95$$

The maximum displacement occurs when  $\frac{dy(x)}{dx} = 0$ , which is at  $L/2$ , i.e., in the middle of the beam.

$$y_{max} = \frac{P_c L^3}{48E_b I_{eq}} \quad 4-96$$

# Chapter 5

## NUMERICAL METHODS

All numerical analyses in this chapter were performed using Ansys Mechanical as the CAE software, which is an Ansys Workbench application with several modules such as Static Structural and Modal, and using SpaceClaim as the CAD software, where the geometry was modelled. Three different models were used to attempt to capture the MMB's behaviour using only beam elements, solid elements, or beam and shell elements, which in this chapter are referred to as "beam + shell". Additionally, numerical simulations of the DLD system are described for the resistance to vertical loads, static torsion, and wind load tests, using internal reinforcements and reinforcing the glazing, as well as to evaluate the dynamic behaviour of the system. To conclude the chapter, the thermal transmittance simulation is described, for a DLD with and without internal reinforcements.

### 5.1 Simulation notes

The modules from Ansys Workbench used for the numerical analyses, as well as the objective of their use, are described in Table 5.1.

**Table 5.1.** Ansys Workbench modules used and their objective.

Workbench Module	Objective
Static Structural	Evaluate the torsional and bending stiffness of a P.2992 brass MMB with different models of the beam, extrapolate the optimized geometry of the internal reinforcement of a P.2972 brass MMB that was bent, and simulate the standardized resistance to vertical loads, static torsion, and wind load tests with a model of the DLD system, testing different reinforcements.
Transient Structural	Verify the independence from inertial effects of the result from a DLD brass system subjected to the resistance to wind load test.
Modal	Find the natural frequencies and mode shapes of brass MMBs with all the OS2 75 profiles using a beam elements model. In the case of the P.2992 profile, different models of the beam were tested with and without damping, and a study of the influence of the polymers' elastic modulus on the results is also performed. The mode shapes and natural frequencies from the brass DLD system were also extracted.
Harmonic Response	This module was connected to the Modal analysis of the brass DLD system, and using the damping found from the first resonant frequency of the physical MMB, the system was tested to an earthquake of instrumental intensity V, with the criteria described in Chapter 2.
Steady-State Thermal	The thermal transmittance of reinforced and unreinforced sections of the system with an insulation panel and with glazing was determined, applying the method described in Chapter 2.

The approaches to solve the various analyses of this chapter using the Finite Element Method (FEM) are well documented and are not discussed in the dissertation. However, there are a few details to be highlighted if to better understand some of the choices and commands used in this chapter, particularly the use of large deformation effects and the Rayleigh damping.

When performing a static analysis, Ansys Mechanical provides the option to account for large deformation effects, when the “Large Deflection” control is turned on. With the control on, the global stiffness matrix,  $[K]$ , is no longer constant and becomes dependent on the displacement vector,  $\{u\}$ , through the addition of certain terms like the stress stiffening matrix which uses a large strain formulation

(p.e. Lagrange strain, which has quadratic terms), rendering the governing equations nonlinear [75], [76]. The governing equation takes the form presented in equation 5-1, where  $\{F\}$  is the force vector [75], [76].

$$\{F\} = [K(\{u\})]\{u\} \quad 5-1$$

Other nonlinearities could arise, for instance, due to a model with nonlinear contacts such as a frictionless contact, or a model with material nonlinearities such as bilinear hardening material models. Because the variations in stiffness, as the structure deforms, are not known, it is extremely hard to compute the displacement vector from an applied force in the same way as with a linear model. The default method in Ansys for solving with the nonlinear behaviour of a structure is the Newton-Raphson method, which is a widely known iterative method that is frequently used in many fields like engineering and economics [77].

Both the formulations for the modal and harmonic analyses derive from the equation of motion (equation 5-2) [76], [78], [79].

$$[M]\{\ddot{u}\} + [C]\{\dot{u}\} + [K]\{u\} = \{F\} \quad 5-2$$

For the modal analysis, the force vector and the damping forces are considered to be zero [76]. Assuming harmonic motion, equation 5-2 can evolve to equation 5-3, which represents an eigenvalue problem, where the eigenvalues are used to find the natural angular frequencies ( $\omega_i$ ), and the eigenvectors are the correspondent modal shape ( $\{\phi\}_i$ ) [76].

$$([M] - \omega_i^2[K])\{\phi\}_i = \{0\} \quad 5-3$$

When damping is present in the modal analysis, the analysis differs and the software uses a different eigensolver, in order to incorporate the damping forces in the analysis [76]. There are two methods to achieve this, the damped method and the QRdamped method, both methods using complex eigenvalues and eigenvectors [76]. The formulation is extensive and is not detailed in this text, however, it can easily be found in detail in the Mechanical APDL 2022 R1 Theory Reference, on the software's help website [76].

The relevance of this topic relies on the way the damping matrix is calculated. Rayleigh damping is linear and proportional to the mass and the stiffness matrices with two terms,  $\alpha$  and  $\beta$  respectively.

Hence, the Rayleigh damping is mathematically convenient, as the damping matrix can be written as [80]:

$$[C] = \alpha[M] + \beta[K] \quad 5-4$$

The terms  $\alpha$  and  $\beta$  are usually not known and can be found from the damping ratio ( $\xi_i$ ) at a particular natural angular frequency by equation 5-5 [80].

$$\xi_i = \frac{\alpha}{2\omega_i} + \frac{\beta\omega_i}{2} \quad 5-5$$

It is a common assumption to consider the mass damping to be zero, so equation 5-5 becomes equation 5-6 [80].

$$\xi_i = \frac{\beta\omega_i}{2} \quad 5-6$$

Using equation 5-6, the  $\beta$  term can be easily calculated from the first resonance frequency of the experimental data and the correspondent damping ratio determined from the half-power bandwidth method. When performing harmonic analyses, in this work, the Mode Superposition (MSUP) Method was used to solve the harmonic equation of motion (equation 5-7, where  $\Omega$  is the imposed circular frequency), which takes the damping ratio as a direct input. This method can be found in the Mechanical APDL 2022 R1 Theory Reference, on the software's help website [76], [79].

$$(-\Omega^2[M] + i\Omega[C] + [K])(\{u_1\} + i\{u_2\}) = (\{F_1\} + i\{F_2\}) \quad 5-7$$

## 5.2 Multi-Material Beam Models

### 5.2.1 Beam Elements Model

Beam elements are fairly used to model the behaviour of structures since they are computationally efficient due to their small number of nodes, and consequently small number of degrees of freedom (DOF), which makes for smaller stiffness and mass matrices, leading to lower simulation times. Ansys references two structural beam elements, BEAM188, which is a two-node linear element,



and BEAM189, which is a three-node element with a quadratic shape/interpolation function. Both elements are based on the Timoshenko beam theory, and take as input the cross-sectional properties of the beam and have their nodes along the length of the beam [81]. However, these elements have in their essence limitations since they cannot capture any changes in the shape of the beam's cross-section.

A beam elements model that accounts for the different materials in the MMB was developed, and was used for the three-point bending and torsion numerical analyses in Static Structural of a brass MMB with the P.2992 profile and used for the modal analyses (in Modal) of brass MMBs with several profiles: P.2901, P.2915, P.2942, P.2942, P.2943, P.2961, P.2962, P.2963, P.2965, P.2971, P.2972, P.2991, P.2995, and P.2992 (in this profile with and without damping), all with a length of 1600 mm.

### 5.2.1.1 Geometry

The modelling of beam elements started with access to 2D sketches of the MMB's profile, in a dwg format, from AutoCAD (Figure 5.1 - A). The files were imported into SpaceClaim and using the "Fill" command, surfaces were created, from which solids could be extruded (1600 mm) with the command "Pull", and with the "No merge" option active, allowing five solids to be created (Figure 5.1 - B). Since the sketch was usually not exempt from defects, some tweaking was sometimes needed in some edges or vertices, for instance, using the "Move" tool. A tool called "Extract" in the "Prepare" tab allowed for a beam to be automatically generated from a solid. From the five solids, the same number of beams were extracted, but because they were created at the original solid's cross-section's centroid, they were spatially distant from one another (Figure 5.1 - C). With the "Move" tool and the option "Up To", all beams were joined together, and the line bodies became coincident in all their points (Figure 5.1 - D). Since the beams were located at the centroid of their respective cross-sections, the cross-section had to be placed at the right location. This was achieved, first by making the cross-sections visible with the command "Display" and the option "Solid Beams", under the tab "Prepare", and then by using the tool "Orient", under the same tab, which allowed for offsets to be given, moving the cross-section with the beam in place (Figure 5.1 - E). The last step was to use the "Share" command, which in the generation of the mesh forces the coincident topologies (in this case, the five beam edges) to share every node, and consequently every node's degree of freedom. Before the last step, for the three-point bending analysis, to make the vertices on which the B.C. would be applied, three cuts were made using planes and the "Split" tool. One vertex was located at the centre, and the other at 30 mm from the extremities.

Because the transfer of the geometrical data between SpaceClaim and Ansys Mechanical has some flaws, defining the same orientation angle of all the beams in their properties avoids further issues

related to the correct element orientation, namely in the generation of mesh. Any changes in Mechanical that arose from an ill oriented beam profile, were dealt with by editing/rotating the profile itself.

Additionally, the beams' cross-sections could be sent to the solver in Ansys Mechanical as “Mesh” or as “Pre-integrated”. The first option sends the cross-section itself to the solver, instead of just the cross-sectional properties from the CAD software like the second option. Because the latter has certain limitations, particularly in some post-processing functionalities like the “beam tool” and in torsion, where the behaviour is anomalous, it was only used for the vibration analysis of the different profiles, since it provided results closer to the experimental data, allowing for a validation the analytical method used with the different MMB profiles. On the three-point bending simulation, both options were also used.

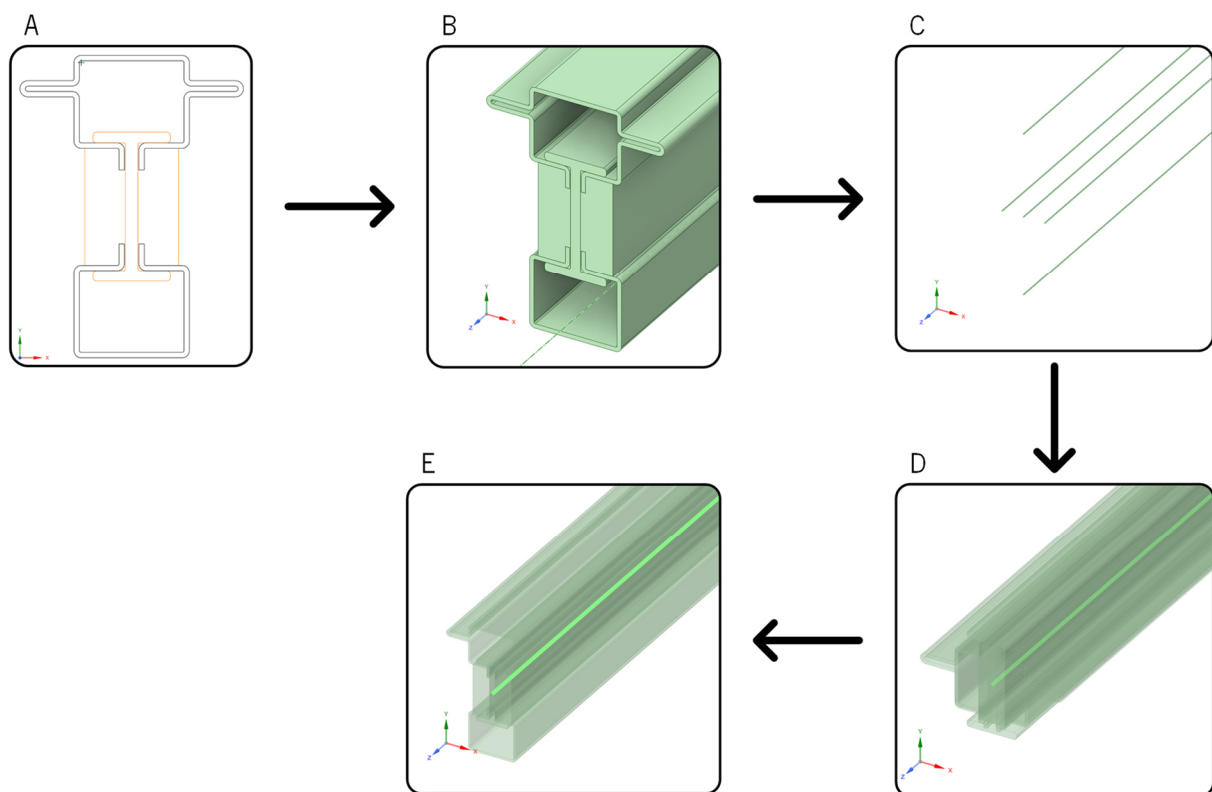


**Figure 5.1.** Beam elements model modelling, starting with the dwg file (A), extruding solid beams (B), extracting beam bodies from the solids (C), making the cross-section of this bodies visible (D), and giving offsets to the different cross-sections with the beam bodies in place (E), so that they were considered in the right position by the software in the simulation.

### 5.2.1.2 Material Assignment

For the torsion and three-point bending analyses, in “Engineering data”, brass, PA, and PU were defined, using as input the properties from in Table 3.1, and Table 3.2, for the brass and PA, and Table 2.3 for the PU. The properties of interest were the elastic modulus, the yield strength, the tangent modulus

(to define the bilinear hardening model), the density and the Poisson's ratio, with a value of 0,3 for all materials. In the absence of more information about this property, the value of 0,3 for the Poisson's ratio was used since most materials orbit around this value [82].

For the modal analyses, only the elastic modulus, Poisson's ratio and the density were used as inputs since they were linear analyses. In Mechanical, the materials were assigned to the correspondent beams, in the properties of the line bodies under "Geometry" in the structure tree.

### 5.2.1.3 Mesh

For the torsion and modal analyses, the only mesh control enacted was a sizing on the edge, of 100 divisions. In the three-point bending simulation, due to the presence of vertices along the MMB (intended for the B.C.), another approach was taken, and a global size of 5 mm was defined. In all cases, quadratic elements (3 nodes) were requested, since they capture bending behaviour better than linear elements due to the higher-order polynomial that is used to interpolate the displacements between nodes [83]. As mentioned, the structural quadratic beam element provided by Ansys is called BEAM189 and is based on Timoshenko's beam theory which includes shear-deformation effects [81].

To verify that the obtained results were independent of the discretization, the size of the elements was varied in the different analyses. This study can be found in Annex C. A representation of the mesh with the cross-sections graphically represented can be seen in Figure 5.2.

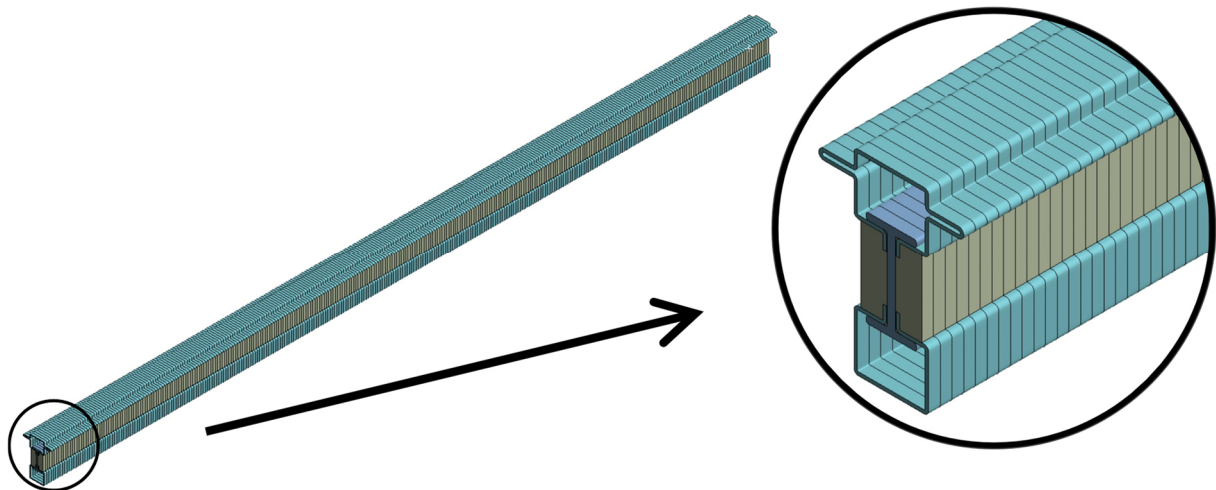


**Figure 5.2.** Mesh from the three-point bending simulation of the beam elements model, with the cross-section of the elements graphically displayed.

#### 5.2.1.4 Boundary Conditions (B.C.)

All B.C. were applied to specific points, which are represented in Figure 5.3 - A for the three-point bending simulation, located at the loading and support pins, and in Figure 5.3 - B for the torsion simulation, located at the extremities. In Figure 5.3, the “u” represents the translational displacements and “rot” the rotations, with the subscript indicating the direction. In the three-point bending simulation, to apply the B.C., the “fixed rotation” and “displacement” commands were used for the rotations and displacements, respectively, as the name suggests. On the other hand, in the torsion simulation, the “fixed support” and “remote displacement” commands were used.

The B.C. mentioned were all directly applied at certain nodes. However, the “remote displacement” is part of a special group of B.C. in the Ansys software called “remote boundary conditions”, which create an internal “remote point” at a certain specified location and then connect this point to the specified geometry using special elements with multipoint constraint (MPC) capabilities as a default, which can provide the geometry with a rigid or deformable behaviour [84]. The B.C. is then applied to the remote point [84].

In this case, the scoped geometry was simply a vertex, which connected to an internally created remote point using TARGET170 elements, and the B.C. were directly applied to the said vertex. The concept of using a remote point connected to the geometry is extensively used in a lot of Ansys features and is explored in more detail throughout this chapter.

The modal analyses consider an unrestrained beam, therefore, no B.C. are specified.

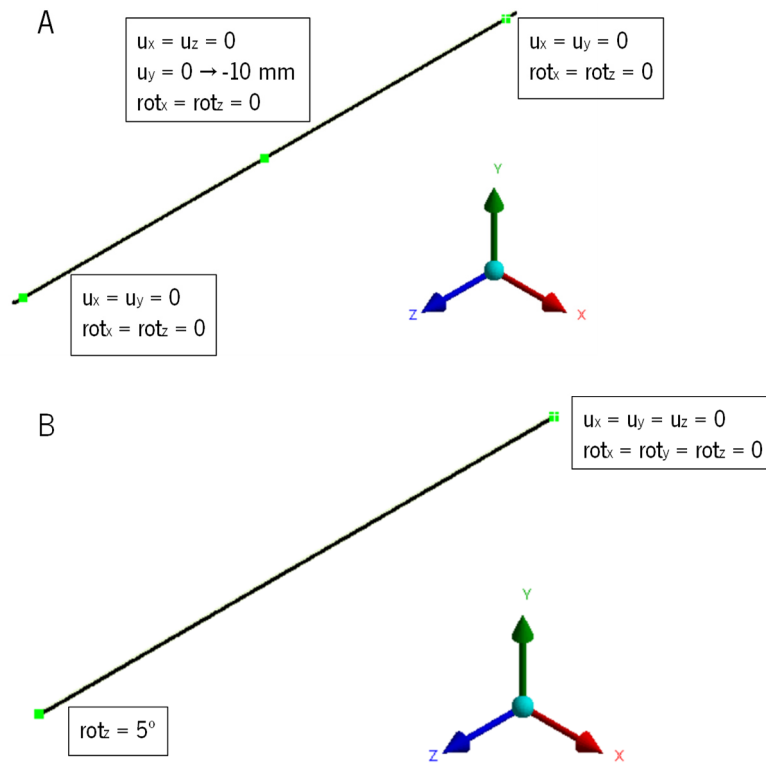


**Figure 5.3.** B.C. on the three-point bending (A) and torsion (B) simulations of the beam elements model.

### 5.2.1.5 Analyses Settings

On the three-point bending and torsion simulations, the “Large Deflection” control was turned on. Additionally, for the three-point bending simulation, 12 timesteps of 1 second each were defined with the displacement being applied at the same rate between timesteps. This amount of time steps would give several points in the post-processing that allowed for a force-displacement curve to be constructed. In each timestep, only one substep was defined by specifying the maximum number of substeps as 1. By default, the solver specified a maximum of 25 iterations on each substep for the solver to achieve convergence using the Newton-Raphson method. If convergence was not achieved, the solver would automatically divide the timestep into more substeps up to a defined maximum (before crashing), which as mentioned, was 1 in these simulations. This number was chosen, because it was expected for the simulations to solve with ease, given the small number of beam elements being used, and if they didn’t, something needed to be corrected.

The undamped modal analysis was specified to find twenty natural frequencies and mode shapes, which made it possible to achieve all the natural frequencies and mode shapes necessary for comparison with the analytical analysis. In the damped modal analysis, damping was turned on, and the first resonance frequency, as well as the correspondent damping ratio from the experimental vibrations test,

were used for the program to calculate the Rayleigh damping, considering the mass damping as zero. In this analysis, a range from 5 Hz to 400 Hz was considered.

### 5.2.1.6 Post-Processing

The directional displacement of the MMB and the reaction force in the Y direction, probed on the displacement B.C. applied in the middle, were collected, in the three-point bending simulation, and used to construct a load-displacement curve in Microsoft Excel. In the torsional analysis, the moment reaction, probed on the fixed support was used, along with the applied rotation of  $5^\circ$ , to evaluate the MMB stiffness. Lastly, for the modal analysis, after running the simulation, all frequencies were selected, and the mode shapes were created.

## 5.2.2 Solid elements model

An MMB model using solid elements is as close as possible to achieve a model capable of reproducing the real behaviour of the MMB using FEM. However, using solid elements the discretization of the geometry was accomplished with more nodes when compared to a beam elements model, which makes the solution processing computationally more demanding. The models used in this chapter have a simplified cross-section to facilitate the mesh generation. All solid elements used in this chapter to model the MMB were SOLID186 elements, which are 20-node quadratic solid elements that exhibit quadratic displacement behaviour and support plasticity [81]. This element is usually a hexahedron with a node at each vertex and at the centre of each edge, however, by merging some of its nodes, the element can take tetrahedral, pyramidal and prismatic shapes (Figure 5.4 - A) [81].

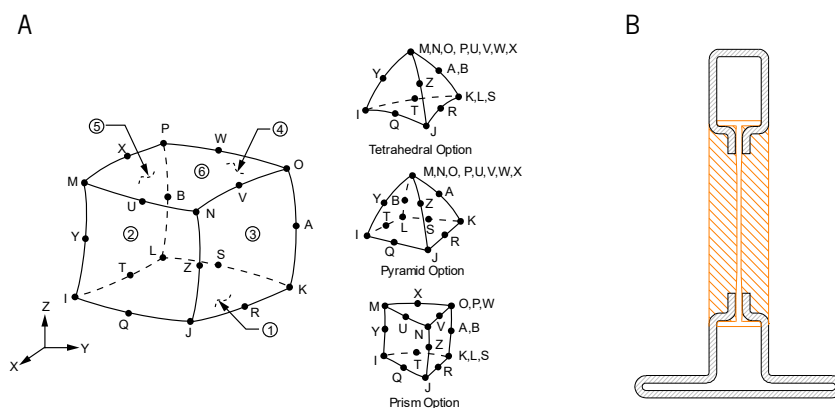


**Figure 5.4.** SOLID186 element, with the different shapes it can take, by merging some nodes (A) (reproduced from [81]), and P.2972 profile (B).

Simulations using a solids elements model were done for brass MMBs with the P.2992 and P.2972 profiles. For the P.2992 profile MMB, a three-point bending, and a torsional simulation were performed in Static Structural, and a dynamic analysis was accomplished in Modal. To evaluate the best reinforcement's shape, a structural optimization was also performed but, because the space available for internal reinforcements in a P.2992 MMB is much larger than the space of most profiles, an MMB with the P.2972 profile was used in this analysis (Figure 5.4 - B).

### 5.2.2.1 Geometry

The geometry definition for the solid elements model was created differently for the three-point bending simulation, and for the torsion and modal analyses. For the three-point bending simulation, the different components of the MMB (of length of 1600 mm) were modelled as solids, with a simplified half cross-section that was exempt of curved edges, with only 800 mm of MMB's length, creating a  $\frac{1}{4}$  model. The solids were then divided on its cross-section and near the punch and support, as shown in Figure 5.5 - A and B, to facilitate the generation of a quality mesh and to increase the number of elements in the contact areas. The support and loading pins were created using surfaces, with the diameter of the support and loading pins of the experimental test. Lastly, the topology was shared, excluding the support, and loading pins.

For the structural optimization analysis only  $\frac{1}{2}$  of the geometry was modelled, as the true length of the MMB was defined as 800 mm. However, using a different MMB profile, the geometry definition was similar to that of the three-point bending analysis, with the same cuts being made on the cross-section and extremes, but with the exclusion of the loading and support pins. Additionally, in the structural optimization geometry, two parallelepipeds that touch the walls of the free space inside the MMB were added at one extreme, as can be seen in Figure 5.5 - C.

For the torsion and the modal analyses, a different approach was taken since  $\frac{1}{4}$  of the model could not be applied in these simulations. A solid body with a simplified cross-section, without curved edges, was created for each component of the MMB, and no subsequent cuts were made in the geometry. Finally, the topology was shared for the coincident faces so all their nodes would be shared when creating the mesh in Mechanical.

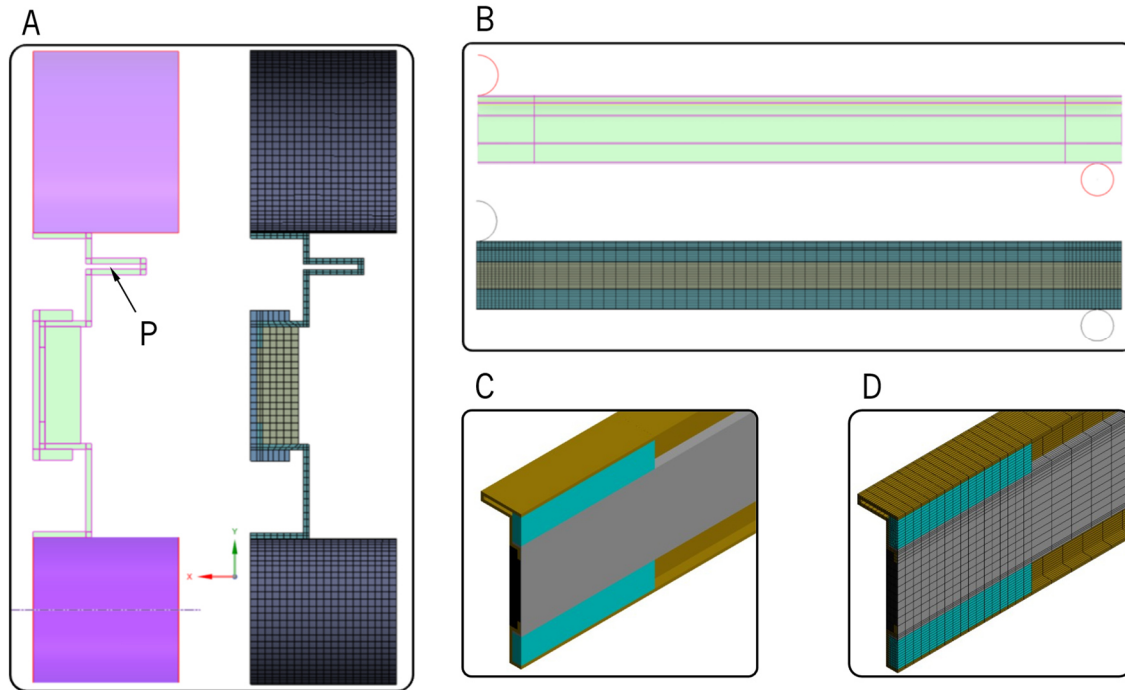


**Figure 5.5.** Mesh from the three-point bending simulation of the solid elements model, and the slashes done in the geometry, from two perspectives (A and B), and geometry (C) and mesh (D) of the extremity of the solid elements model from the structural optimization simulation. In A, the letter P is pointing towards the small space on the cross-section, where contact was defined near the loading pin.

### 5.2.2.2 Material Assignment

The materials defined were the same as those in 5.2.1.2, which were assigned to the correspondent MMB parts. In addition, the loading and support pins in the three-point bending analysis were assigned the default “Structural Steel” ( $E=200$  GPa,  $\rho=7850$  kg/m<sup>3</sup>, and  $\nu=0,3$ ), with an offset pointing toward the centre. This was also the material chosen for the reinforcement in the structural optimization simulation. Since this simulation was linear, material nonlinearities cannot be accounted for. Hence, only the elastic modulus and Poisson’s ratio of the materials was considered in this simulation (other properties like density can be defined for this simulation but were not used by the solver).

### 5.2.2.3 Mesh

For the three-point bending, a “Multizone method” was used to define hexahedron elements for the solid bodies, and an automatic method (quadrilateral dominant) was used to define quadrilateral elements for the surface bodies. In the brass sections, two divisions were specified for the thickness of the sheet, which automatically defined the discretization on the corners in the brass sections. On the remaining faces on the brass section, several sizes were defined in order to get the mesh in Figure 5.5 –



A, on the cross-section. Regarding the length of the MMB, the centre was divided in 45 parts and the extremes in 15 parts each, which can be observed in Figure 5.5 - B. Later, to test mesh independence, the number of divisions along the length was reduced, and the number of divisions on the thickness of the brass sections was reduced to one. The loading and support pins were given an “Automatic method” with a “Quadrilateral dominant” option and a sizing of 2 mm.

The discretization of the MMB used in the structural optimization (Figure 5.5 - D) was similar to the discretization of the three-point bending MMB model, with the exception of the loading and support pins, that weren't modelled for the simulation.

For the torsion and modal analyses, a “Multizone method” was also used, but merely on the polymeric solids, and 100 divisions were defined on the edges along the length of the MMB. In these simulations a global size of 6 was defined, resulting in the discretization that Figure 5.6 shows.

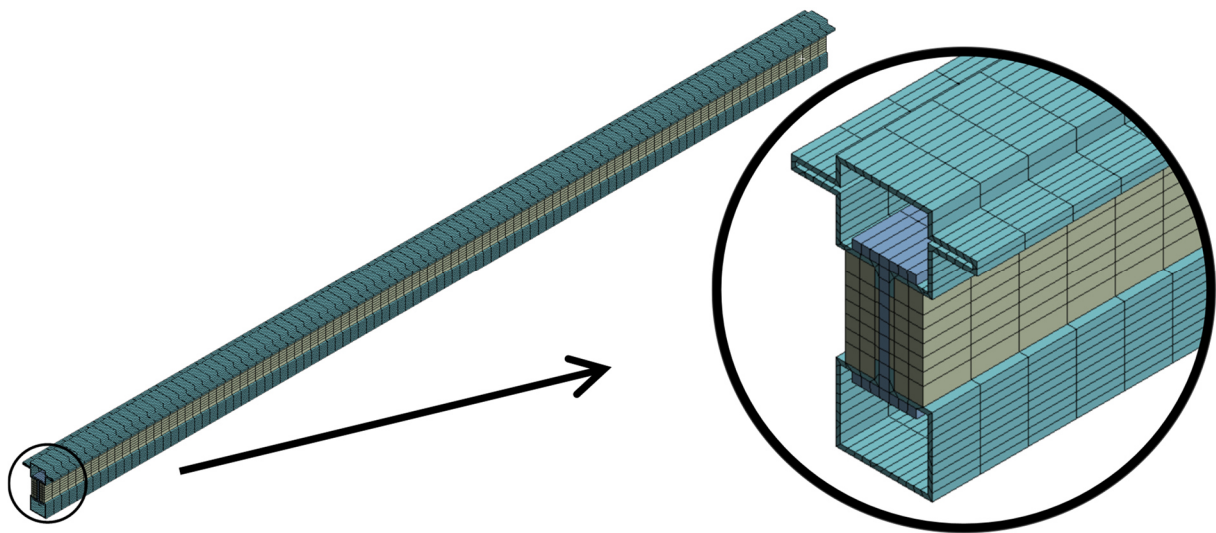


**Figure 5.6.** Mesh from the torsion simulation of the solid elements model, with a detail view of the cross-section.

The different sizing operations mentioned were used with different values, to change the discretization of the models, and evaluate if the results were influenced by the mesh (node count). This analysis can be consulted in Annex C.

#### 5.2.2.4 Connections

The contacts were only defined in the three-point bending simulation since, as it would be observed in the post-processing, no contact took place on any of the other simulations. Between the loading and support pins, and the closest faces of the MMB, a frictionless contact was defined, with a

penetration tolerance of 0,1 mm. In addition, since contact was a strong possibility in the faces of the region denoted by P, in Figure 5.5 - A, a frictionless contact with penetration limited to 0,1 mm was specified.

To define the connections a contact and a target surface were selected, on which the program created CONTA174 and TARGE170 elements, respectively [81], [85]. These elements were used for the program to find and evaluate the contact interaction. On the connection pairs, the contacts were defined to be on the surfaces of the loading and support pin that faced the MMB, as well as on the upper surfaces of the P region in Figure 5.5. The contact behaviour was defined as “symmetric” despite it being the software’s default, which prevented the nodes from the contact surface to enter the target surface, and vice versa [85]. When modelling contacts, it is also a good practice to have a mesh of similar size on the contact pairs, which was the case [85]. The perspective in Figure 5.7 shows the mentioned connections, where the red faces represent the contacts, and the faces in blue (some cannot be seen) were the target.

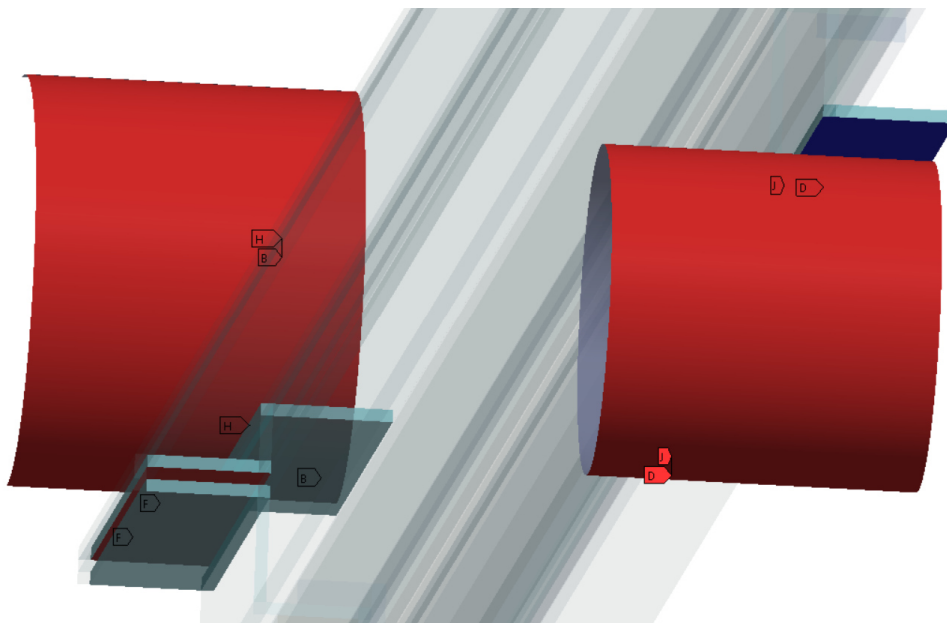


**Figure 5.7.** Connections from the three-point bending simulation, where the red faces represent the contacts, and the faces in blue represent the target, although some are hiding from this perspective.

### 5.2.2.5 Boundary Conditions (B.C.)

Since only  $\frac{1}{4}$  of the MMB was modelled in the three-point bending simulation, two symmetric regions were defined for all geometry that was coincident with the symmetric planes of the model. The supporting pin was fixed, and a displacement was applied to the loading pin, using a “fixed support” and a “displacement”, respectively. The displacement ranges from 0 to 12,27 mm, which was the

displacement correspondent to the maximum load in the experimental test, before removing this B.C. and allowing the MMB to have some elastic recovery. These B.C. are illustrated in Figure 5.8 - A.

In the torsion simulation, the faces on the cross-section of one end of the MMB were fixed, using a “fixed support” and a rotation of  $5^\circ$  was applied to the faces on the cross-section of the other end by employing a “remote displacement” with “deformable” behaviour (Figure 5.8 - B). The “remote displacement” creates an internal remote point at the geometric centre of the selected faces and connects all their nodes to this point [84]. The pivot point was made from TARGE170 elements and connects to CONTA174 elements with the MPC option activated, which establishes a connection using constraint equations [84].

No B.C. were specified for the modal analysis since we're dealing with a free-free beam, and in the structural optimization simulation, the cross-section on the end of the MMB on the reinforcement side was fixed and to the other end's cross-section a displacement of 5 mm was applied, like Figure 5.8 - C illustrates. In this figure, it is also possible to visualize the defined symmetry.

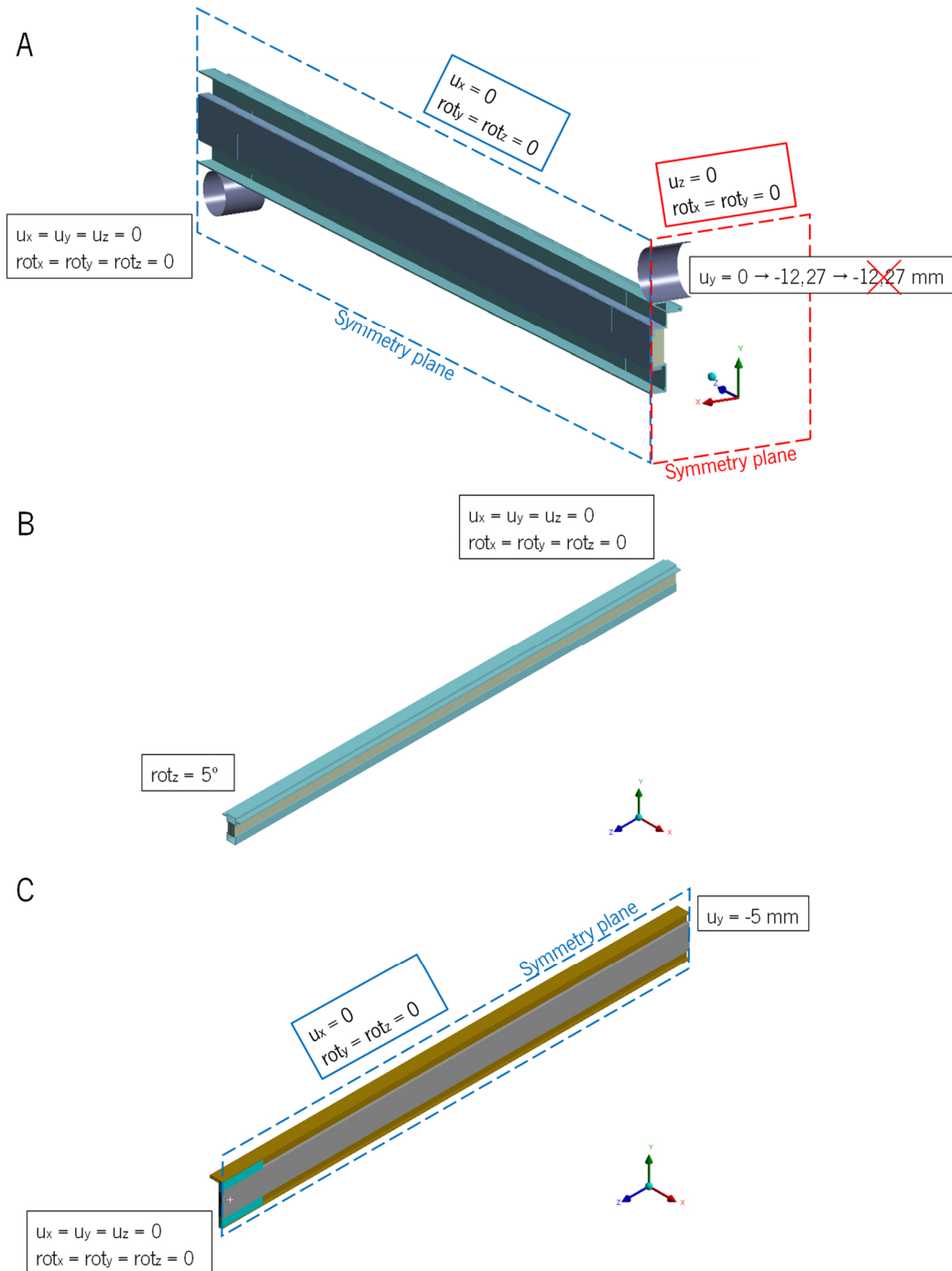


**Figure 5.8.** Boundary conditions of the three-point bending (A), torsion (B), and structural optimization (C) using solid elements models.

### 5.2.2.6 Analyses Settings

All simulations, except for the modal analysis, had large strain deformations considered, by turning on the “Large deflection” command. In the three-point bending simulation, 11 timesteps of 1 second each were defined with a maximum of 10 substeps per timestep. Upon completing the 10<sup>th</sup> timestep, the imposed displacement B.C. would be removed, allowing the elastic return on the MMB.

The damped and undamped modal analyses settings were the same as those defined for the beam elements model, and the settings for the torsion simulation were untampered with, except for the large strain deformations effect, as mentioned.

In Ansys, a structural optimization simulation is based on a set of loads and B.C. provided by at least one preceding analysis. Thus, a static simulation was performed, without tampering with the analysis settings, and then the structural optimization simulation per se was defined, with a maximum of 10 iterations, and the objective of minimizing the compliance. In addition, the constraint of keeping the mass of both reinforcements by at least 20% of the original value was specified.

### 5.2.2.7 Post-Processing

In the three-point bending simulation, from the reaction force multiplied by 4, that was probed in the loading pin and (since the model was  $\frac{1}{4}$  of the MMB), as well as the displacements from a point in the centre of the MMB on the bottom (Figure 5.9 - A) and on the top (Figure 5.9 - B), a force-displacement curve was constructed for the bottom and the top of the MMB, respectively. Moreover, through the introduction of two “path” (with 47 points each) along the length of the MMB and in the symmetry plane (Figure 5.9 - C), at the top and at the bottom, and defining a directional displacement in the Y direction, on the last timestep, it was possible to find the residual deformation on the top and bottom of the MMB.

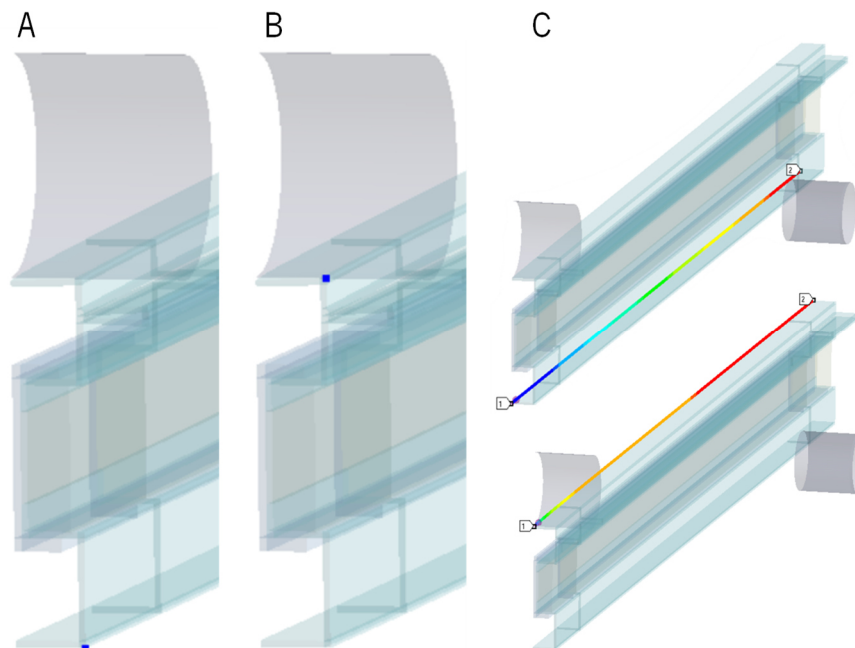


**Figure 5.9.** Points on the bottom (A) and top (B) of the MMB's centre used to find the displacements, for the force-displacement curves, and paths created on the bottom and on top, to find the residual deformation, along the length of the beam (C).

The moment reaction, from the fixed support, along with the applied rotation of  $5^\circ$  was used to find the torsional stiffness from the torsion simulation, and in the modal analysis, mode shapes were created, from each of the resulting natural frequencies. In the “Topology density”, on the structure tree of the structural optimization simulation, the optimized shape of the reinforcement was depicted.

### 5.2.3 Beam + Shell model

This model came as a necessity for a numerically efficient model that was in accordance with the experimental data. Although this model is presented in this chapter, it is only in Chapter 6 that the reason, as well as the necessity for this model, becomes clear. Similar to the solid elements model, the three-point bending, torsion and modal analyses were performed with the P.2992 brass MMB.

This model has similarities to the beam elements model, however, there are some major differences. The beam + shell model divides the MMB into three parts along the MMB’s height: the top and the bottom, which are limited by the metal components of the MMB, and the middle which is only comprised of the central part of the polymeric components of the MMB. The top and bottom parts are modelled with BEAM189 for the different components, and the middle part is modelled using Shell281 elements, which are quadratic shell elements with 8 nodes, that can be used to model surfaces with layered sections and are governed by the first-order shear deformation theory, also known as the Mindlin-Reissner shell theory [81].

#### 5.2.3.1 Geometry

The geometry treatment of the beam + shell model was similar to that of the beam elements model. The most meaningful change was that a surface was created in the middle of the profile, from the limit of one metal section to the limit of the other. This surface was produced from a line sketched as indicated in Figure 5.10 - A, which was used along with the “Pull” tool to make the 2D object with 1600 mm of length. The rest of the sketch was used to produce beams, following the method indicated for the beam elements model, with the cross-sections being inputted to the solver as “Mesh” for all simulations. The result was 10 beam edges, 5 on each side of the surface, that were subsequently moved to their corresponding edges on the surface, as indicated in Figure 5.10 - B and C. To the cross-sections, the correct offsets were given before the topology was shared, to make the nodes with coincident geometry to be shared. To prepare the application of the B.C. in the three-point bending analysis, before the

topology was shared, planes and the “Snip” tool were used to define two vertices on the lower edge of the beam + shell at 30 mm from the extremities, and one vertex on the middle of the top edge.

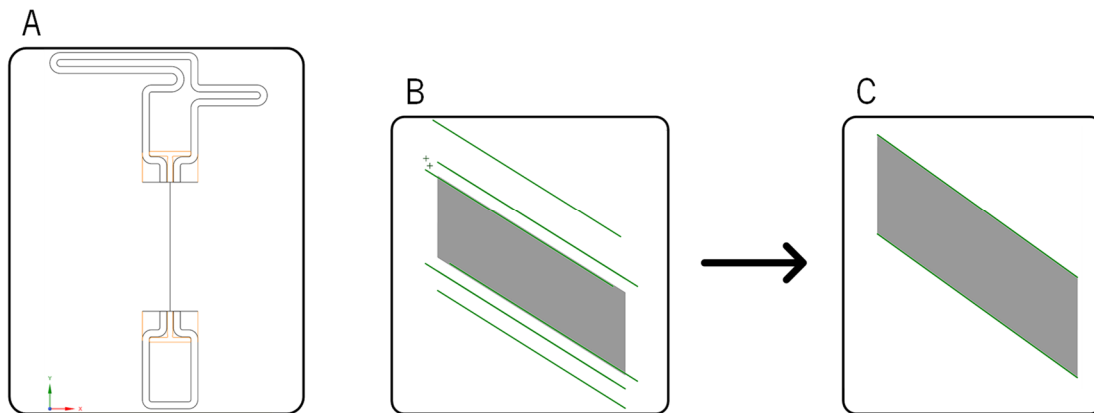


**Figure 5.10.** Modified input drawing to introduce the central line, which would be used to create the surface (A), beam bodies and surface created (B) and joined together (C).

### 5.2.3.2 Material Assignment

The same materials that were applied in 5.2.1.2 were used for the beam + shell model simulations. These materials were directly assigned to the correspondent line bodies and in the central surface, a layered section was defined with a worksheet that allowed for the different materials on this surface to be assigned, i.e., a layer of PA between two layers of PU, with the respective thicknesses. For instance, for an MMB with the P.2972 profile the layered section would be PU (5,6 mm of thickness) – PA (0,8 mm) – PU (5,6 mm).

### 5.2.3.3 Mesh

For all simulations, quadratic elements were requested, which generated SHELL281 and BEAM189 elements, and a global size of 5 mm was defined. The resultant mesh can be seen in Figure 5.11 with a graphical display of the different cross-sections.

Furthermore, the global sizing of the models was varied to evaluate the influence of the mesh (node count) in the results. The results of this analysis are available in Annex C.

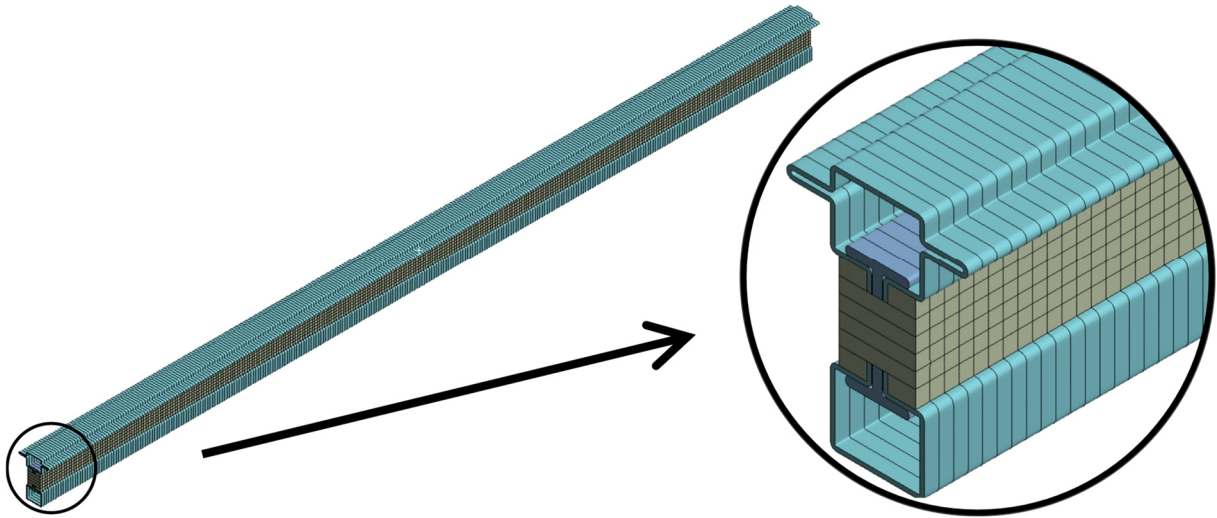


**Figure 5.11.** Mesh from the three-point bending simulation of the beam + shell model, with the cross-section of the elements graphically displayed.

#### 5.2.3.4 Boundary Conditions (B.C.)

The B.C., as well as the procedure used for their application, were the same as described in 5.2.1.4, for the beam elements. The difference to the simulations of 5.2.1 rests in the location of the nodes where the B.C. were applied, i.e., in the three-point bending simulation the B.C. were applied in the points highlighted in Figure 5.12 - A, and in the torsion simulation, they were applied in the edges that represent the MMB's ends, like shown in Figure 5.12 - B.

In the damped and undamped modal analyses it was not necessary to specify the B.C. since the analyses were of an MMB free in space.



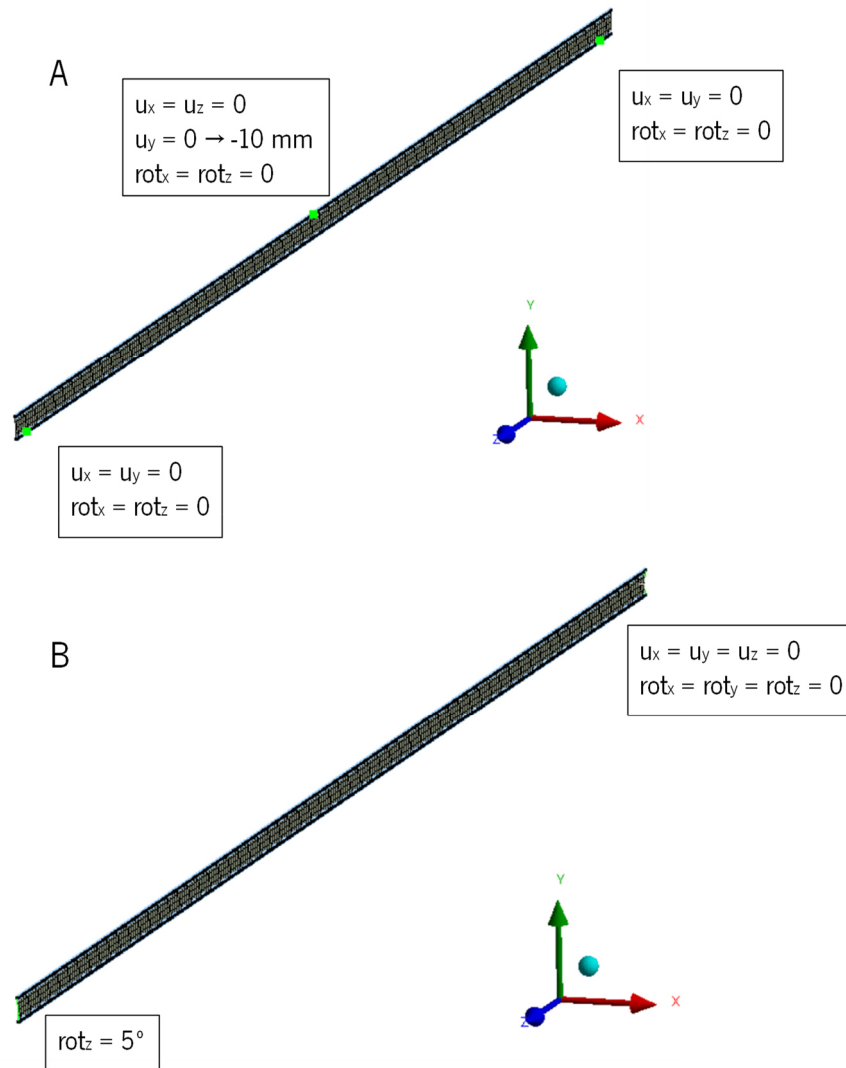


**Figure 5.12.** B.C. on the three-point bending (A) and torsion (B) simulations of the beam + shell model.

### 5.2.3.5 Analyses Settings

Large strain deformation effects were accounted for in the three-point bending and torsion simulation, and the damped and undamped modal analysis settings were the same as those defined for the previous models. The analysis settings of the three-point bending simulation were the same as those used for the beam elements model.

### 5.2.3.6 Post-Processing

The post-processing of this model was the same as that of the beam elements model.

### 5.3 Door System

This chapter describes numerical analyses of a model of the DLD system introduced in Chapter 2, that was used to mimic the certification tests to the wind, the torsional, and the vertical loads described in the same chapter. Additionally, the natural frequencies of the system were found with a modal analysis, and the performance to the criterion defined in Chapter 2 was evaluated through several harmonic analyses. The thermal transmittance of the DLD was also be evaluated, as described in Chapter 2, following ISO 10077-2:2017.

The model of the system used the beam + shell MMB model for the frame structure since it revealed promising results while keeping a relatively small element count, and the triple glazing was modelled considering the hydrostatic pressure, which has a relevant part in the behaviour of the system, as was seen in Chapter 2. Additionally, the hardware of the system was also considered in the model, however, these components were not the object of study, and their main purpose was to introduce constraints on the movement of the system as well as introduce localized rigidity, which was accomplished through joints, constraint equations, and simplified geometries.

For the model to run using the selected elements, some assumptions were made. For instance, the glazing was considered to be clamped on the movable frames, meaning that the stiffness of the rubber sealants was ignored. The contact with the walls was accomplished through the introduction of a frictionless plane that didn't consider the protuberance of the profile, however, as shown later in the chapter, due to the direction of the load, this wasn't a shortcoming. Although gravity was applied on the static analyses, the weight of the hardware, which was mostly represented by remote points, such as the lock and the hinges, was not considered. Additionally, deformations on the hardware and sealants as well as localized deformations that cause certain deformations on the frame were not considered, due to the nature of the elements used in the simulations. In the dynamic analyses, the stoppage between frames was not modelled, and since the damping ratio considered for the system is not known, the damping ratio considered for the simulation was the one found by the application of the half-power bandwidth method on the first resonance frequency from experimental data collected from the test of the single MMB.

Because the model had numerous details, on quite a lot of different regions of the system, this chapter is presented in a progressive way where the geometry, mesh, material, connections, and other aspects of the different components are simultaneously exposed, in order to avoid a morose and time-consuming text. Subsequently, the other considerations of the simulations like the boundary conditions

are discussed. Because a large number of dimensions were needed to define the model, they are not discussed in detail in this chapter, but can be found directly or by calculation, from the dimensions exposed in Annex A. A general view of the door system model, discretized and with a few details, is illustrated in Figure 5.13, where the cross-section of the shell and beam elements is graphically displayed.

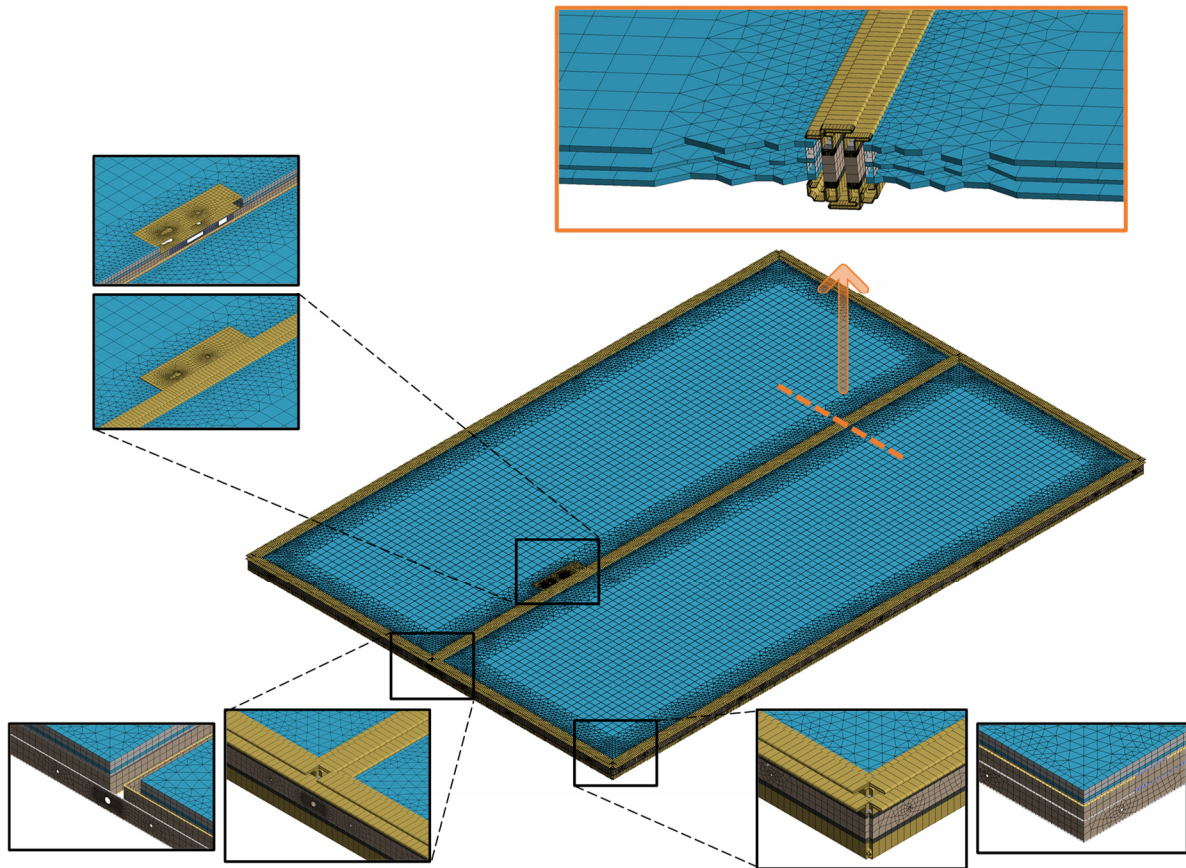


**Figure 5.13.** DLD model, discretized and with a few details, which show the original, and graphical representation of the beams and surfaces' cross-sections. From this graphical representation, it was possible to verify that the orientation of the beam elements was correct.

It is also important to introduce the sequence of the mesh generation, which was proven to generate a cleaner mesh, with fewer nodes and elements with lesser skewness, for the model. To achieve the best possible mesh, it was important for it to be first generated on the beam elements of the system, and only then on the rest of the frame. In addition, it was also important for the mesh to be generated on the centre and spacer regions of the glazing before it was generated on the transition region. The mentioned regions of the glazing are introduced ahead, but it is important to keep the sequence in mind, as it was essential for the mesh to be generated in the intended way. On the mesh, only quadratic elements were employed, and a global size of 10 mm was used. This value was changed, along with

other sizing definitions, like the number of divisions assigned to a certain edge, in order to evaluate if the results are independent of the discretization. This study was made in the simulation of the resistance to wind load test and can be found in Annex C.

The resultant model, despite its size (345310 nodes), remained relatively coarse, and although it was adequate for the calculation of displacements and stresses on the beam elements, it was not adequate for a stress evaluation on the other components of the system. Additionally, an attempt to find a finer model with converged results for the stress on the glass panels was not fully successful, as only the 2,5% mark could be reached, with a model with 968659 nodes (global size of 4 mm), which was computationally very expensive and slow, and not suitable for the large scale parameterized analyses intended (Annex C). Nevertheless, this computationally expensive model was used to evaluate the stresses on the glass panels of the unreinforced system, in the various test simulations.

The objective of the different simulations done in “Static Structural” was to evaluate the change caused by an internal reinforcement or by a different glazing in the stiffness of the system to a certain load that was either a torsional force, a vertical force, or a wind pressure on the door. In the latter case, a negative pressure from the exterior was defined, which incites a larger deformation than a positive pressure, where the frames fit each other and stoppage occurs, resulting in the structure having greater support.

Despite the torsional and vertical load tests being evaluated by the residual displacements, which could imply that plastic deformation took place, a stiffness evaluation was still performed. As shown in the following chapter, although there are some stress concentrations in some regions of the model, the stress on the main components of the system, i.e., the beam bodies and the glass, doesn't come close to yielding. Other causes can explain the residual deformation on these tests, such as localized deformations that cannot be captured in this model (e.g., on the hinges), or a sliding could have occurred between the glazing and the frame that had a return, after the load had been removed, made difficult by the rubber sealants. Other causes for the residual deformation that appeared on the system are discussed in Chapter 6. This approach also allows for a comparison of the order of magnitude of the simulation results with the ones from the OS2 65 system used in the current classification of the produced DLD systems.

Without a detailed report of the behaviour of the systems to these loads, the causes for the residual deformation become speculative, however, the small stress values indicate that the cause was not due to the main structural components. Therefore, a stiffness simulation was performed based on

the assumption that less deformation on the complete system, reduces load eccentricities on the different components, and allows the different components to perform better.

Additionally, a dynamic analysis was performed in “Modal”, to capture the modal shapes and frequencies, coupled to various “Harmonic Response” modules, to evaluate the performance of the system to an earthquake of an instrumental intensity of V, where the PGA is 0,092g (Figure 2.23), in the frequency range of 0 - 50 Hz, which a PGA larger than those recorded from 1979 to 1995 on the sites in Jordan [8].

Because the objective was to study the change in stiffness and the modal characteristics, material nonlinearities were be accounted for, and only the elastic modulus, Poisson’s ratio and the density were employed in the different numerical analyses.

### 5.3.1 Frame Structure

As seen in Chapter 2, the MMBs of the frame structure used in the system have two profiles, the P.2962 and P.2963, and together with the beads, they fix the glazing (Figure 5.14 - A). The frame structure comprises three distinct structures, i.e., the fixed frame, which is fixed to the wall by screws, and two movable frames, one on the primary leaf, and another on the secondary leaf. These frames are made from MMBs, that use the beam + shell model with a polymeric part of PU (5,6 mm) – PA (0,8 mm) – PU (5,6 mm), which also integrate the beads in the movable frames.

The MMBs had assigned the material properties (elastic modulus and density) found in Table 2.1 for stainless steel’s elastic modulus, and Table 2.3, Table 3.1, and Table 3.2 for the other properties. In the dynamic analyses, however, the elastic moduli from Table 2.2 were used for the polymeric parts. Additionally, in all simulations, a Poisson’s ratio of 0,3 was specified for all these materials.

The element size of the frames was defined by the global size, and on the geometry several cuts were made, in the polymeric part or in the beam bodies, in order to define the necessary details to introduce the hardware. The system was fixed to the wall with screws, that were modelled by 3,9 mm holes in the middle of the polymeric part of the frame in the places described in Chapter 2, where joints “body to ground” were defined, connecting a remote point, created by the software, in the middle of the hole, that was connected to the circular edge (sizing of 1 mm) of said hole, with MPC elements with rigid behaviour. On this joint, only rotation around the Z axis, which is represented by the blue vector in Figure 5.14 - B, was allowed.

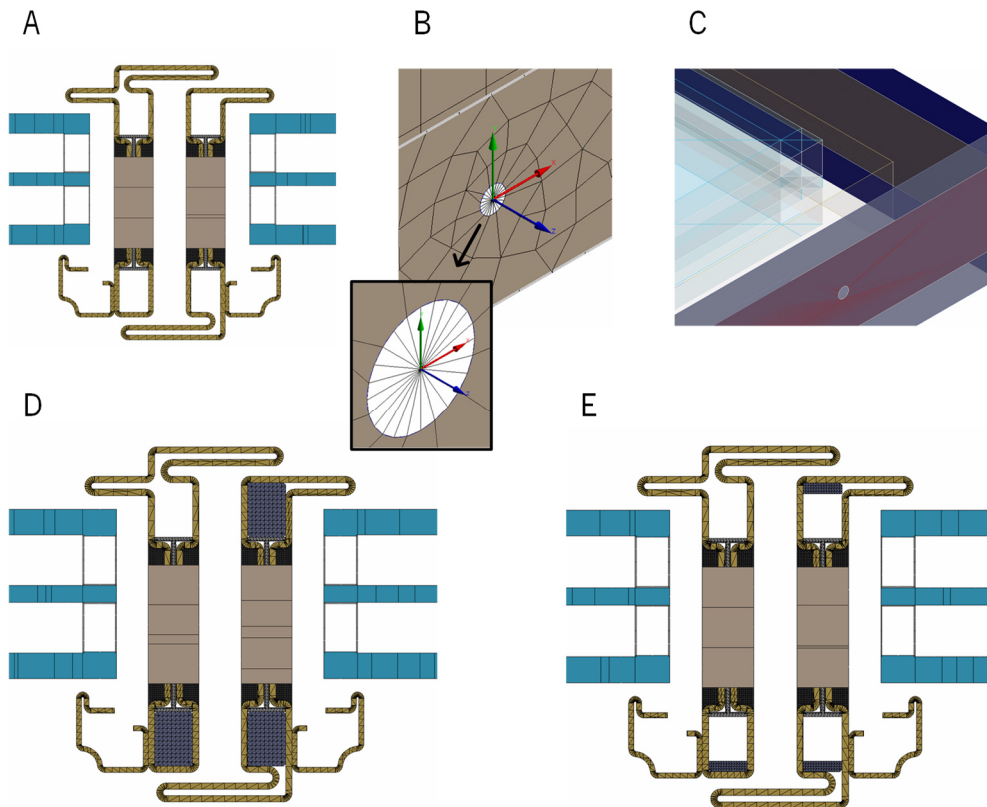


**Figure 5.14.** Unreinforced central junction (A), screws modelled with joints that only allow rotation around the Z axis (B), frictionless connection between the fixed frame (red) and the surface (blue) that mimics a wall (C), central junction with a complete reinforcement (D), and with an optimized reinforcement (E). The internal reinforcements could not occupy one of the cavities since it is occupied by rods and other components of the locking mechanism.

To prevent the fixed frame, from going into the wall, a surface coincident with this structure was created (sizing of 10 mm), and a frictionless contact was defined, with an imposed tolerance of 0,03 mm. The contact and target faces were the outside of the frame and the inside of the wall surface, in that order, and can be visualized in a corner of the system in Figure 5.14 - C in red and blue, respectively.

The most convenient way to reinforce the frames is to use the voids inside the MMBs. In Figure 5.14 - D and E, the section and placement of the reinforcements can be seen, for what was called the complete reinforcement and the optimized reinforcement, respectively. The location of the reinforcements is also relevant, as reinforcing of the entire system inevitably leads to higher stresses on the hinges due to the increased weight from the added material. Thus, different groups of reinforcements were tested in the model, based on the locations of the higher stresses in the frames: reinforcement on all locations (Figure 5.15 - A), tested with complete and optimized sections, reinforcement partially located (Figure 5.15 - B), tested with complete and optimized sections, and reinforcement only at the centre (Figure 5.15 - C), tested with complete sections. It should be noted that one MMB of the frame on the primary leaf,

located at the centre of the system, has one of its internal cavities occupied by the locking mechanism, and therefore could not be reinforced in that location, as can be seen in Figure 5.14 - D and E.

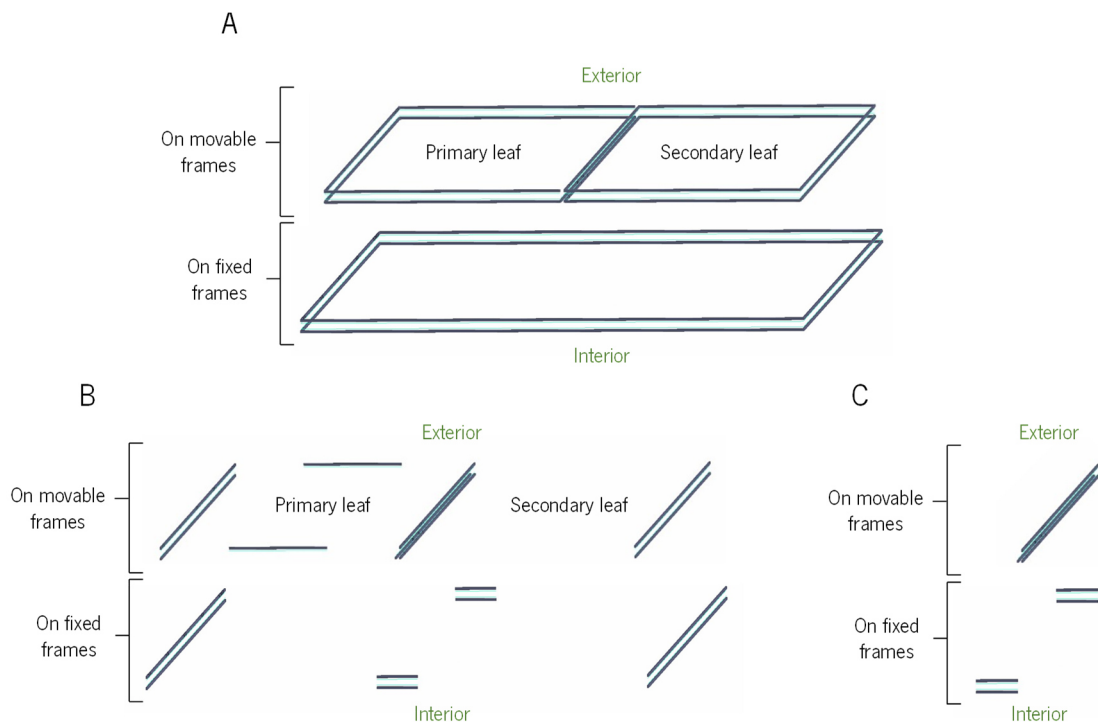


**Figure 5.15.** Configurations of internal reinforcement's locations tested: on all locations (A), partially located (B), and only at the centre (C).

The different reinforcements at the distinct locations were modelled to be all overlapped in the same geometry, but except for the reinforcement being studied, they would all be suppressed in the simulation, and therefore not accounted for.

### 5.3.2 Glazing

The geometry of the glazing was all modelled using surface bodies, except for the middle glass which was modelled by solid bodies. The geometry was cut and then bonded together using the topology share tool in SpaceClaim so that the mesh generation could be controlled. The glazing could then be divided into three main regions: the centre, where the mesh would be coarser, the region that connects to the frames, which were designated as the spacer region (as it is delimited by the glazing's spacers), and lastly, the transition region that connects the centre to the spacer region. The three regions are illustrated in Figure 5.16 - A, where the detail P shows the type of cuts done along the spacer region, that match the cuts done in the beam bodies of the frame of the leaf, which allows for the elements in these

areas to be of the same length and be located side by side with the elements of the frame, facilitating connections as is shown later in the chapter. These cuts were made alongside most of the hardware.

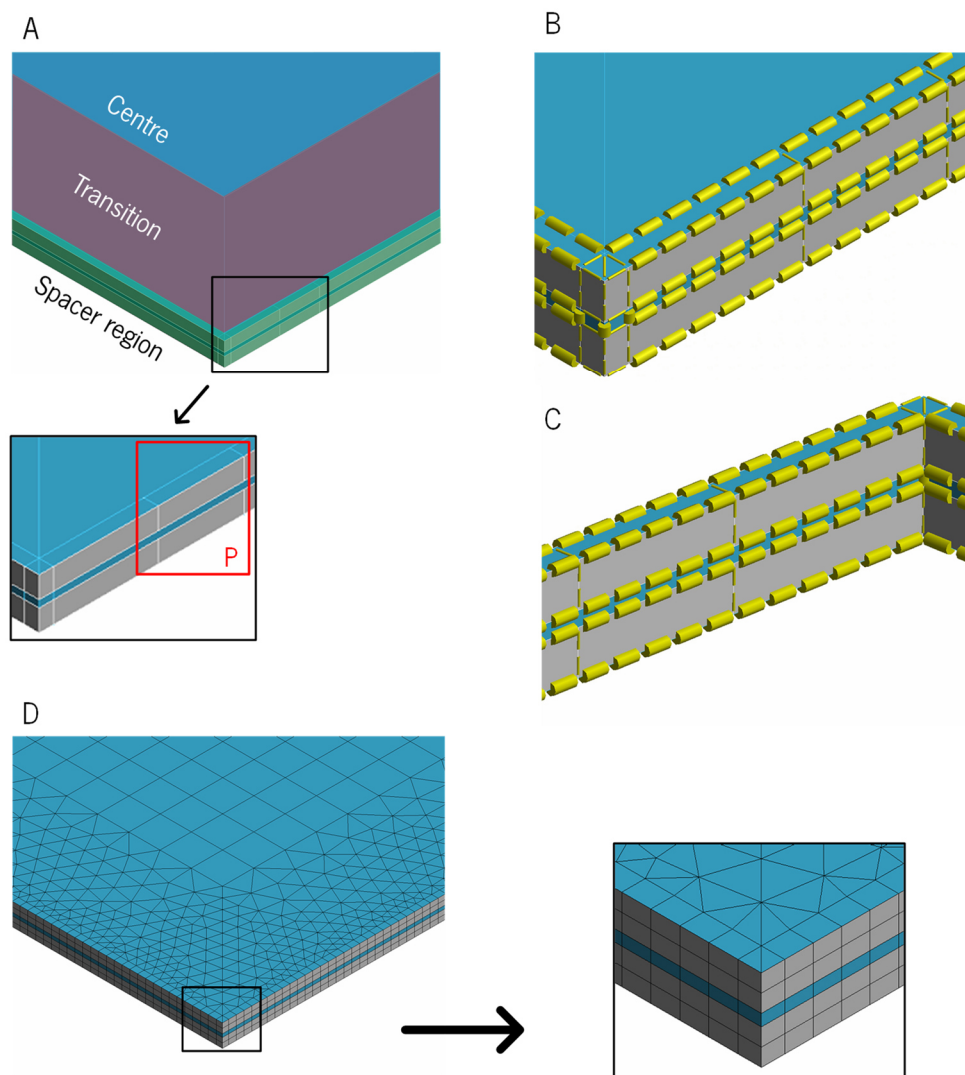


**Figure 5.16.** Three defined regions for the glazing (A) with the geometry cut to facilitate mesh generation and connections, sizings defined on the edges of the spacer region viewed from outside (B) and from inside the glazing (C) represented by yellow cylinders, and corner of glazing after the mesh generation (D), with a courser mesh in the centre, and a finer mesh in the spacer region.

On the middle glass panel (except on the corners of the glazing), MultiZone methods were defined, with hexahedral elements being imposed on the centre and spacer regions, and prismatic elements on the transition. A sizing of 40 mm was specified for the centre region, and on the outer glass panels, MultiZone Quad/Tri methods were defined for the centre and transition regions, with quadrilateral elements of 40 mm in the centre, and triangular elements of 20 mm in the transition. On the methods applied to the transition regions, the surface mesh method control was set to “Uniform”, as it proved to



facilitate a more gradual transition in the element size in this region. On the bead region several divisions were imposed on the edges that can be seen in Figure 5.16- B and C (view from outside and inside the glazing, respectively) represented by the small cylinders, and a sizing with the global size of the model, was applied to the edges along the length of the spacer region, with a hard behaviour, forcing this sizing to be applied, and matching the size of the beam elements of the frame that were alongside. A Face Meshing was also imposed on the lateral surfaces of the spacer (that appear in grey in Figure 5.16 - B and C), and on the top and bottom surfaces of the spacer region, forcing a structured quadrilateral mesh on these faces, when possible. The resulting mesh can be found in Figure 5.16 - D for one corner of the glazing.

Three materials were used on the glazing components. Tempered glass as the same elastic modulus, Poisson's ratio and density of simple annealed glass, and so the common glass from the Ansys library was used ( $E=69930$  MPa,  $\rho=2465$  kg/m<sup>3</sup>,  $\nu=0,2149$ ), similarly, the material AL6061( $E=69040$  MPa,  $\rho=2713$  kg/m<sup>3</sup>,  $\nu=0,33$ ) from the library was used, since it had almost identical properties to AL3003 used by the spacer supplier, and the third material, used in the sheet that covers and seals the lock, was brass (the same used in the frames).

With the introduction of a layered section on the surface bodies, and because the element SHELL281 has the capability, the software allowed for the definition of multi-material surfaces that take as input a worksheet with the material and thickness of each layer that stacked up from the bottom to the top of the surface. Additionally, it was also possible to define offsets for the surface bodies' cross-section, allowing it to be located in the real position. These features of the software were extensively used throughout the whole model and can be seen in the spacer region with the cross-sections graphically displayed in Figure 5.17 - A, where the outer surfaces of this region have two materials stacked up, i.e., 0,28 mm of aluminium and 6 mm of glass, despite only being displayed in one colour (blue). This section was then given a user defined offset, to correct its position, and in turn, on the adjacent glass surface (also displayed in blue), only an offset to the top of the surface was applied. On the remaining spacer surfaces (displayed in grey) all cross-sections were given an offset to the interior, which in this case was the bottom of the surfaces.

A similar case is presented in Figure 5.17 - B, where three materials were applied on the outer surfaces of the spacer region that surrounded the main lock, i.e., 0,28 mm of aluminium, 6 mm of glass, and 2 mm of brass, displayed in the colour of brass between the glass and brass sheets, and on the cross-sections of all surfaces in this image an offset was given. Although not part of the glazing, but of

the hardware and frames, Figure 5.17 - C shows two layered surfaces with an offset on the connection from the secondary leaf to the fixed frame, which is discussed ahead, but is presented now with the introduction of the concept.

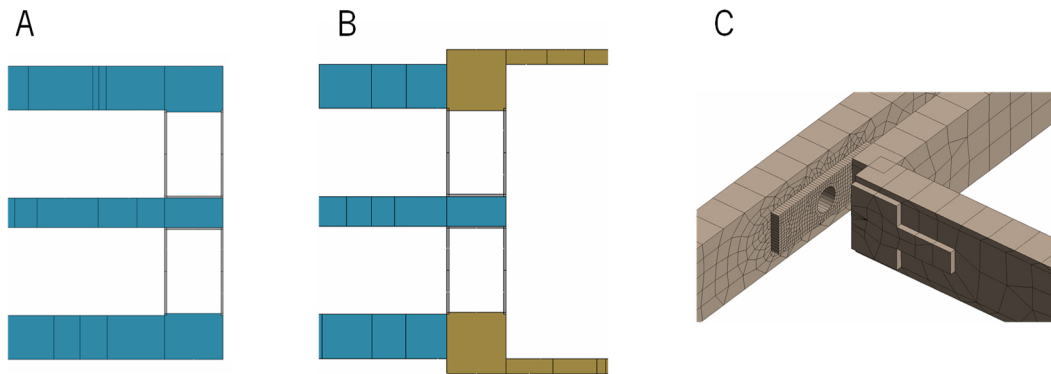


**Figure 5.17.** Graphically displayed cross-sections of the surfaces and offsets of the glazing (A and B, near the lock), and of the polymeric part of the frame on the connection from the secondary leaf to the fixed frame, at the centre of the system (C). In this image, the layered surfaces don't have their layers with distinct colours, and only the thickness and the offset are noticeable.

As stated, an assumption of the glazing being clamped on the movable frames was made, and one way to achieve this effect was by defining a bonded contact between the glazing and the respective frame. The software presents numerous ways of defining bonded contact, however, because the bodies were located with some distance between them, the contact definition revealed itself trickier. It was empirically discovered that the method best suited for this case was the use of the beam formulation with a 25 mm pinball radius, which connects two different bodies using massless BEAM188 linear elements, that have a circular cross-section with a defined radius, and a specified material [84].

This formulation was found to connect a certain node in the contact geometry side to the nearest node in the target geometry. As previously mentioned, the spacer region was cut along its length to match the cuts on the frame (Figure 5.18 - A), and the principal reason for this was for the nodes from the connected geometries to become as aligned as possible, making it possible for the application of this formulation to be done in a way that the created beam elements would become perpendicular to the frame, from the perspective that faces the façade perpendicularly (Figure 5.18 - B). The contact was defined in the beam line bodies of the frame, and the target in the edges of the spacer region of the glazing. Two contacts can be viewed in Figure 5.18 - A, between the top edge of the frame (in red), and the two edges of the top of the spacer region (in purple).

A sample of the created connections between the glazing and the top and bottom of the frame can be found from the post-processing of the simulations and is illustrated in Figure 5.18 - C. To make the contact rigid between the two bodies, it was important for the displacements of the created BEAM188 elements to not influence the simulations' results. This was achieved by assigning an idealized material with an elastic modulus of 2000 GPa (and  $\nu = 0,3$ ), and by giving a radius of 25 mm to the cross-section of each of these elements. The doubling of the elastic modulus made no difference in the results, so the defined value was appropriate.

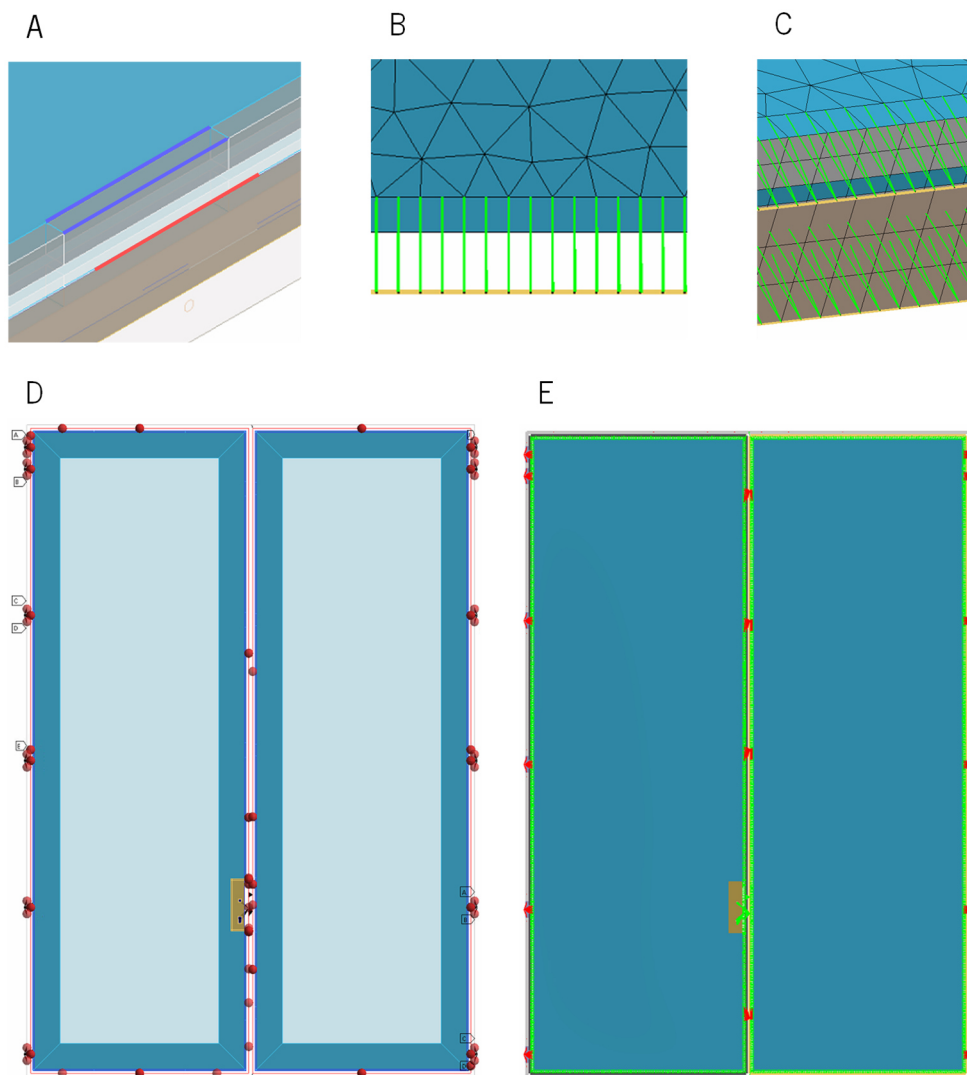


**Figure 5.18.** Connection between the beam bodies of the frame (red) and the edges of the spacer region of the glazing (blue) (A), beams created on the interior and exterior from the beam formulation viewed perpendicularly to the façade (B) and from a different angle (C), pinball from all connections between the frame and the glazing (D), and these connections, displayed in the post-processing in green (E), along with the hardware connections that are in red, except for the lock that is also in green.

The connections between the different edges could not be done all at once, due to some details, such as the contact edges from different geometry from the structure tree not being accepted, which led to a considerable number (84) of connections to be defined, which could lead to human error. Thus, to prevent error, the solver output file was checked while the software was solving to confirm that all connections were successfully processed, and the connections were inspected by visual inspection in the post-processing. In Figure 5.18 - D, the pinball from these connections is displayed, and in Figure 5.18 - E, these connections are displayed across the entire system in green, along with the hardware connections that are in red, except for the lock that is also in green.

In Chapter 2, the importance of the gas inside the chamber was discussed, hence a way to account for the hydrostatic pressure inside the glazing was necessary. This need was met with the introduction of hydrostatic fluid elements, HSFLD242, in the model [86]. The generation of these elements can be done automatically using the ESURF command, which uses the face of existing elements, and from this face and a node that is common to all created elements (called the pressure node) it creates the HSFLD242 element (Figure 5.19 - A) [86].

This type of element supports various fluids, including gases, following the ideal gas law, and can be used in linear and nonlinear static and transient analyses, and modal analyses. Regarding the volume of the element, this can be positive or negative, which is a nonphysical concept introduced to deal with the specification of positive volume in unwanted places. In the Workbench Technology Showcase, from the Ansys support documents, this concept is easily illustrated with the simulation of a tyre [87]. The air inside the tire is generated using HSFLD242 with positive volume, however, this creates elements outside of the desired volume as shown in Figure 5.19 - B. The solution to this problem is the creation of HSFLD242 elements with negative volume (Figure 5.19 - C) on the regions of interest that cancel out the excessive volume of the positive volume elements. The volume of an element is negative if the normal of the face is oriented outward from the pressure node [87]. The orientation of the normal of the cavity's surfaces can be viewed in SpaceClaim on "Normal" under the "Measure" tab and can be flipped at will.

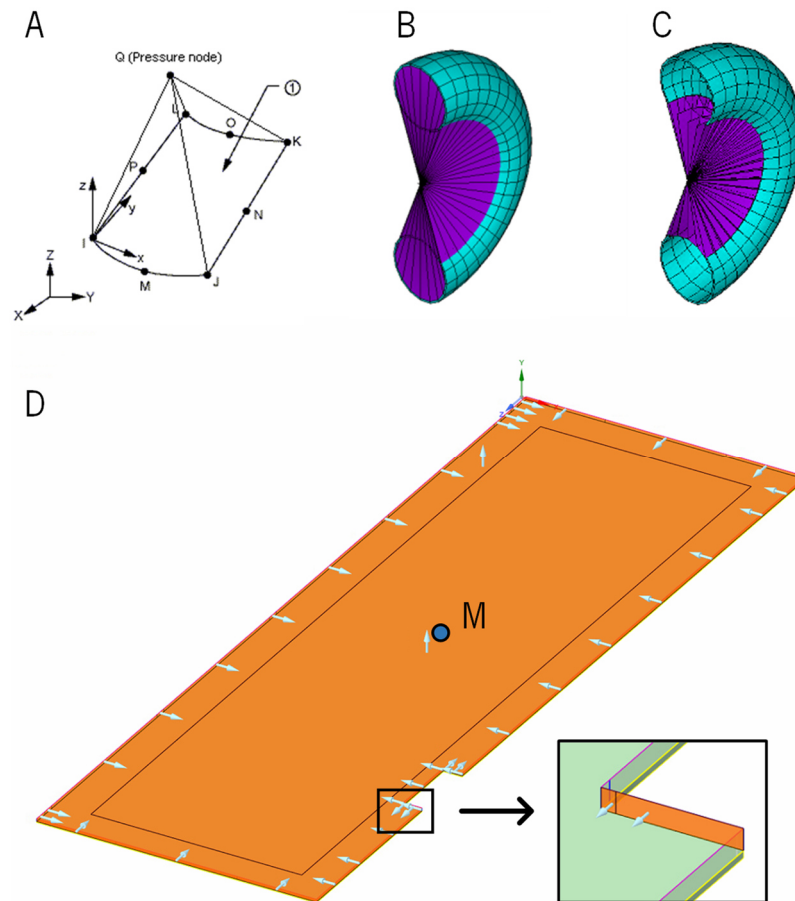


**Figure 5.19.** HSFLD242 element, with the pressure node Q (A), tire with HSFLD242 created with positive (B) and negative (C) volumes, and faces' normal of the cavity's walls of the primary leaf closer to the exterior pointing to the inside of the cavity. In D, a face highlighted in the detail can be seen, pointing away from the pressure point M, that was responsible for compensating the positive volume that goes through the outside of the cavity, as well as the duplicated positive volume that was created from the pressure node, up to the lock area, leaving the cavity with the correct volume.

The creation of the internal hydrostatic elements requires several parameters as input, such as the type of fluid, reference pressure and temperature and the density [81]. To define the boundaries of the positive and negative volumes, named selections with the interior faces of the cavities were created. For the cavities of the primary leaf, an option of dividing the named selection into three groups was made, separating the positive and negative faces of the lock zone from the rest of the faces, but for the cavities of the secondary leaf, only one named selection was used. It was also important to define the position of the pressure node, as it would be the common point for all elements [81]. In all cavities, the correspondent pressure node was positioned at the geometric centre of said cavity, or as close as possible (point M in Figure 5.19 - D), in the case of the primary leaf.

In all cavities, the normal of their walls has to be pointing to the inside of the cavity, which on the primary leaf created a negative volume from the pressure point to the face highlighted in Figure 5.19 –

D that compensates for the positive volume that goes through the outside of the cavity, as well as the duplicated positive volume that was created from the pressure node, up to the lock area, leaving the cavity with the correct volume. The creation of these volumes cannot be done through the user interface of Mechanical, thus, commands were added under the analysis part on the structure tree. Figure 5.20 shows the commands used for the most exterior cavity of the primary leaf, based on [87] and on [88]. For the rest of the cavities, similar APDL commands were used, but with different variables, a distinct location of the pressure node and with their respective named selections of the faces that create the cavity.

```

fini
/prep7
*get,typemax,ETYP,,NUM,MAX      ! max defined element type
*get,realmax,RCON,,NUM,MAX     ! max defined real constant
*get,mat_max,MAT,,NUM,MAX      ! max defined material
*get,nodemax,NODE,,NUM,MAX     ! highest numbered node in model

!Find a new number higher than that of any element type, real const, and material

newnode=nodemax+1000           ! Number for pressure node for HSFLD242
newnumber=typemax+1
*if,realmax,ge,newnumber,then
  newnumber=realmax+1
*endif
*if,mat_max,ge,newnumber,then
  newnumber=mat_max+1
*endif
et,newnumber,HSFLD242          ! 3-D Hydrostatic Fluid Element
r,newnumber,0.101325           ! Atmospheric pressure in MPa
tb,fluid,newnumber,1,,gas      ! Fluid type
tbddata,1,1.225e-9             ! Air density in kg/mm3
mp,reft,newnumber,22           ! Reference temperature in Celsius
toffst,274                     ! Offset from temperature in Kelvins

type,newnumber|
mat,newnumber
real,newnumber

cmsel,s,cimaA_main              ! Select nodes on interior faces without lock
cmsel,a,cimaA_lock              ! Select nodes on the lock for positive volume
cmsel,a,cimaA_neg               ! Select nodes on the lock for negative volume

esln                            ! Select elements that touch these nodes

!Create a new node and define position
n,newnode,618.999993991107,29.1950008642673,1791.49994869158
ESURF,newnode                   ! ESURF HSFLD242 elements over element faces
                                ! Extra node "newnode" with ESURF with HSFLD242

allsel
fini
/solu                            ! return to solving

```

**Figure 5.20.** APDL commands for the creation of HSFLD242 elements on the cavity of the primary leaf closer to the exterior. Adapted and rewritten from [81], [86]–[88].

To visualize the created hydrostatic elements, the APDL commands from Figure 5.21 were introduced under “Solution” in the structure tree, plotting the HSFLD242 elements and exporting the image as a PNG.

```

set,last
/show,png                ! output to png format
/gfile,650              ! adjust size of file
/edge,1,1              ! turn on element outlines
/view,,1,1,1           ! adjust view angle (isometric)
esel,s,ename,,HSFLD242 ! select all HSFLD242 elements
eplot                  ! Display of the selected elements
/show,PNG              ! create a PNG file

```

**Figure 5.21.** APDL commands for the creation of an image with the HSFLD242 elements created in the simulation. Adapted from [89].

The result is the image in Figure 5.22, where it is possible to see that the elements were exactly created as intended, for the four cavities. It is also possible to observe the elements created outside the cavity, that are, in fact, two types of elements overlapped as previously discussed, i.e., elements with positive and negative volumes.

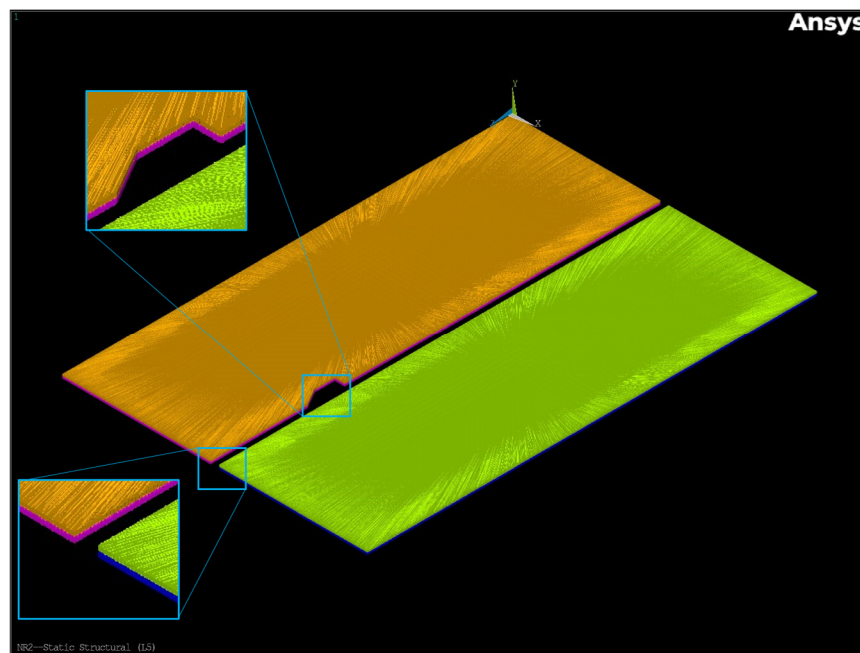


**Figure 5.22.** Image with the HSFLD242 elements created in the simulation, with the elements of the different cavities with distinct colours. One detail shows the elements created outside the cavity that were two types of elements overlapped i.e., elements with positive and negative volumes.

Different thicknesses of outer glass panels were tested, besides the 6 mm of the original glazing, more concretely thicknesses of 4, 5, 7 and 8 mm were tested for the outer glass panels, leaving the

glazing with thicknesses of 36, 38, 42, and 44 mm, in that order. To apply this change in thickness, some parameters of the model need to be adjusted. The thickness of the different surfaces that contain glass need to be changed, as well as the offsets given in the spacer region and in the brass sheet over the lock, to correct the cross-section's position. Additionally, the glazing must be moved either closer to the exterior (for thicknesses of 4 or 5 mm) or to the interior (for thicknesses of 7 or 8 mm), which can be achieved by imposing a "Part Transform" on the glazing and defining a translation. The last step was to correct the offset given to the beads, which lock the glazing on a real system.

### 5.3.3 Locking Points

As indicated, the role of the locks in the simulation was to introduce constraints on the movement of the system, and introduce localized stiffness, since these components were not the object of study. This was accomplished through joints, constraint equations, and simplified geometries.

Starting with the lock, this component is placed on the frame and glazing of the primary leaf. In the polymeric part of the frame, a hole is carved in some areas, for the application of the locking device, and in other areas, only a layer is carved, deep enough for the placement of a steel plate component.

Therefore, with some simplification of the real device, considering the frame in Figure 5.23 - A, three surfaces were created by cutting the geometry, where the surface 1 and 3 were composed of a layered section of PU (5,6 mm) – PA (0,8 mm) – PU (2,6 mm) – Steel (3 mm) with the steel layer on the further side of the correspondent glazing, and in surface 2, representing the bulk of the lock on the frame, only steel was used (12 mm), to increase the stiffness and weight of this region. In the brass sheet on the glazing, holes for the key socket and the handle were also made since they are connected to the locking mechanism in a physical DLD system. It is also important to note that the steel considered in the hardware devices used the properties of the software's library Structural Steel ( $E=200$  GPa,  $\rho=7850$  kg/m<sup>3</sup>, and  $\nu=0,3$ ).

The joints generated by the software create two remote points, that connect to the scoped geometry, where one of the points is the reference, on which a coordinate system is automatically created (but can be changed), and the other is the mobile [84]. The two remote points have associated constraint equations that correlate the chosen degrees of freedom of said points, and with the geometry connected to these points, a joint is created [84]. There are different ways to connect the geometry to these remote points, depending on the type of behaviour chosen for the geometry, which can be "beam", implementing a beam formulation like the one already discussed, or can be "rigid" or "deformable", where the joint is



modelled with elements with MPC capabilities, like the MPC184, but using different formulations [81], [84].

The locking mechanism was modelled as a rigid component, and so, a fixed joint was created, connecting the edges shown in Figure 5.23 - B with the beam formulation (by option, as there were alternatives), using the beam definition already presented in the connections between the frame and the glazing. This joint had the reference defined on the edges of the frame, and the mobile on the other edges, although in the case of a fixed joint with this formulation, these definitions become arbitrary. Furthermore, on the edges that define the lock, and on the edges that surround them in the brass sheet of the glazing, a sizing of 2 mm was defined.

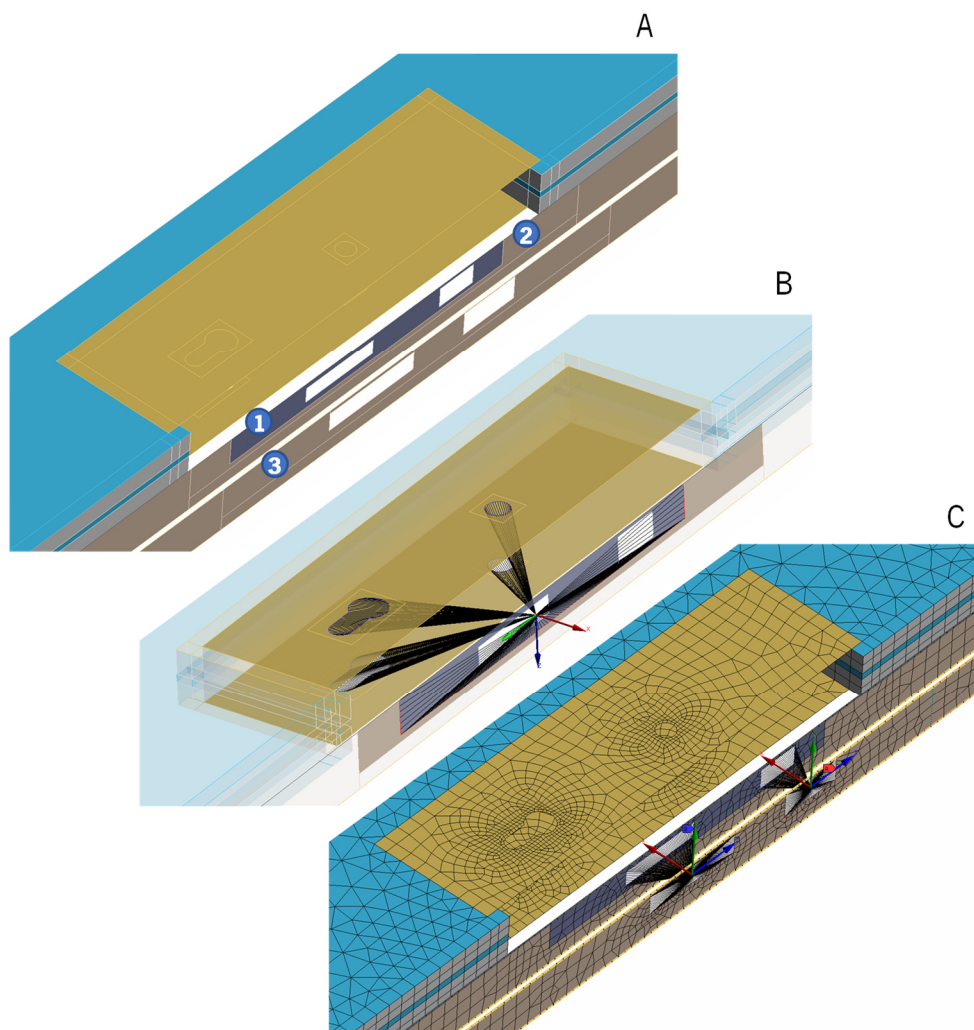


**Figure 5.23.** Main lock geometry (A), fixed joint created with the beam formulation to represent the lock (B), and joints created to represent the plug and socket mechanism of the lock between the primary and secondary leaf's frames (C). On the surfaces 1 and 3, a layered section of PU (5,6 mm) – PA (0,8 mm) – PU (2,6 mm) – Steel (3 mm), with the steel layer on the further side of the correspondent glazing. On C, the joints have freedom in the translational X (red vector) and Z (blue vector) directions, as well as on the rotations about the Y axis (green vector).

Two general joints were specified on the holes created on the frames, and are shown in Figure 5.23 - C. These joints have as reference the edges of the holes in the secondary leaf and have as mobile the edges of the holes in the primary leaf, all defined with rigid behaviour, and have freedom in the translational X (red vector) and Z (blue vector) directions, as well as on the rotations about the Y axis (green vector). This is because, the physical plug components from the lock when engaged and on the socket in the secondary leaf, have some freedom in the Z direction ( $\approx 6,5$  mm), which allows some translation in this direction, as well as some rotation in the Y direction. This meant, that it was important to check that the relative displacement of the remote points in the Z direction was not larger than 6,5 mm, after the simulation.

The hinges were introduced in all locations displayed in Chapter 2 and were modelled using revolute joints, that only allow rotation on the Z axis (displayed in blue in Figure 5.24 - A and B, or pointing out of plane in Figure 5.24 - C), with a deformable behaviour.

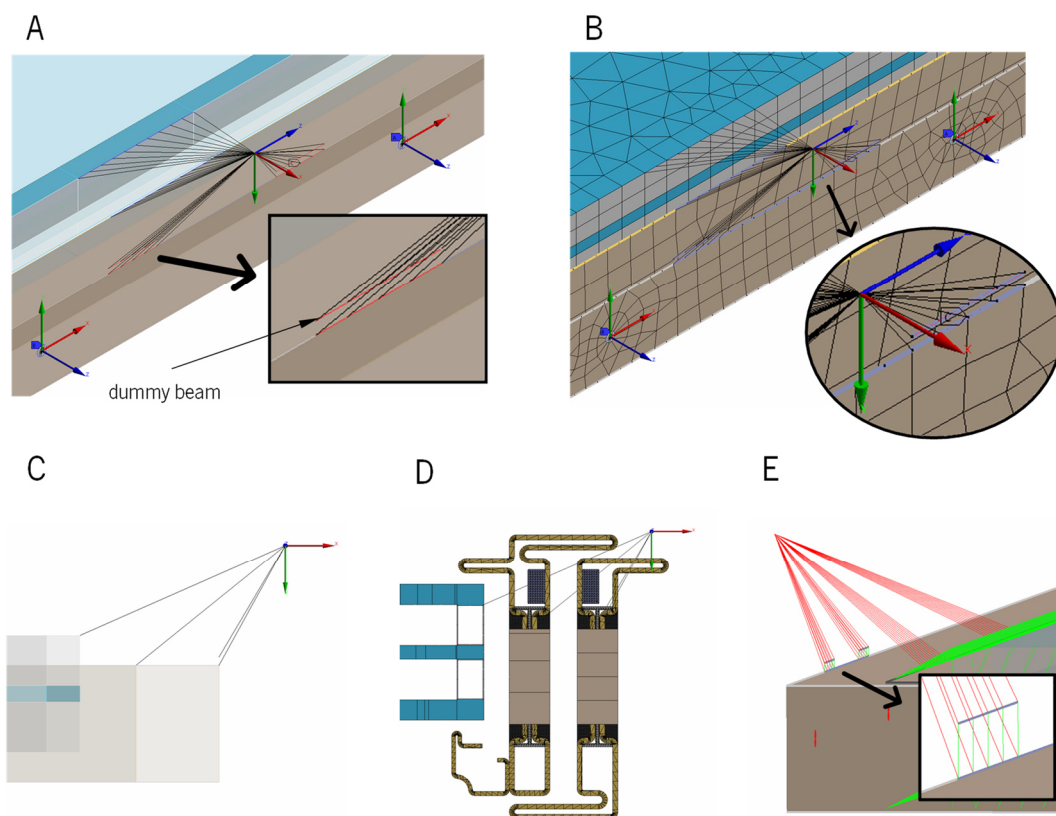


**Figure 5.24.** Hinge joint with the detail of the dummy beam (A), mesh near the hinge (B), lateral view of the hinge without (C) and with (D) cross-sections graphically displayed, and joint connections as well as beam formulations created around the hinges (E). The hinge joints only allow rotation on the Z axis (blue vector), and on B, excluding the dummy beams, the grey beam elements represent the location of the internal reinforcements of the hinge.

It was also seen in Chapter 2 that the hinges have internal steel reinforcements, which were accounted for in the simulations by the introduction of beam elements, for the length in between screws of these reinforcements. In Figure 5.24 - B, the location of these reinforcements can be seen on the frames, as they are represented in grey, and in Figure 5.24 - D the cross-section of these components, as well as their position on the MMBs, are displayed. It is important to note that due to geometric incompatibility, when testing the total reinforcement on all locations, these components cannot be physically introduced, hence, they were not considered in those simulations, i.e., they were suppressed.

It was discussed that joints in Ansys are based on the connection between two different sets of geometry with two different remote points, which have constraint equations that restrain their displacements and rotations. When specifying the connection to a remote point, with the behaviour of the geometry set as deformable, a formulation similar to that of the RBE3 command, which defines a constraint in Mechanical APDL, is used [84], [86]. This command creates constraint equations that make the motion of the independent node (in this case it would be the remote point) as an average from the nodes of the geometry with deformable behaviour [86]. However, only the translational degrees of freedom of the dependent nodes are used for constructing the constraint equations, which means that the translations, as well as the rotations, of the independent node, are calculated from the translations of the dependent nodes [86]. This becomes a problem when the deformable geometry is colinear, like in the case of a beam body, which is a straight-line body. In Ansys Mechanical the RBE3 command is not used, but instead, a similar formulation using MPC is employed, that shares this problem [84], [86].

The way the software deals with this is by extending the nodes that are attached to the remote point to nodes from close geometry that was not scoped for the connection, which in the case of the hinges means that the polymeric parts would be used in the joint. This is not desirable, since unwanted deformations could appear, and the connection in the physical system is made solely on the metal part.

To solve this problem several solutions were employed for the hinges. If the frame belonged to a leaf, the edge of the glazing closest to the frame was scoped together with the edge of the frame, as the mobile geometry, which was acceptable, since the elements on the two edges had already a rigid connection established from the beam formulation employed between the frame and the glazing. This was the reason for the cuts on the spacer region of the glazing that are noticeable in Figure 5.16 – A and Figure 5.24 – A. On the other hand, in the frame fixed to the wall, there were no edges that could be used as “support”, thus, a dummy beam was introduced directly above the edge of the frame, as can be observed in Figure 5.24 - A. This dummy beam had negligible stiffness, as it had an extremely small

cross-section, an elastic modulus of 0,1 MPa and null density. This beam's only purpose was to be connected to a specific edge of the frame using a connection with the characteristics of the already discussed beam formulation, as can be seen in Figure 5.24 – E, which means that the nodes of the dummy beam were directly above the nodes of the edge of the frame. However, the distance to the edge of this dummy could cause undesirable moments in the joint, which were dealt with by probing the results as this distance was reduced, and it was found that up to a distance of 2 mm, directly above the edge of the frame, the results were virtually the same, making this distance acceptable (Annex C).

To fix the two leaves together, besides the lock, other hardware was employed on the system, more specifically, the AC2695S locking device, already introduced in Chapter 2. To model this device a joint was defined, but because the intended degrees of freedom, were not available in any of the joints available, the joint had to be defined manually. Two remote points were created with the origin of the coordinate systems located directly above the MMB of the secondary leaf's frame, in the position where the physical device would be locked. The behaviour of the scoped geometry was defined as deformable, and the same method as described for the mobile geometry of the hinges was applied, hence the cuts in the spacer regions of the glazing's in Figure 5.25 - A.

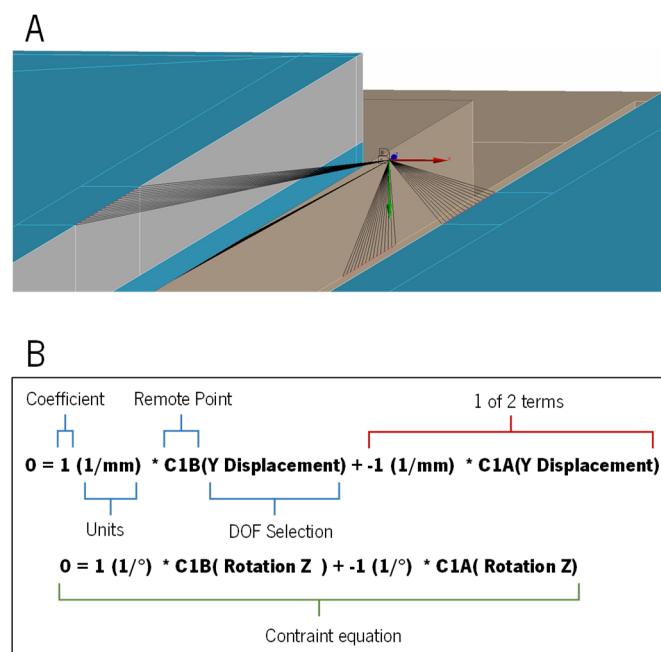


**Figure 5.25.** Joint representing the AC2695S locking device (A), which had fixed the translations between the two remote points in the Y direction (green vector) and the rotations about the Z axis (blue vector). This joint was defined through constraint equations (B).

After specifying the remote points, constraint equations were introduced, for the degrees of freedom that were desired to be fixed. Due to the position of the plug pin in the locked positions, it was inferred that the degrees of freedom to be fixed, would be the translation in the Y direction (green vector in Figure 5.25 - A) and the rotation about the Z axis (blue vector in Figure 5.25 - A). The translation in the Z direction was decided to not be fixed because there is a distance between the plug pin and the socket of 1,25 mm when the device is fully engaged in a physical DLD system. Just like it happened with the lock, it was important to check that the relative displacement of the remote points in the Z direction was not larger than 1,25 mm, after the simulation.

The implementation of the two constraint equations needed to create the manual joint is shown in Figure 5.25 - B, with the different elements that were needed for its definition. This image only shows the constraint equations of the locking device of the kind that was located the highest, as the constraint equations for the other devices were similar and change only on the remote points' name.

The last locking point to be discussed is the connection between the secondary leaf, and the top and bottom MMBs of the fixed frame, at the centre of the system, made with the AC2621 RX. As discussed in Chapter 2, the pin of this mechanism connects to a plate on the fixed frame, which was modelled as the surface shown with tag 1 in Figure 5.26 - A. On the plate, a layered section of PU (5,6 mm) – PA (0,8 mm) – PU (5,6 mm) – Steel (3 mm) was assigned, and a sizing of 1 mm was employed on all the edges of the plate. The pin mechanism had the geometry very simplified and was modelled as shown in Figure 5.26 - B, where the surface 2 had a layered section of PU (5,6 mm) – PA (0,8 mm) – PU (3,6 mm) – Aluminium (2 mm), and surface 3 had a layered section of PU (5,6 mm) – PA (0,8 mm) – PU (2,6 mm) – Steel (5 mm), with the metal layers on both surfaces, placed on the side further from the glazing. The aluminium used to define surface 2 was the same assigned to the spacers of the glazing. On surfaces 1 and 3, an offset was given, which was already displayed in Figure 5.26 - C, and on surface 3, the edge closer to the fixed frame was divided in three, leaving an edge of 8 mm in the middle that had 8 divisions imposed, in the mesh generation. Figure 5.26 - C shows the mesh in this location.

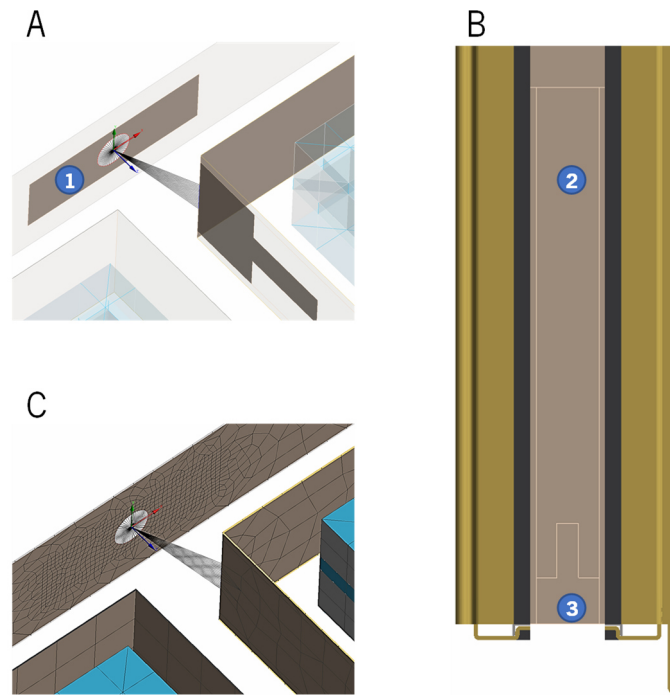


**Figure 5.26.** Joint connecting the secondary leaf to the fixed frame in the centre of the system (A), geometry simplification of the pin mechanism (B), and mesh around the joint (C). In surface 1 (sizing of 1 mm), a layered section of PU (5,6 mm) – PA (0,8 mm) – PU (5,6 mm) – Steel (3 mm) was specified with the steel layer closer to the leaves. Surface 2 had a layered section of PU (5,6 mm) – PA (0,8 mm) – PU (3,6 mm) – Aluminium (2 mm), and surface 3 had a layered section of PU (5,6 mm) – PA (0,8 mm) – PU (2,6 mm) – Steel (5 mm), with the metal layers on both surfaces, placed on the side further from the glazing. Additionally, on surfaces 1 and 3, an offset was given.

This representation of the mechanism was by no means a perfect one, but it introduced stiffness in two locations of the frame, accounting for exaggerated deformations that could occur in this region had it not been added. The use of this method was justified since the objective of the simulations was to study the changes in the internal reinforcements and the glazing of the system, and not the performance of the hardware.

### 5.3.4 Resistance to Wind Loads

For the simulations of the wind pressure test, two timesteps were defined. The first timestep had 1 second, a maximum of 10 substeps, and only had the load from earth's gravity, to let the system settle before the application of the wind load. In the second timestep, the load test correspondent to the third class on the CE marking, 1200 Pa, was specified on the transition and centre surfaces on the exterior side of the glazing. This timestep had also a maximum of 10 substeps defined and was given 4 seconds, where the load was ramped up to the final pressure. Since these were Static Structural analyses, the time

of the timestep was not relevant, though, a simulation with the exact same model, B.C., and settings, was performed in Transient Structural, to capture the inertial effects of the test. However, these effects were found not to be relevant since the results were virtually unchanged (Annex C). Figure 5.27 illustrates the loads and constraints of the simulations, not considering the joints that fix the screw holes to the ground, where the fixed support was applied on the wall surface that was already discussed and is not present in the figure.

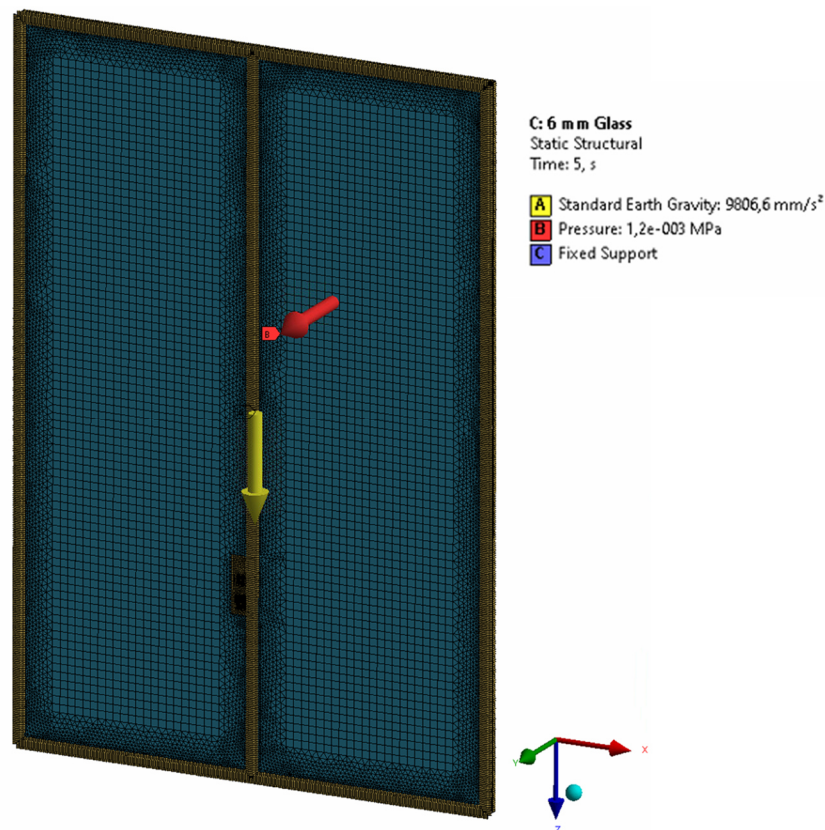


**Figure 5.27.** Loads and constraints of the wind pressure test simulations, without the joints that fix the screw holes to the ground. The pressure was applied on transition and centre surfaces on the exterior side of the glazing, and the fixed support was applied on the wall surface and is not present in the figure.

After running the simulation, the maximum directional displacement in the Y direction (green vector in the coordinate system in Figure 5.27) was found for the frame structure, and through the “Beam tool” the maximum/minimum combined stress was determined, which is a linear combination of the axial stress of a beam, with its maximum/minimum bending stress [84]. Other properties like the maximum principal stress were found for the glass panels (excluding the brass sheet) using the larger model mentioned in the chapter introduction, which had a higher node count, resultant from a lower global size and mode divisions in the spacer region edges. Although the ultimate stress of glass when in

compression is higher than when in tension, which is common to find in brittle materials, and would be better evaluated using the modified Mohr failure criteria, by taking the maximum principal stress and comparing it to the ultimate stress in tension, a conservative approach to the stress evaluation was taken [90].

The maximum directional displacement in the Y direction was found for the different reinforcements and plotted against the various thickness of glass, or against the internal reinforcements' elastic modulus for the different locations' configurations, which allowed the simulations to cover a large number of materials since the results are not dependent on the reinforcement's density (Annex C). Additionally, the percentual relative change in stiffness was plotted similarly, based on equation 5-8, which was derived considering two springs with different constants (k) that were subjected to the same load (F), resulting in different displacements( $\delta$ ).

$$\% \text{Relative change in stiffness} = \left( \frac{k_2 - k_1}{k_1} \right) \times 100 = \left( \frac{\delta_1}{\delta_2} - 1 \right) \times 100 \quad 5-8$$

### 5.3.5 Resistance to Static Torsion

For these simulations, only 1 timestep was specified, with a maximum of 20 substeps. Some simulations could not converge with one substep, as the iterative solver was defaulted to have a maximum of 25 iterations to achieve convergence, before dividing the simulation into more substeps, which could be time consuming. Hence, the command "NEQIT,40" was added so that this number could be increased to 40, giving the solver more iterations to converge on the same substep [86].

The earth's gravity was considered, and a force of 250 N, corresponding to the test's second class was applied at the corner of each leaf, on the interior glass panel, in the X direction (red vector in the coordinate system in Figure 5.28), pointing away from the centre of the system. The forces were applied on elemental faces located on the interior side glass panel, taking advantage of the shape of the mesh, and the same was done with the specified remote displacements, which scoped the elemental faces in the upper corners of the leaf, in the external glass panel, as can be seen in the detail in Figure 5.28, for the secondary leaf. The remote displacement had the internally created remote point fixed in the X direction, and the behaviour of the geometry set as deformable. This way, despite the restriction in the X direction, the deformation of the glazing in these areas was more natural than it would be had a



different constraint been applied, like a fixed displacement, since the B.C. would act directly on the nodes of the scoped faces.

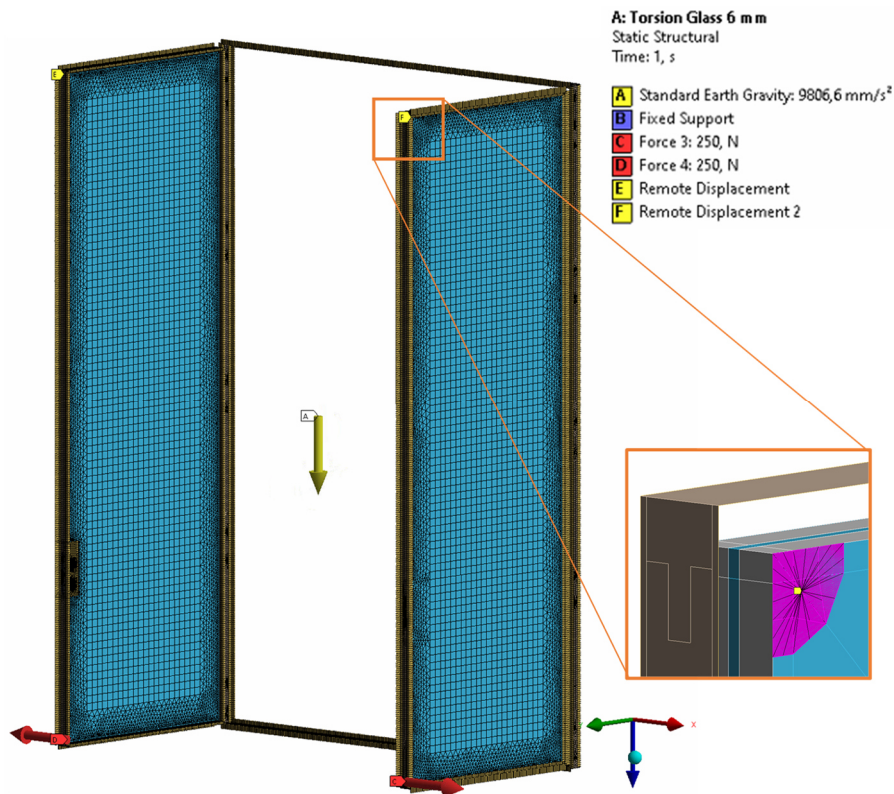


**Figure 5.28.** Loads and constraints of the static torsion test simulations, without the joints that fix the screw holes to the ground. The loads and remote displacements were applied on the elemental faces, as can be seen in the detail, and the fixed support was applied on the wall surface and is not present in the figure.

In these simulations, only two sets of internal reinforcements were used: placed at all locations where it is possible to reinforce (in the physical system) or only placed at the centre. The post-processing was similar to the one described for the wind pressure simulations, with the difference that the displacements of interest were in the X direction. The maximum displacement in this direction corresponded to the maximum displacement in X, in the secondary leaf, whereas the minimum displacement (a negative number) gave the maximum displacement (absolute value), in the primary leaf.

### 5.3.6 Resistance to Vertical Loads

In the resistance to vertical loads test simulations, two timesteps with the same settings as the ones used for the static torsion test simulations were specified. The gravity was applied on the first step, and on the second, a downwards force of 600 N, corresponding to the second class of the test, was

applied on the elemental faces on top, at the end of each leaf, once again, making use of the shape of the elements. Additionally, remote displacements fixed in the X direction (red vector in the coordinate system in Figure 5.29) with deformable geometry behaviour were defined in the elemental faces on the bottom, at the end of each leaf, as illustrated in the detail in Figure 5.29, to prevent the leaves from moving to the side.

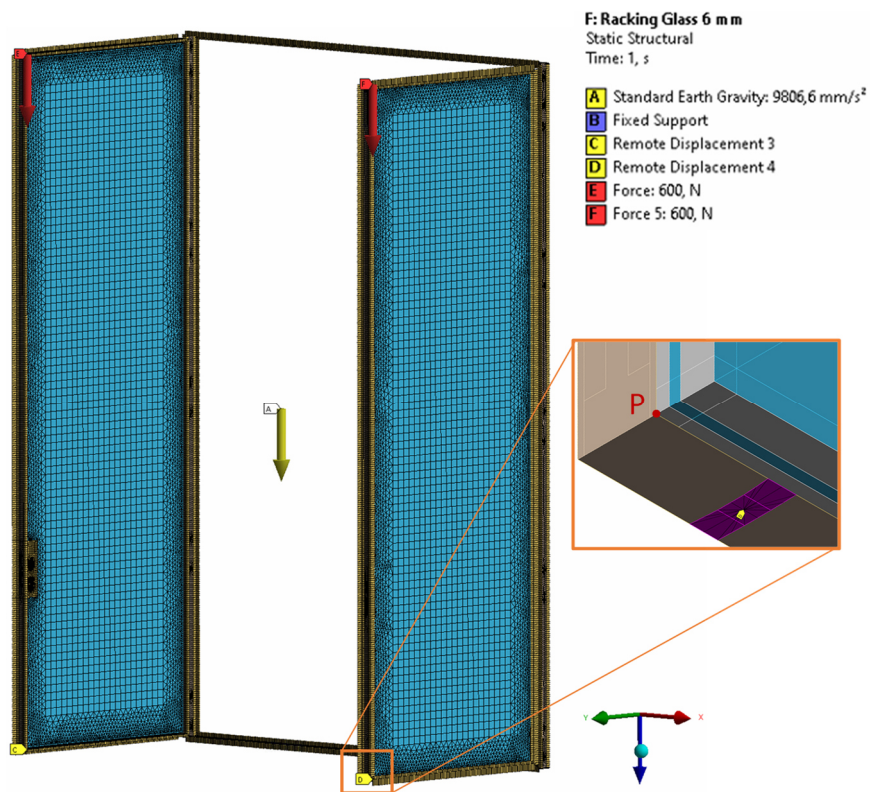


**Figure 5.29.** Loads and constraints of the vertical loads test simulations, without the joints that fix the screw holes to the ground. The loads and remote displacements were applied on the elemental faces, as can be seen in the detail, and the fixed support was applied on the wall surface and is not present in the figure.

Much like the static torsion test simulations, only two sets of internal reinforcements were used, being placed at all locations, or only placed at the centre. The post-processing was identical to that of the previously discussed test simulations, with the difference that the maximum displacements used for the plots and the relative change in stiffness, were measured at the end of each timestep and on the extreme of the lowest MMB of the leaves' frames, with a probe to the point that was the furthest from the centre of the system, which in the secondary leaf was the point P, illustrated in Figure 5.29.

### 5.3.7 Dynamic Vibrations Test

To evaluate the dynamic response of the system, the first simulation performed was a modal analysis, to find the natural frequencies and the mode shapes of the system. Then, three harmonic response analyses were performed, one considering a harmonic acceleration of 0,092g in the Z direction, and two others considering the same acceleration in the X and Y directions (Figure 5.30). In the modal analysis settings, a large number of modes were requested, so that all would be found between 0 to 50 Hz, and in the harmonic response simulations, 100 intervals were asked for, in the same range. Additionally, in the harmonic response simulation, the damping ratio calculated from the data of the experimental modal analysis of the beam was used, due to the lack of better estimation of the damping ratio.

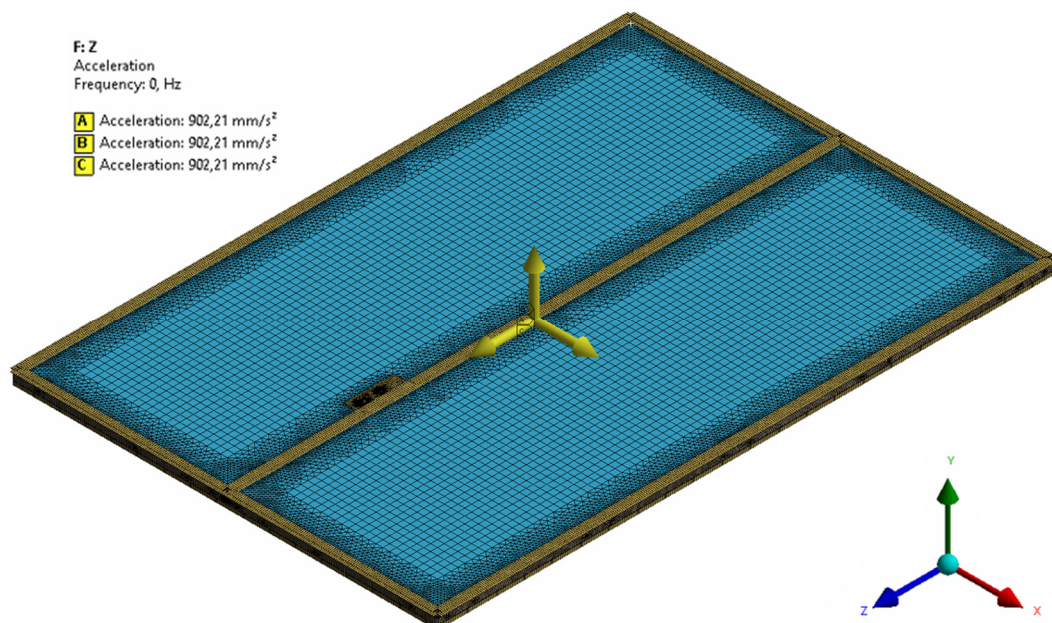


**Figure 5.30.** Harmonic acceleration of 0,092g in the Z direction, X and Y directions, from three different simulations.

Some changes were made for these simulations, which inevitably resulted in a simplified model, so the results of the simulations should be taken as only indicative, and with special caution. These simulations were linear simulations, which means that the wall and its frictionless connection with the fixed frame would create a bonded connection, attaching all DOF of the frame to the wall, which was fixed. Hence, the wall was removed from the model, and only the screw connections were used to fix the system, which in a way increases the freedom of the fixed frame, and larger deformations than those of a real system could be expected in these areas. In addition, the stoppage between the frames of the leaves at the centre, and between the fixed frame and the movable leaves' frames cannot be accounted

for, and the same happens with the influence of the rubber sealants in the natural frequencies, mode shapes and damping ratio in the system. A change was also made in the polymeric materials for this simulation, where the elastic moduli from Table 2.2 were considered, i.e., 2,2 GPa for the PU and 10 GPa for the PA.

After running the simulation, in the modal analysis, the mode shapes were created for each of the natural frequencies, and in the harmonic analyses, the directional displacement of the frame structure was plotted against the frequency, to find at which frequency the peak displacement occurs. Then, another harmonic response simulation was made, with more resolution around the peak displacement, and properties like the maximum displacement of the frame structure and the maximum principal stress on the glass panels was found (using the larger model of the DLD system). Unfortunately, the beam tool was not supported for this type of analysis.

### 5.3.8 Thermal Transmittance

It is important that the introduction of the reinforcements in the frame structure doesn't cause a significant variation in the frame's thermal properties because the capacity of the system to resist the transfer of heat must not change significantly. The study consists of evaluating the thermal transmittance of the system, with and without reinforcement, on the Steady-State Thermal module of Ansys Workbench. The application of the reinforcement considers the worst-case scenario, i.e., when the air cavities 1,2,4, and 5, from Figure 5.31, were filled with steel of  $\lambda = 60 \text{ W/(mK)}$  all over the structure, including cavities at the centre that cannot be reinforced. This is not a realistic reinforcement application, but if the change in thermal transmittance was proved not to be significant in this case, the change with other reinforcement configurations would be expected to be smaller for any reinforcement material, with a  $\lambda$  smaller than the one considered.

The general method for determining the thermal transmittance of the system was already discussed in Chapter 2, so in this chapter, the simulation topics are the focus. The method must be applied on two different frame/glazing sections, more specifically, the side section, which goes around the perimeter of the system, and the central section, which represents the junction between the leaves. A representation of the two sections is depicted in Figure 5.31, where the extension of the glazing/insulation panel is not illustrated, as the mesh shape and the materials used can be easily inferred from this figure. In Figure 5.31, one can also find the modelled surfaces (1 m of thickness), and the assigned materials, that are colour coded and show their corresponding thermal conductivity, which was the only

material property used as input for the simulation. In this figure, there is also a detail that shows the introduction of the insulation panel, in brown, where the rest of the section, which is hidden, is the same as the section with the glazing.

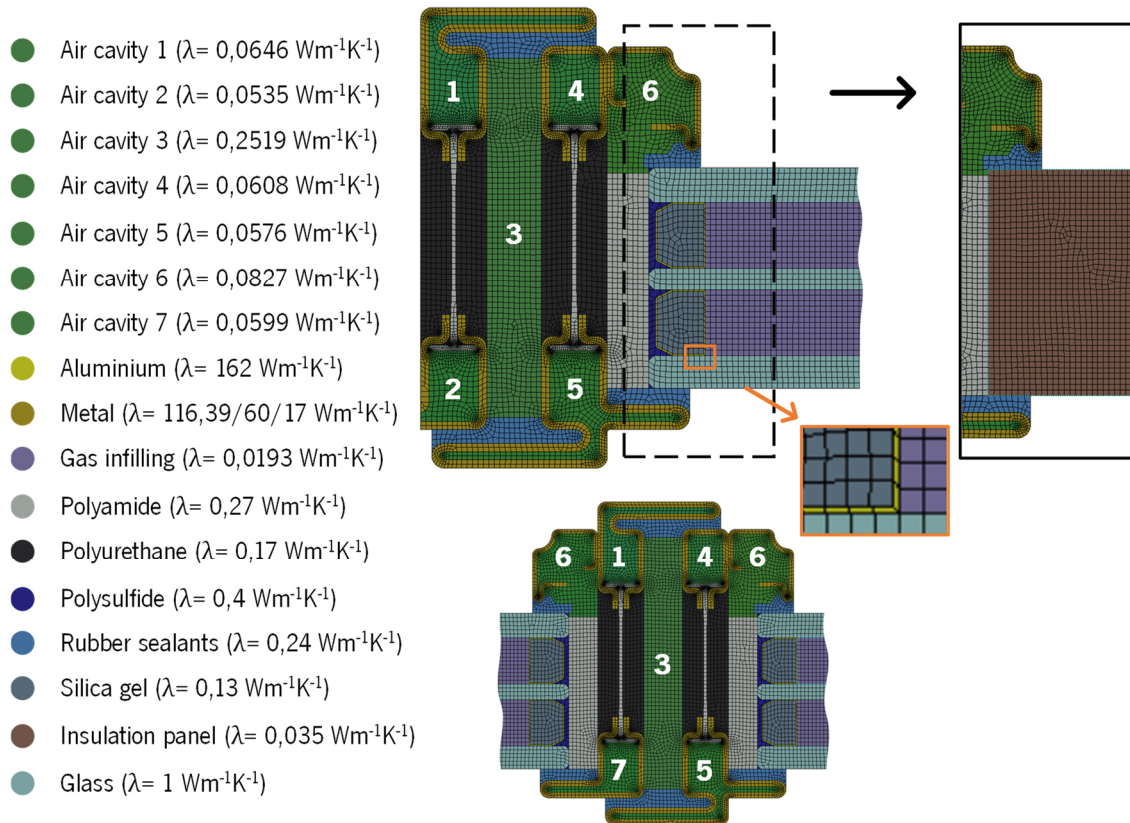


**Figure 5.31.** Geometry, mesh, and materials colour coded with the correspondent  $\lambda$ , of the two models (side and centre sections) in the thermal transmittance simulation. The details show the material colour of the spacer (aluminium) and the introduction of the insulation panel [37].

The air cavities' thermal conductivities were calculated from the method present in Chapter 2, and the value for the gas infilling considers a glazing with a thermal transmittance of  $0,7 \text{ W}/(\text{m}^2\text{K})$ , and its calculation can be consulted in Annex B. The rest of the thermal conductivities were either already defined in the same chapter or were taken from the standard ISO 10077-2:2017, which sets this property for numerous materials for the validation simulations. The mesh is also portrayed in Figure 5.31 and had specified only quadratic elements, with a global sizing of 1 mm, creating PLANE293 elements.

Only convection B.C. were applied to account for the surface thermal resistances defined in Chapter 2 and were applied on the edges of the 2D surfaces, which are the faces of the frame and glazing. On the interior faces without reduction, a film coefficient of  $7,6923 \text{ W}/(\text{m}^2\text{K})$  with a temperature of 293,15 K was defined, whereas on the interior faces with reduction, a film coefficient of  $5 \text{ W}/(\text{m}^2\text{K})$

with a temperature of 293,15 K was specified. On the external faces, a film coefficient of 25 W/(m<sup>2</sup>K) with a temperature of 273,15 K was assigned. The film coefficient was the inverse of the surface thermal resistance predicted by the standard, and Figure 5.32 portrays the concerned faces (viewed as edges) in the two sections, where the edges in green depict the external faces, the edges in blue, the internal non reduced faces, and the boundary edges without highlight colour, the internal faces with reduced resistivity. It is also important to note that in Figure 5.32 the red edges represent adiabatic faces and that the glazing was cut so that the illustration could be displayed with more detail. These B.C. were used for all simulations, be it with glazing or insulation panel.

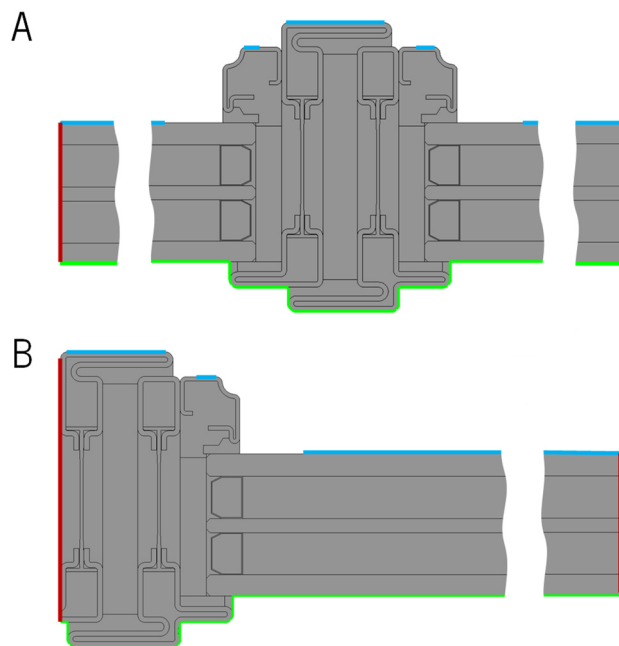


**Figure 5.32.** B.C. in the in the thermal transmittance simulation, where the red edges were made adiabatic, and the other edges (that don't represent cuts on the glazing) had a convection B.C. applied. The green edges with a film coefficient of 25 W/(m<sup>2</sup>K) (at 273,15 K), and the blue and colourless edges with a film coefficient of 7,6923 W/(m<sup>2</sup>K) and 5 W/(m<sup>2</sup>K), respectively, at a temperature of 293,15 K. When simulating with the insulation panel, the B.C. were identical.

The analysis settings weren't manipulated, and the connections between the surfaces were automatically defined by the software, so up to this point, the simulation was fully defined. This procedure was the same procedure used in the validation simulations demanded by the standard to evaluate the capability of the software and the method, whose results are presented in Annex B.

After running the simulation, several results could be found, including the resultant temperature profile. However, for the application of the standard, a reaction probe was specified for the external B.C. (Figure 5.33 - A) to find the amount of heat that crosses the section in Watts. Since all the surfaces had

1 m of thickness, the unit could be updated to W/m, and dividing by the temperature gradient, which was 20°C, it was possible to find the thermal conductance  $L^{2D}$ . In the insulation panel, a “path” (Figure 5.33 - B) was created to find the directional heat flux (perpendicular to the façade), and its average value was the thermal transmittance of the central area of the insulation panel, in W/(m<sup>2</sup>K). In the middle section, two paths had to be created, and since they correspond to equal areas, the obtained values from each path were averaged.

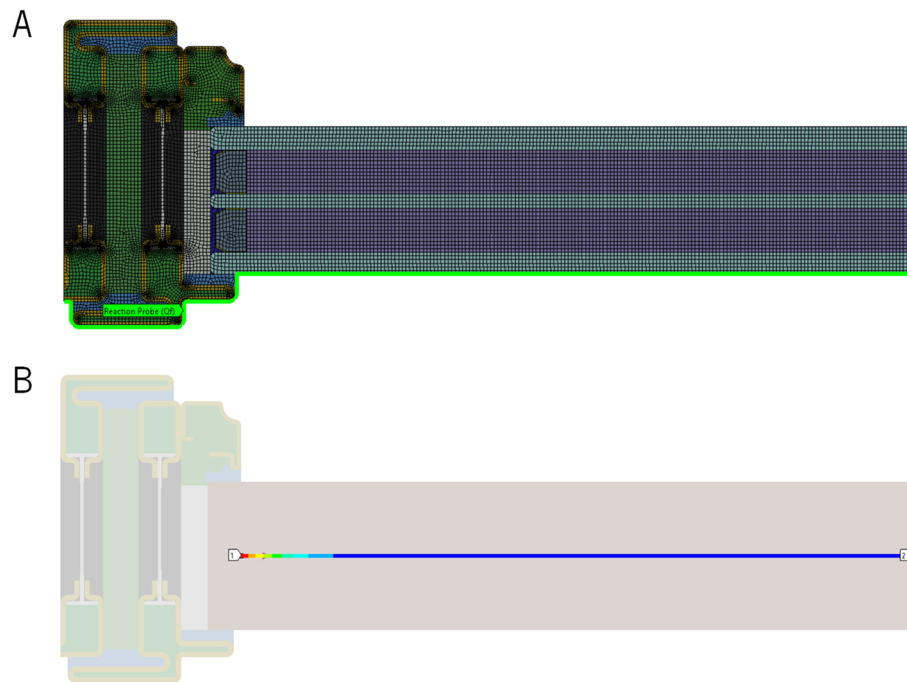


**Figure 5.33.** Probe specified for the external B.C. in green (A) and “path” that was used to find the average value of the directional heat flux, perpendicular to the façade.

With these quantities, the formulation given by the standard, already presented in Chapter 2, as well as the dimensions of the system, the thermal transmittance of the system was calculated, with and without internal reinforcements, making it possible for the differences to be evaluated.

# Chapter 6

## RESULTS AND DISCUSSION

The chapter is organized in the way that the models were exposed in Chapter 5. Therefore, first, the results from the numerical models of the MMB are portrayed, along with the results of the analytical models from Chapter 4, and then the results from the simulation tests with the DLD system are revealed.

### 6.1 Multi-Material Beam

#### 6.1.1 Three-Point Bending

During the experimental test, and after some deformation had already occurred, some cracking noises could be heard, which were speculated to be linked to the break of the bond between the different components of the MMB. At the end of the experiment, the bond between the lower brass component and the rest of the MMB had completely been overcome by the longitudinal shear forces on the MMB. This event was accompanied by a loud noise, an abrupt drop in the MMB's stiffness (detail P, in Figure 6.2 - B), and a large perceptible sliding, which occurred in a fraction of a second, and can be perceived in the transition from Figure 6.1 - A to Figure 6.1 - B.

Figure 6.1 - C, was taken, before the removal of the loading pin and illustrates the sliding of the lower brass component that detached from the rest of the MMB. After the removal of the loading pin, the MMB recovered, and the effects of the sliding between the mentioned components of the MMB could not be perceived with the naked eye.



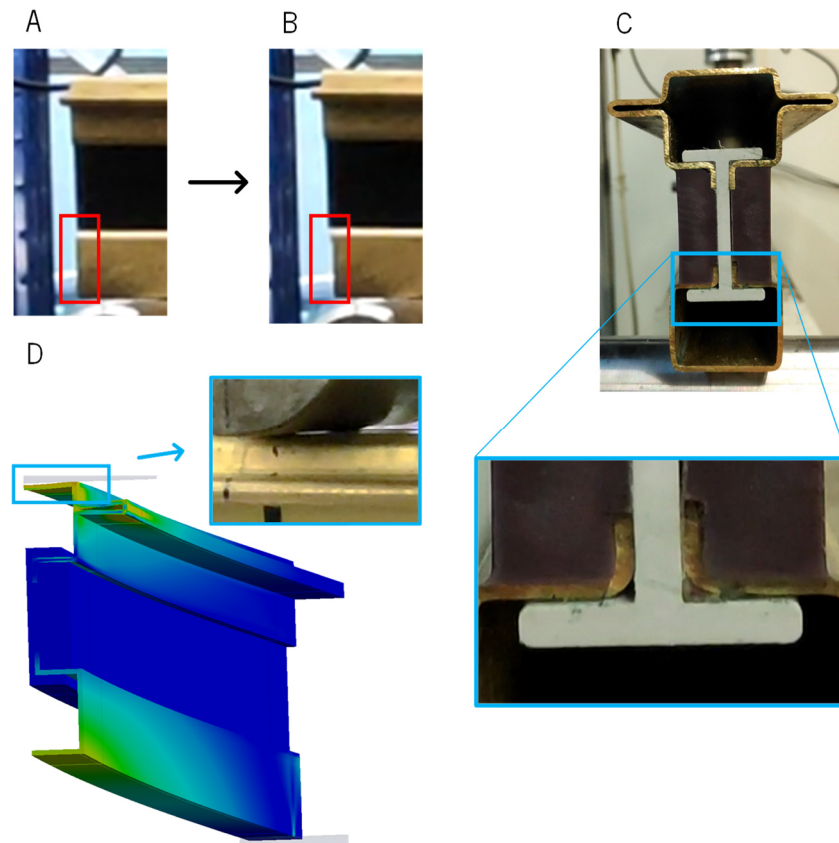


**Figure 6.1.** P.2992 1600 mm brass MMB before (A) and after (B) the abrupt change in stiffness that concluded the experiment. In B a perceptible drawback in the lower brass component is perceptible when compared to A, which exposes the sliding between this component and the rest of the MMB, that is also perceptible in C. The deformation on the MMB could be captured with some detail by the solid elements model, as can be seen, e.g., by the gap that occurs in the top face (D).

Up to this chapter, an analytical, and several numerical models, were used to describe the experimental behaviour of the MMB to bending in three points. The results from these models, as well as the data from the experiment, are plotted in the force-displacement chart A in Figure 6.2, along with the initial part of the experimental curve. In Figure 6.2 - B, a complete load-displacement chart is presented, where only the data from the solid elements model accompanies the experimental data since this is the only model where some plasticity can be perceived in its curves. Furthermore, the solid elements model is the model that best describes the experimental data, and the deformation behaviour of the physical MMB, as can be seen, for instance, by the gap that appears between the top face and the loading pin, in Figure 6.1 - D.

Three distinct groups of curves stand out in chart A, based on the slope proximity of the curves. The first group, composed of the analytical and beam elements model, depicts a clear overestimation of the MMB's stiffness, which is more emphasized in the analytical model and the numerical beam elements model with pre-integrated cross-section, whose results practically overlap each other. The three curves of

this group have a close slope, so the models validate each other, despite not correctly representing the MMB's stiffness, which ultimately suggests that the cause for this to happen is common to all these models.

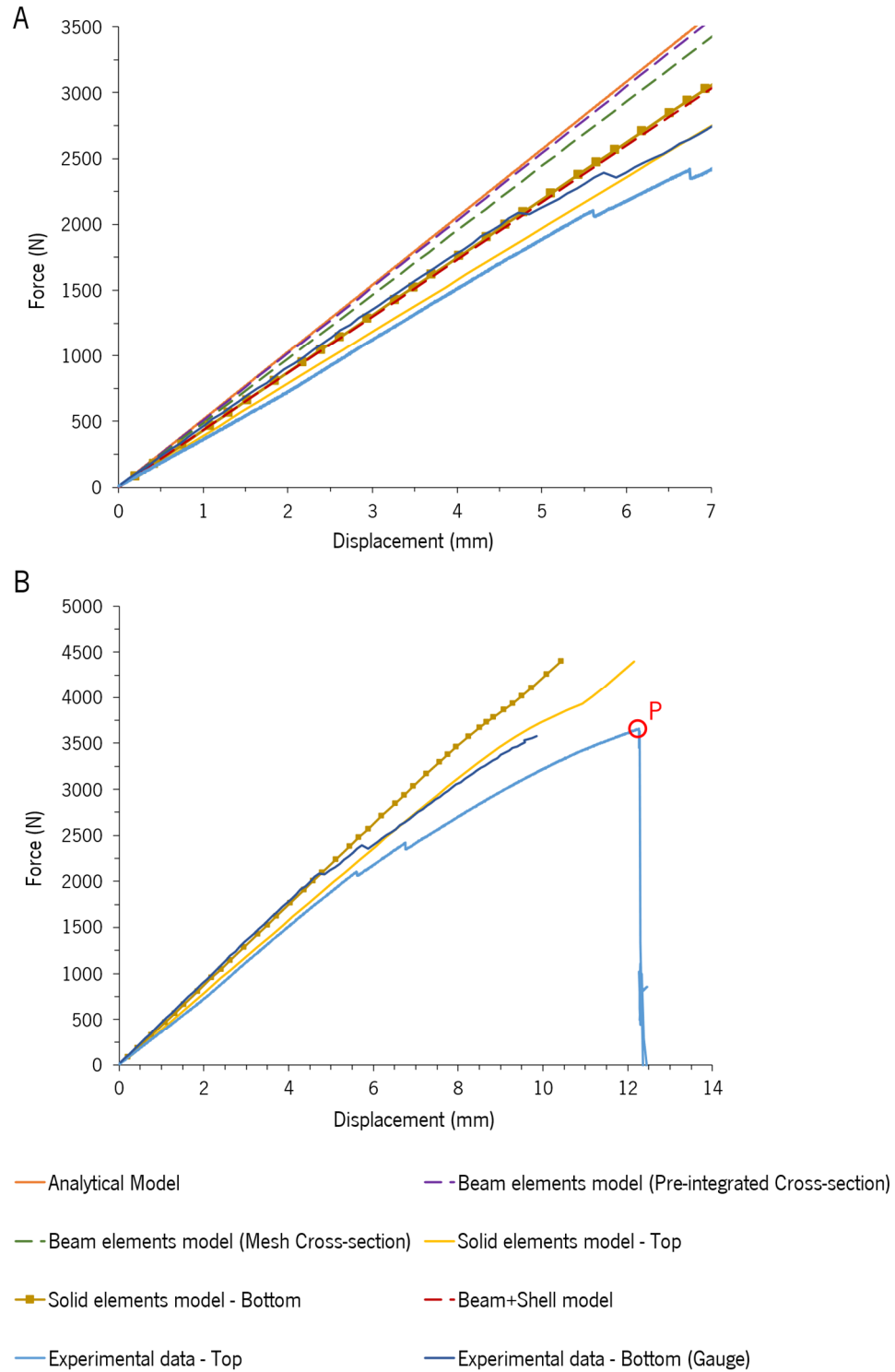


**Figure 6.2.** Initial part of the force-displacement curve of all the brass MMB numerical and analytical models defined as well as of the physical MMB (A), and complete curve of the solid elements model and of the physical MMB, on the top and lower face at the centre (B). In figure B, the detail P highlights the point where the final and sudden drop in stiffness took place.

The second group comprises the experimental data from the gauge, the solid elements model at the bottom of the MMB, and the beam + shell model, which practically overlap each other at the initial part of the curve that goes up to a displacement of about 5 mm. The same occurs in the third group of curves, which has the experimental data and the solid elements model, both measured at the top of the MMB, which are remarkably close, up to 5,5 mm of displacement. Additionally, it can be inferred that the reason that the second and third groups are separated from one another is due to the localized deformation that occurred in the top brass component, causing an increase in the deformation, which resulted in a lower stiffness being displayed in the curves from the third group.

On the curves made from the experimental data, it is possible to spot some small but abrupt drops in force, which are thought to be a consequence of the loss of adhesion in the connection between the different components of the MMB, that was mentioned earlier. This explains why the curves of the solid elements model and the beam + shell model eventually separate from the experimental data since this phenomenon was not considered in these simulations. The final drop seen in the experimental test data of the top face (detail P, in Figure 6.2 - B), is explained by the complete loss of adhesion between the lower brass component and the rest of the MMB, which was already discussed.

In an initial phase, two of the tested models could correctly depict the deformation of the MMB, while the others were overestimating the MMB's stiffness. Looking at the results of the different numerical analyses and increasing the resultant deformation of the MMB by a factor of 40, after the maximum displacement had been applied, Figure 6.3 can be found portraying the end of the MMB. In that image, it can be seen that on the models that could predict the experimental data, the cross-section of the MMB did not remain in the same plane. Contrarywise, on the models that overestimated the MMB's stiffness, the cross-section remains plane, which is an assumption of both the analytical model and the numerical beam elements model, which are based on the Euler-Bernoulli and the Timoshenko beam theory, respectively.

Therefore, a big problem had arisen, since the thermal break polymers, which are an especially important part of the MMB, have low elastic moduli that do not provide the MMB with enough stiffness for its cross-section to remain in-plane. This was the main reason for the use of the beam + shell elements model on the DLD system model since it is a relatively small sized model, nodes wise, that could account for the longitudinal shear stresses that deform the cross-section.

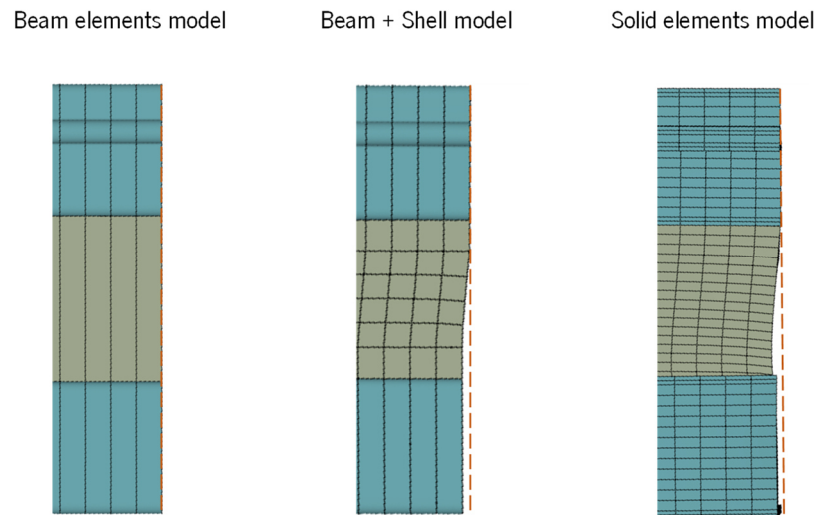


**Figure 6.3.** Deformation at the end of the MMB by a factor of 40 for the numerical models, where the beam elements model is the only one who keeps the cross-section of the MMB in-plane.

On the solid models, from the paths created, the residual deformation could be retrieved, and a comparison with the residual deformation along the length of the beam gathered from the gauge measurements can be seen in Figure 6.4 - A and B, for the bottom and top faces, respectively. In this figure, although the values are have distinct magnitudes, and the data from the gauge measurements is dependent on the face's irregularities, some similarities can be noted, particularly the peak at the top face, resulting from the indentation that was caused by the loading pin (Figure 6.4 - B).

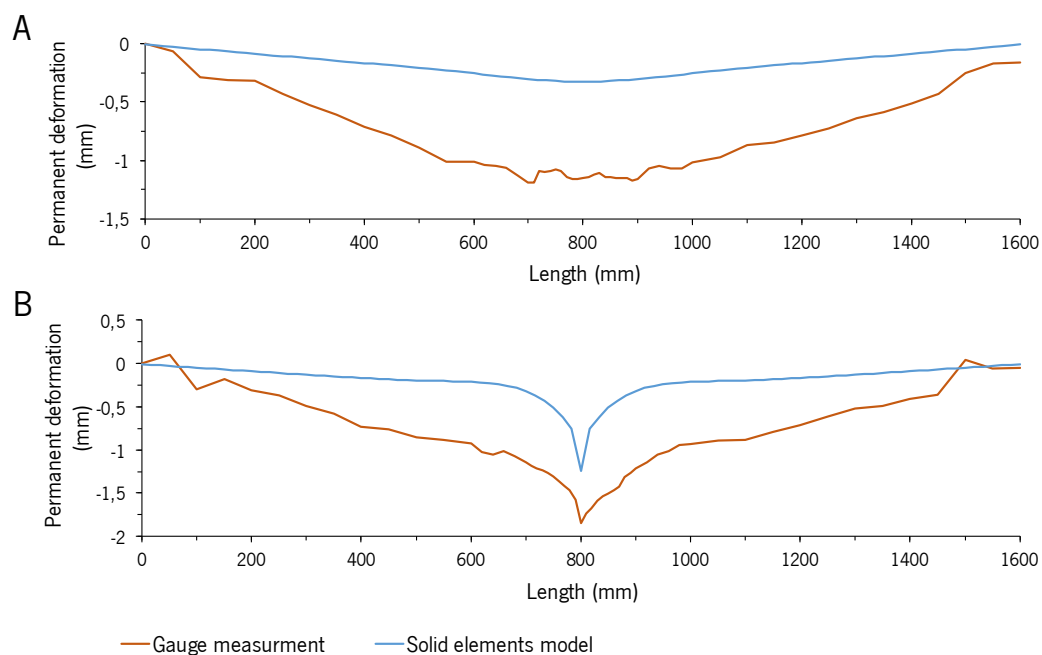


**Figure 6.4.** Residual deformation along the length of the P.2992 brass MMB on the bottom (A) and top (B) faces, from the experimental test and solid elements model.

### 6.1.2 Structural Optimization

The results from the structural optimization simulation, which are depicted in Figure 6.5, showed that the material of the reinforcement is better applied, the furthest from the centroid. This conclusion is coherent with the interpretation taken from beam theory, where along with the material's elastic modulus, the most important parameter to define the bending stiffness of a beam is the second moment of area, which is increased, the further an area of the cross-section is from the neutral plane of the beam. Because the lower cavity is further from the centroid, it is left with more material than the top cavity. It is also possible to observe a greater reduction of material, the further it is located from the clamped surface, which was expected since the internal moments and consequently the stresses due to bending are higher in the clamped end of a beam and decrease along the length of the beam, becoming null at its other end, where the load is applied.

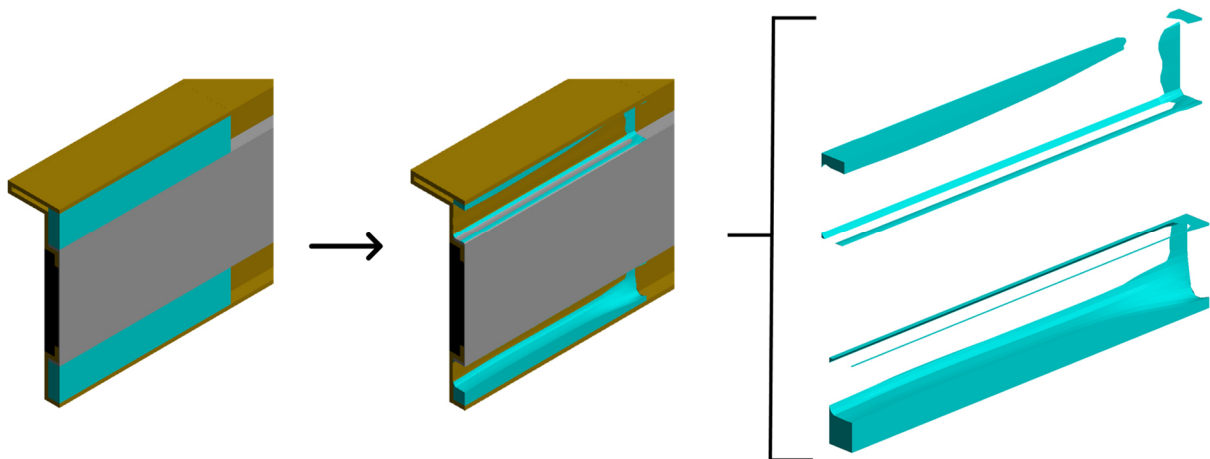


**Figure 6.5.** Results before and after the structural optimization simulation of a 1600 mm brass MMB with the P.2972 profile, where the optimized geometry is in a light blue.

### 6.1.3 Multi-Material Beam Torsion

The results from torsion simulations were not coherent between the models, as can be seen in Figure 6.6. Because no experimental data of a torsional test is available, the solid elements model is taken as the best comparative reference, however, this assumption can be an overestimation since the model doesn't consider the loss of adhesion between the components. In the beam elements model, the resultant torsional stiffness is about 450% that of the reference model and locking at Figure 6.6, it is possible to see that it doesn't appear to be rotating around the same point at which the reference model does. Hence, once again the beam elements model overestimates the stiffness of the MMB, in this case,

by quite a large amount. On the other hand, the beam + shell elements model underestimates the MMB stiffness, presenting only 36% of the stiffness from the reference model, and although the centre of rotation appears to be closer to that of the reference model, it still presents small deviations.

Because the MMBs in the system are subjected to a combination of loads, and since the loads from the standardization tests are either perpendicular or parallel to the glazing, the bending stiffness of the MMBs becomes more meaningful than the torsional stiffness. Moreover, because the beam + shell model, not fully capturing the torsional stiffness of the solid elements model, had a low node count, conservative results in the torsional simulation, and satisfactory results in the bending simulation, it was the MMB model selected for the model of the DLD system.

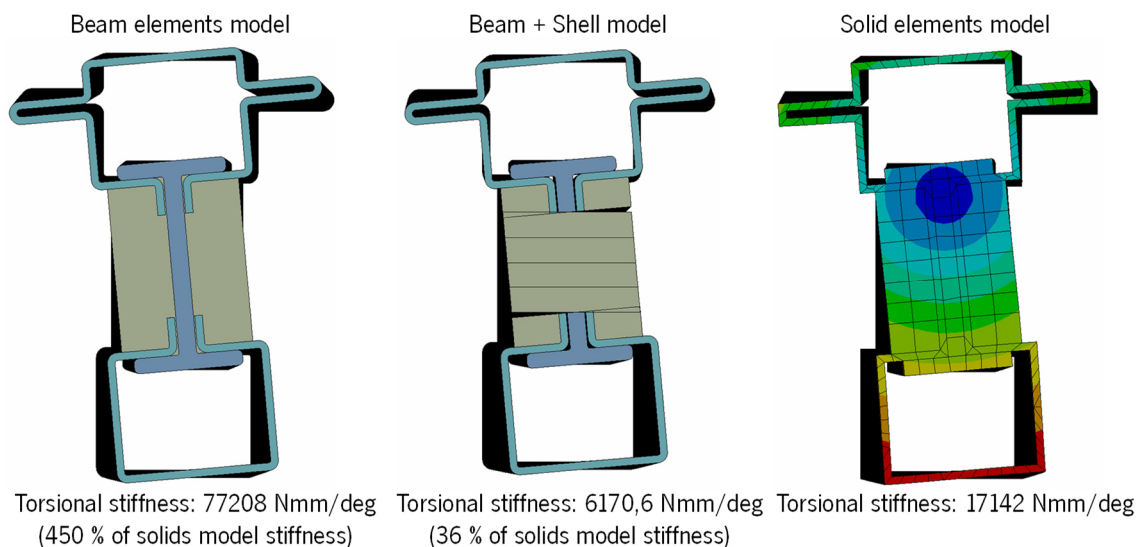


**Figure 6.6.** Torsional stiffness and behaviour from the simulation of a MMB with 1600 mm of length and the P.2992 profile, using the beam elements, beam + shell, and solid elements models.

#### 6.1.4 Multi-Material Beam's Vibration

The results from the experimental modal analysis of the physical MMB can be found in the FRF plotted in Figure 6.7, where three significant peaks can be identified. Curiously, the second peak appears to be a combination of two peaks, which could mean that the discretization (1,6 Hz) was not enough to capture the true magnitude of the peak, or that the peak is the result of two mode shapes with close resonance frequencies. Additionally, using the half-power bandwidth method applied on the first peak, a damping ratio of 0,0135 was determined.

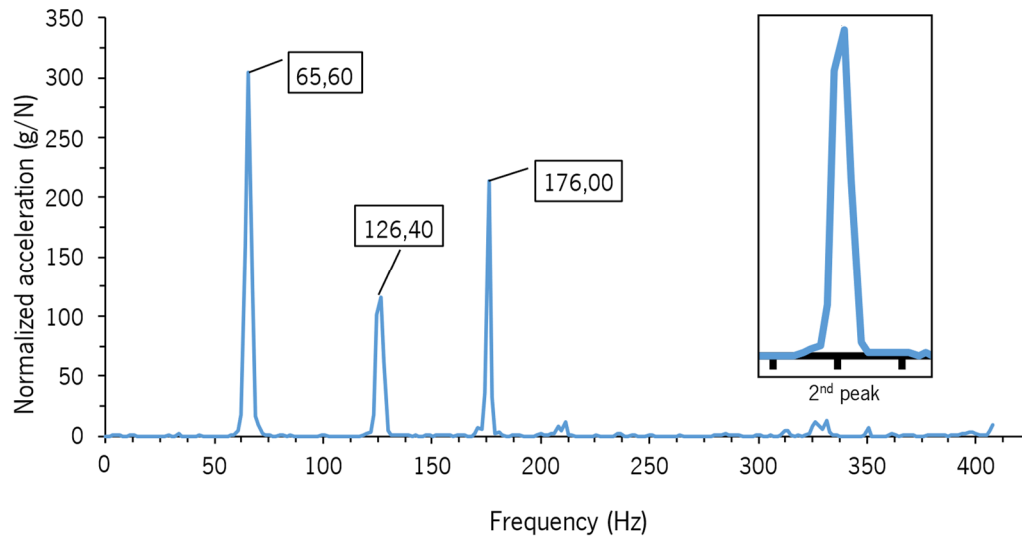


**Figure 6.7.** FRF from the experimental modal analysis of a 1600 mm brass MMB with the P.2992 profile, with the frequencies of the peaks displayed next to them.

Table 6.1 shows a comparison of the natural and resonant (with damping) frequencies, from the analytical and different numerical models to the ones from the experimental data. Considering the results in Table 6.1, the first observation is that the introduction of damping has little influence on the frequency values, but still causes a slight reduction, as would be expected. The first resonance frequency is relatively close to the experimental value on all models, with the error being around 3%, except for the beam + shell model, where it surpasses 5%. On the second resonance frequency, contrary to what had happened in the three-point bending analysis, the analytical and beam elements models gave results closer to the experimental data, and the beam + shell and solid elements models presented results with much lower values, reaching a deviation of almost -10% from the experimental value, for the solid elements model. From the results of the third resonance frequency, similar observations to those from the first resonance frequency results could be made, with the small difference that the analytical and beam elements models agree even better with the experimental data, the solid elements model's error slightly increases and the beam + shell model error has a larger increase, up to almost 8%.

**Table 6.1.** Comparison of the natural and resonant frequencies of a 1600 mm brass MMB with the P.2992 profile, between the results from the analytical and different numerical models, and from the experimental modal analysis.

	Natural frequencies with bending mode shapes	Numerical						Analytical	
		Beam (Hz)	Error	Shell + Beam (Hz)	Error	Solids (Hz)	Error	(Hz)	Error
Undamped	1 <sup>st</sup>	63,50	-3,20%	62,14	-5,28%	64,00	-2,45%	63,79	-2,76%
	2 <sup>nd</sup>	124,66	-1,38%	115,88	-8,32%	114,18	-9,64%	126,28	-0,09%
	3 <sup>rd</sup>	174,00	-1,14%	162,33	-7,77%	171,35	-2,68%	175,84	-0,09%
Damped	1 <sup>st</sup>	63,49	-3,21%	62,13	-5,29%	63,99	-2,46%	-	-
	2 <sup>nd</sup>	124,62	-1,41%	115,85	-8,35%	114,18	-9,67%	-	-
	3 <sup>rd</sup>	173,89	-1,20%	162,24	-7,82%	171,19	-2,73%	-	-

Note: The relative error is found in comparison with the 1<sup>st</sup>, 2<sup>nd</sup>, and 3<sup>rd</sup> resonant frequencies from the experimental test.

The fact that the analytical and beam elements models better represent the dynamic behaviour of the MMB suggests that the MMB's section remained in-plane during the experimental analysis, which as was seen in the three-point bending analysis, is the main factor differentiating between the stiffness between these two models, and the other two numerical models, i.e., beam + shell and the solid elements models. Hence there is a clear distinction between the static elastic modulus and the dynamic elastic modulus of the polymeric materials.

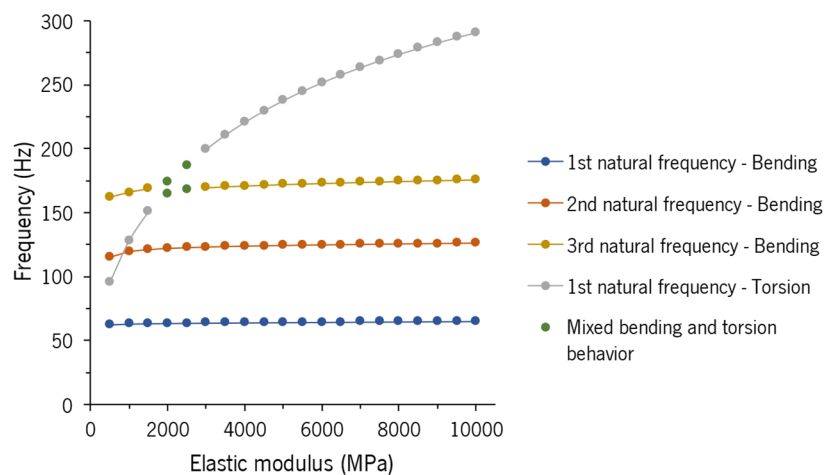
For traditional materials like steel, the elastic modulus is assumed as a constant, however, in the case of polymers, it has been experimentally proved that the value of this property when determined by static and by dynamic methods, varies considerably, due to the viscoelastic behaviour of these materials, which make them dependent on the strain rate, and temperature, and exhibiting hysteresis under cyclic load, dissipating a good amount of energy [91]–[93].

Considering the equation of the natural frequency of a single DOF system (equation 6-1) as reference, it can be seen that this increase in stiffness can explain why the natural frequency is higher in the physical MMB than in the models where the loss of stiffness due to the cross-section of the MMB not remaining in-plane can be captured, since not maintaining the MMB's cross-section in-plane result in a decrease in stiffness, and consequently in a lower natural frequency [40].



$$\omega_n = \sqrt{\frac{k}{m}} \quad 6-1$$

One way to test this hypothesis is by increasing the elastic modulus of the polymeric parts in the beam + shell model, causing the cross-section of the MMB to remain in-plane. Therefore, testing the polymeric elastic moduli from the supplier, introduced in Table 2.2, the first three natural frequencies correspondent to bending mode shapes are obtained with values of 63,44 Hz (-3,29%), 123,62 Hz (-2,2%), and 168,91 Hz (-4,03%) that are closer to the results found in the experimental data, which is the reason why these elastic moduli were used in the dynamic analyses of the DLD system. The increase in the elastic moduli have also an influence on the torsional mode shapes that appeared on this model as the second mode of vibration, as can be seen in Figure 6.8, where a study of the natural frequency of this mode shape is exhibited, considering the same elastic modulus for the two polymers, and parameterizing this value.

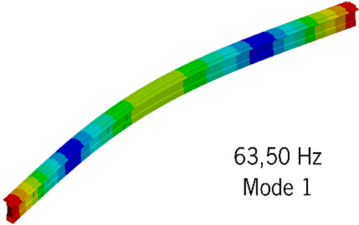
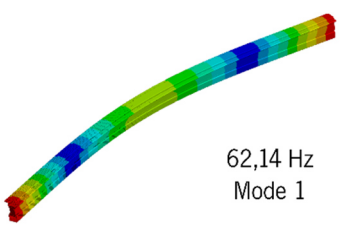
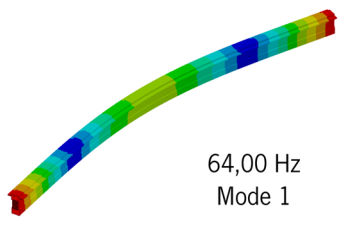
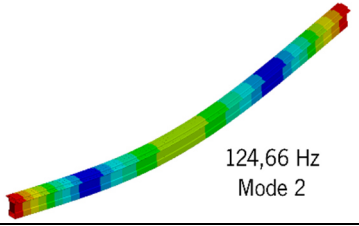
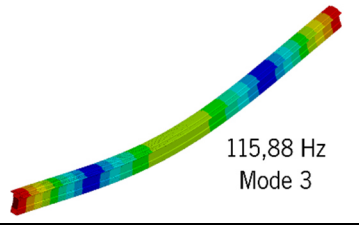
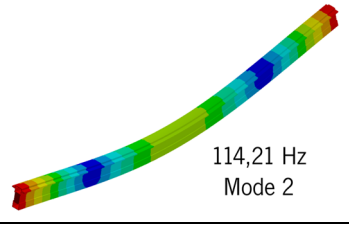
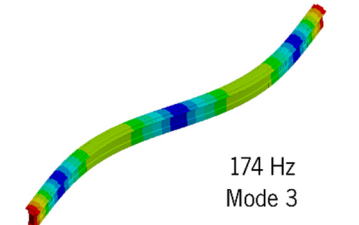
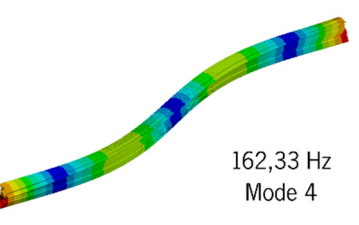
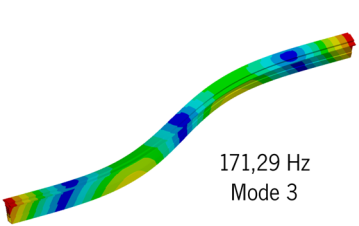
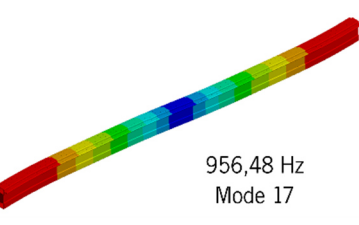
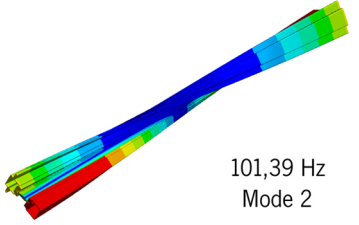
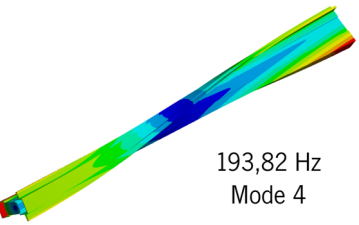
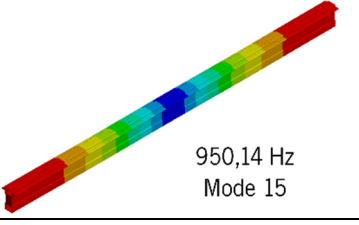
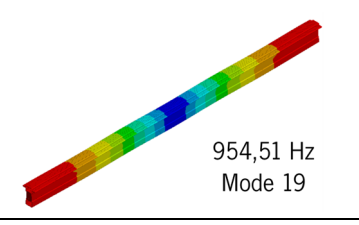
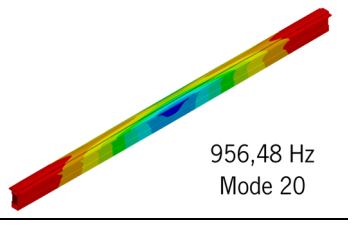


**Figure 6.8.** Study of the natural frequency of the torsional mode shape of a 1600 mm P.2992 brass MMB, considering the same elastic modulus for the two polymers, and parameterizing this value. The values of the first three natural frequencies with bending mode shapes are also depicted in this image.

The modes from the different models can be viewed in Table 6.2, where it can be seen the torsional mode that steps to the second place in the beam + shell model. It is also possible to note that the torsional mode in the beam elements model doesn't appear to be twisting. This is because rotation using beam elements with a "Pre-integrated" cross-section instead of "Mesh", makes the beam have a weird behaviour where instead of twisting, it moves to the side, which was briefly mentioned in Chapter

5. Nevertheless, using this type of cross-section, presented better results, as they were closer to the experimental data.

**Table 6.2.** 1<sup>st</sup>, 2<sup>nd</sup>, and 3<sup>rd</sup> bending, 1<sup>st</sup> torsional, and 1<sup>st</sup> longitudinal mode shapes, resultant from the modal analyses of a P.2992 brass MMB with 1600 mm of length using the beam elements, beam + shell, and solid elements models.

Mode	Beam elements model	Beam + Shell model	Solid elements model
1 <sup>st</sup> Bending	 63,50 Hz Mode 1	 62,14 Hz Mode 1	 64,00 Hz Mode 1
2 <sup>nd</sup> Bending	 124,66 Hz Mode 2	 115,88 Hz Mode 3	 114,21 Hz Mode 2
3 <sup>rd</sup> Bending	 174 Hz Mode 3	 162,33 Hz Mode 4	 171,29 Hz Mode 3
1 <sup>st</sup> Torsional	 956,48 Hz Mode 17	 101,39 Hz Mode 2	 193,82 Hz Mode 4
1 <sup>st</sup> Longitudinal	 950,14 Hz Mode 15	 954,51 Hz Mode 19	 956,48 Hz Mode 20

The order in which the torsional and longitudinal mode shapes appear is very distinct, and in the case of the torsional mode shapes, their correspondent natural frequencies are also very distinct, as opposed to what happens in the longitudinal natural frequencies, which are extremely close. This means that there is some confidence in the value of the longitudinal natural frequencies obtained since the

models validate each other, but there is no way to know with certainty the value of the torsional natural frequency since the models disagree, and it doesn't appear in the FRF from the experimental modal analysis of the MMB. However, there is the possibility the solid elements model is the most accurate, as it can capture deformations from the physical MMB, that the other models can't, but there are other possibilities, like the peculiar shape of the second peak, which could be hiding a second resonance frequency, in which case the value from beam + elements model would be the closest to the experimental data.

The fact that the analytical and the beam elements model first three resonance frequencies with bending mode shapes agree with experimental results, puts some trust in these models. Nevertheless, the tested MMB had a symmetric profile, and so, the question if the vibration behaviour of the MMBs with unsymmetric profiles, could be captured by these models remained. The results in Table 6.3 show agreement under 1,5% between the two models for MMBs with unsymmetric profiles, which, in the absence of experimental data, give some assurance in the results.

**Table 6.3.** Comparison of the 1<sup>st</sup> natural frequencies with bending and longitudinal mode shapes between the analytical and the beam elements models, of 1600 mm brass MMBs with all the OS2 75 profiles.

MMB profile	Bending – Minor principal axis			Bending – Major principal axis			Longitudinal		
	Analytical (Hz)	Numerical (Hz)	Error	Analytical (Hz)	Numerical (Hz)	Error	Analytical (Hz)	Numerical (Hz)	Error
P.2901	32,63	32,60	-0,08%	121,46	120,10	-1,12%	990,25	990,30	0,01%
P.2915	42,78	42,73	-0,13%	133,62	131,90	-1,29%	1010,15	1010,20	≈0%
P.2942	42,18	42,12	-0,13%	117,22	116,00	-1,04%	1001,16	1001,20	≈0%
P.2943	32,56	32,53	-0,08%	138,36	136,44	-1,39%	998,15	998,17	≈0%
P.2961	32,69	32,67	-0,08%	124,49	123,02	-1,18%	985,73	985,79	0,01%
P.2962	43,00	42,94	-0,14%	119,85	118,54	-1,09%	997,63	997,68	≈0%
P.2963	34,75	34,72	-0,09%	139,67	137,69	-1,41%	998,04	998,06	≈0%
P.2965	43,56	43,50	-0,14%	136,10	134,28	-1,34%	1007,34	1007,40	0,01%
P.2971	27,51	27,50	-0,06%	115,25	114,08	-1,01%	963,48	963,50	≈0%
P.2972	39,89	39,84	-0,12%	114,71	113,57	-0,99%	981,36	981,38	≈0%
P.2991	54,82	54,69	-0,24%	126,13	124,58	-1,23%	943,05	943,06	≈0%
P.2992	63,79	63,50	-0,45%	126,28	124,66	-1,28%	954,43	950,14	-0,45%
P.2995	67,27	67,03	-0,35%	131,35	129,65	-1,29%	964,13	964,14	≈0%

## 6.2 Door System

### 6.2.1 Resistance to Wind Loads

Towards a better understanding of the results gathered from the internal reinforcements, it is advantageous to look at the stress distribution of the metal components of the frame structure. This stress distribution can be found in Figure 6.9, for the unreinforced brass door system, where the locations that are under a higher effort in the frame structure are depicted, and their agreement with the locations chosen for the reinforcements that were introduced in Chapter 5 verified. Detail A shows that the stress reaches its highest value on the lower additional locking point that joins the two leaves, and another high stress spot can be seen in the most elevated additional locking point in the centre. On the connections from the secondary leaf to the fixed frame, in the centre of the system, a rise in stress can also be spotted in the fixed frame, as depicted in detail A.

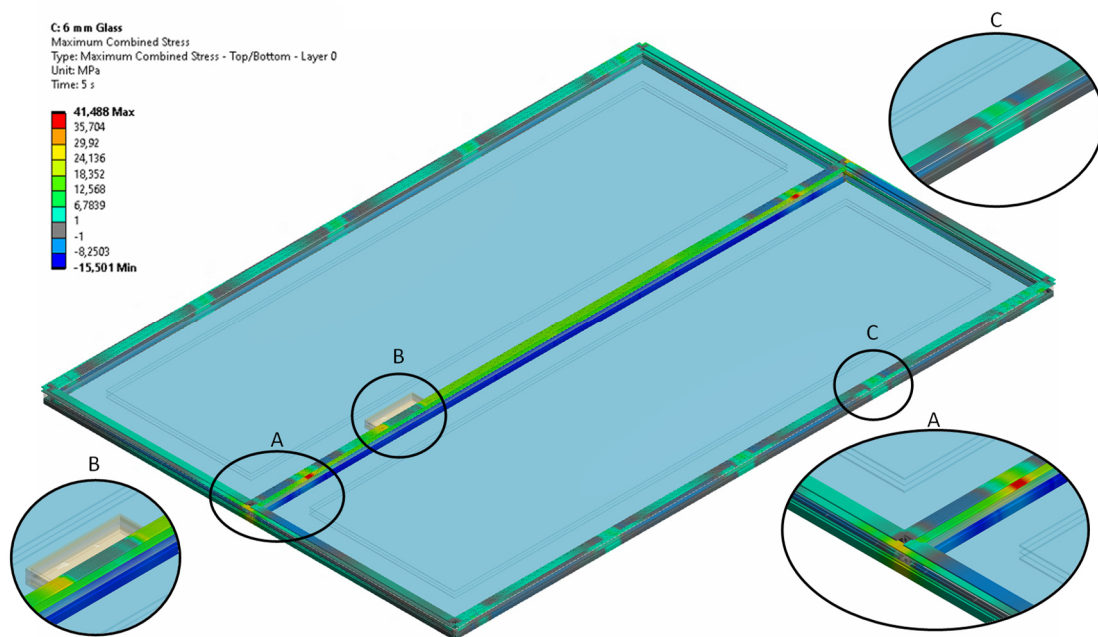


**Figure 6.9.** Stress on the beam elements from the resistance to the wind loads test simulation of the unreinforced brass DLD system.

Detail B shows the effect of the rigidity introduced in the lock, as the stresses drop in this region, and around the hinges, a rise in stress is made evident by detail C. The maximum stress displayed is around 41,5 MPa, however, it is in the stainless steel DLD system where the stress on the frames is the highest, reaching 59,6 MPa, which is still distant to cause yielding on the frame. However, it is important

to keep in mind that this model cannot account for the localized stresses and deformations, that in a real test could arise on the hardware or the section of the beam elements, like indentations, and that the main purpose of this model is to evaluate the stiffness of the system. From Figure 6.9, it becomes clear that the central region of the frame structure should be the main region of reinforcement, as it is the most stressed area. In addition, the stress in the glass panels of the unreinforced models, resulting from the larger model, is the highest in the brass DLD system, reaching around 28,4 MPa, which even adding the errors from the mesh independence study (Annex C), is far from the tensile strength of glass (120 MPa)

Turning the attention to the charts in Figure 6.10, more specifically chart A, referent to the system with the brass metal frame, it becomes apparent that there is a decrease in the deformation of the system, as the elastic modulus of the reinforcement increases. The density of the reinforcement proved to be irrelevant in the results from these simulations, and realistically, materials with an elastic modulus higher than steel ( $\approx 200$  GPa) are more expensive (see Annex D). Hence, steel is taken as the reference reinforcement material, even though other materials with smaller densities would reduce the loads on the hinges. The variation of the location of the reinforcement followed very close results, so the reinforcement at the middle is the more appellative since it would put less weight on the hinges. The difference in results between the simulation with the optimized and the complete reinforcement's cross-sections is also very apparent, as when using steel reinforcements, the first has roughly a 5% increase in stiffness, and the latter surpasses a 15% increase, as is depicted in Figure 6.10. From these results a complete reinforcement placed only at the centre of the system seems to be the most viable option, as the stiffness of the system to wind loads is maximized, and the weight of the reinforcement is kept at a minimum, which keeps the increase of load at the hinges also at a minimum.

Although with different magnitudes, similar results are found for the models of the systems with other base materials, which are depicted in graphs C and D, for the corten steel frame, and E and F, for the galvanized steel frame in Figure 6.10, and in the graphs G and H for the stainless steel frame in Figure 6.11. These charts make it noticeable that the increase in stiffness due to the presence of the reinforcement diminishes as the elastic modulus of the frame's base metal increases, due to the concavity of the relative increase in stiffness curves. Furthermore, the introduction of the reinforcement has a better effect when the system has brass as the base metal of the frame structure than when it has stainless steel, thus, the higher the elastic modulus of the base metal of the frame structure, the lower the effect from the internal reinforcement.

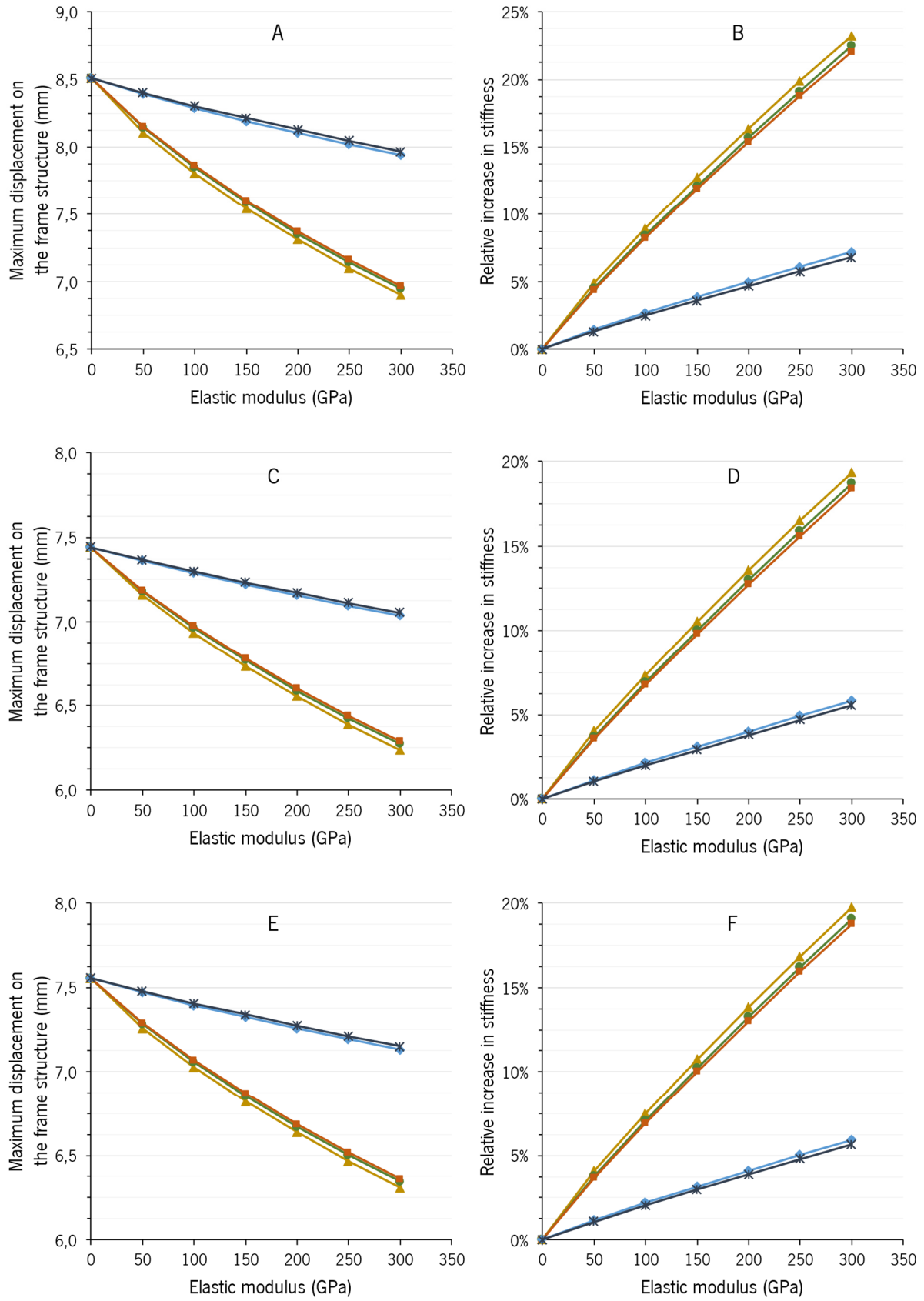


**Figure 6.10.** Maximum displacement on the frame structure and relative increase in stiffness against the elastic modulus of the reinforcement for the brass (A and B), corten steel (C and D), and galvanized steel (E and F) DLD systems, from the wind loads test simulations. Charts continue in Figure 6.11, where the legend is presented.

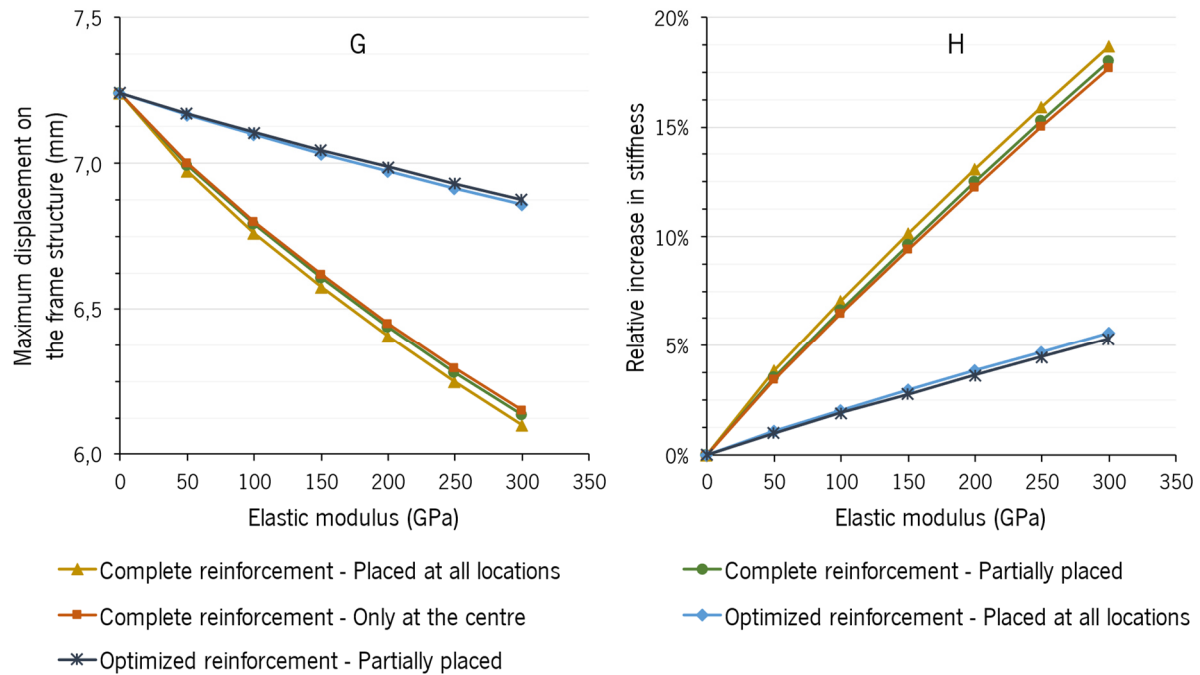


**Figure 6.11.** Maximum displacement on the frame structure (G) and relative increase in stiffness (H) against the elastic modulus of the reinforcement for the stainless steel DLD system, from the wind loads test simulations.

Figure 6.12 shows the charts with the results from the changes in the thickness of the outer glass panels. Figure 6.12 - A, shows that the drop in displacement with the increase in thickness of the outer glass panels is steeper in the brass system, compared to the other systems, and in Figure 6.12 - B, it is perceptible that the increase in the stiffness of the outer glass panels is more effective in the models of the system whose elastic modulus of the base metal is smaller, similar to what happened with the introduction of the internal reinforcement. It is also possible to, from Figure 6.12 - B, that by using 7 mm instead of 6 mm in the outer glass panels, the results get closer to those of a complete steel reinforcement in the centre, and using 8 mm in the outer glass panels, this increase duplicates, surpassing 30% in all metals, and even surpassing 35% in the case of the brass system.

Additionally, on the curves in chart B, a small convexity can be observed, which means that a further increase in the outer glass thickness could produce even better results, due to the slope at that point being higher.

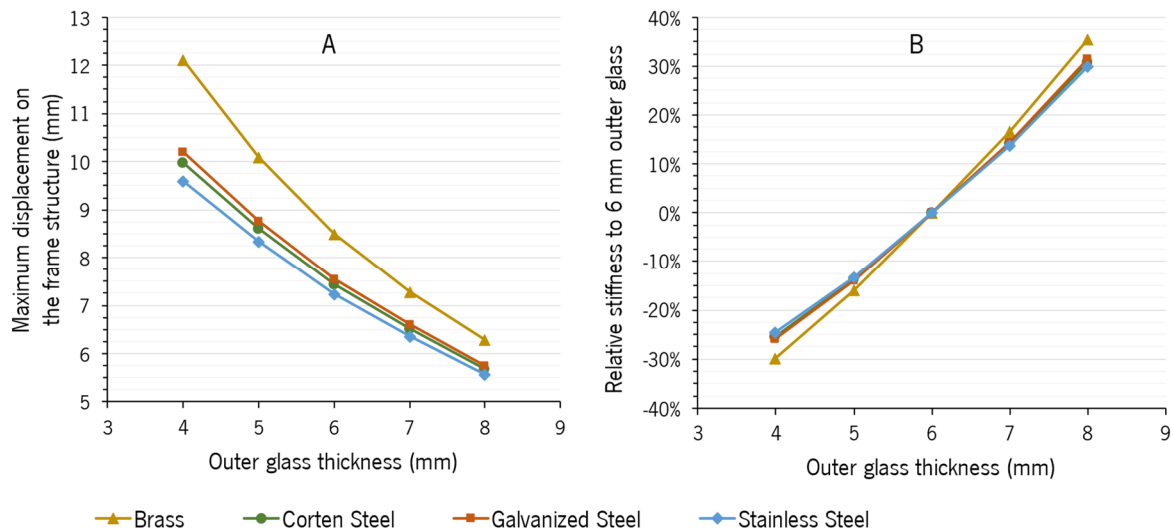


**Figure 6.12.** Maximum displacement on the frame structure (A) and relative increase in stiffness against (B) the outer glass panels thickness for the brass, corten steel, galvanized steel, and stainless steel DLD systems, from the wind loads test simulations.

However, increasing the thickness of the outer glass panels comes at a cost, since for each millimetre added, 10 kg of glass are added to each leaf, whereas using a complete steel reinforcement on the centre of the system, only 0,61kg are added per bar. This can have an influence on the forces that the hardware must endure, for instance, using 8 mm instead of 6 mm in the outer glass panels, the vertical force on the top hinge of the primary leaf varies from 286,5 N to 334,3 N, which is roughly a 17% increase. The selected hinges are assured by the supplier to withstand 100 kg each, which would give a large room for adding weight, but since other loads and moments are at play, simulation of the hardware under the loads that can be found probing the joints of the model of the system would be advantageous, though it is not covered in this work.

Simulating the DLD System with 8 mm outer glass panels and complete reinforcements located at the centre with 200 GPa, the results give an increase in stiffness of 49%, 42%, 43%, and 41%, for the brass, corten steel, galvanized steel, and stainless steel base metals. It is important to understand that because the reinforcement in the simulations is bonded to the other frame components, the assumption is that in the real system it is not loose inside the frame, but instead, it is connected to the rest of the frame, either through a very strong glue, a screwed connection, or another method, that doesn't let the reinforcement slide inside the frame.

Lastly, the maximum displacement of the physical DLD system used in the classification is registered as 13 mm, due to the negative pressure, which caused the largest displacement. This system



had frames with MMBs of the OS2 65 series, which have less strength and stiffness to bending than the OS2 75 series used in the studied DLD system. Additionally, the system from the classification had a double glazing with two laminated glass panels, which along with the type of MMB used, can justify the worse performance, when compared to the values from the system numerically studied, despite the dimensions on the latter being 25% larger.

## 6.2.2 Resistance to Static Torsion

Dealing with the static torsion of the leaves and considering Figure 6.13, details A and C, it can be seen that the higher stresses on the metal of the frames appear at the top and bottom hinges, although in the lower MMBs of the leaves a stress above average can also be spotted. The maximum stress from Figure 6.13 comes from a model with brass as the base metal, but the stress value can go up to 40,4 MPa with stainless steel as the base metal.

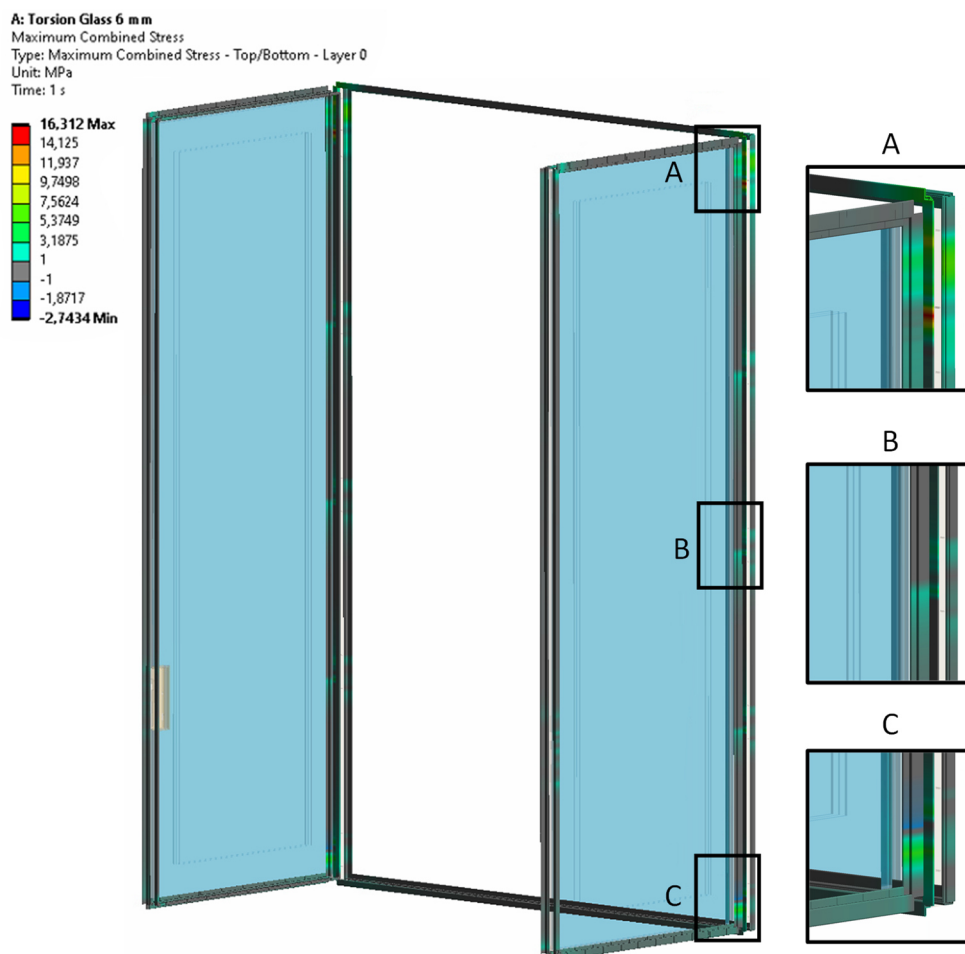


**Figure 6.13.** Stress on the beam elements from the resistance to static torsion test simulation of the unreinforced brass DLD system.

The highest stress at the hinges occurs in the fixed frame, and because the maximum stress on a stainless steel model increases by 26% with the use of 8 mm outer glass panels on the glazing, the weight of the leaves has a very strong contribution on the stress, which ultimately is an indicator that the test doesn't demand a lot of effort from the frame structure. The stress in the glass panels also remains far from the tensile strength, where the maximum value of the unreinforced models occurs on the stainless steel DLD system, reaching 18,8 MPa.

The outcome of using internal reinforcements can be seen in Figure 6.14 - A and B for the maximum displacement and stiffness increase on the primary leaf, and in Figure 6.14 - C and D for the same parameters on the secondary leaf, in that order. The results are similar between the two leaves, with the displacement values on the primary leaf being slightly higher than those of the secondary leaf, which can be speculated to be linked to the irregularities in the geometry of the glazing caused by the lock.

Considering charts B and D, it becomes apparent that the smaller the elastic modulus of the base metal, the larger the effect of the reinforcements. However, the increase in stiffness due to the internal reinforcement is generally small, as the maximum value doesn't reach the 3% mark, using a material with an elastic modulus of 300 GPa. But the increase is particularly small when the internal reinforcements is placed at the centre, which agrees with the stress distribution presented in Figure 6.13, where the central region of the system is not very stressed, especially when compared with the stresses of the frame located at the hinges (Figure 6.13 - details A, B, and C).

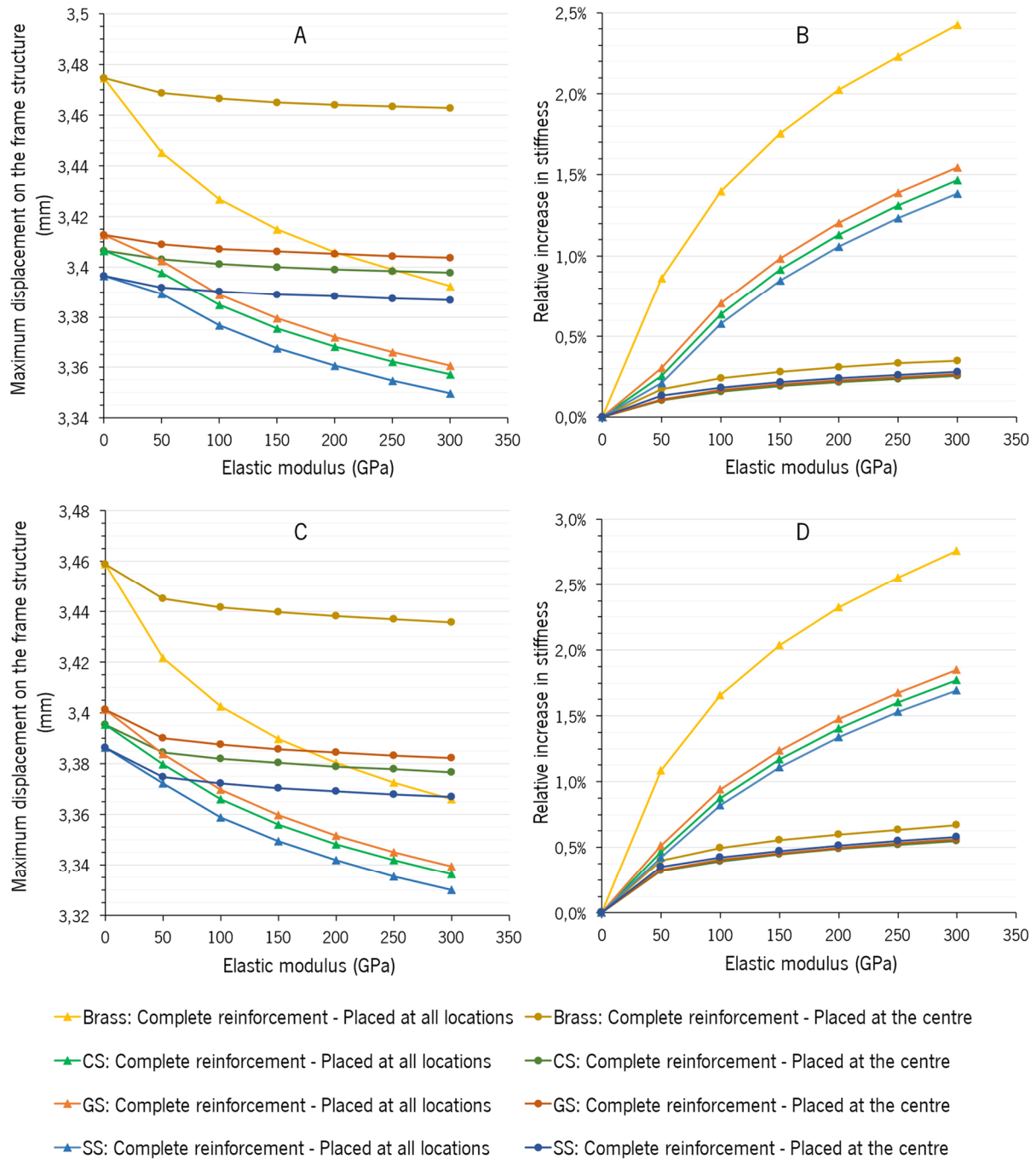


**Figure 6.14.** Maximum displacement on the frame structure and relative increase in stiffness against the elastic modulus of the reinforcement for the brass, corten steel (CS), galvanized steel (GS), and stainless steel (SS) DLD systems in the primary (A and B) and secondary (C and D) leaves, from the static torsion test simulations.

The results gathered from varying the thickness of the outer glass are very identical between the models of the system with different frame base metals, as the resultant curves from Figure 6.15 almost overlap. In Figure 6.15, charts A and B refer to the primary leaf and charts C and D refer to the secondary leaf, although there is very little distinction between the results from the two leaves. The gain in stiffness from increasing the thickness of the glass panels in this test is much larger than the gain from the wind

pressure test, as with a 1 mm increase on each outer panel of the glazing, a 20% increase in stiffness is achieved, and with 8 mm outer glass panels, a 40% increase from the original stiffness is obtained. Moreover, by decreasing the thickness of the outer glass panels, a decrease of roughly the same percentual values (although slightly lower) could be expected, and similarly to the previous test, although not as evident, charts B and C display some convexity.

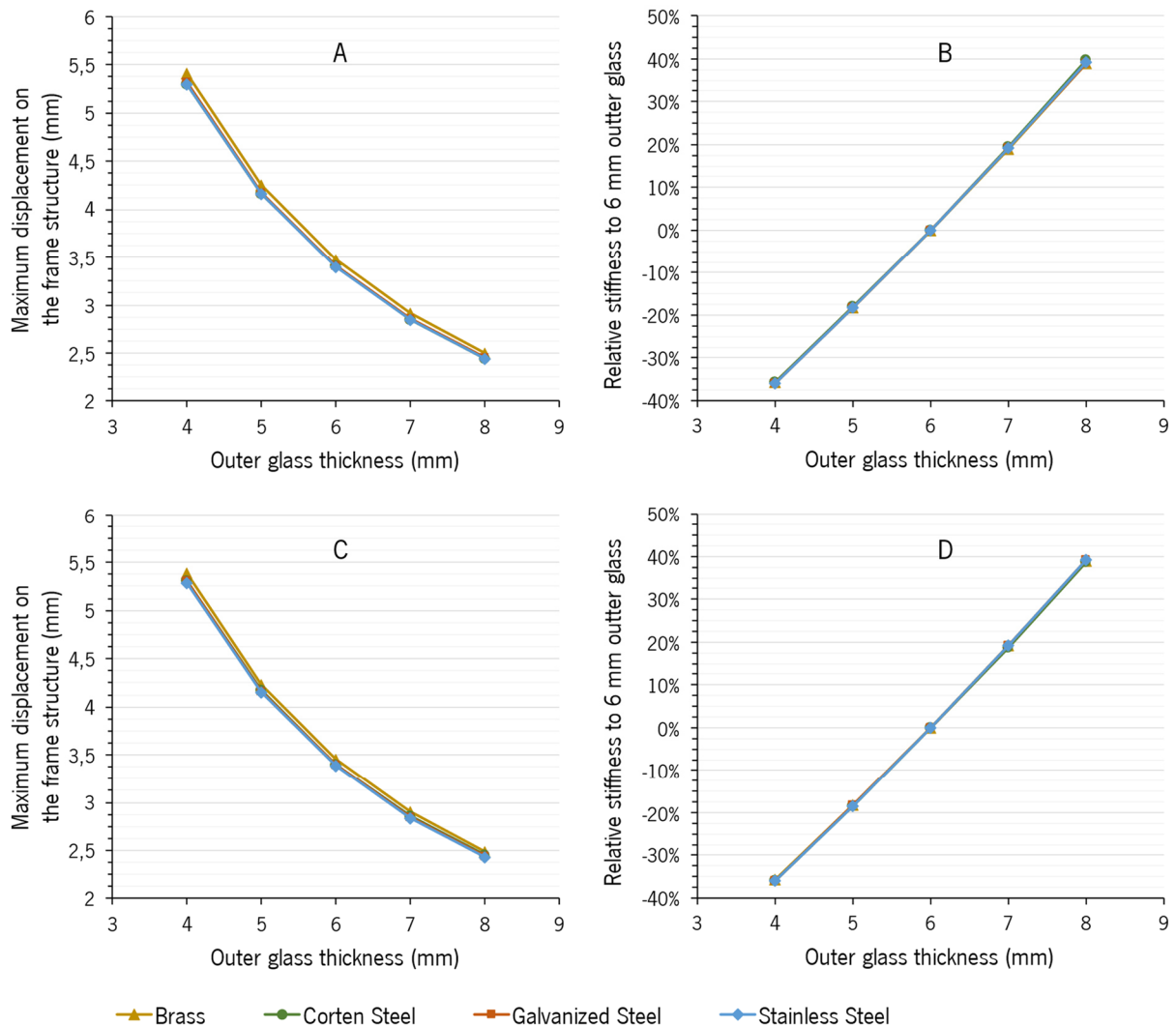


**Figure 6.15.** Maximum displacement on the frame structure and relative increase in stiffness against the outer glass panels thickness for the brass, corten steel, galvanized steel, and stainless steel DLD systems in the primary (A and B) and secondary (C and D) leaves, from the resistance to static torsion test simulations.

Because the relevance of the base metal of the frame is evidently small, in the results from Figure 6.15, and the introduction of internal reinforcements has little effect, as determined by looking at Figure 6.14, it is possible to conclude that the glazing is the main source of resistance to the deformation by the

torsion on the leaf, and consequently, it is where enhancements should be made to improve the capacity of the system to the static torsion of the leaves.

As previously mentioned, the physical evaluation of this test is made from the residual deformation of the leaves, measured by the gauge. On the OS2 65 DLD system of which the class was achieved, a maximum deformation of 99,6 and 56,6 mm is registered for the primary and secondary leaves, respectively, that left a residual deformation of 46,1 and 1,5 mm, in that order.

Even though they are different systems, the numerical test of the studied DLD system's stiffness allows for the direct comparison with the maximum displacement values from the physical system used in the classification, and the values from the classification reports are far from those determined by the simulation and expressed in Figure 6.14 and Figure 6.15. Since the same load was applied in the experimental test and the simulations, despite the DLD system model representing a much more robust system than the OS2 65 DLD system, with superior glazing and frames, there is some incoherence between the two sets of results.

A hypothesis for this to happen is that the components of the frame structure of the leaf could have lost their bond, dropping the stiffness of the overall system to static torsion, and when the load was removed, the friction on the interface of these components did not allow for a full elastic return, explaining the residual deformation. Because a double glazing with laminated glass was used in the test of the physical system, the resistance from the glazing to the deformation of the leaf is also smaller, than that of the simulation' system, partly because the panels are closer together, and partly because the polymeric layer between the glass plies can't keep the section of the laminated glass panels in-plane, similar to what happened in the three-point bending experiment of the P.2992 brass MMB [94]. However, to make definitive conclusions, a detailed report or the observation of the test would be necessary, as there is also the possibility, that plastic deformation occurred on the components of the physical system.

### **6.2.3 Resistance to Vertical Loads**

In the vertical loads test simulations, in the frame structure, the stresses are higher around the hinges (details A, B, and C, in Figure 6.16), even more so in the bottom hinge. The stresses on the frame structure of the unreinforced models are low, and far from yielding, being higher on the stainless steel DLD system, where they reach 12,6 MPa. On the glass panels, the stresses also exhibit a small value, and the highest value of all the unreinforced base metal models occurs in the brass DLD system, reaching 11,7 MPa, far from the tensile strength of glass.

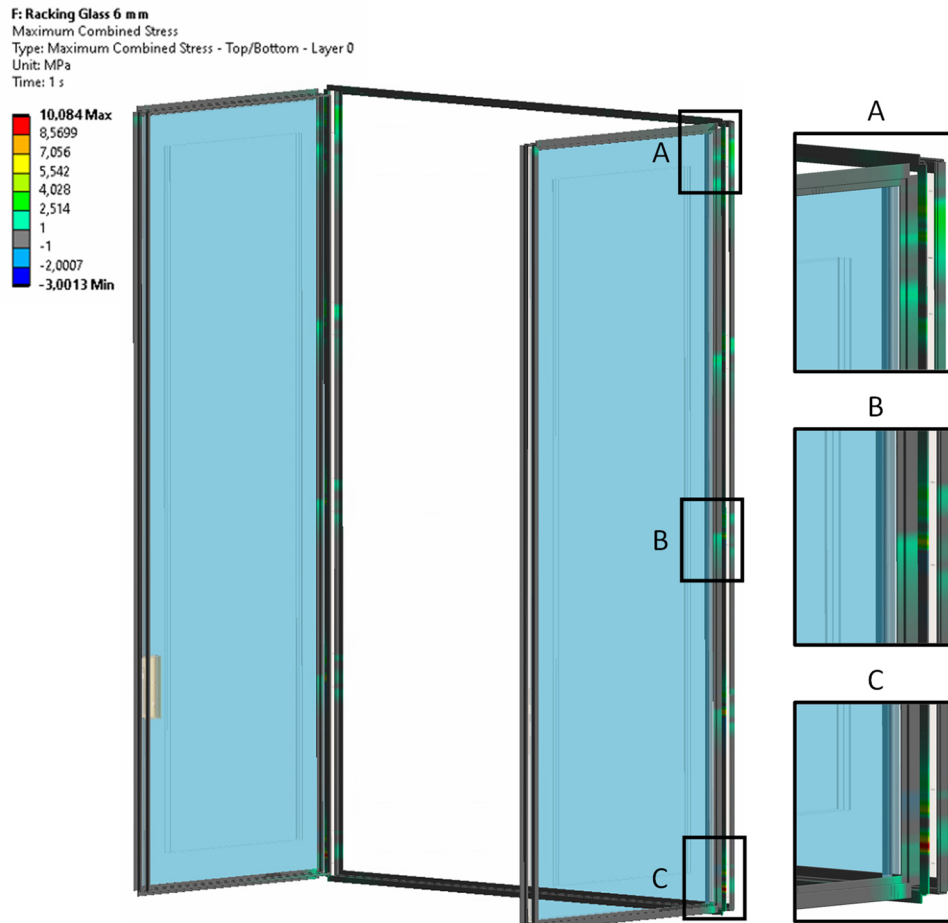


**Figure 6.16.** Stress on the beam elements from the resistance to vertical loads test simulation of the unreinforced brass DLD system.

Figure 6.17 depicts the displacements and relative stiffness changes recorded for the two different configurations of reinforcements that were tested. With the reinforcements only at the centre, a small decrease in stiffness (around 3% for steel) could be expected, opposing to the results from the reinforcement placed at all locations, where a gain of over 9,4% for a steel was registered. With the reinforcement placed at all locations, it can be seen an increase in the effect of the reinforcement with the increase of the elastic modulus of the base metal of the system. For all reinforcements, it is possible to observe that the values are exceptionally close between the two leaves.

The use of an internal reinforcement only at the centre worsens the results in comparison to the unreinforced system, which indicates that although the weight of the interior reinforcements doesn't cause a significant decrease in stiffness of the system (see Annex C), the increase of stiffness on the centre edges of the leaves could cause bigger displacements to occur, which is backed by the decrease of stiffness with the increase of the elastic modulus of the reinforcements (Figure 6.17 – B and D).

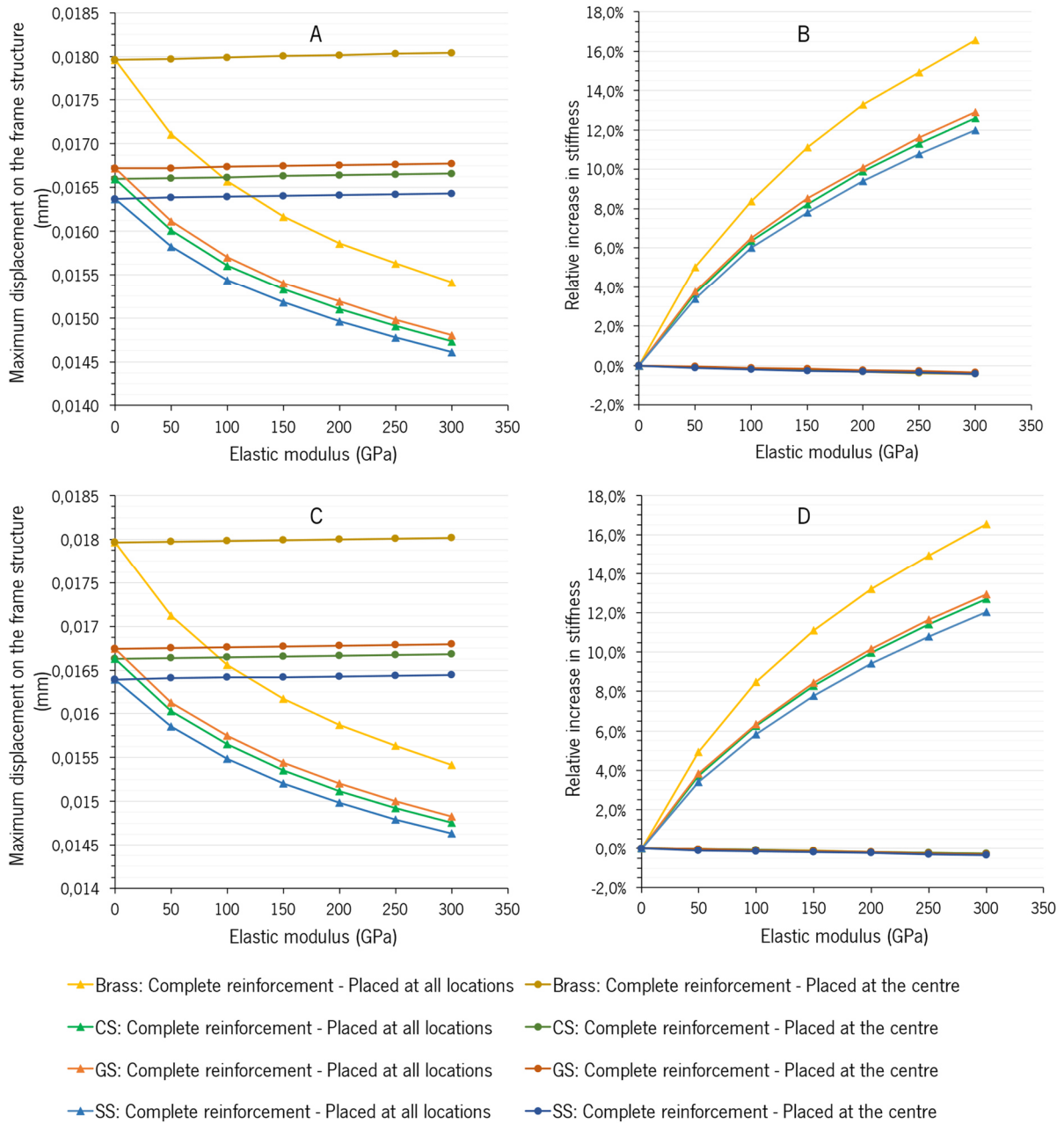


**Figure 6.17.** Maximum displacement on the frame structure and relative increase in stiffness against the elastic modulus of the reinforcement for the brass, corten steel (CS), galvanized steel (GS), and stainless steel (SS) DLD systems in the primary (A and B) and secondary (C and D) leaves, from the vertical loads test simulations.

In Figure 6.18 - A and C, it is possible to observe the proximity between the displacements on the primary and secondary leaves, respectively. These charts, also show a distinction between the results of the systems with the different base metals of the frame structure. The increase in the thickness of the glass panels has a much smaller effect when compared to the results of the previous tests, reaching only around a 4% increase with the maximum glass thickness tested, as can be seen in charts B and D. Unlike the previous tests, the curves from these two charts are concavely shaped, meaning that further increases

in the thickness of the outer glass panels cannot be expected to produce the same effect. The relative increase in stiffness, between the models of the system with frames of different metals, is similar, as can be seen by the almost overlap of the curves from charts B and D, or even by looking at the almost constant difference kept between the results of the different frame metals for each thickness in charts A and C.

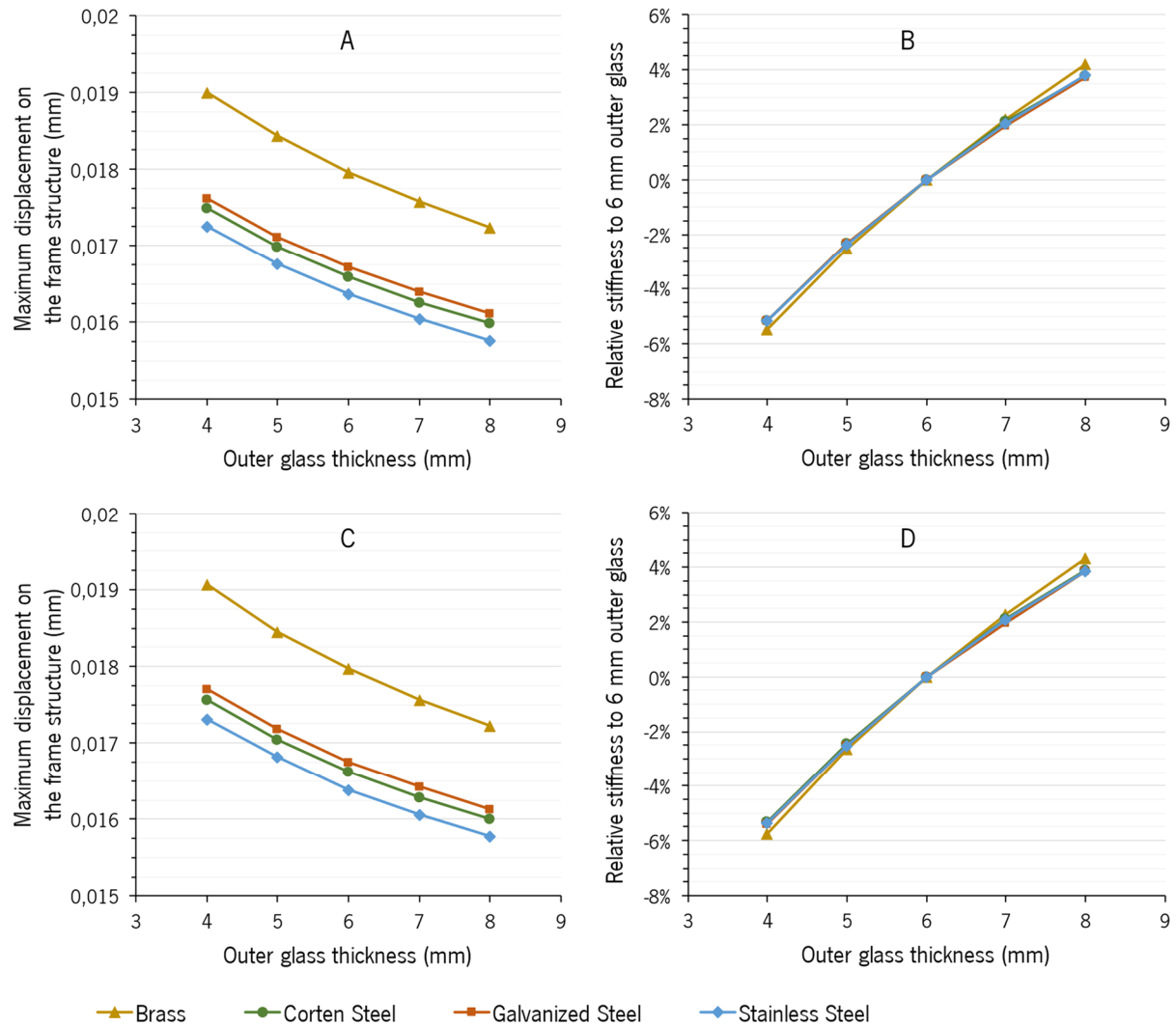


**Figure 6.18.** Maximum displacement on the frame structure and relative increase in stiffness against the outer glass panels thickness for the brass, corten steel, galvanized steel, and stainless steel DLD systems in the primary (A and B) and secondary (C and D) leaves, from the resistance to vertical loads test simulations.

Overall, the use of the complete internal reinforcements in all locations was the most advantageous type of reinforcement on this test, as the increase in thickness of the outer glass panels of the glazing, didn't prove to be nearly as effective as it was for the other tests. The obvious explanation for this could be the increase in the weight of the leaves by around 10 kg per millimetre of glass thickness, which places more effort on the system, increasing the strain. But the displacements from the charts do



not depend on the initial weight since they are a difference between the displacements after and before the load is applied. The better performance from the complete internal reinforcements could be related to the increase in stiffness around the hinges, on both the fixed frame and the leaves' frames, since this location is the most stressed of the model (Figure 6.16).

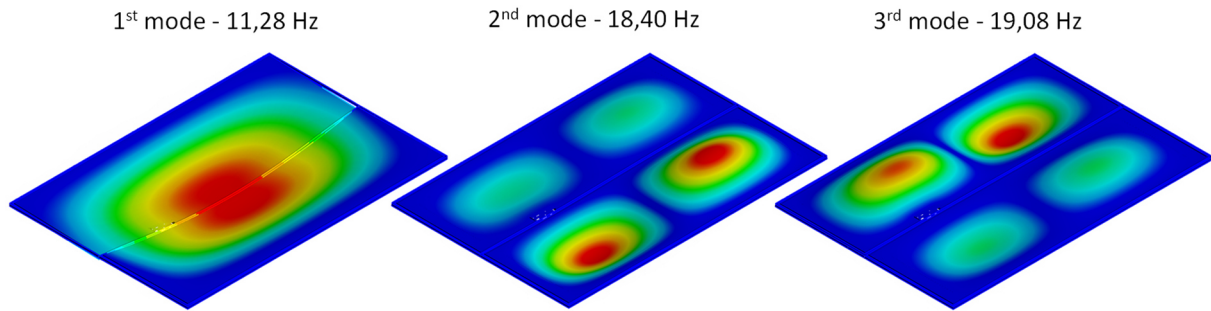
Nevertheless, the most important information from the data in Figure 6.18, is that there is an improvement in stiffness from increasing the thickness of the glass panels, which indicates that the added weight doesn't have a negative effect on the displacements of this test.

However, the validity of these conclusions can be questioned for a real system, since the values of the displacement of all simulations are particularly small, not reaching  $\frac{1}{50}$  of the millimetre on all reinforcements. Larger displacements could arise in the real system due to the accommodation of the real components like the hardware, which cannot be captured in the numerical simulation, or due to some other factors such as some displacement that could occur between the frame and the glazing, invalidating the assumption that they form a clamped connection. Other reasons could arise to differentiate these simulations from a real-world application, that without experimental testing are just speculative. This is not only true for the simulations to vertical loads and extends to all simulations, but the small values in these simulations raise suspicion.

Nevertheless, considering the maximum displacements from the OS2 65 DLD system used for the classification, the maximum displacement on the primary and secondary leaves were 1 mm and 0 mm (accuracy not specified in the test report), respectively, which on the secondary leave is close to the simulation results. Since the system of the numeric analyses is more robust than the one used in the classification, there is the possibility that the results are close to the real values.

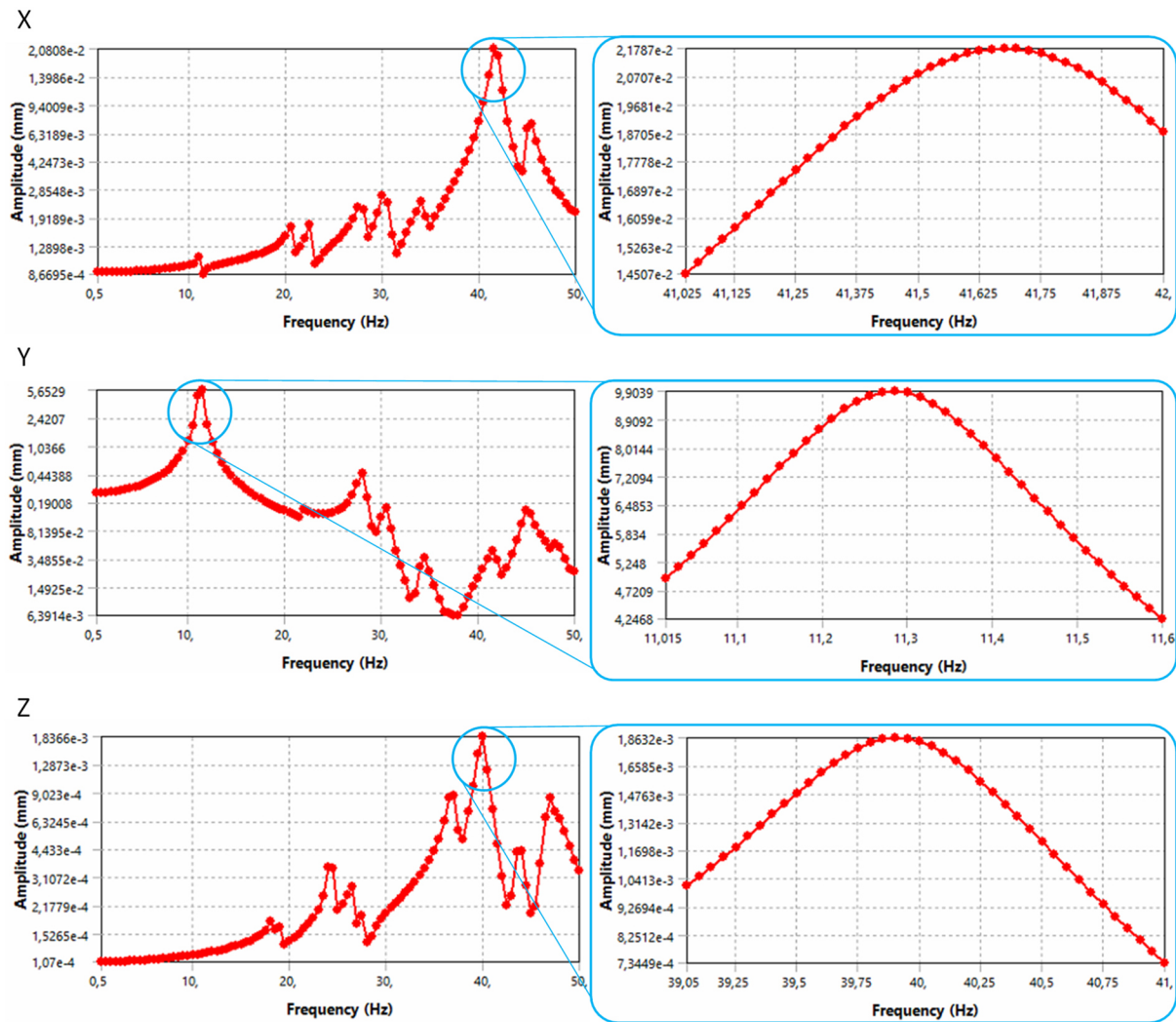
#### **6.2.4 Dynamic Vibrations Test**

Figure 6.19 shows the first three mode shapes of the system, where the behaviour of the DLD system on the first mode shape resembles the behaviour of the response to a wind load.



**Figure 6.19.** First three mode shapes of the DLD brass system. For clearness, the images of the 2<sup>nd</sup> and 3<sup>rd</sup> modes only show the middle glass panel, as the two outer glass panels, were just blue surfaces, meaning they were not excited.

The results from the FRFs in Figure 6.20 show that only significant displacement is observed in the Y direction, which is the direction perpendicular to the façade that was already expected to trigger the first mode shape. In the other directions, small displacements are observed, particularly in the Z direction where the displacement is kept in the order of the microns. In the Y direction, a displacement even larger than the one from the results of the wind loads test was obtained. Although no stress evaluation could be performed on the beam elements, due to the impossibility to use the beam tool in a harmonic response analysis, the stresses on the glass panels (excluding the lock surfaces) obtained with the larger model, show a value of 23,1 MPa, which is well below the tensile strength of glass.



**Figure 6.20.** FRFs of the amplitude of the frame structure in the direction of the harmonic acceleration (X, Y, and Z), and FRFs with more resolution around the highest peak.

It is important to keep in mind that the model for these analyses was extremely simplified and that the criterion defined assumed harmonic acceleration of the PGA, which doesn't happen in an earthquake since the PGA only happens once [45]. Hence, because the glass doesn't reach the tensile strength and the criterion is extremely conservative there is a high possibility that the system could endure an earthquake of instrumental intensity of V or lower (possibly even a higher level), but because a lot of simplifications were made, to have certainties, an experimental test using a shaker would be necessary. Moreover, it is prudent to recall that no vibration tests are demanded to obtain the CE marking of a door or window system, but the study of a system's dynamic response could be advantageous in regions with high seismic intensity.

### 6.2.5 Change in Thermal Transmittance

The evaluation of the influence of the internal reinforcements on the thermal properties of the DLD system was essential to determine their viability. These results are present in Table 6.4, where it can be seen that there is some influence of the reinforcement in the thermal transmittance of the frame  $U_f$ , going up to almost 7% on the side cross-section of the system with stainless steel as the base metal, whereas on the systems with other base metals, this value is kept under 2,5%. The linear thermal transmittance, registers a low increase, reaching 1,56% with stainless steel as the base metal, and keeps below 0,065% with the other base metals, with the maximum in all cases taking place on the centre of the system.

It is notable that the lower the thermal conductivity of the base metal, the higher the influence of the reinforcement on the parameters in Table 6.4, so a system with stainless steel ( $\lambda=17$  W/(mK)) as the base material, will have a larger increase on its thermal transmittance than a system with brass ( $\lambda=116,4$  W/(mK)) as the base material. Nevertheless, the presence of the reinforcement, which was tested filling all the cavities of the frame, won't have a significant influence on the thermal transmittance of the door,  $U_D$ , as the maximum relative change determined is just below 2,1%.

**Table 6.4.** Thermal transmittance of the frame ( $U_f$ ), door ( $U_D$ ), and linear thermal transmittance ( $\Psi_g$ ) of reinforced and unreinforced DLD systems with all base metals.

Base metal	Section location	Unreinforced			Reinforced					
		$U_f$ (W/m <sup>2</sup> K)	$\Psi_g$ (W/mK)	$U_D$ (W/m <sup>2</sup> K)	$U_f$ (W/m <sup>2</sup> K)	Error	$\Psi_g$ (W/mK)	Error	$U_D$ (W/m <sup>2</sup> K)	Error
Brass	Side	3,18	0,12	1,32	3,22	1,43%	0,12	0,40%	1,33	0,44%
	Centre	3,02	0,30		3,05	1,12%	0,30	0,53%		
Corten Steel	Side	3,13	0,12	1,31	3,21	2,50%	0,12	0,79%	1,32	0,78%
	Centre	2,98	0,30		3,04	2,10%	0,30	0,95%		
Galvanized Steel	Side	3,13	0,12	1,31	3,21	2,50%	0,12	0,79%	1,32	0,78%
	Centre	2,98	0,30		3,04	2,10%	0,30	0,95%		
Stainless Steel	Side	2,96	0,12	1,29	3,17	6,93%	0,12	1,94%	1,32	2,07%
	Centre	2,83	0,29		3,01	6,27%	0,30	2,34%		

Figure 6.21, shows that the difference in the temperature profiles, from the reinforced and unreinforced side cross-sections for the brass system, are very similar, which agrees with the results from Table 6.4, that the presence of the reinforcement doesn't have a significant influence on the heat propagation inside the section of the frame for this base material.

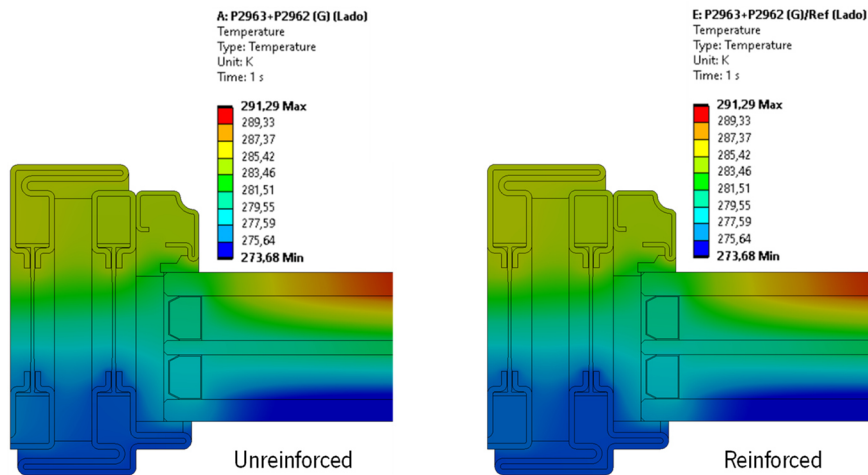


**Figure 6.21.** Colour coded temperature after the thermal simulation on the reinforced and unreinforced side cross-sections of the DLD brass system.

The results are not surprising, since the thermal break of the frame structure was kept intact with the introduction of the reinforcement, and because a worst-case scenario was tested, with all cavities being completely filled with steel, the increase in thermal transmittance of the door should be even lower for the reinforcement configurations tested in the different static simulations of the CE tests, as long as the thermal conductivity of the reinforcement doesn't surpass the value of 60 W/(mK) of the tested steel reinforcement.

# Chapter 7

## GENERAL CONCLUSIONS AND FUTURE WORK

### 7.1 General Conclusions

The dissertation aimed to attain more detail about a type of system that had previously not been studied by the company, which includes a better understanding of the system's behaviour and its change in performance when employing different reinforcements and configurations of its elements.

The standardization was studied, and the main structural tests on the DLD system case study were identified to be the resistance to vertical loads, static torsion, and wind load tests, which would be later simulated to extract results. Other tests that depend mainly on gaskets, such as the tests of air permeability and watertightness, were not studied in this work, as the structural component of these tests can be evaluated by the resistance to wind load test simulations since it depends on a pressure perpendicularly applied to the façade.

The material characterization showed the brass test specimens had similar properties to those given by the supplier. However, the properties gathered from the PA test specimens were very distinct and generally worse than those given by a report which uses PBT in the place of the PA, not including the density which was relatively close. Despite being dissimilar materials there is a strong possibility that the values of PA properties determined were below those intended by the supplier. The gathered material properties would later be confirmed in the study of the three-point bending behaviour of an MMB.

From all the models used for the MMB, it was found that only the solid elements and beam + shell models could capture the bending behaviour of the physical MMB in the three-point bending. And the opposite occurred with the experimental modal analysis of the MMB, as only the analytical and the beam elements models resulted in resonance frequencies close to the frequencies at which the peaks occurred in the FRF from the experiment.

It was discovered that the major causes for this to happen were both the formulation used by the analytical and beam elements model, and the distinct elastic modulus of the MMB in the static and dynamic experiments, which is characteristic of polymeric materials. Both formulations of the analytical (Euler-Bernoulli) and beam elements (Timoshenko) models depict the MMB with a cross-section that

remains in-plane throughout its deformation. This does not happen in the physical MMB, due to the high difference between the elastic modulus of the metal and the polymers, so these models cannot capture the MMB's behaviour, unlike the solid elements and beam + shell models, which can account for this cross-sectional change.

On the other hand, the dynamic modulus of the polymers is higher than the static elastic modulus and reaches a value that allows for the cross-section of the physical MMB to remain in-plane to a degree where the analytical and beam elements models can capture its resonant frequencies. Because the solid elements and beam + shell models don't account for this change in the elastic moduli, they cannot capture the complete set of resonant frequencies of the physical MMB. However, increasing the polymers' elastic modulus resulted in the cross-section of the beam + shell model remaining in-plane, capturing the resonant frequencies of the physical MMB.

These inferences confirmed the need for the experimental tests and allowed for the selection of the beam + shell model for the DLD system model, despite the smaller torsional stiffness in comparison with the solid elements model, since it was possible to create a frame structure with far fewer nodes, and consequently less computation time. An experiment to determine the torsional stiffness of the beam would help determine the most adequate model, but since the load on the tests is applied either perpendicularly or parallelly to the leaf's plane, the bending behaviour ought to be predominant on the MMBs of the frame structure.

Besides a conservative torsional stiffness, the use of the elastic modulus of the polymers from the tensile tests in the simulations of the DLD system was also a conservative approach since there is a chance that these properties are slightly higher in the standardized tests which are not quasi-static, unlike the tensile and three-point bending tests.

The structural optimization simulation showed an increase in stiffness of the MMB the further the reinforcement material is from the cross-section's centroid, confirming the second moment of area as the main geometric property used to improve the bending stiffness of a beam. In the study of the vibration of MMBs with unsymmetric profiles, the analytical and beam elements models provided similar results, and because these models could represent the physical vibratory behaviour of a (symmetrical) MMB, the confidence in these results increases.

The resistance to the wind load test simulations revealed that an optimized section of the internal reinforcements results in a relatively low increase in stiffness when compared with a more complete section and that the resistance to the deformation of the frame structure caused by the load, occurs mainly at the centre of the system, which resulted in the reinforcement placed only at the centre delivering

almost the same increase in stiffness as the frame structure fully reinforced. Additionally, it was found in this test that the effect of increasing the thickness of the outer glass panels of the glazing had a more noticeable influence on the increase of stiffness than the internal reinforcements, despite the larger increase in weight. Additionally, the results were in the same magnitude order as the results from the physical DLD OS2 65 system used in the certification test.

In the static torsion test with the DLD model, it was clear that improving the glazing was more effective than using internal reinforcements, as the increase in stiffness was higher. The use of internal reinforcements only at the centre didn't produce a significant improvement, and the use of internal complete reinforcements in all locations produced a small improvement. The displacements registered from these simulations were smaller and on a different order of magnitude than those registered in the physical DLD OS2 65 system used in the certification test. There is a possibility that the components of the leaf's frame lost their adhesion, dropping the stiffness of the overall system to static torsion, but without a meticulously detailed report or the observation of the test, there is no way of having certainties.

The vertical loads test displacements were overall particularly small, being in accordance with the experimental data from the physical DLD OS2 65 system, and the most effective reinforcement was the use of a complete reinforcement in all locations of the frame structure. Increasing the thickness of the outer glass panels of the glazing produced a smaller increase, and using a complete reinforcement only at the centre caused a slight decrease in the stiffness of the system to this test.

Overall, the best reinforcement of the system came from the improvement of the glazing, followed by the complete reinforcement placed only at the centre, due to its satisfactory performance in the resistance to the wind load test, giving that it can also improve the structural component of the watertightness and the air permeability tests. The improvement of the glazing is also the easiest way to improve the performance since the glazing suppliers used by the company already fabricate the thicknesses tested, and the use of internal reinforcements requires more labour and a solution to bond the internal reinforcement to the frame, as they were simulated in that manner.

The harmonic response simulation revealed some confidence in the capacity of the system to withstand an earthquake of instrumental intensity V, since the glass panels reached a stress state that is far from the tensile stress of glass, and the criterion used is very conservative. However, a lot of simplifications were made in the model, and an experimental test should be made to draw more trustworthy conclusions.



Lastly, the thermal evaluation of the use of steel internal reinforcements resulted in no significant changes in the thermal transmittance of the DLD system, which is consequence of the thermal break remaining intact with the addition of the reinforcements.

## 7.2 Future Work

After extracting the conclusions from the dissertation's outputs, a few suggestions can be made for subsequent projects. Some are of more interest to the company, and some are more prone to academic projects.

From the study of the standardization tests, three stand out as being achievable without a considerable investment, given their simplicity. Therefore, it would be interesting for the company to create a structural system capable of replicating the resistance to vertical loads and to static torsion tests, as well as a structure with nozzles capable of reproducing the watertightness test. Besides these structures giving a direct indication of what classes to expect, the first one will allow for a direct comparison with the FEM model of a system, building confidence in the other tests performed in the numerical analyses, and the later structure would allow for a direct evaluation of the rubber gaskets. In a more distant future, the investment in a test chamber capable of evaluating the strength and stiffness to a wind load and the air permeability of a system could also be considered.

From the numerical model of a system, the forces and moments at the joints can be extracted, so a test of the hardware by FEM is possible and should be done to evaluate its performance. In addition, this could be also used to evaluate off the shelf hardware from manufacturers other than the frame's supplier, hence exploring other options that could perform better.

A more complete characterization of the polymers to study their strain rate dependencies could be accomplished, as well as the study of the adhesion at the interface between the different components of the MMB, (the latter) similar to the work done by S. Huang et al. [95]. The company revealed the intention of developing its own MMBs for the frame structure, in a not-so-distant future. With these studies as a foundation, a better attempt could be made to develop a new MMB that keeping its thermic barrier, tries to solve the loss of adhesion at the interface problem, as well as the cross-section not staying in place problematic.

If an earthquake is a big cause of concern for a certain region, the test of a specimen with a shaker that inputs a random earthquake characteristic signal to the system could be advantageous.

## REFERENCES

- [1] D. Thorpe, *Sustainable home refurbishment: the Earthscan expert guide to retrofitting homes for efficiency*. London: Earthscan, 2010.
- [2] L. Ma, N. Shao, J. Zhang, and T. Zhao, 'The Influence of Doors and Windows on the Indoor Temperature in Rural House', *Procedia Eng.*, vol. 121, pp. 621–627, Jan. 2015, doi: 10.1016/j.proeng.2015.08.1051.
- [3] 'JFAN - ARCHITECTURAL GLAZING SPECIALIST'. <https://www.jfan.pt/> (accessed Mar. 31, 2022).
- [4] 'Cottage in Sicilia - Secco Sistemi'. <https://www.seccosistemi.com/en/projects/cottage-in-sicilia/> (accessed Jan. 26, 2022).
- [5] *Windows and pedestrian doors - Terminology*, EN 12519:2019. 2019.
- [6] 'CE marking'. [https://ec.europa.eu/growth/single-market/ce-marking\\_pt](https://ec.europa.eu/growth/single-market/ce-marking_pt) (accessed Mar. 03, 2022).
- [7] 'Latest North American Fenestration Standard Published'. <https://fgiaonline.org/news/latest-north-american-fenestration-standard-published> (accessed Mar. 01, 2022).
- [8] A. S. AL-HOMOUD and A.-Q. FANDI AMRAT, 'Comparison Between Recorded and Derived Seismic Peak Horizontal Ground Acceleration Data in Jordan', *Environ. Eng. Geosci.*, vol. III, no. 4, pp. 513–521, Jan. 1997, doi: 10.2113/gseegeosci.III.4.513.
- [9] S. R. Chao, B. Ghansah, and R. J. Grant, 'An exploratory model to characterize the vulnerability of coastal buildings to storm surge flooding in Miami-Dade County, Florida', *Appl. Geogr.*, vol. 128, p. 102413, Mar. 2021, doi: 10.1016/j.apgeog.2021.102413.
- [10] 'OS2 75 Technical Catalogue'. Secco sistemi, May 2017.
- [11] 'Catalogue'. Secco sistemi, Oct. 2020.
- [12] 'BASF Ultradur® B 4300 G6 30% Glass Filled PBT', *MatWeb*. <https://www.matweb.com/search/datasheet.aspx?matguid=81e052f22f9d4dd59719f8cc4ccb5718&ckck=1> (accessed Mar. 01, 2022).
- [13] *Structural use of glass in buildings*, 2nd ed. The Institution of Structural Engineers, 2015.
- [14] 'Physical properties of glass | Saint Gobain Building Glass UK'. <https://uk.saint-gobain-building-glass.com/en-gb/architects/physical-properties> (accessed Jan. 18, 2022).
- [15] 'Technical Information | Glass and Thermal Insulation | Saint-Gobain'. <https://uk.saint-gobain-building-glass.com/en-gb/glass-and-thermal-insulation> (accessed Jan. 20, 2022).

- [16] 'Aluminum / Aluminium 3003 Alloy (UNS A93003)', *AZoM.com*, Aug. 30, 2012. <https://www.azom.com/article.aspx?ArticleID=6618> (accessed Jan. 20, 2022).
- [17] S. Bizoňová and M. Bagoňa, 'Gas filling in glass system', Sep. 2018.
- [18] M. J. Moran, *Fundamentals of Engineering Thermodynamics*, 9th ed. New York: John Wiley & Sons, Incorporated, 2019. Accessed: Mar. 26, 2022. [Online]. Available: <http://public.eblib.com/choice/PublicFullRecord.aspx?p=6488460>
- [19] *Windows and doors - Product standard, performance characteristics - Part 1: Windows and external pedestrian doorsets without resistance to fire and/or smoke leakage characteristics*, EN 14351-1:2006+A2 2019, 2019.
- [20] 'OS2 65 Technical Catalogue'. Secco sistemi, May 2017.
- [21] *Windows - Classification of mechanical properties - Racking, torsion and operating forces*, EN 13115:2020, 2020.
- [22] *Windows and pedestrian doors - Mechanical durability - Requirements and classification*, EN 12400:2002, 2002.
- [23] *Operating forces. Test method Windows*, EN 12046-1:2020, 2020.
- [24] *Doors. Classification of strength requirements*, EN 1192:2000, 2000.
- [25] *Hinged or pivoted doors. Determination of the resistance to vertical load*, EN 947:1999, 1999.
- [26] *Hinged or pivoted doors. Determination of the resistance to static torsion*, EN 948:1999, 1999.
- [27] *Windows. Soft and heavy body impact. Test method, safety requirements and classification*, EN 13049:2003, 2003.
- [28] *Glass in building. Pendulum test. Impact test method and classification for flat glass*, EN 12600:2002, 2010.
- [29] *Windows and doors. Resistance to wind load. Classification*, EN 12210:2016, 2016.
- [30] *Windows and doors. Resistance to wind load. Test method*, EN 12211:2016, 2016.
- [31] *Windows and doors. Air permeability. Classification*, EN 12207:2016, 2017.
- [32] *Windows and doors. Air permeability. Test method*, EN 1026:2016, 2016.
- [33] *Windows and doors. Watertightness. Classification*, EN 12208:2000, 2000.
- [34] *Windows and doors. Water tightness. Test method*, EN 1027:2016, 2016.
- [35] J. Willoughby, *Plant Engineer's Reference Book*, 2nd ed. Oxford: Butterworth-Heinemann, 2002. doi: 10.1016/B978-075064452-5/50085-7.

- [36] *Thermal performance of windows, doors and shutters. Calculation of thermal transmittance General*, ISO 10077-1:2017, 2020.
- [37] *Thermal performance of windows, doors and shutters. Calculation of thermal transmittance Numerical method for frames*, ISO 10077-2:2017, 2017.
- [38] G. Solari, 'Wind Response Spectrum', *J. Eng. Mech.*, vol. 115, no. 9, pp. 2057–2073, Sep. 1989, doi: 10.1061/(ASCE)0733-9399(1989)115:9(2057).
- [39] C. Dyrbye and S. O. Hansen, *Wind loads on structures*. Chichester ; New York: J. Wiley, 1997.
- [40] A. Brandt, *Noise and Vibration Analysis: Signal Analysis and Experimental Procedures*, 1st ed. Wiley, 2011. doi: 10.1002/9780470978160.
- [41] D. Boggs and J. Dragovich, 'The Nature of Wind Loads and Dynamic Response', *Symp. Pap.*, vol. 240, 2006, doi: 10.14359/18290.
- [42] *Eurocode 1: Actions on structures - Part 1-4: General actions - Wind actions*, EN 1991-1-4:2005+A 1, 2010.
- [43] T. Balendra, *Vibration of Buildings to Wind and Earthquake Loads*. London: Springer London, 1993. doi: 10.1007/978-1-4471-2055-1.
- [44] M. A. Morsy and A. M. Abed, 'Attenuation of seismic waves in Central Egypt', *NRIAG J. Astron. Geophys.*, vol. 2, no. 1, pp. 8–17, Jun. 2013, doi: 10.1016/j.nrjag.2013.06.003.
- [45] W. H. K. Lee, International Association of Seismology and Physics of the Earth's Interior, and International Association for Earthquake Engineering, Eds., *International handbook of earthquake and engineering seismology*. Amsterdam ; Boston: Academic Press, 2002.
- [46] B. Mohraz and F. Sadek, 'Earthquake Ground Motion and Response Spectra', in *The Seismic Design Handbook*, F. Naeim, Ed. Boston, MA: Springer US, 2001, pp. 47–124. doi: 10.1007/978-1-4615-1693-4\_2.
- [47] D. Hiriart, J. L. Ochoa, and B. García, 'Wind Power Spectrum measured at the San Pedro Mártir Sierra', *Rev. Mex. Astron. Astrofísica*, vol. 37, pp. 213–220, Oct. 2001.
- [48] J. P. P. Beaupuits, A. Otárola, F. T. Rantakyro, R. C. Rivera, E. Radford, and L.-Å. Nyman, 'Analysis Of Wind Data Gathered At Chajnantor', ALMA observatory, Chile, Memo 497, 2004.
- [49] Nathan M. Newmark and W. J. Hall, *Earthquake Spectra and Design*. Earthquake Engineering Research Institute, 1982.
- [50] Trevor I. Allen, David J. Wald, Alicia J. Hotovec, Kuowan Lin, Paul S. Earle, and Kristin D. Marano, 'An Atlas of ShakeMaps for Selected Global Earthquakes', United States Geological Survey, 2008.

- [51] B. Huang and W. Lu, 'Evaluation of the Floor Acceleration Amplification Demand of Instrumented Buildings', *Adv. Civ. Eng.*, vol. 2021, pp. 1–20, Aug. 2021, doi: 10.1155/2021/7612101.
- [52] S. ray chaudhuri and T. Hutchinson, 'Distribution of peak horizontal floor acceleration for estimating nonstructural element vulnerability', presented at the 13th World Conference on Earthquake Engineering, Vancouver, B.C., Canada, Jun. 2004.
- [53] H. Akhlaghi, 'Height-Wise Distribution of Peak Horizontal Floor Acceleration (PHFA)', presented at the 14th World Conference on Earthquake Engineering, Beijing, China, Dec. 2008.
- [54] *Metallic materials – Tensile testing – Part 1: Method of test at room temperature*, ISO 6892-1:2019, 2019.
- [55] *Plastics – Determination of tensile properties – Part 2: Test conditions for moulding and extrusion plastics*, ISO 527-2:2012, 2012.
- [56] *Plastics – Determination of tensile properties – Part 1: General principles*, ISO 527-1:2019, 2019.
- [57] J.P.Davim and A.G.Magalhães, *Ensaaios Mecânicos e Tecnológicos*, 3rd ed. Porto: Publindústria, 2010.
- [58] D. Li, C. Xiong, T. Huang, R. Wei, N. Han, and F. Xing, 'A simplified constitutive model for corroded steel bars', *Constr. Build. Mater.*, vol. 186, pp. 11–19, Oct. 2018, doi: 10.1016/j.conbuildmat.2018.07.019.
- [59] C. Xiong, C. Zeng, Y. Li, L. Li, P. Li, and D. Li, 'The Constitutive Relationship for Corroded Steel Bars: Model and Analysis', *Materials*, vol. 12, no. 24, p. 4058, Dec. 2019, doi: 10.3390/ma12244058.
- [60] A. I. Salahaldin, M. K. Ali, and M. M. Kassim, 'Analysis of Fiber Reinforced Concrete Deep Beams with Large Opening Strengthened by CFRP Laminates', *Kirkuk Univ. J.-Sci. Stud.*, vol. 10, no. 1, pp. 29–46, Mar. 2015, doi: 10.32894/kujss.2015.101354.
- [61] *Standard Test Method For Tensile Properties Of Plastics*, ASTM D638-14. 2017.
- [62] A. Maas, T. K. Kim, R. K. Miehlike, T. Hagen, and T. M. Grupp, 'Differences in Anatomy and Kinematics in Asian and Caucasian TKA Patients: Influence on Implant Positioning and Subsequent Loading Conditions in Mobile Bearing Knees', *BioMed Res. Int.*, vol. 2014, pp. 1–10, 2014, doi: 10.1155/2014/612838.
- [63] N. W. Brooks, R. A. Duckett, and I. M. Ward, 'Investigation into double yield points in polyethylene', *Polymer*, vol. 33, no. 9, pp. 1872–1880, Jan. 1992, doi: 10.1016/0032-3861(92)90486-G.

- [64] *Standard Test Method for Density, Relative Density, and API Gravity of Liquids by Digital Density Meter*, ASTM D4052-16.
- [65] D. J. Alarcón, S. Schneider, R. Kamenzky, and P. Blaschke, 'Across the Picket Fence: Influence of Sampling Frequency in Automatic Impact Modal Testing', in *Special Topics in Structural Dynamics, Volume 5*, N. Dervilis, Ed. Cham: Springer International Publishing, 2019, pp. 137–143. doi: 10.1007/978-3-319-75390-4\_11.
- [66] P. Avitabile, *Modal Testing: A Practitioner's Guide: A Practitioner's Guide*. Chichester, UK: John Wiley & Sons Ltd, 2017. doi: 10.1002/9781119222989.
- [67] G. A. Papagiannopoulos and G. D. Hatzigeorgiou, 'On the use of the half-power bandwidth method to estimate damping in building structures', *Soil Dyn. Earthq. Eng.*, vol. 31, no. 7, pp. 1075–1079, Jul. 2011, doi: 10.1016/j.soildyn.2011.02.007.
- [68] V. H. Carneiro, H. Puga, and J. Meireles, 'Heat treatment as a route to tailor the yield-damping properties in A356 alloys', *Mater. Sci. Eng. A*, vol. 729, pp. 1–8, Jun. 2018, doi: 10.1016/j.msea.2018.05.042.
- [69] R. D. Copetti, J. R. Claeysen, D. de R. Tolfo, and B. S. Pavlack, 'The fundamental modal response of elastically connected parallel Timoshenko beams', *J. Sound Vib.*, vol. 530, p. 116920, Jul. 2022, doi: 10.1016/j.jsv.2022.116920.
- [70] R. Eberle and M. Oberguggenberger, 'A new method for estimating the bending stiffness curve of non-uniform Euler-Bernoulli beams using static deflection data', *Appl. Math. Model.*, vol. 105, pp. 514–533, May 2022, doi: 10.1016/j.apm.2021.12.042.
- [71] F. P. Beer, E. Russel Johnston Jr., John T. DeWolf, and David F. Mazurek, *Mechanics of materials*, 8th ed. New York, NY: McGraw-Hill Education, 2020.
- [72] T. H. G. Megson, *Structural and stress analysis*, 4th ed. Kidlington, Oxford Cambridge, MA: Butterworth-Heinemann, 2019.
- [73] Clarence W. de Silva, *Vibration: Fundamentals and Practice*. Boca Raton, Florida: CRC Press, 2000.
- [74] Jorge Figueiredo and Carolina Ribeiro, *Apontamentos de Equações diferenciais (Complementos de Análise Matemática EE)*. Universidade do Minho: Departamento de Matemática e Aplicações, 2013.
- [75] 'Large Deformation - Large Deformation Governing Equations', *ANSYS Innovation Courses*. <https://courses.ansys.com/index.php/courses/large-deformation/lessons/large-deformations-governing-equations-lesson-3/> (accessed Jan. 02, 2022).

- [76] *Theory Reference*, Release 2021 R1. Ansys, 2021.
- [77] 'Computational Considerations - Intro to Nonlinear Solver', *ANSYS Innovation Courses*. <https://courses.ansys.com/index.php/courses/computational-resource-considerations-recommended/lessons/intro-to-nonlinear-solver-lesson-2/> (accessed Feb. 01, 2022).
- [78] 'Modal Analysis - Governing Equations for Modal Analysis', *ANSYS Innovation Courses*. <https://courses.ansys.com/index.php/courses/modal-analysis/lessons/governing-equations-of-modal-analysis-lesson-2/> (accessed Jan. 02, 2022).
- [79] 'Harmonic Analysis of Structures - Formulation of Harmonic Analysis', *ANSYS Innovation Courses*. <https://courses.ansys.com/index.php/courses/harmonic-analysis-of-structures/lessons/formulation-of-harmonic-analysis-lesson-2/> (accessed Jan. 02, 2022).
- [80] 'Damping Effects - Fundamentals of Damping', *ANSYS Innovation Courses*. <https://courses.ansys.com/index.php/courses/damping-effects/lessons/fundamentals-of-damping-lesson-2/> (accessed Jan. 02, 2022).
- [81] *Element Reference*, Release 2021 R1. Ansys, 2021.
- [82] William D. Callister, Jr. and David G. Rethwisch, *Materials Science and Engineering, an Introduction*, 9th ed. John Wiley & Sons, Inc., 2014.
- [83] Huei-Huang Lee, *Finite Element Simulations with Ansys Workbench 2021*. Taiwan: SDC Publications, 2021.
- [84] *Mechanical User's Guide*, Release 2021 R1. Ansys, 2021.
- [85] *Contact Technology Guide*, Release 2021 R1. Ansys, 2021.
- [86] *Command Reference*, Release 2021 R1. Ansys, 2021.
- [87] 'Chapter 24: Hydrostatic Fluid Analysis of an Inflating and Rolling Tire', in *Workbench Technology Showcase: Example problems*, Release 2021 R1., Ansys, 2021.
- [88] 'Contained Fluid in FEA Model with Hydrostatic Elements | SimuTech', *SimuTech Group*, Feb. 08, 2022. <https://simutechgroup.com/contained-fluid-in-mechanical-fea-model-working-with-hsflid242-elements/> (accessed Oct. 11, 2021).
- [89] 'Hydrostatic fluid element in structural analysis with convex geometry', *Ansys Learning Forum*. <https://forum.ansys.com/discussion/3588/hydrostatic-fluid-element-in-structural-analysis-with-convex-geometry> (accessed Dec. 10, 2021).
- [90] R. G. Budynas and J. K. Nisbett, *Shigley's mechanical engineering design*, 9th ed. New York: McGraw-Hill, 2011.

- [91] P. I and S. S, 'Comparative analysis of static and dynamic elastic modulus of polymer concrete polymers', *Mach. Technol. Mater.*, vol. 10, no. 12, pp. 38–41, 2016.
- [92] J. Fan, X. Fan, and A. Chen, 'Dynamic Mechanical Behaviour of Polymer Materials', in *Aspects of Polyurethanes*, F. Yilmaz, Ed. InTech, 2017. doi: 10.5772/intechopen.69570.
- [93] A. Massaq, A. Rusinek, and M. Klosak, 'Method for Determination of the Dynamic Elastic Modulus for Composite Materials', *Eng. Trans.*, vol. 61, pp. 301–315, Dec. 2013.
- [94] L. Galuppi and G. Royer-Carfagni, 'Optimal cold bending of laminated glass', *Int. J. Solids Struct.*, vol. 67–68, pp. 231–243, Aug. 2015, doi: 10.1016/j.ijsolstr.2015.04.023.
- [95] S. Huang, B. Samali, and J. Li, 'Numerical and experimental investigations of a thermal break composite façade mullion under four-point bending', *J. Build. Eng.*, vol. 34, p. 101590, Feb. 2021, doi: 10.1016/j.job.2020.101590.
- [96] M. F. Ashby, *Materials selection in mechanical design*, 4th ed. Burlington, MA: Butterworth-Heinemann, 2011.
- [97] 'Advanced Search - Matmatch'. <https://matmatch.com/advanced-search?categories=biological-material,ceramic,composite,glass,metal,polymer&properties=elastic-modulus&header=elastic-modulus:d&tags=application:aerospace-structures,application:general-automotive-parts,application:composite-reinforcements,application:building-structures,application:construction-materials,application:other-shafts-couplings&view=plot-materials> (accessed Aug. 27, 2021).
- [98] 'SupremEX® 640XA (6061B) T6 Billet - Aluminium Matrix Composite - Matmatch'. <https://matmatch.com/materials/mabr0020-supremex-640xa-6061b-t6-billet> (accessed Aug. 27, 2021).
- [99] 'Ferro-Titanit® WFN - Iron Matrix Composite - Matmatch'. <https://matmatch.com/materials/destferrowfn-ferro-titanit-wfn> (accessed Aug. 27, 2021).
- [100] Pinto Soares, *AÇOS - Características, Tratamentos*, 6th ed. ROCHA/artes gráficas.
- [101] 'UGI® 4114 Drawn Bar - Ferritic Stainless Steel - Matmatch'. <https://matmatch.com/materials/ugit0088-ugi-4114-drawn-bar> (accessed Aug. 27, 2021).
- [102] 'Densimet® 185 Tungsten Heavy Alloy (D185) - Metal Matrix Composite - Matmatch'. <https://matmatch.com/materials/plana109-densimet-185-tungsten-heavy-alloy-d185-> (accessed Aug. 27, 2021).
- [103] 'ZYLON® PBO HS - Thermosetting - Matmatch'. <https://matmatch.com/materials/mama00002-zylon-pbo-hs> (accessed Aug. 27, 2021).



- [104] 'Carbon Fibre Tenax HTA Multi Filament Tow - Carbon - Matmatch'.  
<https://matmatch.com/materials/mamagood00026-carbon-fibre-tenax-hta-multi-filament-tow>  
(accessed Aug. 27, 2021).
- [105] L. Jenner, 'The Amazing Anatomy of James Webb Space Telescope Mirrors', *NASA*, Mar. 20, 2014. <http://www.nasa.gov/content/goddard/the-amazing-anatomy-of-james-webb-space-telescope-mirrors> (accessed Aug. 27, 2021).
- [106] 'S-200-F H Beryllium Structural grades - Beryllium - Matmatch'.  
<https://matmatch.com/materials/mabr0024-s-200-f-h-beryllium-structural-grades> (accessed Aug. 27, 2021).
- [107] 'Densimet®176 rod - Ø 10+0,2/+0,4x330+5 in the Plansee Online Shop | Plansee'.  
<https://www.plansee.com/shop/en/product/standard-products/rods/densimet-176-rod-10-0-2-0-4x330-5-11284448> (accessed Aug. 28, 2021).
- [108] 'ZYLON | ZYLON is a new high-performance fiber developed by TOYOBO | 【TOYOBO】 東洋紡'.  
<https://www.toyobo-global.com/seihin/kc/pbo/> (accessed Aug. 28, 2021).
- [109] C. C. Group, 'Creative Composites Group'. <https://www.creativecompositesgroup.com> (accessed Aug. 28, 2021).
- [110] 'Beryllium and Beryllium Metal Products from Materion'.  
<https://materion.com/products/beryllium-products> (accessed Aug. 28, 2021).
- [111] 'Materion Environmental Health and Safety'. <https://materion.com/resource-center/environmental-health-and-safety> (accessed Aug. 28, 2021).
- [112] 'Carbon Steel Flat Bar', *Steel Supply LP*. <https://www.steelupplylp.com/structural-steel/steel-supply-store/flat/flat-carbon-steel> (accessed Aug. 28, 2021).

# Annex A

## PROFILES AND DLD COMPONENT'S DIMENSIONS

### A.1 Multi-Material Beam's Profiles

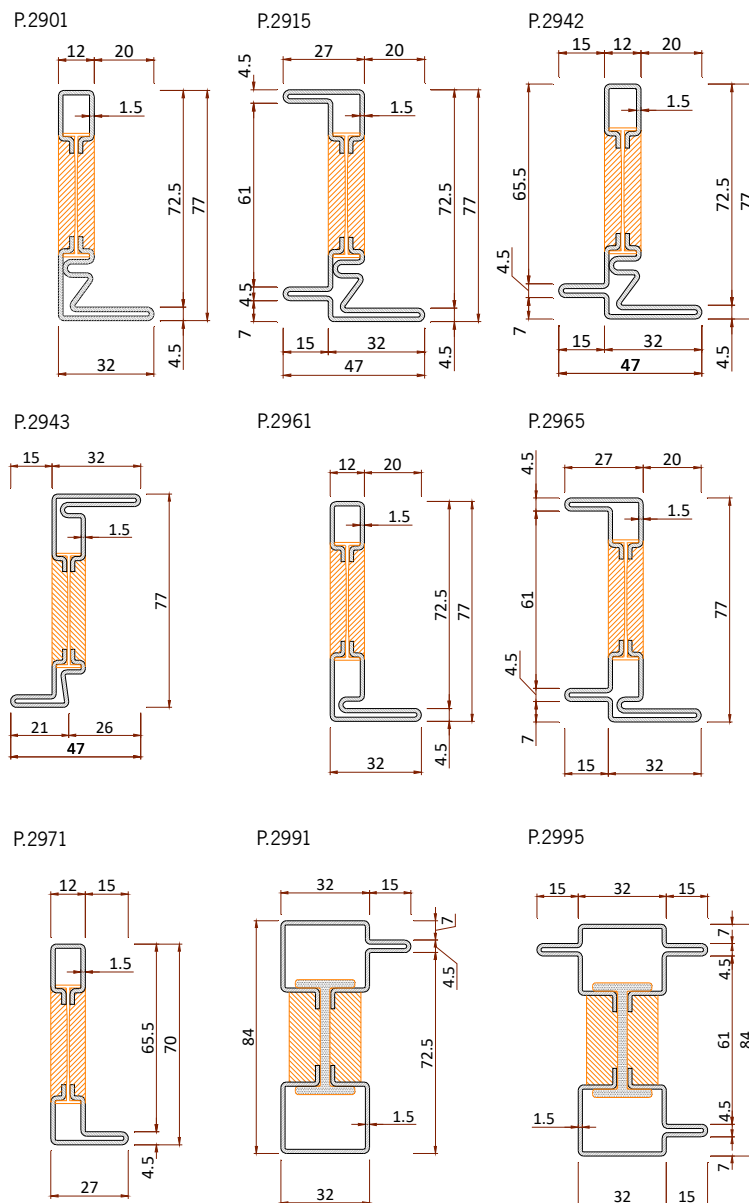


**Figure A.1.** Additional MMBs used in the modal analyses with the beam elements model and in the analytical model to find the first natural frequencies with bending and longitudinal mode shapes. The dimensions are in millimetres, the grey area represents the base metal, the orange area represents the PU, and the white area limited by an orange line represents the PA.

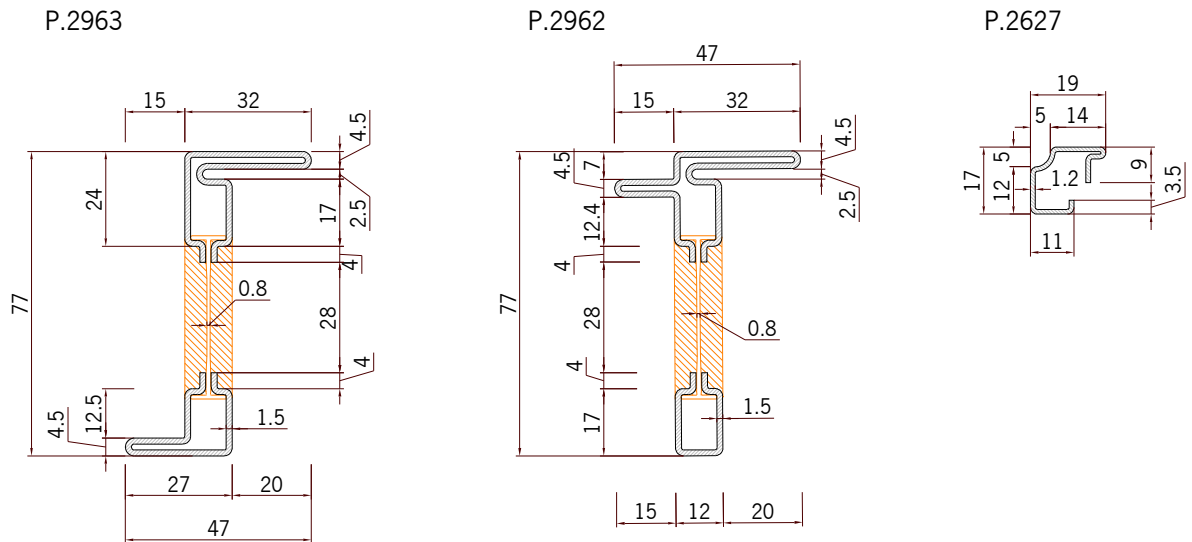


**Figure A.2.** MMBs and bead profiles used for the DLD system. The MMBs were also used in the modal analyses with the beam elements model and in the analytical model to find the first natural frequencies with bending and longitudinal mode shapes. The dimensions are in millimetres, the grey area represents the base metal, the orange area represents the PU, and the white area limited by an orange line represents the PA.

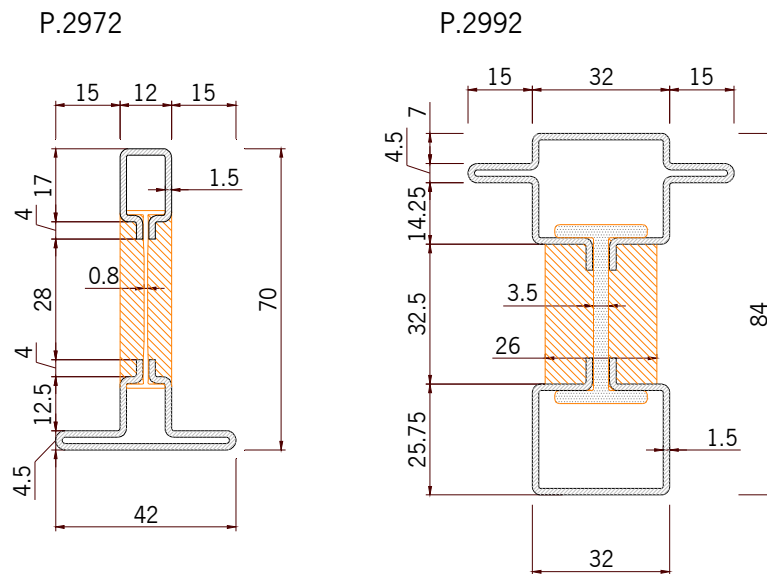


**Figure A.3.** MMBs profiles used in the structural optimization (P.2972) and experimental tests, three-point bending, torsion and modal analyses simulations with the beam + shell model, and solid elements model (P.2992). Both profiles were used in the modal analyses with the beam elements model and in the analytical model to find the first natural frequencies with bending and longitudinal mode shapes. The P.2992 model was also used in the three-point bending analytical model and three-point bending, torsion simulations with the beam elements model. The dimensions are in millimetres, the grey area represents the base metal, the orange area represents the PU, and the white area limited by an orange line represents the PA.

## A.2 DLD System

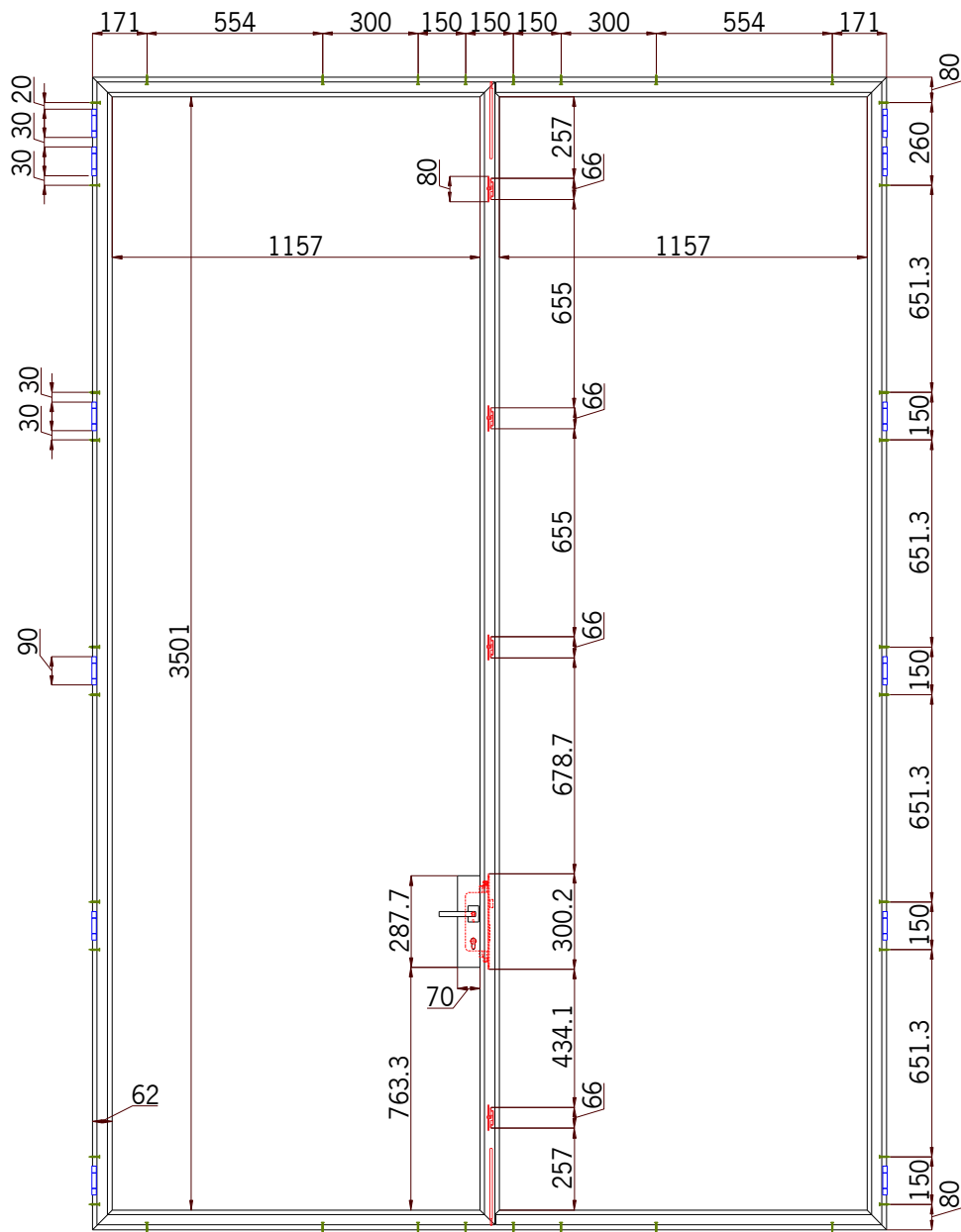


**Figure A.4.** Dimensions in millimetres between the different components of the system, needed for the definition of the DLD numerical model. The locking devices are illustrated in red, the hinges in blue, the screws in green, and the frame and glazing drawn with black lines.

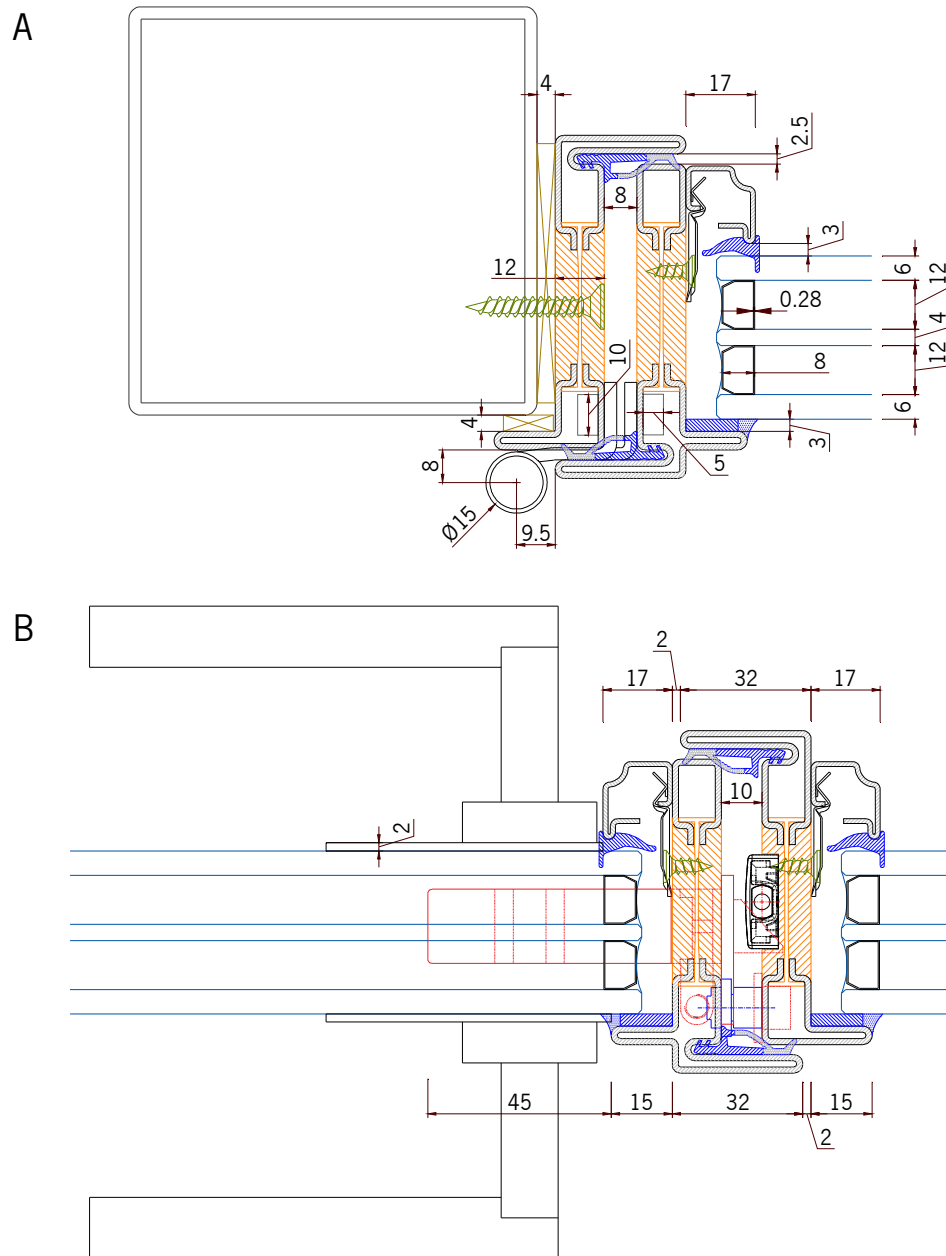


**Figure A.5.** Detailed section view of the connections between the gazing and the frames on the Side (A) and on the centre (B), with some dimensions in millimetres between the components, needed for the definition of the DLD numerical model.

### A.3 Hardware

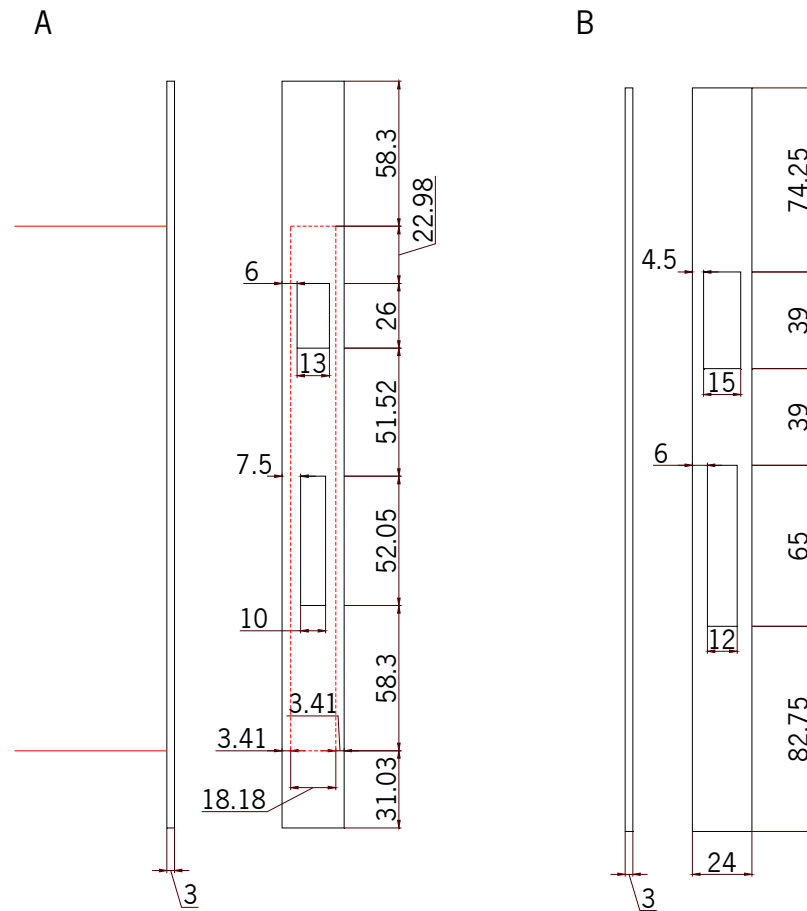


**Figure A.6.** Main lock dimensions in millimetres on the primary (A) and secondary (B) leaves that were used in the definition of the DLD numerical model.

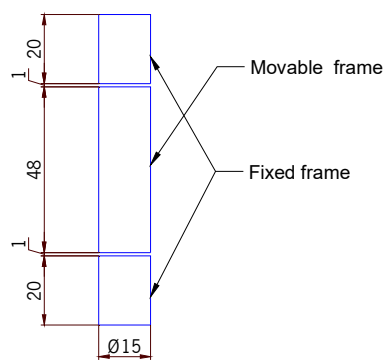


**Figure A.7.** Hinge dimensions in millimetres that were used in the definition of the DLD numerical model.

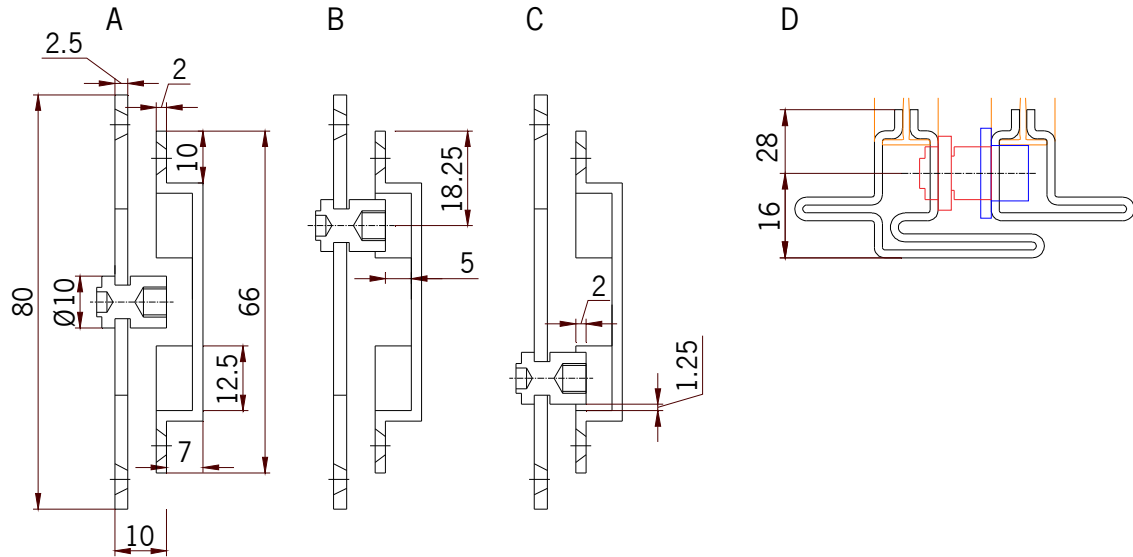


**Figure A.8.** AC2695S when the primary leaf stops onto the secondary leaf (A), the device after it is activated and locks above (B) and below (C) the main lock, and the position of the device on the frames. The dimensions in millimetres were used in the definition of the DLD numerical model.

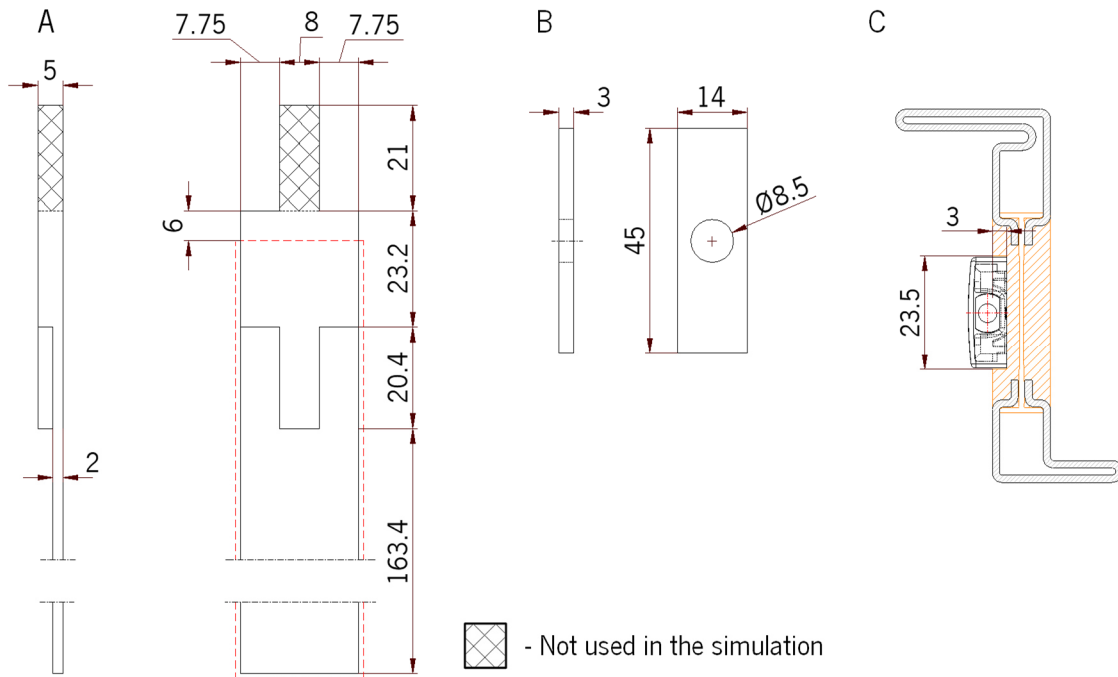


**Figure A.9.** Simplified geometry of the AC2621 RX locking device (A), the plate on the fixed frame (B), and the position of the device on the frame. The dimensions in millimetres were used in the definition of the DLD numerical model.

# Annex B

## ISO 10077-2:2017 SOFTWARE VALIDATION AND INFILLING

### GAS THERMAL CONDUCTIVITY

#### B.1 ISO 10077-2:2017 Validation

The method described in Chapter 2 and the simulation described in Chapter 5 for the thermal transmittance evaluation were employed on the ten cases specified in ISO 10077-2:2012, that are exhibited after simulation with slashed insulation panels and glazing in Figure B.1.

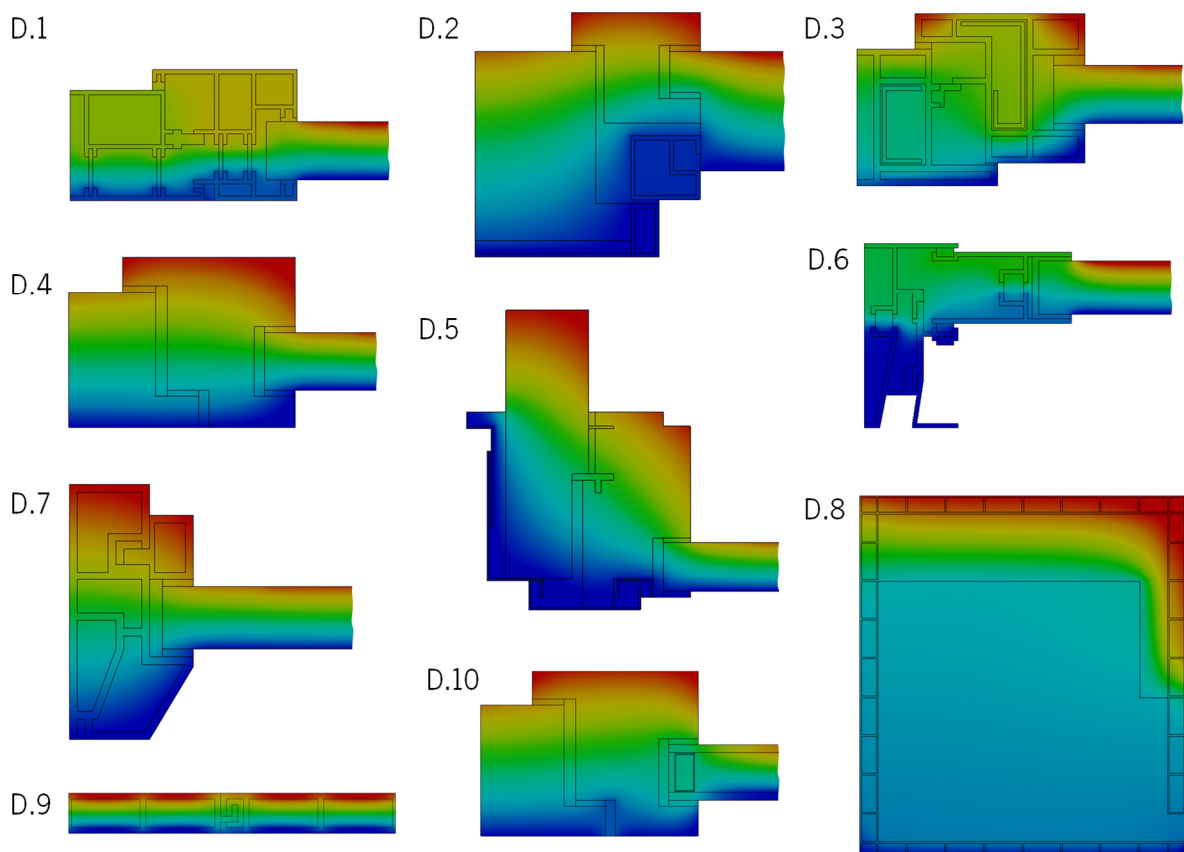


**Figure B.1.** Sections from ISO 10077-2:2017 that were simulated, to validate the software [37]. The colour profile of the sections represents the Temperature distribution under the steady state conditions of the simulation. The images of the sections had their insulation panels and glazing slashed, so that they could be presented in a more compact manner, and even though sections D.8 and D.9, are form a roller shutter box and PVC shutter profile, respectively, they were still tested.



Because the values from Table B.1 and Table B.2 are within the limits and tolerance imposed by ISO 10077-2:2017, the software was validated and can be applied.

**Table B.1.** Thermal conductance and thermal transmittance validation results for cases D.1 to D.9 of ISO 10077-2:2017 [37].

Section	Thermal conductance $L^{2D}$ (W/(m.K))			Thermal transmittance $U_f$ (W/(m <sup>2</sup> .K))		
	ANSYS	EN 10077-2	Error ( $\pm 3\%$ )	ANSYS	EN 10077-2	Error ( $\approx 5\%$ )
D.1	0,56	0,55	-1,02%	3,30	3,22	-2,53%
D.2	0,26	0,26	-0,38%	1,43	1,44	0,78%
D.3	0,43	0,42	-1,42%	2,16	2,07	-4,18%
D.4	0,35	0,35	0,06%	1,39	1,36	-2,33%
D.5	0,40	0,41	1,46%	2,08	2,08	0,12%
D.6	0,67	0,66	-1,58%	4,83	4,67	-3,36%
D.7	0,28	0,29	0,06%	1,38	1,31	-5,45%
D.8	0,18	0,18	0,67%	1,01	1,05	3,90%
D.9	0,21	0,21	-0,24%	3,64	3,64	-0,01%

**Table B.2.** Thermal conductance and linear thermal transmittance validation for the case D.10 of ISO 10077-2:2017.

Section	Thermal conductance $L_{\psi}^{2D}$ (W/(m.K))			Linear thermal transmittance $\Psi_s$ (W/(m <sup>2</sup> .K))		
	ANSYS	EN 10077-2	Error ( $\pm 3\%$ )	ANSYS	EN 10077-2	Error ( $\approx 5\%$ )
D.10	0,47	0,48	-1,14%	0,086	0,084	-2,84%

## B.2 Infilling Gas Equivalent Thermal Conductivity

The infilling was given an equivalent thermal conductivity  $\lambda_{infill}$ , following the pattern of the example D.10 of ISO 10077-2: 2017. The thermal transmittance of the glazing doesn't consider the effect of the junction with the frame nor the effect of the spacer [37]. Figure B.2, portrays the thermal resistances to heat propagation, considering the surface thermal resistances already discussed in Chapter 2.

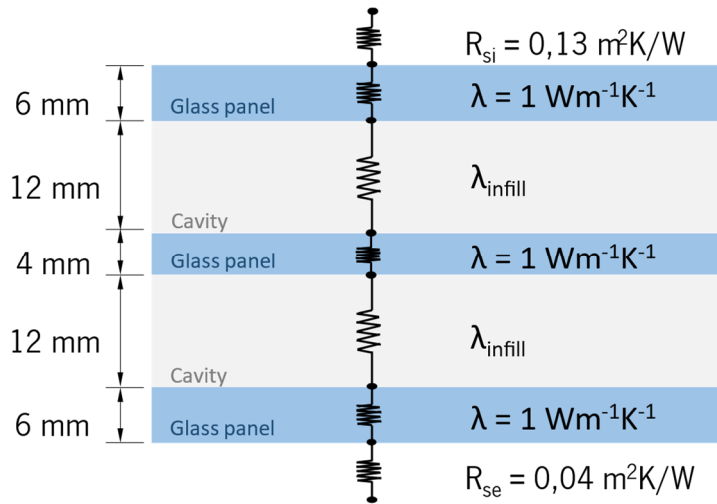


**Figure B.2.** Different thermal resistance components in series, in the middle of the glazing, without the influence of the aluminium spacer or the frame.

The total thermal resistance ( $R_g$ ) can be expressed as the sum of the individual thermal resistances since they are in series [35]:

$$R_g = \sum R_i = R_{si} + \sum \frac{\Delta x_i}{\lambda_i} + R_{se} \quad \text{B-1}$$

Where  $\Delta x_i$  is the thickness of the glass panel or the “thickness” of the cavity, and  $\lambda_i$  is its thermal conductivity (or equivalent thermal conductivity). On the other hand, equation B-2 relates the total thermal resistance and the thermal transmittance [35]:

$$R_g = \frac{1}{U_g} \quad \text{B-2}$$

Combining equation B-1 with equation B-2, it follows that:

$$\frac{1}{U_g} = R_{si} + \sum \frac{\Delta x_i}{\lambda_i} + R_{se} \quad \text{B-3}$$

Inputting the values from Figure B.2, and considering the same  $U_g$  as that of the Secco catalogue, 0,7 W/(m<sup>2</sup>K), the result is:

$$\frac{1}{0,7} = 0,13 + \frac{0,006}{1} + \frac{0,012}{\lambda_{infill}} + \frac{0,004}{1} + \frac{0,012}{\lambda_{infill}} + \frac{0,006}{1} + 0,04 \quad \text{B-4}$$

$$\Leftrightarrow \lambda_{infill} = 0,0193 \text{ W/mK}$$

B-5

# Annex C

## VALIDATION OF THE NUMERICAL MODELS

### C.1 Beam Elements Model: Verification of Mesh Independence

No mesh dependence was perceived from the results in Figure C.1.

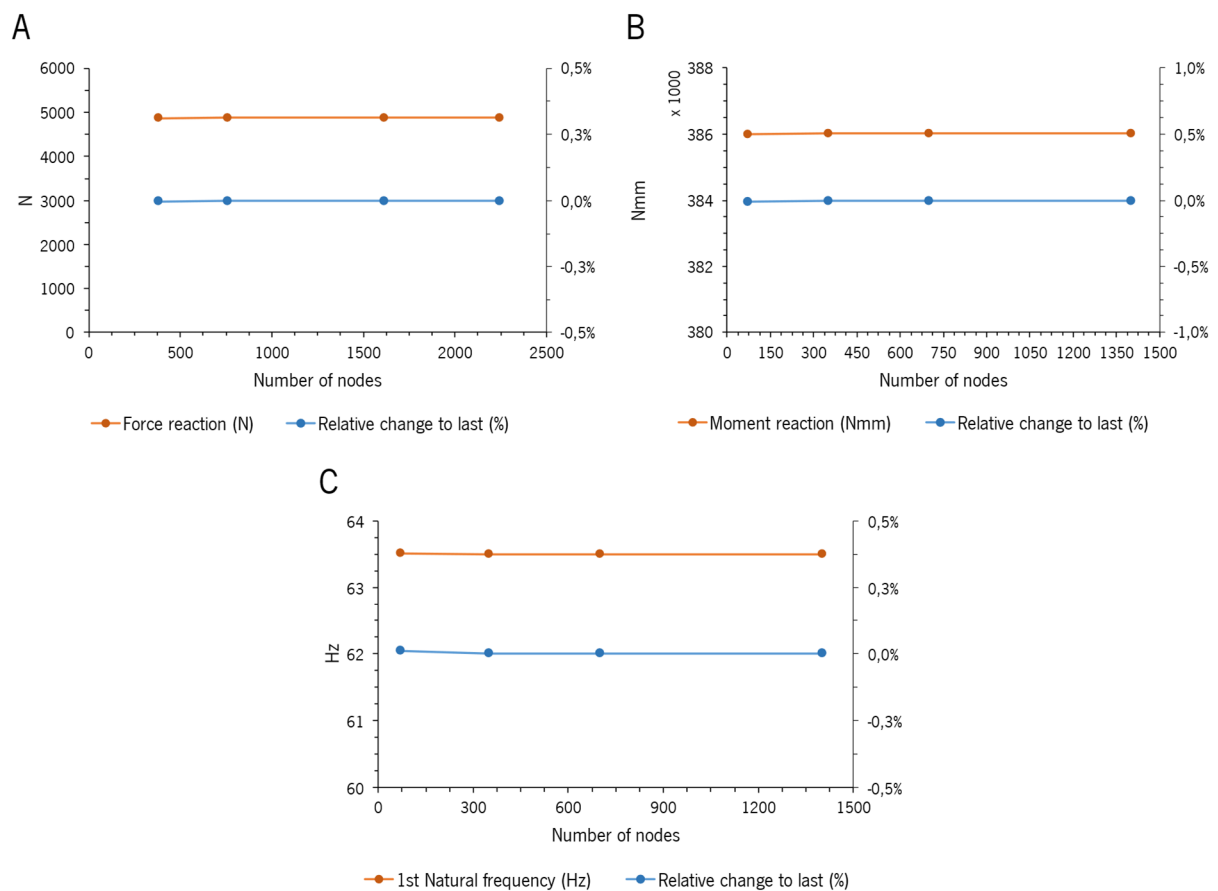


**Figure C.1.** Verification of mesh independence on the three-point bending (A), torsion (B), and undamped modal (C) simulations with the beam elements model of a P.2992 MMB with 1600 mm of length.

### C.2 Beam + Shell Model: Verification of Mesh Independence

In a mesh with a node count of 2900 (global size of 10 mm) or higher, there is no perceptible change in the results, as can be seen in Figure C.2.

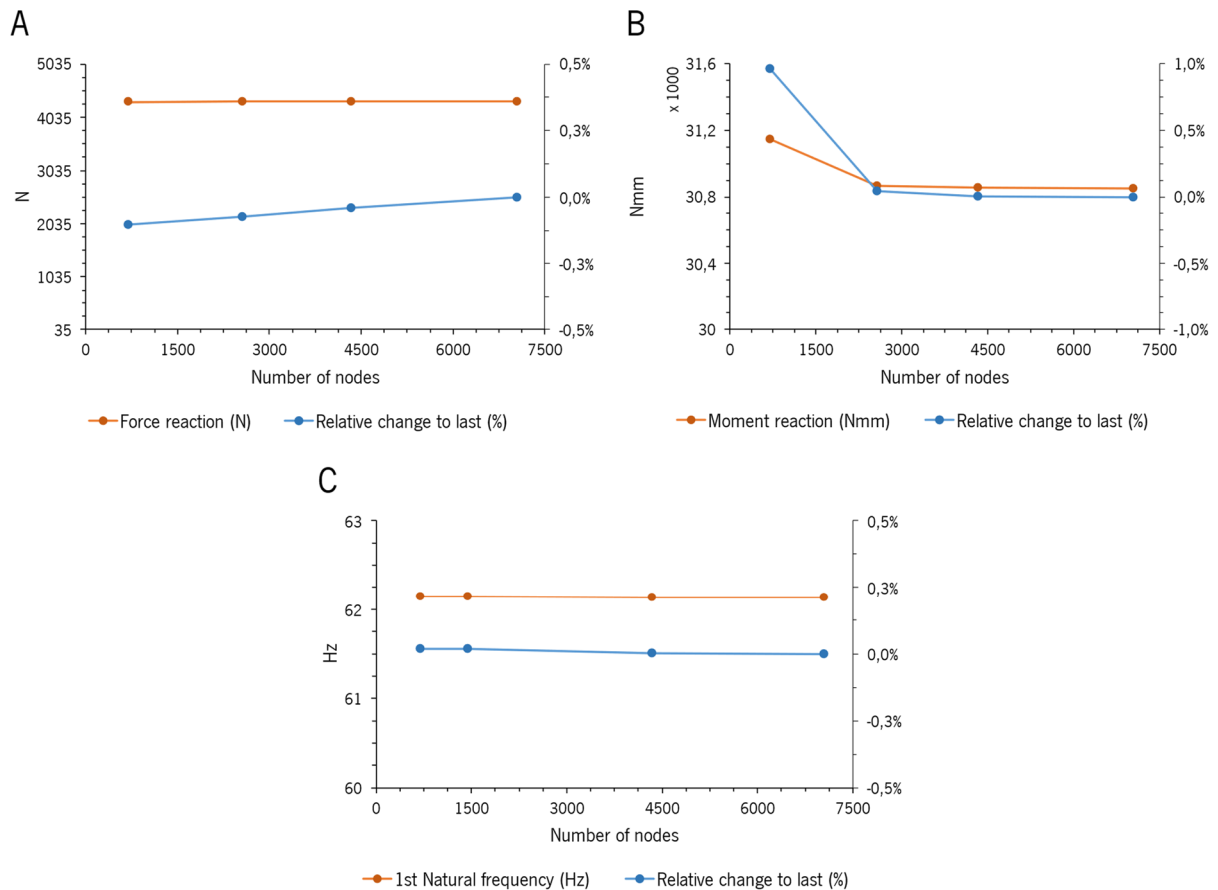


**Figure C.2.** Verification of mesh independence on the three-point bending (A), torsion (B), and undamped modal (C) simulations with the beam + shell model of a P.2992 frame with 1600 mm of length.

### C.3 Solid Elements Model: Verification of Mesh Independence

Although this model would be expected to present the best results, the node count is too high, even on the courser mesh that could be generated., which would render the model of the system an enormous size, meaning that much longer times and much better hardware than the one available would be required for the simulations. The results with the courser mesh were still reasonable in the torsion simulation results, as can be seen in Figure C.3, however, mesh with less than 29 k nodes of a P.2992 MMB with 1600 mm of length could not be generated. Moreover, with this node count, the elements were so large and distorted, that the introduction of details similar to those described for the DLD system model with the beam + shell model, would force the creation of more elements around these regions, further increasing the number of nodes. Hence, this model is not viable to be used in the DLD system.

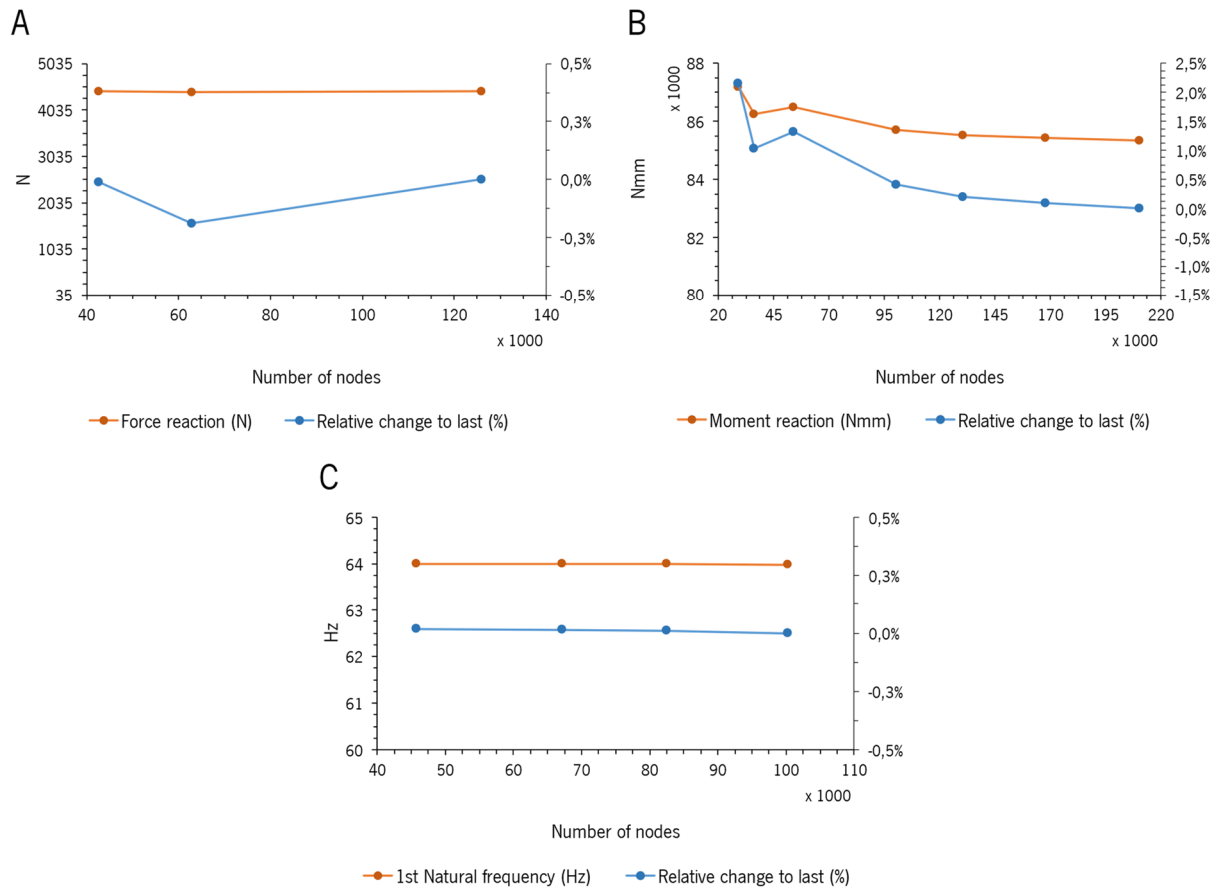


**Figure C.3.** Verification of mesh independence on the three-point bending (A), torsion (B), and undamped modal (C) simulations with the solid elements model of a P.2992 MMB with 1600 mm of length.

## C.4 Model of the DLD System: Verification of Mesh Independence and Influence of Other Modelling Choices

The mesh independence study is lengthy and slow, so it was only done for the wind loads test simulation of the brass DLD system, which is the simulation with more contacts, constraint equations and joints connected to the geometry, i.e., locations where mesh dependent results could arise. It is also the simulation, apart from the harmonic response simulation, where the displacements on the frame structure are the biggest, and that takes longer to solve. Hence, if the results of this simulation are independent of the mesh, the assumption that they are independent in all the other simulations is made. The result for the wind loads test simulation of the brass DLD system can be seen in Figure C.4.

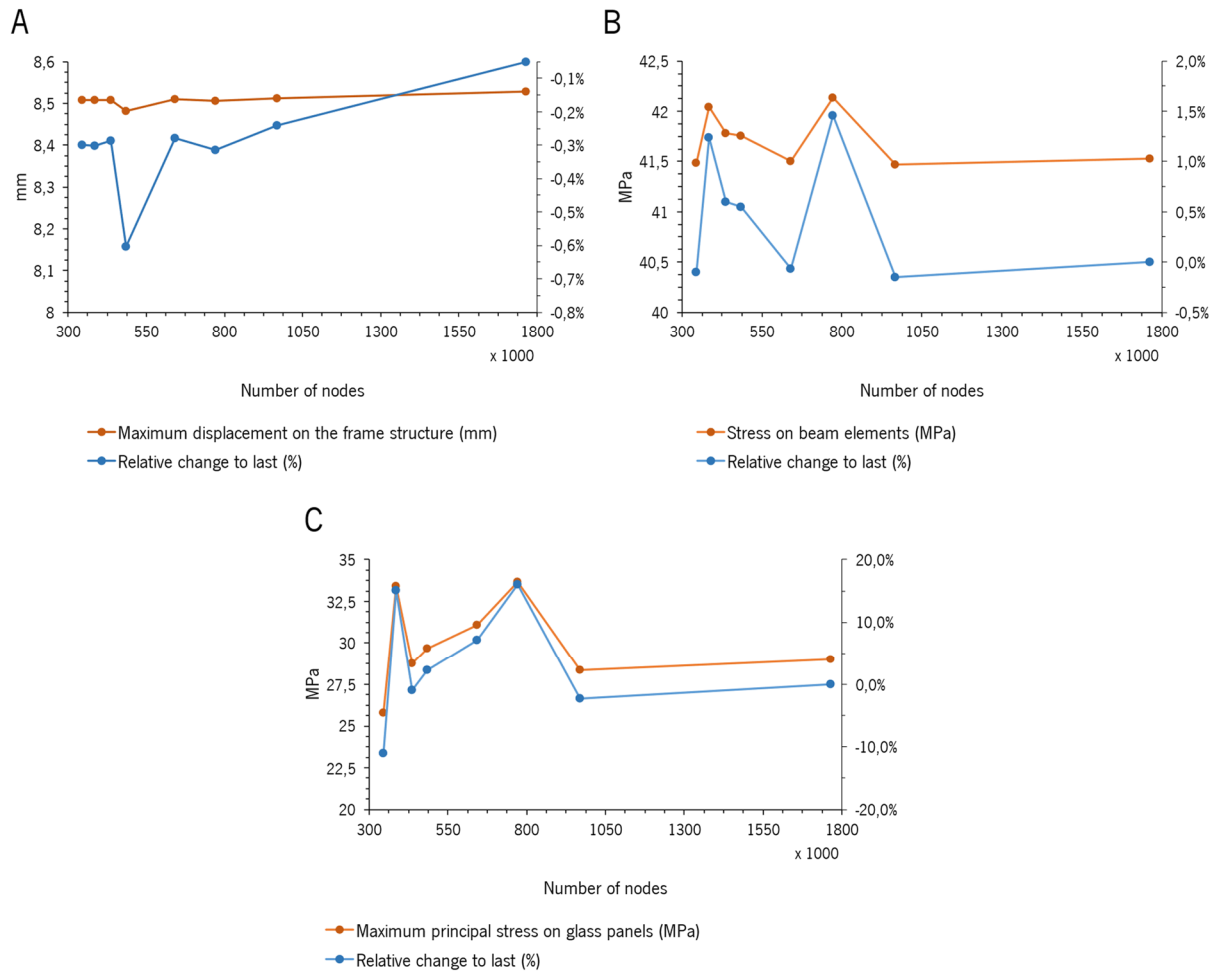


**Figure C.4.** Verification of mesh independence on the maximum displacement on the frame structure (A) and on the maximum combined stress on the beam elements of the frame structure (B), in the wind loads test simulation of the DLD system. The lack of convergence from the maximum principal stress on the glass panels for small models can be seen in C.

In addition to the verification of the mesh independence, which was conducted by varying the global element size and the number of divisions on the edges of the spacer region of the glazing, other simulations testing the influence of some modelling choices were made and evaluated by the relative difference of the maximum displacement on the frame structure, to the one from the model described in Chapter 5. In addition, the influence of the weight of the internal reinforcements was evaluated in the three static test simulations (Table C.1).

**Table C.1.** Influence of additional changes in the model of the DLD system.

Change in the model of the DLD system	Maximum displacement		Error	
On the wind load test simulation				
Distance of the dummy beam to the frame: 1 mm.	8,51		0,00%	
Elastic modulus of the beam formulation material: 4000 GPa.	8,51		-0,01%	
Element size of the central region of the glazing: 30 mm.	8,51		0,00%	
Same simulation conducted in the Transient Structural.	8,51		-0,01%	
Removal of HSFLD242 elements.	8,07		-5,09%	
Use of a complete reinforcement on all locations with a material of $E=0,1$ MPa, $\rho=20000$ kg/m <sup>3</sup> , and $\nu=0,3$ to evaluate the effect of the weight of the internal reinforcements.	8,51		-0,04%	
On the static torsion test simulation				
Use of a complete reinforcement on all locations with a material of $E=0,1$ MPa, $\rho=20000$ kg/m <sup>3</sup> , and $\nu=0,3$ to evaluate the effect of the weight of the internal reinforcements.	Primary leaf	Secondary leaf	Primary leaf	Secondary leaf
	3,47	3,44	-0,03%	-0,51%
On the static torsion test simulation				
Use of a complete reinforcement on all locations with a material of $E=0,1$ MPa, $\rho=20000$ kg/m <sup>3</sup> , and $\nu=0,3$ to evaluate the effect of the weight of the internal reinforcements.	Primary leaf	Secondary leaf	Primary leaf	Secondary leaf
	0,018	0,018	-0,10%	-0,20%



# Annex D

## INTERNAL REINFORCEMENT'S MATERIAL SELECTION

When choosing the reinforcement's material, several aspects need to be accounted for. The aim is to search for a material, with the capacity to increase the stiffness of the beam to an extent where it remains economically viable, without significantly increasing its mass, as it would increase the load on the hinges.

Though there are other ways to initiate this selection process, a graphical approach was used, by observation of Ashby's diagrams, as well as other graphs that allow for the visualization of a categorization of the materials based on a certain property [96]. Ashby's charts often plot two material properties and are accompanied by indices that evaluate the performance of the material in the function, objective and constrain of the studied component. For a beam under bending (function), which is expected to have its weight minimized (objective), while retaining its stiffness (constrain), the material index is circled in green in Figure D.1 [96].

Although a mention of material indices is relevant, it is important to keep in mind that the reinforcement beam must be bonded to a multi-material beam, that is part of a larger system that defines a window/door. Consequently, since the index was determined for a single beam, and not the whole system, it is of no-good use [96]. For similar reasons, the range of materials, taken by the reinforcement, that could have any measurable influence on the stiffness of the whole system becomes even more limited, and the value of 100 GPa was arbitrarily defined as the minimum elastic modulus so that using the complete reinforcement in the centre of the system provides an increase well above 5% in the wind load test simulations (Figure 6.11).

To evaluate the relation between the stiffness a certain material provides with the amount of weight the beam inherits from it, a plot of the material's elastic modulus and density, with logarithmic axes, was used.

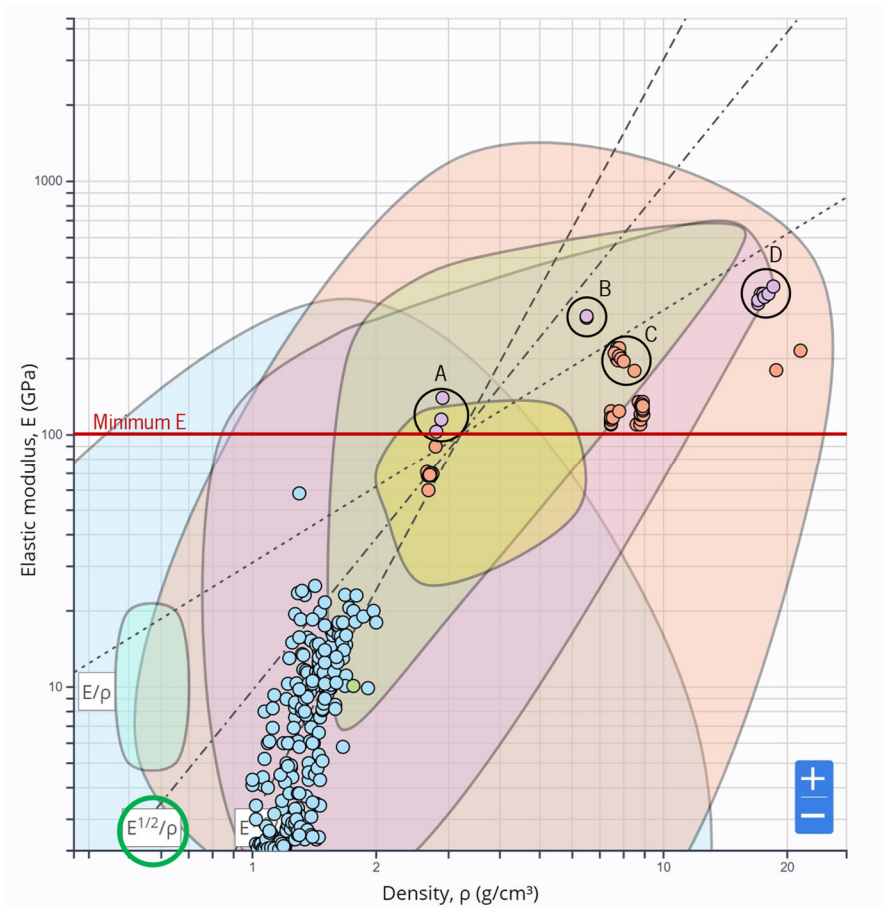


**Figure D.1.** Ashby chart from Matmach, resultant of the application filter: “Aerospace Structures”, “Composite Reinforcements”, “Building Structures”, “Construction Materials”, “Other Shafts & Couplings” and “General Automotive Parts”. In the chart, the minimum elastic modulus defined was drawn by a red line, the material index for a bending application of a beam is circled in green, and four groups are highlighted by black circles (A, B, C, and D). Adapted from [97].

The chart in Figure D.1, was taken from Matmach.com, which is a website intended for material selection [97]. Matmach’s database is big, free and deals with real commercially available materials that are linked to suppliers. However, more complete (but paid) databases are available, one of which is Ansys Granta Selector, which is the most known. Matmach provides various filters, and the adopted procedure was to filter by application, with the property of interest being the elastic modulus [97]. Thus, the material’s database was filtered by the following applications: “Aerospace Structures”, “Composite Reinforcements”, “Building Structures”, “Construction Materials”, “Other Shafts & Couplings”, and “General Automotive Parts” [97]. The application spectre could be broader, but it was appropriate to keep the choice of applications as objective as possible since the position of a certain material in the chart could be appealing, but of difficult to manufacture. The application field is the first indicator (although flawed) that the manufacturing of a long bar with a relatively small cross-section might be possible.

For the selected filters several materials appear. Taking Figure D.1 as a guide, group A consists of metal composites of aluminium base and silicon carbide reinforcement, intended for aerospace use, where the maximum elastic modulus was 140 GPa, with a density of 2,9 g/cm<sup>3</sup> [98]. Group B locates ferro-titanites, another metal matrix composite, but of iron and titanium carbide (up to 45%), used for metalworking tools and wear parts, being able to reach an elastic modulus of 294 GPa, with a density of 6,5 g/cm<sup>3</sup> [99]. In group C, the steels can be found, sometimes alloyed with chromium, manganese, and silicon, that can slightly increase the elasticity of the material, besides improving other properties [100]. The maximum and minimum elastic modulus is 220 GPa and 195 GPa, respectively, with the density ranging from 7,6 to 8 g/cm<sup>3</sup> [101]. In group D, tungsten alloys can be seen, which can have elastic modulus as high as 385 GPa, with a density of 18,5 g/cm<sup>3</sup> [102]. The other materials in the chart are outperformed by the groups already mentioned, particularly group C, containing steel, and so those materials become irrelevant for this application.

By a website error, not all materials that passed the applied search filter are present in Figure D.1, and a few appear only in a list that accompanies the chart. That is the case of Zylon PBO a synthetic fibre with high stiffness (270 GPa) and low density (1,56 g/cm<sup>3</sup>), that has many applications like ballistics, firefighters' clothing and bicycle spokes [103]. High stiffness carbon fibre composites also appear in the list, with an elastic modulus of 238 GPa and a density of 1,76 g/cm<sup>3</sup>, having applications that vary from the aerospace industry to sports goods [104]. A material that also stands out in the list is beryllium, which has structural applications in aerospace engineering, being used in the structure of the recently launched James Webb Space Telescope [105]. Several beryllium-based materials appear in the database, with the stiffer being "S-200-F H Beryllium Structural grades", with an elastic modulus of 303 GPa and a density of 1,84 g/cm<sup>3</sup> [106].

The most difficult role in material selection lies in determining the real cost of a finished product, which includes not only the cost of the material but also the cost inherent to all the necessary stages to obtain the final shape, the cost of transportation, etc [96]. Consequently, more robust research involving numerous interactions with different suppliers would be needed. In this chapter, although a few suppliers were contacted, not all contacts were fruitful, and the price of the bar of a certain material is inferred based on its common application, as well as the cost in Figure D.2, taken from [96].

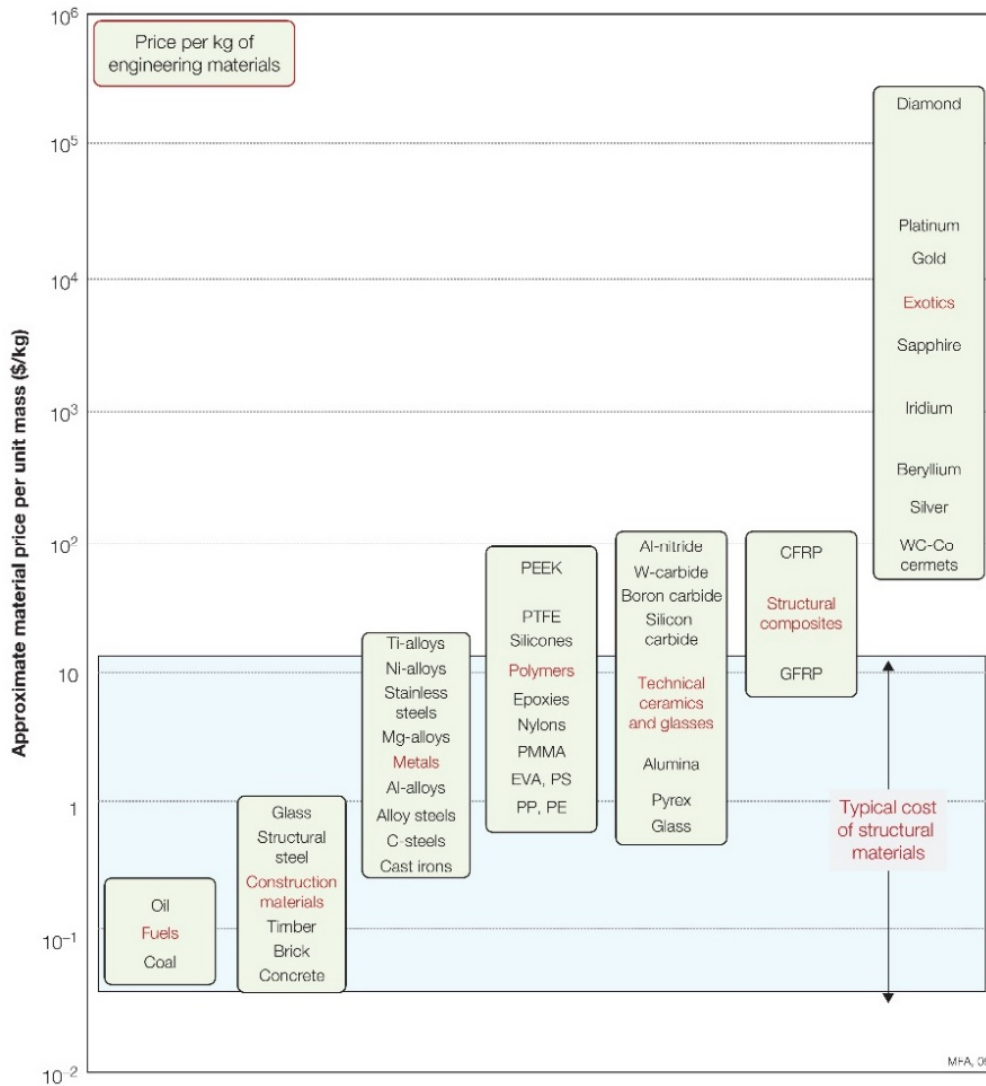


**Figure D.2.** Price per unite weight for materials. The shaded band spans the range where the most widely used commodity materials of manufacture and construction. Reproduced from [96].

From the selection groups A, B, C, and D, the most attractive materials would be the ferro-titanites and the tungsten alloys, since they possess a high elastic modulus that would certainly increase the stiffness of the door system, in a way that the materials in group A and C couldn't. However, the application of these materials is generally destined for smaller components, for instance, smaller than 9×12×3625 mm rectangular bars, which is approximately the dimension of a reinforcement that uses all the available space on the MMB of bigger dimension in the frame structure. Moreover, looking at the manufacturer of the tungsten website (Plansee), in their product datasheet, a rod with a diameter of 8,5 mm with a length of 330 mm of the product Densimet® – D176, would cost around 104 € without taxation, so a full bar of 3625 mm would cost around 1142 €, without taxes, for a product already on the shelf, which is assuming that a bar of that length is manufacturable by the company and that it keeps

the price proportional to the price of the smaller rod, that would hardly be true [107]. Since the manufacturer doesn't include rectangular bars in the product datasheet, the bar would be a custom product, and would certainly be the costlier. The elastic modulus is considered more important than the weight of the reinforcement since the added weight only had a perceptible influence on the results from the vertical loads test simulation, so the density of tungsten alloys wouldn't be a major problem.

From the materials that only appear in the list, Zylon PBO has some very advantageous properties, however, a supplier is not listed for the material. After finding a supplier (Toyobo) of the material it was discovered that the compressive strength of this material is very low, and "It is impossible for you to use Zylon 100% composites as a structural material" [108].

The company ICE was contacted for a budget estimation, and although a 9×12×3625 mm rectangular bar, was "definitely possible" for them to manufacture, they take projects that involve 500-1000 units and recommended the search of a pultrusion company, like Creative Pultrusions (which is now part of the CCG group), in the hope to tag on to an existing production run they are doing, but some flexibility on the dimensions would be needed [109]. Any attempts to contact the pultrusion company were in vain.

The last company contacted was the beryllium company Materion, which would be the most exotic material on the list [110]. The company can produce a maximum of 9×12×500 mm reinforcement, so the bar would need to be joined together, and a lot of safety measures would need to be taken for the operation of this material, as it raises some health concerns [111]. For a batch of 8, each bar would cost 3,356 USD, meaning that budget for the reinforcement would be largely surpassed.

This Annex was ultimately an exercise on what materials are available that came from the company asking the search to not be limited to conventional materials, the advantages they could provide to a door or window system, as well as the cost at which this reinforcement would come, as many of these materials are not usually applied with this purpose. As expected, the better performing materials are more difficult to access, some of them are even destined for applications with much higher budgets than the construction of doors and windows, like space exploration. In the end, steel would prevail as the most reasonable option since it provided good results in Chapter 6 and is cheaper than the other materials when comparing prices with the suppliers' information and with Figure D.2. A 25,4x9,53x6000 mm bar that could be split into 2 reinforcements for the larger side of the leaf plus two for the smaller side of the leaf, costs around 25,47€, for an A36 Steel, which is a much more realistic value [112].

# Annex E

## NUMERICAL ANALYSIS OF THE BRASS TENSILE TEST AND TENSILE TEST SPECIMENS' TECHNICAL DRAWINGS

### E.1 Numerical Analysis of the Brass Tensile Test

To define the bilinear hardening model of brass, a 3D numerical analysis of the brass test specimen in the Static Structural module of Ansys Workbench was performed, where the tangent modulus was parameterized, and only the elastic modulus (102,65 GPa), Poisson's ratio (0,3) and yield strength (248,6 MPa) were used as material inputs. The model was ¼ of the test specimen, had the correct symmetries applied at the faces (Figure E.1 - A), the displacement applied at the grips (Figure E.1 - A), and the reaction probe to this B.C. was used to find the reaction force in the axial direction. Additionally, a fine mesh was achieved by turning the option "Capture proximity" on in the sizing definitions (Figure E.1 - B) and the default analysis settings were used.

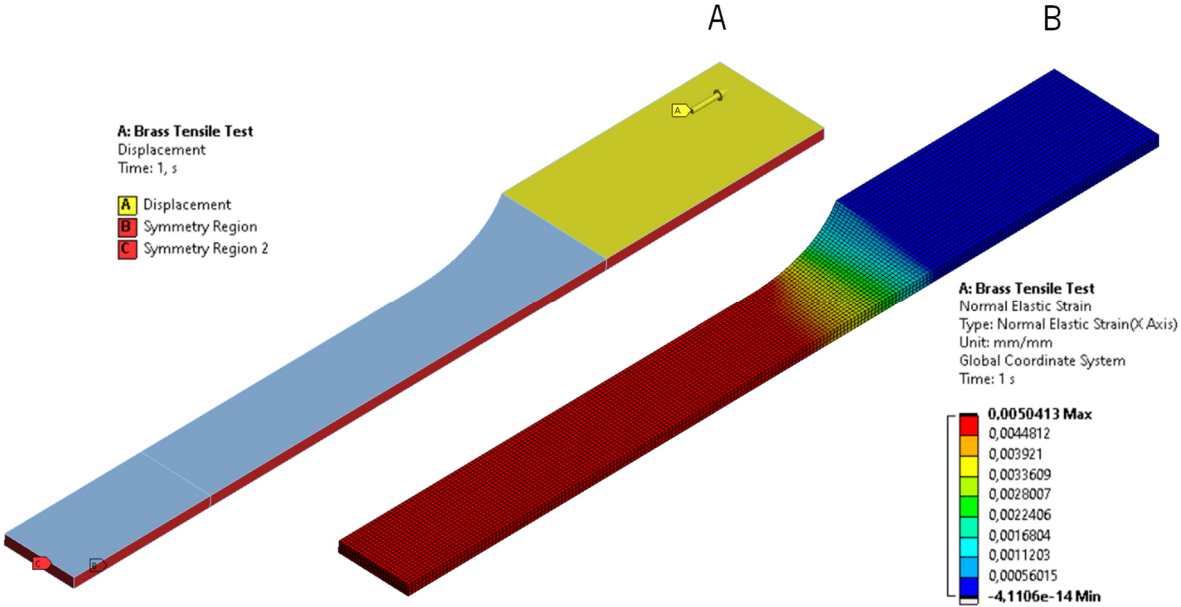
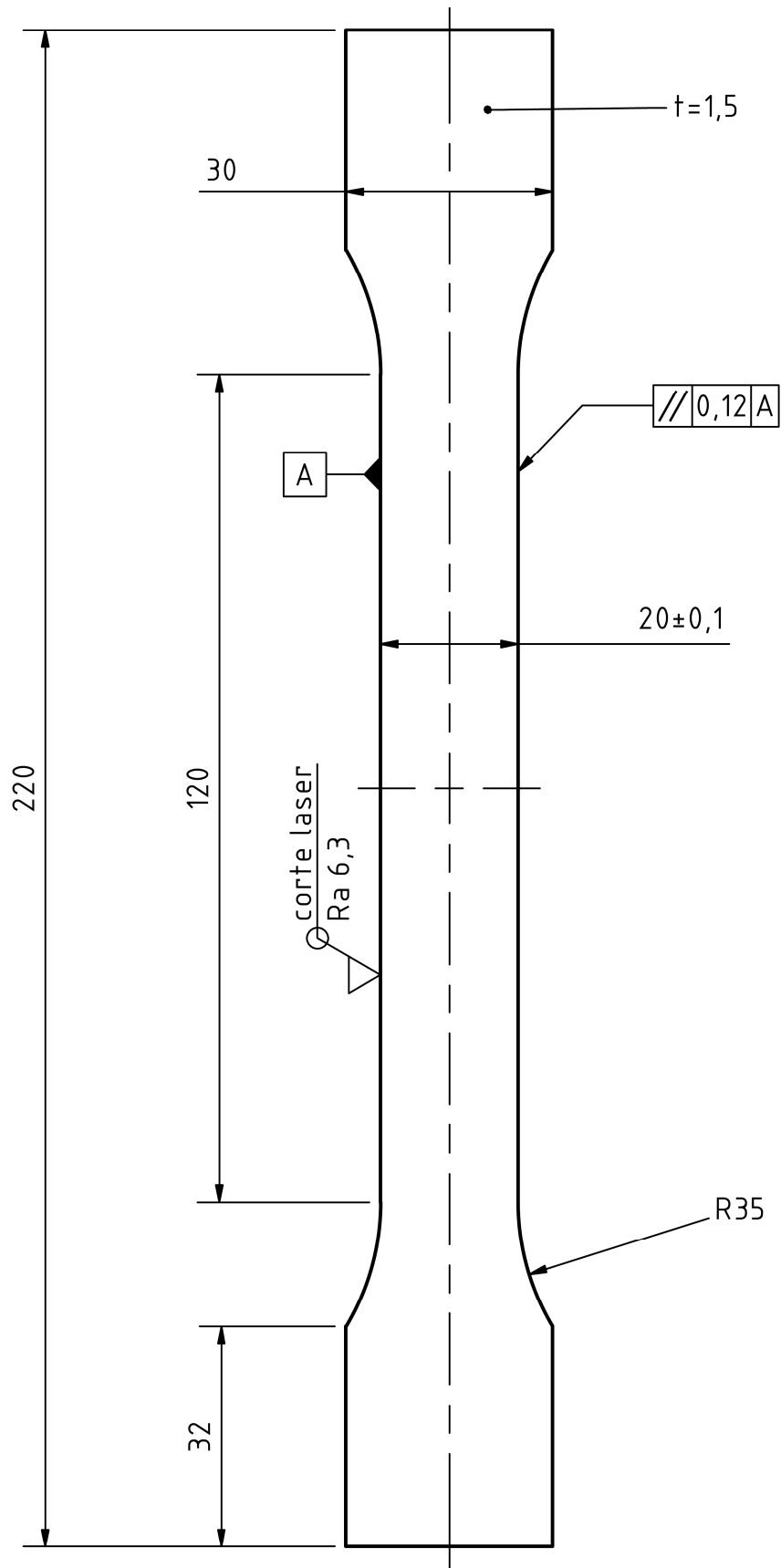


Figure E.1. Boundary conditions (A), mesh (B), and results of the elastic component of the strain in the X direction (B) of the simulation of the brass test specimen's the tensile test.

The objective was to find the reaction force that corresponded to half of the force retrieved from the experimental results at the ultimate stress point, when half the displacement at that point was applied. The force in the ultimate stress point is the highest force achieved in the experimental test (11539,1 N), and both the force as well as the displacement (46,6 mm) at that point were taken as an average made from the three experimental tests. Despite this being a numerical analysis, due to its simplicity and relevance, it wouldn't be pertinent to expose it in Chapter 5, thus it is presented in this annex.

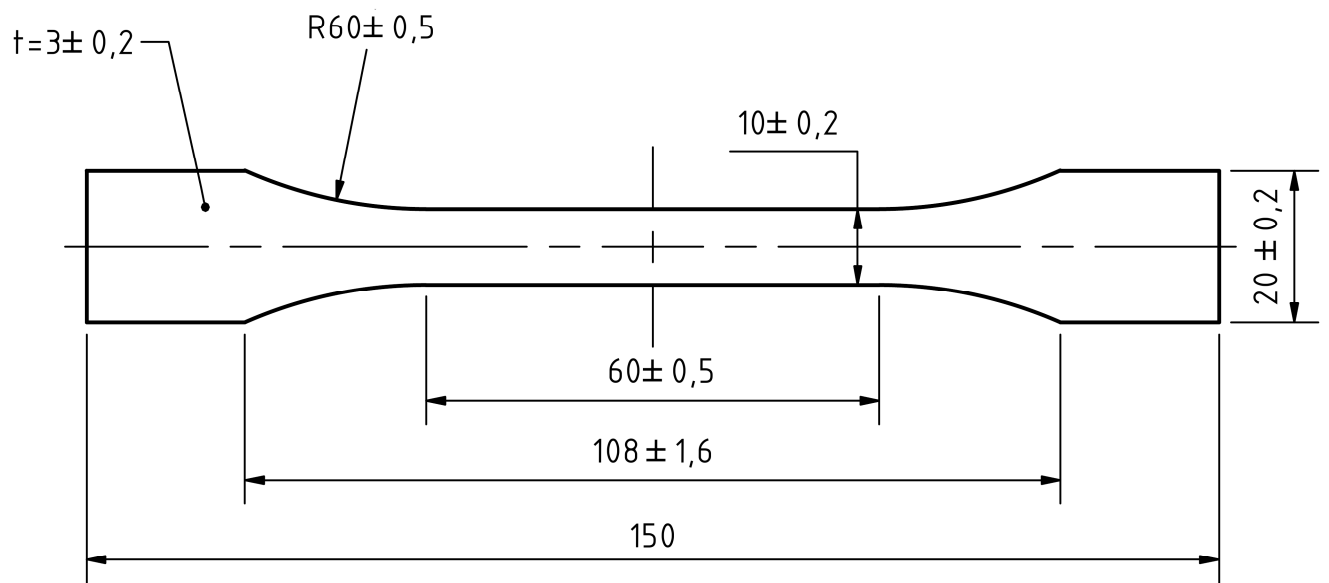
## **E.2 Tensile Test Specimens' Technical Drawings**

The brass and PA test specimens were obtained from an MMB of the EBE 85 profile series, with the appropriate dimensions and tolerances as defined by ISO 6892-1:2009 for the brass test specimen and by ISO 527-2:2012(E) for the PA test specimen.



Proj.	22/04/21	António Alves	Universidade do Minho Departamento de Engenharia Mecânica	JFAN Steel					
Des.	22/04/21	António Alves							
Copiou									
Verific.									
Escala 1:1	Provete Metal			1					
ISO 6892-1: 2009									
Substituiu desenho nº:									
Substituído por:									





Proj.	22/04/21	Anf3nio Alves	Universidade do Minho Departamento de Engenharia Mecânica	JFAN Steel					
Des.	22/04/21	Anf3nio Alves							
Copiou									
Verific.									
Escala 1:1	Provete Poliamida			2					
ISO 527-2: 2012(E)									
Substituiu desenho n3:									
Substituido por:									

# **Annex F**

**PAPER ACCEPTED FOR SUBMISSION IN THE 4<sup>TH</sup> INTERNATIONAL**

**CONFERENCE ON MATERIALS DESIGN AND APPLICATIONS**

**2022**

# Simulation strategies for dynamic and static behaviour of composite beams

**A.C. Alves, S. Alves, N. Peixinho, V.H. Carneiro, João P. Mendonça, O. Rodrigues**

## Abstract

Doors and windows represent a vital role in domestic energy efficiency, and multi-material beams with a thermal break can be fundamental in terms of energetic sustainability. Their static and dynamic structural performance is fundamental to ensure a proper thermal insulation. Two multimaterial composite beam topologies were tested in a three-point bending, while one was subjected to an experimental frequency response analysis. FEM models were created for the composite beams, using beam elements (BEAM189) and solid elements (SOLID186) with a shared topology configuration. Their capacity to predict the static and dynamic behaviour of the beams was assessed by comparing the numerical results with the experimental and analytical data. It is shown that the three-point bending behaviour of the physical beam could not be realistically captured by the 1D beam elements model, as their cross-section with different components could not be coupled due to the relatively low stiffness of the polymeric components. However, the eigenfrequencies from the beam elements were very close to those measured experimentally, meaning the dynamic modulus at low strain values could keep the beam's cross-section in-plane during the experiment. On the other hand, the 3D solid elements had the opposite outcome, agreeing with the experimental three-point bending test but not with the experimental modal analysis.

**Keywords:** Composite beam, three-point bending, multi-material beam, beam elements, solid elements.

## 1. Introduction

The current design trends of doors and windows systems were, and continue to be, heavily influenced by the rising demand in Europe for energy-efficient doors and windows. [1] For this reason, it became imperative to develop solutions that cater to sustainable living. To comply with additional consumer demands, such as a sense of space, natural light and better ventilation, glazing has taken over most surface space in door and window structures. [2] In addition, with innovative glass technology and assembly, it is possible to achieve excellent thermal performances while making glazing the primary building material. [3] Furthermore, to assure adequate natural light and ventilation, the size of doors and windows can be increased, and their positioning can be altered, sometimes spanning over entire walls. Hence, taller, wider doors and windows, with almost non-visible frames, are a popular option nowadays. [2] In addition, aesthetically, there is a preference for slender door and window frames that showcase the exterior view and allow more surface space for the glass panel. [4] Ideally, given the current trends, the beams that make up the frame of these systems should be as thin as possible. However, this constitutes a structural problem since these systems must abide by European standards and

manufacturer technical guidelines that often require stiff beams. Therefore, the design of door and window systems, of large dimensions, with very slender frames has to take into account European certification tests that require a minimum level of structural strength and stiffness.

An efficient and practical solution to the mentioned problems would be to increase the width of the beams used in the design of these structures. However, given the aesthetic requirements for slenderness, the said solution is often not feasible. In other words, the increased mechanical properties provided by a stiff beam are forgone. Instead, a slender option is selected, more visually appealing, despite the increasing cost and demand for additional structural reinforcement. In these cases, the door and window systems must be designed outside the manufacturer's specification, and their rigidity and resistance must be increased without hindering their CE certification.

In addition, and despite not directly affecting the certification of doors and windows, dynamic vibration analyses are essential in the interest of escaping the frequencies of the loads caused by natural phenomena such as earthquakes and hurricanes, and, consequently, prevent resonant effects in these systems. These loads are random and therefore non-deterministic, meaning that the future of the displacements, velocities and accelerations generated by these loads are hard to predict. These phenomena produce loads distributed in a wide frequency range, without significant peaks occurring in the frequency domain graphs. However, if such type of event has been measured on many occasions for a sufficiently long period, its statistical properties can be deduced. These phenomena are then described as a stationary stochastic process, and it is possible to assume that they follow, e.g. a Gaussian distribution. The frequencies at which the loads are applied can be plotted statistically using a power spectral density (PSD) [5][6][7]. Furthermore, to estimate the performance of the door or window system, its displacements and stresses must be evaluated. Consequently, since these values depend on damping, a correct damping characterization is essential to predict the dynamic behaviour of the structure in analysis.

To guarantee that door or window structures are designed well enough to pass the necessary certification, it is essential to predict their performance. The trial and error method implies unnecessary costs that would otherwise not exist if numerical simulation were used. Hence, numeric methods, such as the Finite Element Method, combined with parameterized analyses, can be a precious help. Some scientific works can be cited regarding the application of FEM in static structural analysis to increase the resistance or rigidity of beams.

In 2016, Zhang et al. [8] used LS-DYNA, a non-linear explicit finite element code, to simulate the three-point bending test of empty and reinforced multi-cell square tubes, which would then be validated by experimental testing. The goal was to then develop parametric studies that would investigate the influence of geometry configurations and loading conditions on the bending resistance of the tubes. Xiong et al. [9] also analyzed the bending behaviour of structures using experimental data and a numerical model to simulate a three-point bending test. The analyzed structures were thin-walled square beams under quasi-static and dynamic loading. In terms of composite structures, Aguib et al. [10] analyzed the static behaviour of sandwich beams subjected to bending by a transverse load. The performed FEM analysis allowed the determination of the displacement response of the beams. Afterwards, the authors used Abaqus software to analyze the static behaviour of the sandwich beams. In 2022, approaches have been conducted for the case of a block matrix formulation of an uncoupled double Timoshenko beam, separated by a Winker elastic interlayer, that allowed the determination of its modal response[11].

Additionally, computational methods have been developed, by R. Eberle and M. Oberguggenberger [12], based on experimental results from bending tests and analytical data, for an Euler-Bernoulli beam with a varying cross-section along its length. All these developments can be helpful, for instance, to describe the modal response of sandwich composites or laminated beams and in defining the bending stiffness of irregular beams [11] [12]. Furthermore, it is evident that the study of beams that possess geometrical details that increase the complexity of their behaviour, e.g. variable cross-section along their length and/or multiple components, is still evolving.

This study details different approaches simulate the static and dynamic behaviour of multimaterial composite beams, using door and window frames as benchmark. Two multimaterial composite beams with complex section topologies were subjected to a three-point bending tests. One of the beam topologies was also subjected to vibrations analysis to determine its frequency response. Finally, two FEM models were created to simulate the performance of the composite beams using 1D beam and 3D solid elements. Conclusions were obtained regarding their capability to depict the static and dynamic behaviour of the tested beams once the numerical results were compared with analytical and experimental data.

## 2. Methodology

### 2.1. Beam detail

Multimaterial complex beams with complex section topologies were selected from the Secco Sistemi catalogue [13]. Their manufacturing process consists of machine rolling of the brass sheets to form the shells which are combined with polyamide and polyurethane cores (Figure 1). These models are referred by Secco Sistemi as EBE85 P.1102 and P.2992.

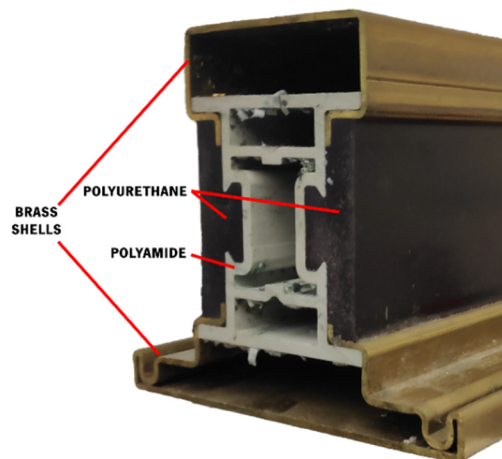


**Figure 1** - Standard Secco Sistemi material combination exemplified on an EBE85 P.1102 beam.

While the metal shells define the external geometry of the composite and influence the type of opening system the final product will have, the thermal break contributes mostly toward thermal insulation.

## 2.2. Material properties

Tensile properties of the beam materials were previously determined as part of an ongoing study. Their elastic, elastoplastic, physical properties are presented in Table 1. It may be determined that these are the fundamental properties to perform static elastoplastic structural analysis with a bilinear hardening models and harmonic analysis using FEA. The Poisson's ratio of these materials was assumed as 0.33.

**Table 1** - Experimentally obtained properties of Secco Sistemi brass, polyurethane, and polyamide. The values of the tangent moduli were retrieved from [14][15].

Material	$E$ (GPa) $\pm$ STD	$\sigma_y$ (MPa) $\pm$ STD	$\rho$ (kg/m <sup>3</sup> ) $\pm$ STD	$E_t$ (MPa)
Brass	102,64 $\pm$ 1,48	248,55 $\pm$ 6,36	8491,97 $\pm$ 4,22	926
Polyurethane	0,57 $\pm$ 0,02	31,11 $\pm$ 1,27	1134,00 $\pm$ 0,16	20
Polyamide	0,65 $\pm$ 0,01	46,29 $\pm$ 1,07	1336,03 $\pm$ 1,12	86,91

## 2.3. Experimental methods

In order to test the static and dynamic performance of the composite beams, these were subjected to a three-point bending test and an FRF modal testing. The Secco Sistemi OS275 P.2992 composite beam will be taken as an example for all other tested beams for the following detailed experimental methods.

### 2.3.1. Three-point bending

An example of the three-point bending testing is depicted in Figure 2 for the symmetric Secco Sistemi composite beam OS275 P.2992 in its brass version with a length of 1600 mm.

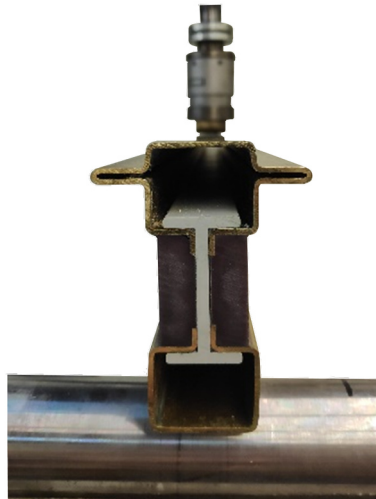


**Figure 2** - Lateral view of the Secco Sistemi OS275 P.2992 during the three-point bending test.

This test was performed in an Instron 8874 universal testing machine, with a half cylinder steel mounted at the end of the hydraulic cylinder and a steel base structure with two steel cylindrical supports. The supporting cylinders on the base structure were 1540 mm apart, and the base structure was mounted in a way that put the loading half cylinder, which was attached to the hydraulic ram at the same distance

from each supporting pin. Each beam was then placed on the supporting pins so that a transversal plane would pass at the centre of the loading cylinder, which was then lowered to be tangent to the top face of the beam. A digital gauge with a magnetic base was placed on the base structure, measuring the displacement of the beam on the bottom face on its mid-length. The Instron Bluehill data acquisition software was used again for the data collection. This detailed setup is represented in Figure 3.

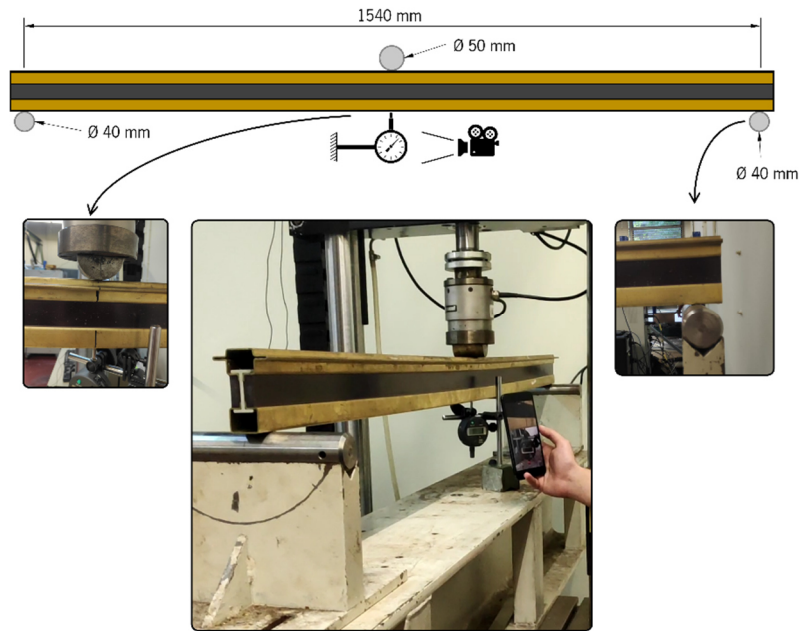


**Figure 3** - Three-point bending test setup.

Two displacement measurements took place on the mid-length of the beam during the test, one on the top face registered by the Instron Bluehill software and another at the bottom face recorded by the digital gauge. Once the displacement registered on the digital gauge reached 10 mm, it was removed since enough data was gathered to calculate the stiffness. During the test, the hydraulic ram imposed a 0.025 mm/s displacement rate until collapse was monitored.

### **2.3.2. FRF modal analysis**

The experimental vibration analysis (Figure 4) required a PCB Piezoelectric model 086c01 impact hammer was used to impose an impact excitation, while a PCB model 356A1 triaxial piezoelectric accelerometer monitored the dynamic behaviour of the beam. A LMS Scadas Mobile spectrum analyser was used to process and analyse the signal and obtain the frequency response function (FRF). After obtaining the general FRF of the system, in the z-direction, the damping ratio was determined from the first resonance frequency using the half-power bandwidth method.

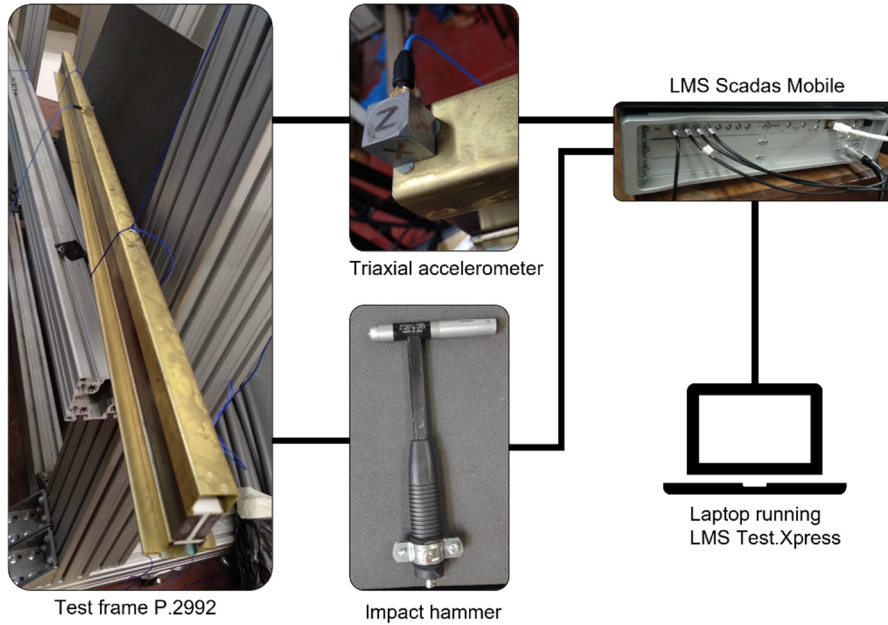


**Figure 4** - Experimental modal analysis setup.

## 2.4. Analytical method

The analytical model of the composite beams behaviour was necessary to validate the experimentally obtained results. Therefore, an analytical method was used to transform the studied composite beams into homogenous transformed versions that facilitated calculations and variable manipulation.

### 2.4.1. Equivalent beam concept

The analytical method was based on the Euler-Bernoulli beam theory. The following assumptions were made: the distinct beam elements are bonded together at the various interfaces, and the beam cross-section remains unchanged after bending. This allows for the multi-material beam to be defined as a single beam since the centre of curvature of the different elements, when bent, is the same at any point along the length of the beam.

The resulting bending moment of the beam,  $M$ , from the applied external loads, will match the resistance offered by its distinct elements, as depicted in Figure 5. Therefore, the total moment of resistance of the beam will equal the sum of the moments supported by each element as stated by equation ( 1 ).

$$M = \sum M_i = \sum -E_i I_i \frac{d^2 y}{dx^2} \quad (1)$$



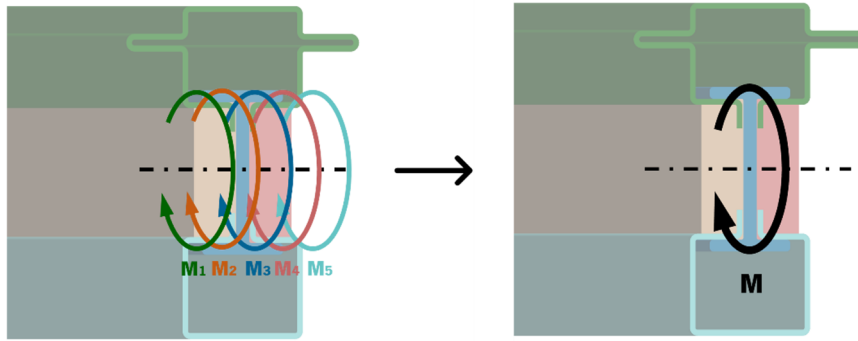


**Figure 5** - The internal moments from the five components of an MMB compose the internal bending moment that results from applying the external loads.

By rearranging equation ( 1 ) into equation (2) it is possible to obtain an equivalent homogenous beam, made of a single and arbitrarily chosen material, with an equivalent second moment of area,  $I_{eq}$ , to the original beam determined by equation (3). Figure 6 illustrates the cross-section of this transformed homogenous equivalent beam, where the material of the different components influences the weight of its elemental areas in the equivalent beam's cross-section. In this case, the equivalent beam is illustrated by expanding each elemental area by the correspondent  $n_i$  in a direction parallel to the axis of rotation. The variables  $d$  and  $b$  represent the distance between the centroid of a component's cross-section and the equivalent beam's neutral plane or the CAD software's axis, respectively.

$$M = -E_b I_{eq} \frac{d^2 y}{dx^2} \quad (2)$$

$$I_{eq} = \sum \frac{E_i}{E_b} I_i \quad (3)$$

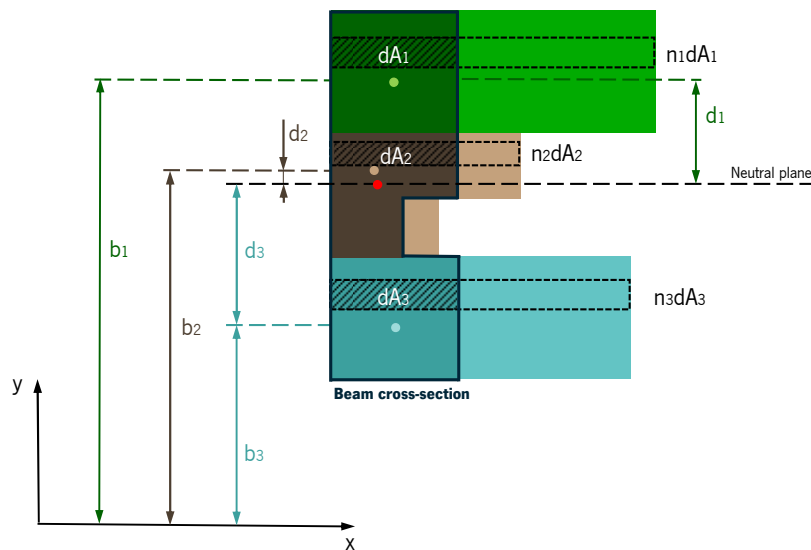


**Figure 6** - Representation of the cross-section of the equivalent beam, from the cross-section of a composite beam.

Analysing the contribution of element  $i$  to the second moment of area, a factor  $n_i$  can be singled out, being multiplied by the elemental area,  $dA$ , as shown in equation (4). Consequently, and as represented in equation (5), the position on the centroid to consider,  $\bar{Y}$ , needs to account for the factors  $n_i$ .

$$\frac{E_i}{E_b} I_i = n_i I_i = n_i \int y^2 dA = \int y^2 n_i dA \quad (4)$$

$$\bar{Y} = \frac{\sum \int y n_i dA}{\sum \int n_i dA} = \frac{\sum n_i b_i A_i}{\sum n_i A_i} \quad (5)$$

With this, other equations can be found, for instance, for a composite beam of length  $L$ , the three-point bending deflection, represented by equation (6), and the natural frequencies of the beam in the transverse direction, represented by equation (7).

$$\delta_{max} = \frac{PL^3}{48E_b I_{eq}} \quad (6)$$

$$w_n = \beta_n^2 \sqrt{\frac{E_b I_{eq}}{\sum \rho_i A_i}}; \quad \beta_n = 4,7300L; 7,8532L; \dots \quad (7)$$

## 2.5. Numerical method

The data from the experimental tests was compared to the data from numerical models developed to capture the static and dynamic behaviour of the composite beam. These models were constructed with beam elements (BEAM189, based on Timoshenko's beam theory) and solid elements (SOLID185 and SOLID186). Additionally, the geometry was prepared in Design Modeler, and the numerical simulations were performed on Ansys Workbench. The three-point bending simulation was performed in the Static Structural module, and the Modal module was used to find the natural frequencies of the composite beam's models.

### 2.5.1. 1D Beam elements model

The first developed numerical model used five 1D beam elements to represent the different components of the composite beams in analysis. This numerical model consisted of five line bodies representing each beam component and the corresponding material data, boundary conditions, and applied loads that simulated the physical problem. The static and dynamic simulations considered 1540 mm and 1600 mm lengths, respectively.

The first step in creating the beam elements model was defining a Static Structural analysis in ANSYS Workbench and adding the materials to the Engineering Data of the project. More specifically, only the elastic modulus, density, Poisson's ratio and tangent modulus were used (see section 2.2).

After defining the necessary material properties in the Engineering Data of the project, the geometry of the composite beam was defined in Design Modeler where five separated parallel line bodies, already cut for the boundary conditions to be applied in Ansys Mechanical (in the static analysis), were given the cross-sections relative to each of the composite beam's components. With the "Connect" tool, the line

bodies were joined without being merged, each vertex at a time, to the location of one of the line bodies. Then, the correct offsets were given to each line body's cross-section, as illustrated in Figure 7, before these line bodies were joined using the "Share Topology" tool. This tool resulted in coincident nodes being created on coincident geometry and the DOF of these nodes being bonded together. This step will guarantee that the separate elements will be treated as a single multi-component beam in the numerical model.

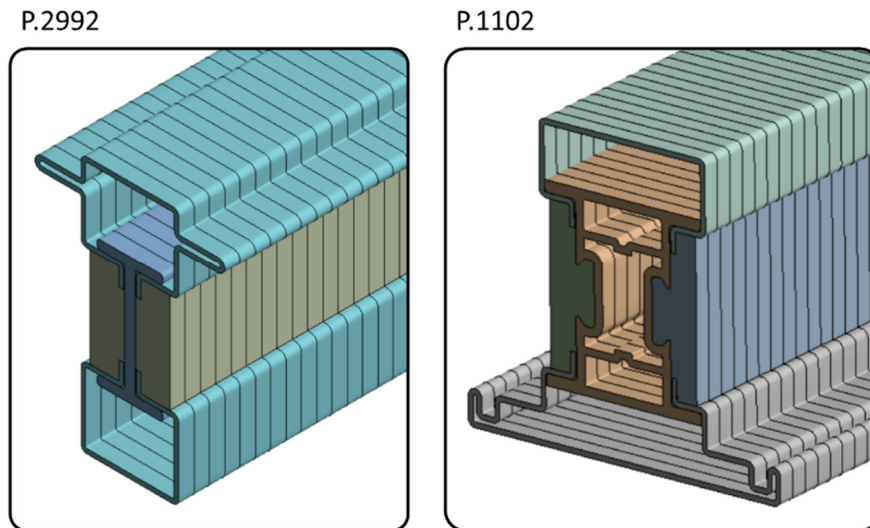


**Figure 7** - Beam elements models with the different cross-sections graphically displayed, taken in Ansys Mechanical.

A quadratic element was used in this model, more specifically BEAM189, when defining the mesh. Additionally, for the static analysis, an element size of 5 mm was selected, and for the modal analysis, a division of 100 was employed on the line bodies without the geometry split.

Once the materials, geometry and mesh properties were defined, it was possible to characterize the numerical model's boundary conditions, which represent a simply supported beam in pure bending physical problem, as depicted in Figure 8. Additionally, the large deformation effects were turned on, and several timesteps were defined. Relating the load and displacement in the vertical direction at each timestep, it was possible to build the force-displacement curve.

For the modal analyses, damped and undamped, the goal was to find nine natural/resonant frequencies, which made it possible to achieve all the values for comparison with the analytical model and the experimental data. In the damped modal analysis, damping was turned on, and the first resonance frequency and the correspondent damping ratio from the experimental modal analysis were used for the program to calculate the Rayleigh damping, considering the mass damping as zero. A range from 5 Hz to 400 Hz was considered for both analyses.

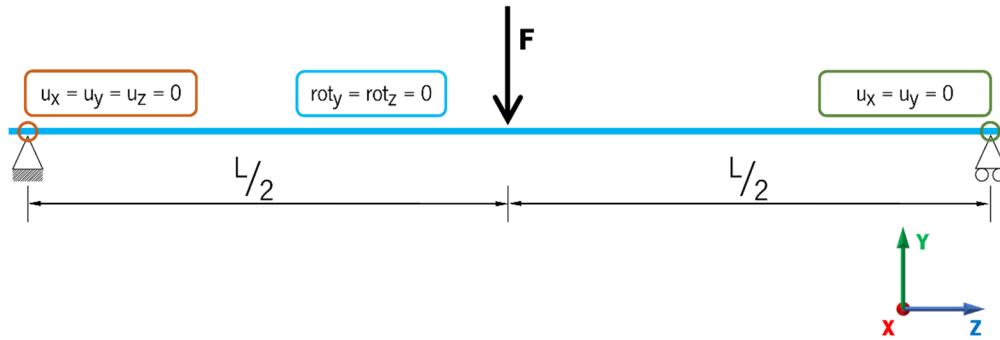


**Figure 8** - Constraints/boundary conditions applied in the static analysis of the beam elements model.

### 2.5.2. 3D Solid elements model

Compared to the beam elements model, there was no simplification of the boundary conditions in the solid elements model, and the maximum deformation could be determined for any point of the composite beam, not exclusively the neutral axis. However, there was a simplification of the beams' cross-sections. The simulations with this model were also performed in ANSYS Workbench, in a Static Structural module, for the static study, and in the Modal module, for the dynamic study, and the same materials introduced in the Engineering Data of the simulations with the beam elements model were also considered in these simulations.

For the three-point bending simulations,  $\frac{1}{4}$  of the brass composite beam was modelled, and symmetry conditions were applied in the model. By reducing the geometry to  $\frac{1}{4}$ , a significant amount of computational time was saved without affecting the results. For the P.2992 and P.1102 beams, a length of 1600 mm and 1540 mm was considered, respectively. Additionally, for the static analyses, to prepare the mesh, the geometry of the beam was cut into several bodies and strategically split near the ends to further refine the mesh in the zones where contact was expected with the loading and support pins. These pins were modelled as surfaces and had symmetry conditions applied to them. The cut geometry was bonded together using the "Share" tool, which in the case of the P.1102 profile also considered the geometry from the loading and support pins.

For the dynamic analysis, the 1600 mm beam was modelled without cuts, and the different bodies had their topology shared to bond the beam components. In the static simulation, each material was assigned to its corresponding component. The thickness of the surfaces was defined, with an offset to the interior of the loading and support pins, as their radius. Frictionless contacts with penetration of 0.1 mm and a symmetric behaviour were defined between the loading and support pins and the contacting faces of the beam, as well as between the internal beam surfaces that became into contact during the three-point bending experiment.

The static and dynamic simulations both used quadratic elements, SOLID185 (P.1102) and SOLID186 (P.2992) for the beam geometry and SHELL181 (P.1102) and SHELL281 (P.2992) for the pins. Figure 9 and Figure 10 show the meshed geometry used in the static and dynamic analyses, respectively.

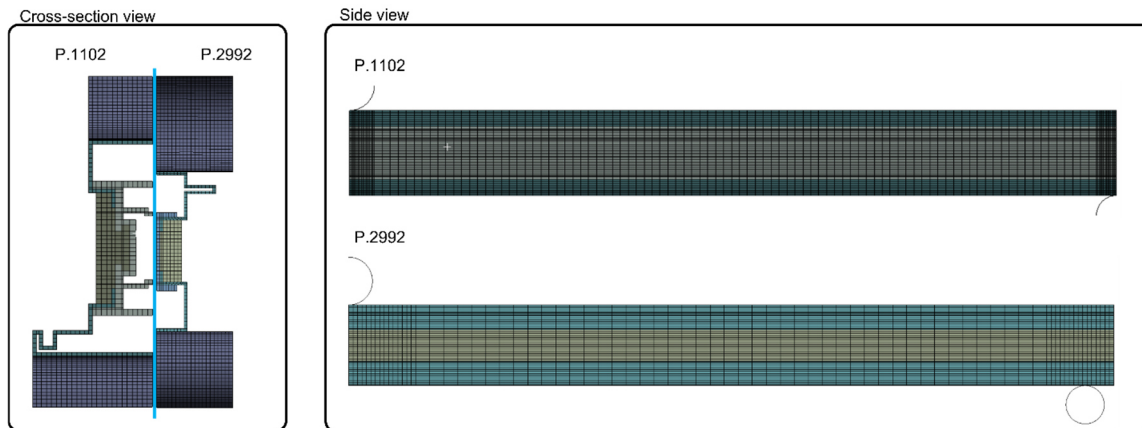


**Figure 9** - Solid elements model of the three-point bending analysis.

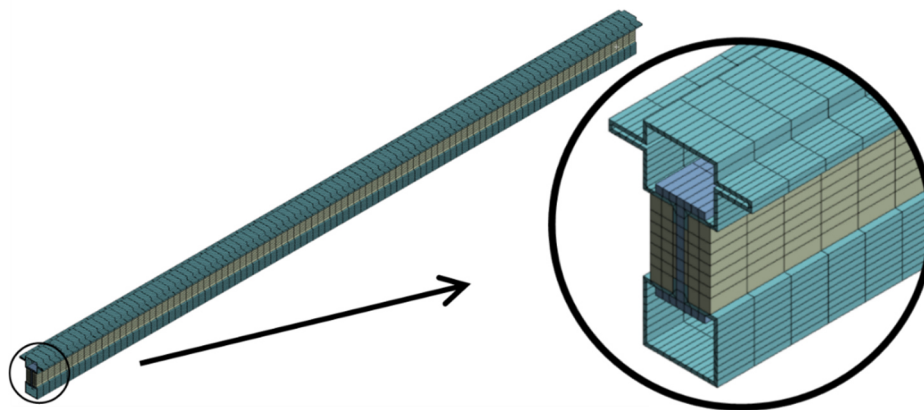


**Figure 10** - Solid elements model of the frequency response analysis.

In the post-processing phase, the displacements at the bottom and the top of the composite beam were then probed at the central symmetry plane and plotted against the reaction force ( $\times 4$ ) in the vertical direction at each timestep, allowing for a force-displacement curve to be constructed and compared with the three-point bending experimental data. Since the frequency response analysis considered the composite beam free in space, no boundary conditions were specified.

## 3. Results

### 3.1. Static analysis

In Figure 11, it is possible to observe that the analytical and numerical models have similar results despite overestimating the actual stiffness of the tested composite beams.

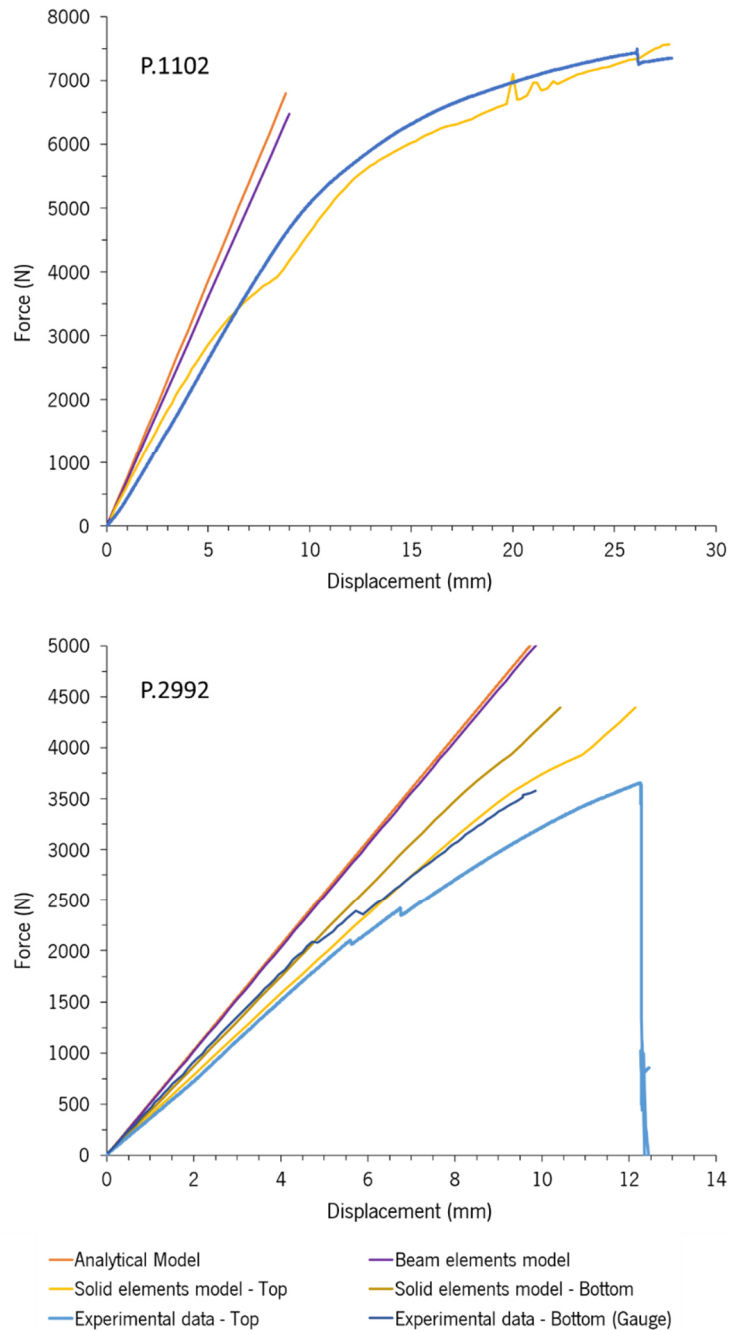


**Figure 11** - Force-displacement curves for analytical, numerical, and experimental results.

When discussing the graph related to the P.1102 beam's top face, it is possible to conclude that the curves for the solid elements model and the experimental data essentially overlap. For the P.2992 beam, this only occurs in the initial section of the graph. In addition, for the same beam, it can be observed that there are small but abrupt drops in force in the experimental data, which are linked to the loss of adhesion between the composite beam components. The final drop is related to the complete loss of adhesion between one of the brass components and the rest of the beam. Since the adhesion of the interface between the different components of the beam was not accounted for in the solid elements model, this model only depicts the experimental data on the initial part of the curve. It could also be observed that indentation caused by the loading pin occurred on the top face of both the solid elements model and the experimental test.

As shown in the P.2992 graph, the solid elements models can also depict the deformation of the physical beam at the bottom face, where indentation did not occur on the supports or the loading pin, meaning that this curve can be taken as representative of the composite beam's real force-displacement curve.

The analytical and the beam elements models overestimate the stiffness of the physical beam, however this is not observed in the solid element models. This can be attributed to the formulation and the elastic moduli of polymers. Both the analytical method and the beam elements models assume the beam's cross-section remains in-plane, i.e., they follow the Euler-Bernoulli and the Timoshenko beam theories. However, this doesn't happen, as the elastic moduli of the polymers do not provide these components with enough stiffness to resist the deformation that results from the longitudinal shear stresses that appear when the composite beam is bent. As the solid elements model can capture this drop in stiffness, its results are coherent with the experimental data at the bottom of the beam. Figure 12 details the deformed shapes that support this hypothesis.

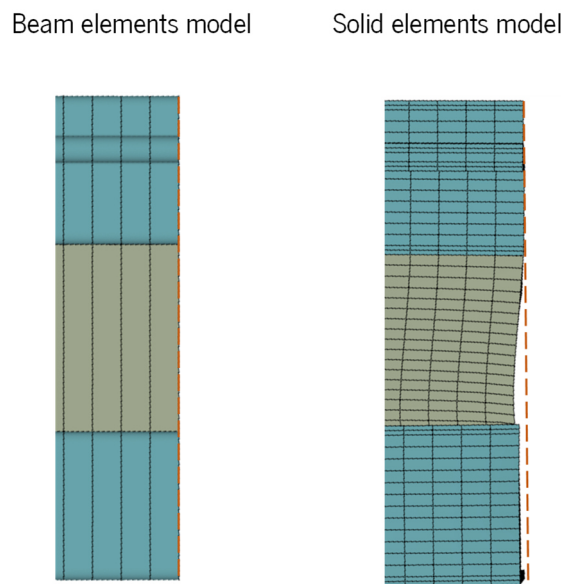


**Figure 12** - Deformation at the end of the composite beam by a factor of 40 for the numerical models, where the beam elements model is the only one that keeps the cross-section of the composite beam in-plane.

### 3.2. Frequency response analysis

The results from the experimental modal analysis of the composite beam can be found in the FRF plotted in Figure 13, where three significant eigenfrequency peaks can be identified. Using the half-power bandwidth method applied on the first peak, a damping ratio of 0.0135 was determined.

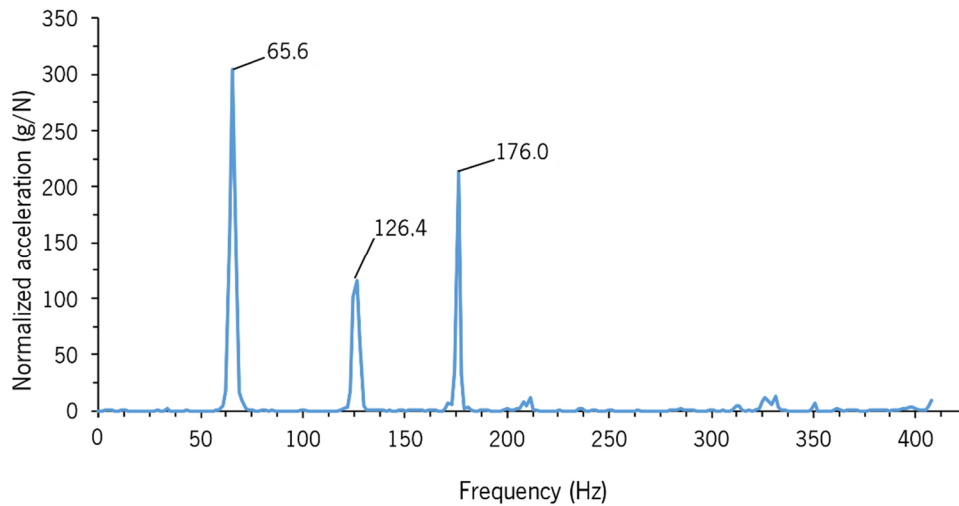


**Figure 13** - FRF modal analysis of P.2992 beam with peak frequencies.

Table 2 compares the eigenfrequency values from the analytical and numerical models to those obtained from the experimental data. With this, it is possible to note that the introduction of damping has little influence on the frequency values but still causes a slight reduction, as expected by for damped eigenfrequencies. The first eigenfrequency ( $\omega_1$ ) is relatively close to the experimental value on all models, with the error being around 3%. For the second eigenfrequency ( $\omega_2$ ), contrary to what had happened in the three-point bending analysis, the analytical and beam elements models had results closer to the experimental data, and the solid elements models presented results with much lower values, reaching a deviation of almost -10% from the experimental value. From the results of the third eigenfrequency ( $\omega_3$ ), similar observations to those from the first resonance frequency results could be made, with the slight difference that the analytical and beam elements model agree even better with the experimental data, and the solid elements model error is slightly higher.

**Table 2** - Natural and resonant frequencies results, of a P.2992 beam, from numerical models and frequency response analysis.

	Eigenfrequencies (bending modes)	Numerical				Analytical	
		Beam (Hz)	Error	Solids (Hz)	Error		Error
Undamped	$\omega_1$	63,50	-3,20%	64,00	-2,45%	63,79	-2,76%
	$\omega_2$	124,66	-1,38%	114,18	-9,64%	126,28	-0,09%
	$\omega_3$	174,00	-1,14%	171,35	-2,68%	175,84	-0,09%
Damped	$\omega_1$	63,49	-3,21%	63,99	-2,46%	-	-
	$\omega_2$	124,62	-1,41%	114,18	-9,67%	-	-
	$\omega_3$	173,89	-1,20%	171,19	-2,73%	-	-

For traditional materials (e.g. steel), the elastic modulus is assumed to be constant. However, for polymers, it has been experimentally proved that the value of this property, when determined by static and by dynamic methods, varies considerably due to the viscoelastic behaviour of these materials, which



makes them dependent on the strain rate and temperature, and exhibiting hysteresis under cyclic load, dissipating a good amount of energy. [16][17][18]

The increase of stiffness of the beam in vibration, due to the increase in the elastic modulus, can explain why the second resonant frequency in the physical frame is higher than in the solid elements model while presenting relatively similar results to the analytical and beam elements models. The higher modulus causes the beam's cross-section to remain in-plane. Since the analytical and beam elements models' formulation depicts the beam's cross-section in-plane throughout its deformation, they can capture the behaviour of the physical beam since once the cross-section is in-plane, most of the beam's bending stiffness comes from the metal components, and the elastic modulus of the polymers has less influence. On the other hand, because the polymers cannot maintain the beam's cross-section in-plane on the solid elements model, there is a significant loss in stiffness, and the second resonant frequency appears earlier.

This conclusion makes sense with the three-point bending results. The main differentiating factor between the stiffness of the analytical, beam elements and solid elements model was whether the cross-section could remain in-plane or not. Hence there is a clear distinction between the static elastic modulus and the dynamic elastic modulus of the polymeric materials.

## **4. Conclusion**

The results for both the analytical data and the beam elements models showed agreement in the static analysis and presented a similar stiffness. However, these models overestimated the stiffness of the real beam since, in the experiment, the cross-section of the composite beam did not remain in-plane due to the high difference between the elastic modulus of the brass and polymeric components. Since the formulation of these models assumes the beam keeps its cross-section in-plane, throughout its deformation, they are not very realistic. On the other hand, the solid elements model captured the deformation behaviour of the beam's cross-section and therefore depicted the real bending behaviour of the tested composite beam. Because the interface between components was not studied and therefore not accounted for in this numerical model, the sliding between components that occurred in the experiment could not be captured. In addition, despite this sliding taking place for the P.2992 beam, it never happened in the experimental test with the P.1102 beam.

In the dynamic analysis, since the dynamic modulus of the polymers was higher than their static elastic modulus and the cross-section of the physical beam remained in-plane during the experiment, opposite results from the static analysis were observed. The analytical method and the beam elements models maintained the beam's cross-section in-plane as it was deformed and exhibited similar outcomes. In addition, both could depict the resonant frequencies of the physical composite beam. On the other hand, the solid elements model did not account for the change in elastic modulus for a dynamic application, so it still depicted an unrealistic deformation behaviour for the cross-section of the beam and underestimated the stiffness of the beam. This resulted in smaller values for the resonant frequencies with mode shapes that depended on the behaviour of the cross-section of the beam.

## References

- [1]. Architecture & Design. New study indicates upward trend for global windows and doors market. Architecture news & editorial desk. July 2021. URL: <https://www.architectureanddesign.com.au/news/upward-trend-for-global-windows-and-doorsmarket#> (accessed on 12/12/2021)
- [2]. Woodland Windows & Doors Blog. 2021 Trends in Windows and Doors. Feb. 2021. URL: <https://www.woodlandwindows.com/support/blog/2021-trends-in-windowsdoors> (accessed on 12/12/2021)
- [3]. Thames Valley Window Company Blog. The 2021 Architectural Glazing Trends you need to know about. Dec. 2021. URL: <https://www.twindows.com/blog/the-2021-architectural-glazing-trends-you-need-to-know-about> (accessed on 12/12/2021).
- [4]. Thames Valley Window Company Blog. The 2021 Architectural Glazing Trends you need to know about. Dec. 2021. URL: <https://www.twindows.com/blog/the-2021-architectural-glazing-trends-you-need-to-know-about> (accessed on 12/12/2021).
- [5]. G. Solari, 'Wind Response Spectrum', J. Eng. Mech., vol. 115, no. 9, pp. 2057–2073, Sep. 1989, doi: 10.1061/(ASCE)0733-9399(1989)115:9(2057).
- [6]. C. Dyrbye and S. O. Hansen, Wind loads on structures. Chichester; New York: J. Wiley, 1997.
- [7]. A. Brandt, Noise and Vibration Analysis: Signal Analysis and Experimental Procedures, 1st ed. Wiley, 2011. doi: 10.1002/9780470978160.
- [8]. Zong Wang, Zhenhuan Li and Xiong Zhang. 'Bending resistance of thin-walled multi-cell square tubes'. In: Thin-Walled Structures 107 (2016), pp. 287–299. ISSN: 0263-8231. DOI: <https://doi.org/10.1016/j.tws.2016.06.017>.
- [9]. Xiong Zhang and Hui Zhang. 'Static and dynamic bending collapse of thin-walled square beams with tube filler'. In: International Journal of Impact Engineering 112 (2018), pp. 165–179. ISSN: 0734-743X. DOI: <https://doi.org/10.1016/j.ijimpeng.2017.11.001>.
- [10]. Liu Jin et al. 'Numerical analysis of the mechanical behavior of the impact-damaged RC beams strengthened with CFRP'. In: Composite Structures (2021). ISSN: 0263-8223. DOI: <https://doi.org/10.1016/j.compstruct.2021.114353>.
- [11]. R. D. Copetti, J. R. Claeysen, D. de R. Tolfo, and B. S. Pavlack, 'The fundamental modal response of elastically connected parallel Timoshenko beams', J. Sound Vib., vol. 530, p. 116920, Jul. 2022, doi: 10.1016/j.jsv.2022.116920.
- [12]. R. Eberle and M. Oberguggenberger, 'A new method for estimating the bending stiffness curve of non-uniform Euler-Bernoulli beams using static deflection data', Appl. Math. Model., vol. 105, pp. 514–533, May 2022, doi: 10.1016/j.apm.2021.12.042.
- [13]. 'Catalogue'. Secco sistemi, Oct. 2020.
- [14]. A. C. Alves, "Study, modelling, and dynamic analysis of construction solutions for doors and windows of buildings", MSc Dissertation, Dept. of Mechanical Engineering, Univ. of Minho, Guimarães, Portugal, 2022.
- [15]. S. Alves, "Study, modelling, and static analysis of construction solutions for doors and windows of buildings", MSc Dissertation, Dept. of Mechanical Engineering, Univ. of Minho, Guimarães, Portugal, 2022.
- [16]. P. I and S. S, 'Comparative analysis of static and dynamic elastic modulus of polymer concrete polymers', *Mach. Technol. Mater.*, vol. 10, no. 12, pp. 38–41, 2016.

- [17]. J. Fan, X. Fan, and A. Chen, 'Dynamic Mechanical Behaviour of Polymer Materials', in Aspects of Polyurethanes, F. Yilmaz, Ed. InTech, 2017. doi: 10.5772/intechopen.69570.
- [18]. A. Massa, A. Rusinek, and M. Klosak, 'Method for Determination of the Dynamic Elastic Modulus for Composite Materials', Eng. Trans., vol. 61, pp. 301–315, Dec. 2013.